

博士論文

**Experimental and Numerical Study on  
Thermal Response Test for  
Design Accuracy Improvement of  
Vertical Closed-loop Ground Heat Exchanger**

(垂直密閉型地中熱交換器の設計精度向上のための  
熱応答試験に関する実験的、数値的研究)

崔 元準



**Experimental and Numerical Study on  
Thermal Response Test for  
Design Accuracy Improvement of  
Vertical Closed-loop Ground Heat Exchanger**

by  
Wonjun Choi

A Dissertation  
Submitted to the Department of Architecture of the  
School of Engineering of the  
University of Tokyo  
in partial fulfillment of the requirements  
for the Degree of  
Doctor of Philosophy

June, 2015







# ABSTRACT

## Experimental and Numerical Study on Thermal Response Test for Design Accuracy Improvement of Vertical Closed-loop Ground Heat Exchanger

The vertical closed-loop borehole heat exchanger (BHE) is a type of ground heat exchanger, which is a key component of ground-source heat pumps (GSHPs). The design of a vertical closed-loop borehole heat exchanger requires the effective thermal conductivity of the ground and the borehole thermal resistance to be determined. During the design of a large borefield, an in situ thermal response test (TRT) is conducted to obtain reliable values for these parameters. Because the TRT setup is fully exposed to the outdoor environment, disturbances occur that can increase the error in the results. Although many new TRT and interpretation methods have been suggested, the actual practice remains the same: injecting a constant heat rate and interpreting the response data with the infinite line source (ILS) model. This is due to the high level of difficulty and greater cost of the new methods compared to the conventional method. If experimenters stay with the conventional TRT method, they should at least be equipped with comprehensive guidelines or literature that provides insights into conducting TRTs and designing the TRT setup to obtain quality data. This is the starting point of this thesis.

As an inverse problem, the TRT should satisfy the following two requirements for reliable estimation: (1) the assumptions made in the physical model (e.g., analytical or numerical) used for the inverse estimation and the experimental conditions should be consistent, and (2) the physical model should appropriately represent actual physical phenomena.

The former is with regard to the disturbances to the TRT and the resulting inconsistency between the assumptions of the physical model and the experiment. Because of the heat exchange between the surrounding environment and the TRT setup, the constant heat rate assumption of the ILS model is violated. This perturbs the temperature response, which leads to an estimation error. The latter is with regard to if the physical model can properly reflect the actual heat transfer process in the ground. Specifically, the effect of natural convection in a saturated porous formation leads the TRT results to show a heat rate dependence, which generally has been not considered or neglected.

The first half of this thesis addresses the disturbance problem. First, an analytical model that describes the heat exchange between the circulating fluid and outdoor environment in an aboveground TRT setup was derived. Based on the derived model, a parametric study and sensitivity analysis were conducted in a systematic manner using disturbance-related parameters, such as the test settings (heat injection rate and

flow rate), aboveground connecting circuit parameters (insulation thickness, length, and radiation absorptivity), temperature of fluid, and weather conditions (solar irradiation, environmental temperature, and wind velocity). Based on the results, suggestions are provided for experimenters on designing TRT setups and conducting TRTs to obtain quality data.

Second, the effect of disturbances from the outdoor environment on TRT interpretation using the ILS model was quantitatively examined with numerical methods. The derived analytical model considering disturbances was incorporated as the boundary condition of a numerical model. Typical synthetic weather data of different seasons and 36 cases of measured weather data were used to numerically conduct and interpret TRTs. Some characteristic interpreted behaviors related to weather conditions were explained. Based on the 36 cases of numerical TRTs, changes in the error range with the TRT duration were analyzed to clarify the applicability and limitations of conventional interpretation using the ILS model. Some practical suggestions regarding the performance and interpretation of TRTs are provided.

Lastly, as a solution to interpreting disturbed TRT data and to utilize additional information from the sequential estimation method, an alternative method is proposed using a temporal superposition-applied ILS model combined with the quasi-Newton optimization method. To verify the effectiveness, the proposed method was applied to in situ TRTs, and the results were compared with those from the conventional method with regard to the estimation stability and convergence speed. The objectives for the development of the new estimation method were strong robustness, fast convergence, and low computation costs for a wide practical applicability.

The second half of this thesis concerns the effect of natural convection in a saturated porous formation on the TRT results. First, to examine the performance dependence of a BHE installed in a saturated porous formation on the heat injection rate, TRTs were conducted in two BHEs having the same geometry but different backfill materials: one was cement-grouted, and the other was gravel-backfilled. TRTs were conducted for each BHE at two different single-heat injection rates (approximately 40 and 80 W/m). The TRT data were analyzed with the developed estimation method. Based on the results, discussions are presented on existing design methods related to typical practices in TRTs and the advantages of backfilled BHEs from the perspectives of performance and constructability.

Lastly, new practical TRT and interpretation methods are suggested to overcome the temporal changes in the ground conditions when examining the heat rate dependence of the TRT results. The proposed TRT method uses multiple heat injection rates. The developed parameter estimation method using the ILS model and quasi-Newton method was corrected to successfully handle multi-heat injection rate TRTs. The effectiveness of the proposed method was verified using numerically generated multi-heat injection rate TRT data. Four TRTs were conducted with two different BHEs installed in a saturated sandy formation.

Because the estimation method was sufficiently fast and robust, a real-time estimation method for onsite TRTs is also proposed to reduce the test time.

In summary, this thesis examines the experimental disturbances to a TRT and the heat rate dependence of the TRT results caused by natural convection in the ground with the ultimate objective of improving the accuracy of BHE designs. Through theoretical, numerical, and experimental examinations and verifications, insights into TRTs were generated. The obtained theoretical and numerical results will be helpful to experimenters and can be used to elaborate upon existing guidelines. Alternative interpretation methods are proposed to consider the disturbance effect and examine the heat rate dependence in a saturated porous formation. The suggested interpretation method is computationally fast and robust. Therefore, it is expected to be of practical use for in situ TRTs. The use of the proposed methods will improve the accuracy of BHE designs.



# TABLE OF CONTENTS

Table of contents.....	i
List of figures.....	v
List of tables.....	xi
Nomenclature.....	i
Chapter 1 Introduction.....	1
1.1 Background.....	2
1.1.1 Disturbances in thermal response test.....	4
1.1.2 Effect of natural convection in thermal response test.....	6
1.2 Research objectives.....	7
1.3 Thesis structure.....	10
Chapter 2 Basic theory.....	13
2.1 Transport model in ground.....	14
2.1.1 Continuum approach in porous media.....	14
2.1.2 Momentum conservation (Darcy's law).....	16
2.1.3 Mass conservation.....	19
2.1.4 Energy conservation.....	19
2.2 Design method of borehole heat exchanger.....	20
2.2.1 Simulation-based design method.....	21
2.2.2 ASHRAE design method.....	23
2.3 Thermal response test and infinite line source model.....	26
2.4 Thermal response test as inverse problem.....	29
2.4.1 Inverse parameter estimation.....	30
2.4.2 Issues with thermal response test from inverse problem perspective.....	31
Chapter 3 Experimental setup and uncertainty analysis.....	33
3.1 Borehole heat exchangers.....	34

3.2 Thermal response test apparatus .....	37
3.3 Uncertainty analysis.....	43
3.3.1 Standard uncertainty.....	44
3.3.2 Combined standard uncertainty.....	47
3.3.3 Uncertainty analysis of TRT interpretation .....	49
3.3.4 Expanded uncertainty of TRT .....	51
 Chapter 4 Development of analytical disturbance model, parametric study, and sensitivity analysis .....	 53
4.1 Introduction.....	54
4.2 Analytical Model considering disturbance in thermal response test.....	56
4.2.1 Derivation of disturbance model .....	56
4.2.2 Description of parameters in derived model.....	59
4.3 Parametric study using disturbance model .....	64
4.3.1 Reference conditions .....	65
4.3.2 Settings of TRT rig and temperature of circulating fluid .....	66
4.3.3 Aboveground hydraulic circuit .....	72
4.3.4 Weather conditions .....	75
4.4 Sensitivity analysis .....	77
4.5 Conclusions.....	81
 Chapter 5 Applicability and limitations of infinite line source model for interpretation of disturbed response data .....	 83
5.1 Introduction.....	84
5.2 Description of numerical model.....	84
5.2.1 Governing equation .....	84
5.2.2 1-D representation of flow in U-tube and governing equations of linear element.	85
5.2.3 Effective pipe thermal conductivity .....	87
5.2.4 Discretized model and element properties .....	88
5.2.5 Disturbance model combined as boundary condition of BHE.....	90
5.3 Validation of numerical model.....	93
5.3.1 Validation against infinite line source model .....	93
5.3.2 Validation using in-situ TRT data.....	95

---

5.4 Analysis of disturbance effect .....	98
5.4.1 Effect of outdoor environment: using synthetic weather data .....	98
5.4.2 Effect of outdoor environment: using measured weather data .....	104
5.5 Discussion and conclusion.....	114
<b>Chapter 6 Development of interpretation method considering disturbance .....</b>	<b>117</b>
6.1 Introduction.....	118
6.2 Theoretical analysis: why disturbance effect should be included .....	119
6.3 Development of disturbance-considered interpretation method .....	121
6.3.1 Infinite line source model with temporal superposition principle .....	121
6.3.2 Parameter estimation using quasi-Newton method .....	123
6.3.3 Sensitivity analysis of parameter estimation .....	129
6.4 Thermal response test .....	131
6.4.1 Test conditions.....	131
6.4.2 Temperature response .....	131
6.4.3 Developed parameter estimation method versus conventional regression method .....	132
6.5 Advantages of proposed method .....	137
6.6 Conclusion.....	139
<b>Chapter 7 Effect of natural convection on thermal response test .....</b>	<b>141</b>
7.1 Introduction.....	142
7.2 Temperature response test: single-heat injection rate TRT .....	144
7.2.1 Test conditions.....	144
7.2.2 Temperature response and interpretation of TRT data.....	145
7.3 Interpretation of TRT data.....	147
7.4 Discussion .....	153
7.4.1 Guidelines for consideration of heat rate dependence of TRT in testing .....	153
7.4.2 Advantages of gravel-backfilled BHE in saturated porous formation.....	154
7.5 Conclusion.....	155

Chapter 8 Parameter estimation method to determine heat injection rate dependence in saturated porous formation .....	157
8.1 Introduction.....	158
8.2 Multi-heat injection rate TRT and parameter estimation methods .....	159
8.2.1 Multi-heat injection rate TRT method .....	159
8.2.2 Parameter estimation method .....	160
8.2.3 Verification of proposed estimation method .....	163
8.4 Multi-heat injection TRT and results.....	167
8.4.1 Test condition.....	167
8.4.2 Temperature response .....	167
8.4.3 Interpretation results .....	168
8.4 Real-time interpretation method for onsite TRT .....	176
8.5 Conclusion.....	178
Chapter 9 Conclusions and future studies.....	179
9.1 Conclusions.....	180
9.2 Recommendations for future studies .....	182
References.....	183
Appendix A. Developed subroutine used in Chapter 5 .....	195
A.1 Main code .....	195
A.2 Header code 1 (TRTheatload.h).....	204
A.3 Header code 2 (TRTflowrate.h).....	205
Publications.....	209
Acknowledgments .....	211

# LIST OF FIGURES

## Chapter 1

<b>Fig. 1.1</b> Schematic of two heat pumps using different source and sink temperatures: (a) air-source heat pump and (b) ground-source heat pump using vertical-closed loop borehole heat exchanger.....	3
<b>Fig. 1.2</b> Schematic of thermal response test setup. ....	4
<b>Fig. 1.3</b> Schematic of heat transfer in aboveground hydraulic circuit. ....	5
<b>Fig. 1.4</b> Schematic of line heat source in saturated porous formation and macroscopic convection currents.....	7
<b>Fig. 1.5</b> Research flow and structure of thesis. ....	11

## Chapter 2

<b>Fig. 2.1</b> Schematic of representative elementary volume (REV), $s$ : solid, $f$ : fluid (= liquid). ....	14
<b>Fig. 2.2</b> Porosity as function of averaging volume. $\delta$ : microscopic length scale, $D$ : macroscopic length scale, and $L$ : length scale of gross inhomogeneities.....	15
<b>Fig. 2.3</b> Schematic of aquifer and different types of viscous stress terms. ....	17
<b>Fig. 2.4</b> Three load pulses of different lengths.....	25

## Chapter 3

<b>Fig. 3.1</b> TRT setup at site: (1) gravel-backfilled BHE, (2) observation well, and (3) cement-grouted BHE.....	35
<b>Fig. 3.2</b> Schematic illustration of (a) drill log of the experiment site and (b) experimental setup....	35
<b>Fig. 3.3</b> Spacer used to maintain shank space of U-tube (units of ruler: cm). ....	36
<b>Fig. 3.4</b> Grain size of the gravel used in backfilled BHE (units of ruler: cm). ....	36
<b>Fig. 3.5</b> T-type thermocouples installed on surface of U-tube.....	37
<b>Fig. 3.6</b> Schematic diagram of thermal response test apparatus. ....	38
<b>Fig. 3.7</b> Control sequence of TRT apparatus. ....	39
<b>Fig. 3.8</b> Schematic of electrical circuit of TRT apparatus. ....	40
<b>Fig. 3.9</b> Schematic of control circuit of TRT apparatus.....	41

## Chapter 4

<b>Fig. 4.1</b> Schematic of aboveground thermal response test (TRT) setup. ....	56
<b>Fig. 4.2</b> Radiative heat transfer on surface of aboveground hydraulic circuit. ....	60
<b>Fig. 4.3</b> Thermal resistance network for heat transfer between circulating fluid and outdoor environment.....	63
<b>Fig. 4.4</b> Change in disturbed heat rate in inflow circuit due to changes in heat injection rate per unit length of borehole heat exchanger (left vertical axis: daytime of intermediate season; right vertical axis: nighttime of winter). ....	67
<b>Fig. 4.5</b> Changes in disturbed heat rate ratio with changes in heat injection rate per unit length of borehole heat exchanger ( $Q_{d,tot}$ : total disturbed heat rate; $Q_{rig}$ : heat injection rate; Int-day: daytime of intermediate season; Win-night: nighttime of winter). ....	68
<b>Fig. 4.6</b> Changes in the disturbed heat rate in aboveground hydraulic circuit with changes in outlet fluid temperature of borehole heat exchanger, $T_{cf,out,BHE}$ (Sum-day: daytime of summer; Sum-night: nighttime of summer; Win-night: nighttime of winter).....	69
<b>Fig. 4.7</b> Changes in disturbance ratio with changes in outlet fluid temperature of borehole heat exchanger, $T_{cf,out,BHE}$ .....	69
<b>Fig. 4.8</b> Changes in overall thermal resistance of outflow circuit with changes in volumetric flow rate.....	70
<b>Fig. 4.9</b> Changes in disturbed heat rate ratio with changes in volumetric flow rate; (a) daytime of intermediate season and (b) nighttime of intermediate season.....	71
<b>Fig. 4.10</b> Changes in disturbed heat rate ratio with changes in length of hydraulic circuit, $L$ .....	72
<b>Fig. 4.11</b> Changes in thermal resistance of insulation layer with changes in thickness of insulation, $\tau_{ins}$ .....	73
<b>Fig. 4.12</b> Changes in disturbed heat rate ratio with changes in insulation thickness, $\tau_{ins}$ .....	73
<b>Fig. 4.13</b> Changes in disturbed heat rate ratio with changes in radiation absorptivity of insulation surface, $a_{ins}$ .....	74
<b>Fig. 4.14</b> Changes in overall thermal resistance $R_{tot,out}$ of outflow circuit and sol-air temperature $T_{sol,a}$ with changes in wind velocity (daytime of summer).....	75
<b>Fig. 4.15</b> Changes in disturbed heat rate ratio with changes of wind velocity, $v_w$ .....	76
<b>Fig. 4.16</b> Changes in global solar irradiation, $I_{sol}$ , and resulting changes in (a) environmental temperature, $T_{sol,a}$ or $T_{amb}$ , and (b) total disturbed heat rate, $Q_{d,tot}$ .....	76
<b>Fig. 4.17</b> Changes in disturbed heat rate ratio with changes in global solar irradiation, $I_{sol}$ .....	77

## Chapter 5

- Fig. 5.1** Schematic of simplified flow and heat transfer in the U-tube; (a) actual pipe flow and (b) simplified flow model using linear flow element based on the Hagen–Poiseuille law and a solid with anisotropic thermal conductivity. .... 85
- Fig. 5.2** Details of discretized numerical model (not to scale); (a) overview of model, (b) plan, and (c) enlarged plan around BHE..... 89
- Fig. 5.3** Comparison of the numerical model and ILS model; (a) temperature response of the two models and (b) sequential estimation using the temperature data from the numerical model. .... 94
- Fig. 5.4** Comparison of the experimental and numerical temperature responses using actual heat injection rate (the heat injection rate was calculated from the measured inlet and outlet temperatures and the volumetric flow rate)..... 95
- Fig. 5.5** Weather data measured from the start of heat injection during the thermal response test (from May 15, 2014 at 22:00). .... 97
- Fig. 5.6** Comparison of the experimental and numerical temperature responses using the heat injection rate from the wattmeter; (a) disturbance model not applied and (b) disturbance model applied. .... 97
- Fig. 5.7** Generated synthetic weather data using Eq. (5.30) and Eq. (5.31); (a) summer, (b) intermediate season, and (c) winter. .... 99
- Fig. 5.8** Numerical thermal response test using synthetic weather data of summer and the estimated results; (a) temperature response and absolute relative error compared with the ILS model, (b) disturbed heat rate and its ratio, and (c) sequential plot. .... 101
- Fig. 5.9** Numerical thermal response test using synthetic weather data of intermediate season and the estimated results; (a) temperature response and absolute relative error compared with the ILS model, (b) disturbed heat rate and its ratio, and (c) sequential plot..... 102
- Fig. 5.10** Numerical thermal response test using synthetic weather data of winter and the estimated results; (a) temperature response and absolute relative error compared with the ILS model, (b) disturbed heat rate and its ratio, and (c) sequential plot..... 103
- Fig. 5.11** Numerical thermal response test (TRT7) using measured weather data (from Jun. 27, 2013, 00:00) and the estimated results; (a) weather data, (b) temperature response and absolute relative error compared with the ILS model, (c) disturbed heat rate and its ratio, and (d) sequential plot. .... 107
- Fig. 5.12** Numerical thermal response test (TRT18) using measured weather data (from Oct. 03, 2014, 00:00) and the estimated results; (a) weather data, (b) temperature response and absolute relative error compared with the ILS model, (c) disturbed heat rate and its ratio, and (d) sequential plot. .... 108
- Fig. 5.13** Numerical thermal response test (TRT23) using measured weather data (from Nov. 08, 2014, 00:00) and the estimated results; (a) weather data, (b) temperature response and absolute relative error compared with the ILS model, (c) disturbed heat rate and its ratio, and (d) sequential plot. .... 109

<b>Fig. 5.14</b> Numerical thermal response test (TRT25) using measured weather data (from Jan. 21, 2015, 00:00) and the estimated results; (a) weather data, (b) temperature response and absolute relative error compared with the ILS model, (c) disturbed heat rate and its ratio, and (d) sequential plot. ....	110
<b>Fig. 5.15</b> Maximum, minimum, average, and standard deviations at different estimation times based on data of 36 numerical thermal response tests; (a) effective thermal conductivity and (b) borehole thermal resistance. ....	112
<b>Chapter 6</b>	
<b>Fig. 6.1</b> Temporal superposition of heat pulses. ....	122
<b>Fig. 6.2</b> Calculation flow of the quasi-Newton method. ....	126
<b>Fig. 6.3</b> Flow chart of the parameter estimation. ....	127
<b>Fig. 6.4</b> Comparison of the computation time between the downhill Simplex method and quasi-Newton method. ....	128
<b>Fig. 6.5</b> Relative sensitivity coefficients of effective thermal conductivity and borehole thermal resistance. ....	130
<b>Fig. 6.6</b> Temperature response from GR4 showing the (a) average fluid temperature, heat injection rate, and outdoor dry-bulb temperature and (b) semi-logarithm plot of the average water temperature. ....	133
<b>Fig. 6.7</b> Temperature response from GR2 showing the (a) average fluid temperature, heat injection rate, and outdoor dry-bulb temperature and (b) semi-logarithm plot of the average water temperature. ....	134
<b>Fig. 6.8</b> Estimated effective thermal conductivity and borehole thermal resistance of GR4 using the sequential method (GR4-Seq) and the developed parameter estimation method (GR4-PE). ....	135
<b>Fig. 6.9</b> Estimated effective thermal conductivity and borehole thermal resistance from GR2 using the sequential method (GR2-Seq) and the developed parameter estimation method (GR2-PE). ....	135
<b>Chapter 7</b>	
<b>Fig. 7.1</b> Schematic diagrams of two borehole heat exchanger (BHE) configurations: (a) groundwater-filled BHE and (b) backfilled BHE installed in porous formation. ....	143
<b>Fig. 7.2</b> Temperature response curve and heat injection rate of two TRTs using 2 kW heater; (a) GR2: cement-grouted BHE using 2 kW heater and (b) BF2: gravel-backfilled BHE using 2 kW heater. ....	146
<b>Fig. 7.3</b> Temperature response curve and heat injection rate of two TRTs using 4 kW heater; (a) GR4: grouted BHE using 4 kW heater and (b) BF4: backfilled BHE using 4 kW heater. ....	147
<b>Fig. 7.4</b> Sequential estimation using TRT data from GR-BHE; (a) GR2: grouted BHE using 2 kW heater and (b) GR4: grouted BHE using 4 kW heater. ....	148

<b>Fig. 7.5</b> Sequential estimation using TRT data from BF-BHE; (a) BF2: gravel-backfilled BHE using 2 kW heater and (b) BF4: gravel-backfilled BHE using 4 kW heater.....	149
<b>Fig. 7.6</b> Results of parameter estimation using the TRT data of cement grouted BHE; (a) estimation using GR2 data and (b) estimation using GR4 data. ....	151
<b>Fig. 7.7</b> Results of parameter estimation using the TRT data of gravel backfilled BHE; (a) estimation using BF2 data and (b) estimation using BF4 data. ....	152
 <b>Chapter 8</b>	
<b>Fig. 8.1</b> Schematic illustration of temporal changes in ground conditions. ....	159
<b>Fig. 8.2</b> Example of piecewise square pulses (6 min) and measured heat injection rate. In the study, each pulse was 3 min long. However, the pulses presented here are 6 min long for clarity. ....	161
<b>Fig. 8.3</b> Flowchart of parameter estimation for multi-heat injection rate thermal response test.....	163
<b>Fig. 8.4</b> Overview of discretized numerical model and size of model domain (not to scale). ....	164
<b>Fig. 8.5</b> Temperature response curve and heat injection rate from numerical thermal response test. ....	166
<b>Fig. 8.6</b> Estimated results and deviation of borehole thermal resistance based on final estimated value in first injection period ( $t_{pl} = 48$ h): (a) estimated effective thermal conductivity and borehole thermal resistance and (b) absolute and relative errors of borehole thermal resistance based on final estimated value in first injection period. ....	166
<b>Fig. 8.7</b> Temperature response curve and heat injection rate of 24–48 h cases: (a) GR1 and (b) BF1. ....	169
<b>Fig. 8.8</b> Temperature response curve and heat injection rate of 48–72 h cases: (a) GR2 and (b) BF2. ....	170
<b>Fig. 8.9</b> Sequential estimation of first injection period ( $t_{pl} = 48$ h): (a) GR1 and (b) BF1. ....	171
<b>Fig. 8.10</b> Sequential estimation of first injection period ( $t_{pl} = 72$ h): (a) GR2 and (b) BF2. ....	172
<b>Fig. 8.11</b> Estimated effective thermal conductivity and borehole thermal resistance using developed method; (a) GR1 and (b) BF1. ....	173
<b>Fig. 8.12</b> Estimated effective thermal conductivity and borehole thermal resistance using developed method; (a) GR2 and (b) BF2. ....	174
<b>Fig. 8.13</b> Residuals of BF1 estimation (3 min intervals from 15 h to 72 h; 1140 time steps in total). ....	174
<b>Fig. 8.14</b> TRT results obtained at same site from February 2014 to March 2015. ....	175
<b>Fig. 8.15</b> Computation time for estimation of GR2 (3 min intervals from 15 h to 120 h, 2100 time steps in total, total computation time of 49.0 s).....	176
<b>Fig. 8.16</b> Flowchart for real-time application of developed method.....	177



# LIST OF TABLES

## Chapter 3

<b>Table 3.1</b> Detailed parameters of borehole heat exchanger (BHE) setup and soil. ....	34
<b>Table 3.2</b> Details of components used in the TRT apparatus. ....	38
<b>Table 3.3</b> Abbreviations used in Fig. 3.8 and Fig. 3.9 for electrical and control circuits.....	42
<b>Table 3.4</b> Schematic of probability distribution shapes.....	47
<b>Table 3.5</b> Specified and assumed error range and used uncertainty of individual input quantities..	50
<b>Table 3.6</b> Calculated results and error contribution of each input variable. ....	51

## Chapter 4

<b>Table 4.1</b> Reference conditions and parameters for analysis.....	65
<b>Table 4.2</b> Reference weather conditions and resulting disturbance (positive: heat gain from environment to fluid, negative: heat loss from fluid to environment). ....	66
<b>Table 4.3</b> Differences between environmental temperature and borehole heat exchanger outlet temperature of circulating fluid, and normalized relative sensitivity coefficients of each parameter in six weather conditions. ....	79

## Chapter 5

<b>Table 5.1</b> Parameters of borehole heat exchanger (BHE), thermal response test (TRT) setup, soil, and settings of test. ....	90
<b>Table 5.2</b> Parameters of aboveground hydraulic circuit used for validation of the numerical model. ....	96
<b>Table 5.3</b> Coefficients for the synthetic ambient temperature (Eq. (5.30)). ....	98
<b>Table 5.4</b> Coefficients for the synthetic global solar irradiation (Eq. (5.31)).....	98
<b>Table 5.5</b> Simulated results using synthetic weather data; averaged heat rate, final estimated results, maximum and minimum values, and standard deviations based on the final estimated values.....	100
<b>Table 5.6</b> Simulated results using measured weather data; averaged heat rate, final estimated results, maximum and minimum values, and standard deviations based on the final estimated values.....	104
<b>Table 5.7</b> Summary of 36 numerical thermal response tests (TRTs). ....	105
<b>Table 5.8</b> Average, minimum, maximum, and standard deviations of the effective thermal conductivity at different estimation times based on 36 numerical thermal response tests (unit: W/(m·K)).....	113

<b>Table 5.9</b> Average, minimum, maximum, and standard deviations of the borehole thermal resistance at different estimation times based on 36 numerical thermal response tests (unit: m·K/W). .....	113
--	-----

## Chapter 6

<b>Table 6.1</b> Experimental conditions for the two thermal response tests (TRTs).....	131
<b>Table 6.2</b> Final estimated values for each of the methods along with the maximum and minimum values, and the standard deviations that were obtained over time intervals of 17–70 h and 17–140 h (the max and min values were obtained from the estimated values at 17–140 h). .....	137

## Chapter 7

<b>Table 7.1</b> Experimental conditions for the thermal response tests. ....	145
<b>Table 7.2</b> Final values obtained by sequential estimation using the ILS model.....	149
<b>Table 7.3</b> Estimated effective thermal conductivity and borehole thermal resistance and their rates of change based on 2 kW TRT cases.....	151

## Chapter 8

<b>Table 8.1</b> Thermal properties used in numerical model and settings for TRT. ....	165
<b>Table 8.2</b> Initial guess values and estimated values. ....	167
<b>Table 8.3.</b> Experimental conditions for four thermal response tests (averaged values during each test). .....	168
<b>Table 8.4.</b> Final average temperature of each injection period.....	168
<b>Table 8.5</b> Initial guess values used for the estimations, estimated effective thermal conductivity, borehole thermal resistance, and rate of change in borehole thermal resistance from first injection period to second injection period.....	173

# NOMENCLATURE

$a_i$	upper or lower bound of measurement distribution
$a_{ins}$	radiation absorptivity of surface, [J/(kg·K)]
$B$	thickness of layer or aquifer, [m]
$B$	distance between boreholes in a borefield, [m]
$c$	specific heat capacity, [J/(kg·K)]
$c_i$	sensitivity coefficient
$C$	volumetric heat capacity, [J/(m <sup>3</sup> ·K)]
$D$	depth of upper end of borehole heat exchanger, [m]
Ei	exponential integral
$f$	friction coefficient
$f_{obj}$	objective function
$f_\mu$	viscosity relation function
Fo	Fourier number ( $= \alpha_s t / r_b^2$ )
$F_{cor}$	correction factor for sol-air temperature
$g$	gravitational acceleration, [m/s <sup>2</sup> ]
$g_n$	g-function of $n$ BHEs based on FLS model
$G$	g-factor of BHE based on ICS model
$h$	hydraulic head, [m]
$h_i$	convective heat transfer coefficient of pipe inner surface, [W/(m <sup>2</sup> ·K)]
$h_o$	overall heat transfer coefficient of outer surface, [W/(m <sup>2</sup> ·K)]
$H$	Heaviside step function; length of BHE, [m]
$I_{sol}$	global solar irradiation, [W/m <sup>2</sup> ]
$J_0, J_1$	Bessel functions of the first kind of the zeroth and first orders
$k$	gradient of temperature response in the semi-log plot
$k$	coverage factor for the confidence interval
$\mathbf{k}$	permeability tensor, [m <sup>2</sup> ]
$K$	overall heat transfer coefficient per unit pipe length, [W/(m·K)]
$\mathbf{K}$	hydraulic conductivity, [m/s]
$l$	a certain location on aboveground hydraulic circuit

$L$	half-length of the aboveground hydraulic circuit, [m]
$n$	time step number
$N$	the number of time steps or measured data
$N$	the number of borehole heat exchangers
$Nu$	Nusselt number
$p$	pressure, [Pa]
$P$	dimensionless distance based on radius of BHE ( $= r/r_b$ )
$P(x_i)$	probability of $x_i$
$P_i$	$i$ -th parameter
$Pr$	Prandtl number
$q$	Heat rate per unit length of BHE, [W/m]
$\mathbf{q}$	Darcy velocity, [m/s]
$q_{avg}$	averaged heat injection rate per unit length of BHE, [W/m]
$q_{load}$	internal heat load, [W]
$q_h$	hourly peak heat load, [W]
$q_{hp}$	heat injection/rejection from heat pump, [W]
$q_k$	$k$ -th measured input quantity
$q_m$	average monthly heat load, [W]
$q_y$	average yearly heat load, [W]
$q_0$	step constant heat flux per unit length of BHE, [W/m]
$Q$	heat exchange rate between the TRT system and the outdoor environment, [W]
$Q_{amb}$	heat exchange rate between the circulating fluid and the outdoor environment by convection and conduction, [W]
$Q_B$	correction source/sink term of mass, [1/s]
$Q_{BHE}$	actual heat injection rate to BHE, [W]
$Q_d$	disturbed heat rate between the circulating fluid and the outdoor environment, [W]
$Q_{d,ratio}$	disturbance ratio ( $= Q_{d,tot}/Q_{rig}$ ), [W]
$Q_{p1}, Q_{p2}, Q_{p3}$	heat injection rate of first, second, and third injection periods, [W]
$Q_{rig}$	generated heat from heater and pump in TRT rig, [W]
$Q_T$	source/sink term of internal energy, [W/m <sup>3</sup> ]
$Q_\rho$	source/sink term of fluid mass, [1/s]
$r$	cylindrical coordinates; radius, [m]
$r$	correlation coefficient

$r_b$	radius of borehole, [m]
$r_{hydr}$	hydraulic radius (= flow area/wetted perimeter), [m]
$R$	thermal resistance, [m·K/W]
$R_b$	borehole thermal resistance, [m·K/W]
$R_{tot}$	overall thermal resistance, [m·K/W]
$\Delta R$	difference between longwave radiation incident on surface from sky and surroundings and radiation emitted by blackbody at outdoor air temperature, [W/m <sup>2</sup> ]
$Re$	Reynolds number
$s$	shank spacing, [m]
$s^2$	variance from measurement
$S_o$	the specific storage due to fluid and medium compressibility, [1/m]
$t$	time, elapsed time after heat injection, [s]
$t_{cur}$	current time from heat injection, [h]
$t_j$	time step of estimation
$t_n$	discrete elapsed time after heat injection, [s]
$t_{p1}, t_{p2}, t_{p3}$	final time or duration of first, second, and third heat injection periods, [h]
$t_s$	steady-state time scale (= $H^2/9\alpha_s$ ), [s]
$T$	temperature, [°C]
$T_b$	temperature of borehole wall, [°C]
$T_{bf}$	average borehole wall temperature of borefield, [°C]
$\bar{T}_{cf}$	average temperature of circulating fluid, [°C]
$T_{env}$	environmental temperature ( $T_{amb}$ or $T_{sol,a}$ ), [°C]
$T_g$	undisturbed ground temperature, [°C]
$T_p$	temperature penalty, [°C]
$T_{sol,a}$	sol-air temperature, [°C]
$u$	standard uncertainty (=standard deviation of a measured quantity)
$u_c$	combined uncertainty
$v$	velocity, [m/s]
$\bar{v}$	averaged velocity, [m/s]
$v_w$	wind velocity, [m/s]
$V$	volume, [m <sup>3</sup> ]
$\dot{V}$	volumetric flow rate, [m <sup>3</sup> /s]
$V_{eff}$	effective pore volume, [m <sup>3</sup> ]

$x$	input estimates from measurement
$X$	input quantity
$y$	output estimate from measurement
$Y$	measurand (measured quantity)
$\mathbf{Y}$	measured temperature vectors, [°C]
$Y_0, Y_1$	Bessel functions of the second kind of the zeroth and first orders
$z$	altitude; height above ground, [m]

**Subscripts**

0	reference, initial
$amb$	ambient air
$avg$	average
$b$	borehole
$BHE$	borehole heat exchanger
$c$	convective
$cal$	calculated
$cf$	circulating fluid
$dist$	disturbance
$eff$	effective
$exp$	experimental
$f$	final, fluid phase
$i$	inner
$in$	inflow circuit (from outlet of TRT rig to BHE inlet)
$ini$	initial value of parameter estimation
$ins$	insulation
$lat$	latent heat
$lim$	limit condition
$m$	measured site
$n$	time step number
$o$	outer
$out$	outflow circuit (from BHE outlet to inlet of TRT rig)
$p$	pipe

$r$	radius of borehole; location of borehole wall
$rad$	radiation
$rig$	TRT rig
$s$	soil, solid phase
$surr$	surroundings
$tot$	total
$w$	wind
$\alpha$	$\alpha$ -phase

### Superscripts

$t_j$	time step of estimation
$t_0$	first time step of estimation
$T$	transpose of matrix or vector
$\alpha$	exponent of power-law

### Greek letters

$\alpha$	thermal diffusivity, [m <sup>2</sup> /s]
$\alpha_L$	longitudinal thermal dispersivity, [m]
$\alpha_T$	transverse thermal dispersivity, [m]
$\beta$	thermal expansion coefficient, [1/K]
$\varepsilon$	porosity of soil, emissivity of surface
$\varepsilon_i$	error contribution of input parameter, [%]
$\varepsilon_{rel}$	absolute relative error, [%]
$\gamma$	the Euler–Mascheroni’s constant ( $\cong 0.5772$ )
$\gamma$	solid compressibility, [1/Pa]
$\bar{\gamma}$	fluid compressibility, [1/Pa]
$\gamma_f$	fluid compressibility, [1/Pa]
$\delta$	unit (identity) tensor
$\kappa$	non-dimensional parameter
$\lambda$	thermal conductivity, [W/(m·K)]
$\lambda_b$	bulk thermal conductivity tensor, [W/(m·K)]
$\lambda_{disp}$	thermal dispersion tensor, [W/(m·K)]

$\mu$	dynamic viscosity, [kg/(m·s)]
$\nu$	kinematic viscosity, [m <sup>2</sup> /s]
$\rho$	density, [kg/m <sup>3</sup> ]
$\sigma$	standard deviation; Stefan-Boltzmann constant, [W/(m <sup>2</sup> ·K <sup>4</sup> )]
$\boldsymbol{\sigma}^B$	shear stress tensor at the bottom of aquifer, [kg/m <sup>2</sup> s <sup>2</sup> ]
$\boldsymbol{\sigma}^{int}$	momentum exchange tensor at the interface between solid and liquid
$\boldsymbol{\sigma}^T$	shear stress tensor at the top of aquifer, [kg/m <sup>2</sup> s <sup>2</sup> ]
$\tau$	thickness, [m]
$\psi$	scalar quantity
$\chi$	buoyancy coefficient

**Acronyms, abbreviations**

BF	gravel-backfilled
FLS	finite line source model
GR	cement-grouted
ICS	infinite cylindrical source model
ILS	infinite line source model
PE	parameter estimation method
SC	sensitivity coefficient
Seq	sequential plot method
RSC	relative sensitivity coefficient
RSC*	normalized relative sensitivity coefficient

**Symbols, operators**

$\otimes$	tensor product
$\  \quad \ $	vector norm

All bold characters represent a vector or matrix form.





CHAPTER 1  
INTRODUCTION

## 1.1 Background

The term “sustainable development” gained popularity and became a global issue after the publication of the Brundtland Report [1]. In this context, the utilization of renewable energy has received much attention. According to the International Energy Agency [2], the building sector accounts for 35% of the global energy consumption. Space heating, space cooling, and water heating are estimated to account for nearly 60% of the global energy consumption by buildings. This means that the utilization of renewable energy and the equipment efficiency of buildings have a significant impact on reducing the energy consumption of buildings and improving energy security.

Air-source heat pumps (ASHPs) are widely used for space cooling and heating and sometimes water heating. ASHPs are applicable to a wide range of uses, but one drawback is that their performance is very sensitive to outdoor conditions (Fig. 1.1(a)). Specifically, when the peak cooling or heating load occurs while the operating conditions of the heat pump are very unfavorable, the performance becomes very poor. Recently, the use of ground-source heat pumps (GSHP) has been steadily increasing. Compared to an ASHP, a GSHP has the advantage of utilizing the ground, which has a stable and moderate temperature, as the heat source or sink; thus, a relatively high level of performance can be achieved regardless of the outdoor conditions (Fig. 1.1(b)). Therefore, GSHPs are being increasingly discussed and promoted as an alternative method to reducing the use of fossil fuels.

Despite its advantages, the relatively high initial cost from the installation of ground heat exchanges (GHEs) is the biggest barrier to the widespread application of GSHPs. Given that buildings and related equipment have a long lifetime, the lower operating costs of GSHP should be considered a very attractive feature. However, many building owners still prefer existing systems because there is no confidence that the life-cycle cost will be minimized with a GSHP system. Overcoming this barrier involves considering various angles, such as construction and design perspectives with regard to the GHE. The latter can involve the design method itself or information required about the thermal properties of the ground and GHE parameters for the GHE design.

This thesis focuses on the design parameters, especially for the vertical GHE; this is also known as a vertical closed-loop borehole heat exchanger (BHE). This is one of the most frequently installed types of GHEs because it requires less space than horizontal or slinky-type GHEs and is not strictly affected by regulations related to the use of groundwater.

For BHE design, the effective thermal conductivity of the ground (e.g., spatial-averaged thermal conductivity in the vicinity of the BHE) and borehole thermal resistance must be known to select an appropriate size for the BHE. The former is a site-specific value, whereas the latter depends on the geometry of the BHE and the thermal properties of the pipes and materials (e.g., grout and backfill soil)

that fill the annular space of the borehole. In the design of large-scale borefields, these values have a significant impact [3], so many engineers conduct in situ thermal response tests (TRTs) to obtain them.

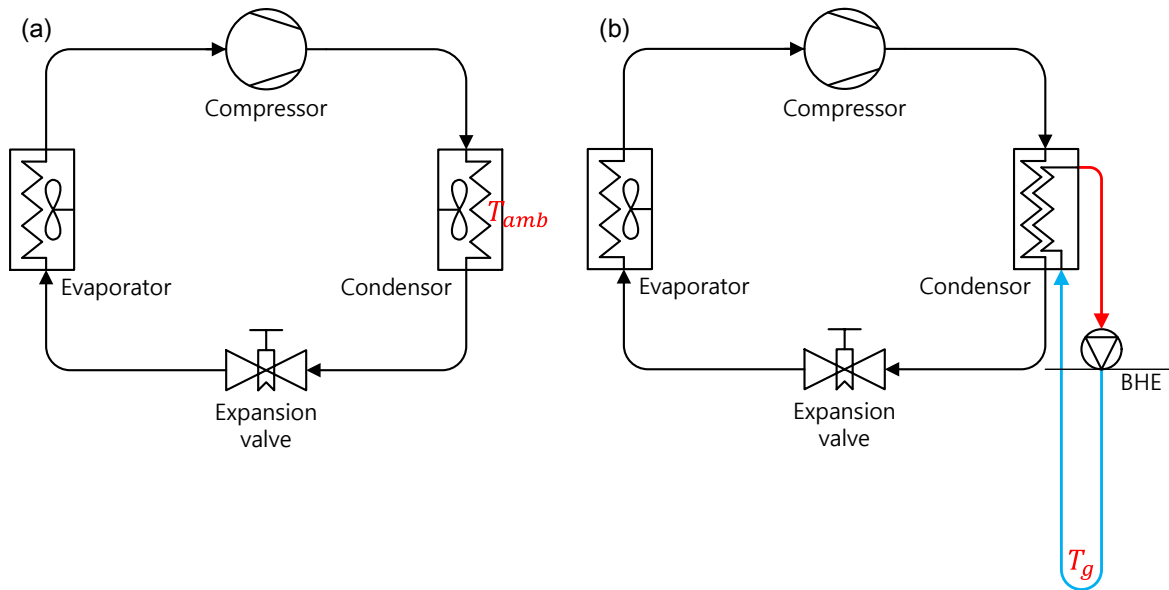


**Fig. 1.1** Schematic of two heat pumps using different source and sink temperatures: (a) air-source heat pump and (b) ground-source heat pump using vertical-closed loop borehole heat exchanger.

The TRT is a process to inversely estimate the thermal properties of the ground from its measured temperature response. Generally, the TRT setup consists of a BHE installed at the building site and TRT apparatus that can generate heat, circulate heat carrier fluid, and measure data (Fig. 1.2). This basic concept has been applied in similar engineering fields, such as in geothermal power plants to determine the true formation temperature or in well tests by the petroleum industry. After Mogensen [4] first proposed the idea of a TRT, pioneering studies involving in situ TRTs were conducted with mobile test rigs in the mid-1990s [5,6] on shallow geothermal fields.

There are some issues regarding the accuracy and reliability of TRT results. When a TRT is considered from the perspective of an inverse problem, where parameters are estimated from the measurement of dependent variables, the accuracy issues should be closely considered from two perspectives: (1) whether the assumptions made in the physical model (e.g., analytical or numerical) used for the inverse estimation and the experimental conditions are consistent, and (2) whether the physical model can appropriately represent actual physical phenomena. These two perspectives are commonly considered in inverse problems. The former is with regard to disturbances in the TRT and the resulting inconsistency between the assumptions of the physical model and the experiment, and the latter is with regard to the actual heat

transfer process in the ground. The accuracy and reliability issues are explained in the following subsections based on these two perspectives.

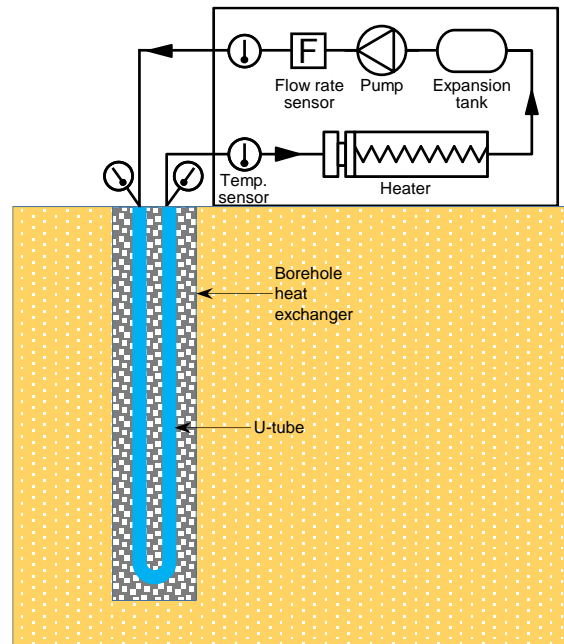


**Fig. 1.2** Schematic of thermal response test setup.

### 1.1.1 Disturbances in thermal response test

Significant efforts have been made to increase the cost efficiency, time efficiency, and accuracy of TRTs. Many new experimental and analytical methods have been proposed. As one example, the distributed TRT has been proposed to obtain the vertical distribution of the thermal conductivity of the ground [7,8] in order to gain more information than just the effective thermal conductivity, which represents the spatial-averaged thermal conductivity in the vicinity of the BHE. However, the effective thermal conductivity is generally sufficient for BHE design, and the most common TRT method is to use a constant heat injection rate and flow rate. This experimental method is based on analytical models that assume a constant heat flux from the source, such as the infinite line source (ILS) model [9,10], infinite cylindrical source (ICS) model [10], and finite line source (FLS) model [11–13]. These models are frequently used to interpret the measured temperature response.

At actual TRT sites, there are many problems with the use of the conventional TRT method and its interpretation because, in contrast to well-controlled laboratory conditions, a TRT is fully exposed to the outdoor environment. The surrounding outdoor environment of the TRT setup continuously changes. As shown in Fig. 1.3, radiative, convective, conductive, and sometimes evaporative heat transfers always

affect the TRT setup installed aboveground. Therefore, the constant heat rate assumption in the analytical model is violated by the heat exchange between the circulating fluid and outdoor environment in the aboveground hydraulic circuit connecting the BHE and TRT apparatus and the unstable heat generation caused by fluctuations in the supply voltage.

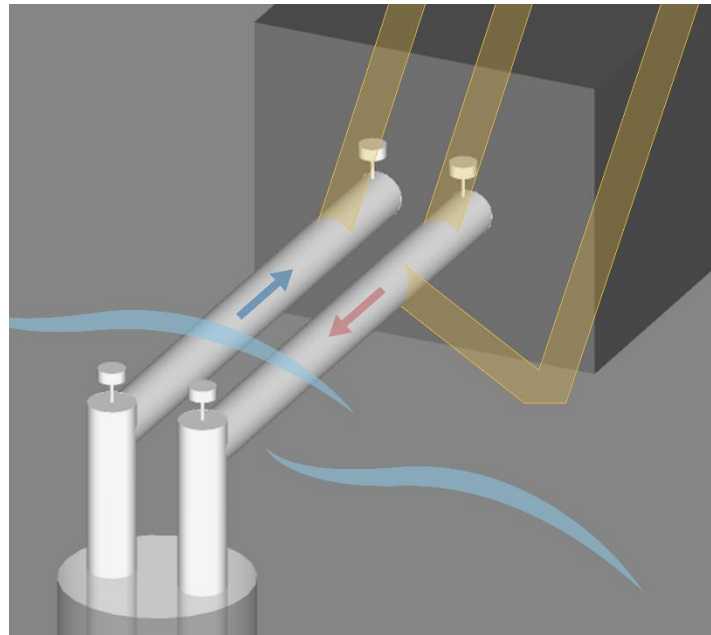


**Fig. 1.3** Schematic of heat transfer in aboveground hydraulic circuit.

Although, many researchers have recognized such disturbances to the TRT and the resulting estimation error [7,14–22], the effects can be found in the response curves from many studies [8,23–27]. Although many new experimental and analysis methods have been developed, as described previously, the same conventional TRT method and estimation method continue to be used in actual applications: linear regressive estimation using the exponential integral-approximated ILS model. In practice, this is very easy to use; however, the estimation accuracy is not guaranteed, and large error are easily produced.

The main reason for the continued use of the conventional estimation method is the lack of practicality of newly proposed methods, particularly with regard to the time, cost, and difficulty of use. Alternative methods require a tremendous amount of time for estimation—especially when numerical methods and parameter estimation techniques are combined—expensive measuring equipment, many additional measurements to gain supplementary information, or excessively complex post-processing of the measured data. These alternatives are not always an option in the design phase, when TRTs are actually conducted. Therefore, a practical alternative method is needed.

Other issues need to be examined and addressed with regard to disturbances to a TRT. As noted

previously, although new TRT methods and analysis methods have been proposed to increase the accuracy of the results, it is difficult to find literature and guidelines for systemic analysis on which parameters significantly impact perturbations of the temperature response, for controlling and conducting a TRT with less-perturbed data, and for suggestions on interpreting disturbed data. Considering the impact of the design parameters of the BHE and the increased use of GSHPs, the lack of information about these matters is concerning. This should be resolved through systematic analyses.

### 1.1.2 Effect of natural convection in thermal response test

In general, the heat transfer in the ground is assumed to be dominated by conduction. However, in some cases the groundwater flow and consequent advection heat transfer in the aquifer cannot be neglected. In this case, if a physical model based on the thermal diffusion equation is used for inverse parameter estimation, the estimated thermal conductivity would fluctuate or increase with time because the model cannot consider the advective heat transfer. Therefore, a model that can consider advective heat transfer should be selected for the inverse problem. For example, an energy conservation equation that includes the advective term can be used.

Many studies have considered the effect of the groundwater flow on the BHE performance [28–38]. In contrast, the natural convection in the ground has rarely been examined. The ASHRAE Handbook [39] can be referred to for representative guidelines on TRTs, but it does not comment on the effect of natural convection. The final report of IEA ECES Annex 21, which was published at the end of 2013 [40], stated that the effect of natural convection in an aquifer has not yet been examined. Examining the effect of natural convection on a TRT is very important because this phenomenon can affect the TRT results and lead to improper BHE designs if conventional TRT and estimation methods are used.

A situation where a linear heat source is located in a saturated porous medium is the same as one where a BHE is installed in a saturated porous formation. Because of the heat flux from the source and resulting density differences in the fluids, the warmer (lighter) fluids rise, while the cooler (heavier) fluids sink. This produces convection currents in porous media, as shown in Fig. 1.4. The convection currents improve the speed of the thermal diffusion from the source to the ground. Considering the degree of the natural convection depends on the temperature difference between the source and ground, methods to determine the TRT setting (heat injection rate) related to the actual operation of a GSHP and the BHE design should also be examined.

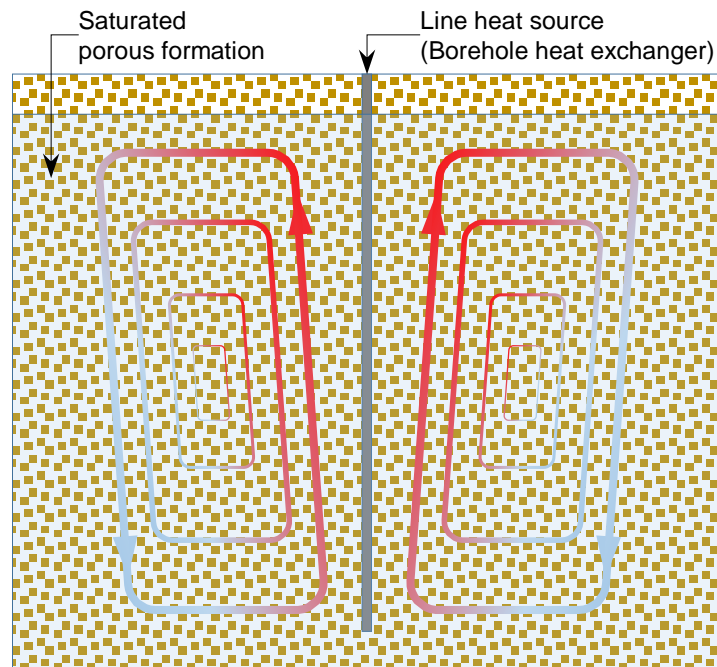


**Fig. 1.4** Schematic of line heat source in saturated porous formation and macroscopic convection currents.

Explicitly considering natural convection phenomena in saturated porous media is very difficult, especially when the porous media have random shapes and inhomogeneous properties as in the case of natural ground. The momentum and energy conservation equations should include a buoyancy term, which requires additional parameters such as the permeability and porosity of the formation. This results in a very difficult inverse problem. Therefore, developing a practical method that can examine the performance dependence of the BHE caused by the natural convection in the ground while suiting the purpose of the BHE design is very important.

## 1.2 Research objectives

The ultimate objective of this study was to improve the accuracy of the BHE design. Theoretical, numerical, and experimental examinations were performed to develop insights into the TRT and alternative methods. With regard to the suggested new methods, practicality is the most important theme running through this thesis. The thesis can be divided into two major subjects: disturbances to the TRT, and the natural convection in the ground and its effect on a TRT. The following sub-topics were examined in detail.

### **(1) Derivation of analytical model to describe heat transfer in aboveground hydraulic circuit, parametric study, and sensitivity analysis using derived model**

Before an alternative method is suggested to interpret the disturbed temperature response, a method for the experimenter to obtain quality data must be considered. In this study, an analytical model was derived to describe the heat exchange between the circulating fluid and outdoor environment in an aboveground TRT setup. Based on the derived model, a parametric study and sensitivity analysis were conducted in a systematic manner using disturbance-related parameters such as the test settings (heat injection rate and flow rate), aboveground connecting circuit parameters (insulation thickness, length, and radiation absorptivity), temperature of the fluid, and weather conditions (solar irradiation, environmental temperature, and wind velocity). Based on the results, suggestions are provided for experimenters on designing TRT setups and conducting TRTs to obtain quality data.

### **(2) Numerical study on applicability and limitations of estimations with ILS model when temperature response is disturbed**

The ILS model is one of the most frequently used to interpret TRT data because of its simplicity. It assumes that the heat flux from the source is constant, but this assumption is violated under real field conditions by the heat exchange between the circulating fluid and outdoor environment in an aboveground TRT setup. This results in fluctuating behavior and an estimation error. In this study, the effect of disturbances from the outdoor environment on TRT analysis using the ILS model was quantitatively examined with numerical methods. The derived analytical model was incorporated as the boundary condition of a numerical model. Typical synthetic weather data of different seasons and 36 cases of measured weather data were used to generate disturbed TRT data. Interpretation behavior related to weather conditions was characterized, and changes in the error range with the testing duration were analyzed to clarify the applicability and limitations of analysis using the ILS model. Some practical suggestions regarding conducting and interpreting TRTs are provided.

### **(3) Proposal of alternative estimation method to interpret disturbed TRT data in fast, accurate and robust manner**

Providing additional information about the estimation behavior and convergence is another reason many experimenters still use the regressive sequential estimation method using the approximated ILS model. As a solution to interpreting disturbed TRT data and utilizing additional information from the sequential plot method, an alternative method is proposed that combines a temporal superposition-applied ILS model with the quasi-Newton optimization method. To verify the effectiveness, the proposed method was applied to in situ TRTs, and the results were compared with those from the conventional method in terms of the

estimation stability and convergence speed. The developmental objectives of the new estimation method were robustness, fast convergence, and low computation cost for wide applicability.

#### **(4) Effect of natural convection on thermal response test conducted in saturated porous formation**

The effect of natural convection on the annular space of a groundwater-filled BHE has mainly been reported by researchers from northern Europe. Even in a backfilled or grouted BHE, if the formation is saturated and composed of a porous medium, the estimation results depend on the heat injection rate because of the natural convection in the ground. In this study, the effect of natural convection on TRTs conducted in a saturated porous formation was examined. TRTs were conducted with two BHEs having the same geometry but different backfill materials: one was cement-grouted, and the other was gravel-backfilled. TRTs were conducted for each BHE at two different heat injection rates (approximately 40 and 80 W/m). The TRT data were analyzed with the developed estimation method. Based on the results, a discussion on existing design methods related to typical practices in TRTs and the advantages of a backfilled BHE from the perspectives of performance and constructability is presented in this thesis.

#### **(5) Heat rate dependence examination method using multi-heat injection rate TRT combined with parameter estimation to overcome temporal change of ground conditions**

Multiple TRTs that using different single-heat injection rates to examine the heat rate dependence in saturated porous formations require a long time to recover to the initial temperature between tests; thus, performing these tests is expensive and time-consuming. Moreover, ground conditions such as the depth-averaged initial temperature, moisture content, thermal conductivity, and groundwater level can vary during the long recovery period. Therefore, the results of multiple TRTs, each using a different heat injection rate, would not solely depend on the heat injection rate; many uncertainties may be included. In this study, a new practical method was developed to minimize the effect of temporal changes in the ground conditions. The developed parameter estimation method that uses the infinite line source model and quasi-Newton method was corrected to handle a multi-heat injection rate TRT successfully. The effectiveness of the proposed method was verified with numerically generated multi-heat injection rate TRT data. Four TRTs were conducted with two different BHEs installed in a saturated sandy formation. Because the estimation method is sufficiently fast and robust, a real-time estimation method for an onsite TRT was also developed to reduce the test time.

In summary, this thesis deals with the factors that can affect the results of a TRT: disturbances to the TRT and natural convection in the saturated porous formation. Starting from an analysis on the causes that affect the results of a TRT, insights into the design of the TRT setup and conducting a TRT are presented.

Based on the analysis results, alternative methods for conducting and interpreting TRTs were developed to consider the disturbance effect and examine the heat rate dependence with a strong emphasis on practicality. The developed method should be fast and robust. Therefore, the proposed methods are easy to use, widely applicable, and improve the design accuracy of a GSHP.

### 1.3 Thesis structure

This thesis is composed of nine chapters that discuss the objectives of the study. The research flow is shown in Fig. 1.5. The literature review is not presented as an independent chapter; instead, it is presented at the beginning of each chapter for better readability. This chapter presents the background, defines the problems, and outlines the research questions and objectives. The structure of the thesis is as follows:

Chapter 2 provides the basic theory used in this thesis.

Chapter 3 describes the experimental setup for a TRT. The geometry and components of BHEs and the hydraulic circuit, electrical circuit, control circuit, and measuring system of the TRT apparatus are described. The uncertainty of the experimental system is also discussed.

Chapter 4–6 discuss disturbances to TRTs and the development of an estimation method that considers disturbances.

Chapter 4 presents the derivation of the disturbance-considering analytical model to describe the heat transfer in an aboveground hydraulic circuit. This model was used for a parametric study and sensitivity analysis to develop insights into the quality control of a TRT.

Chapter 5 presents the applicability and limitations of the conventional estimation method using the ILS model. A 3-D numerical model was combined with the developed analytical model presented in Chapter 4 as the boundary condition to generate disturbed temperature responses under various weather conditions, and the results were interpreted to provide insights into the appropriate use of the conventional estimation method.

Chapter 6 presents the development of the disturbance-considering estimation method. The in situ TRT data were used to compare the interpreted results with the conventional estimation method to verify the effectiveness of the proposed method.

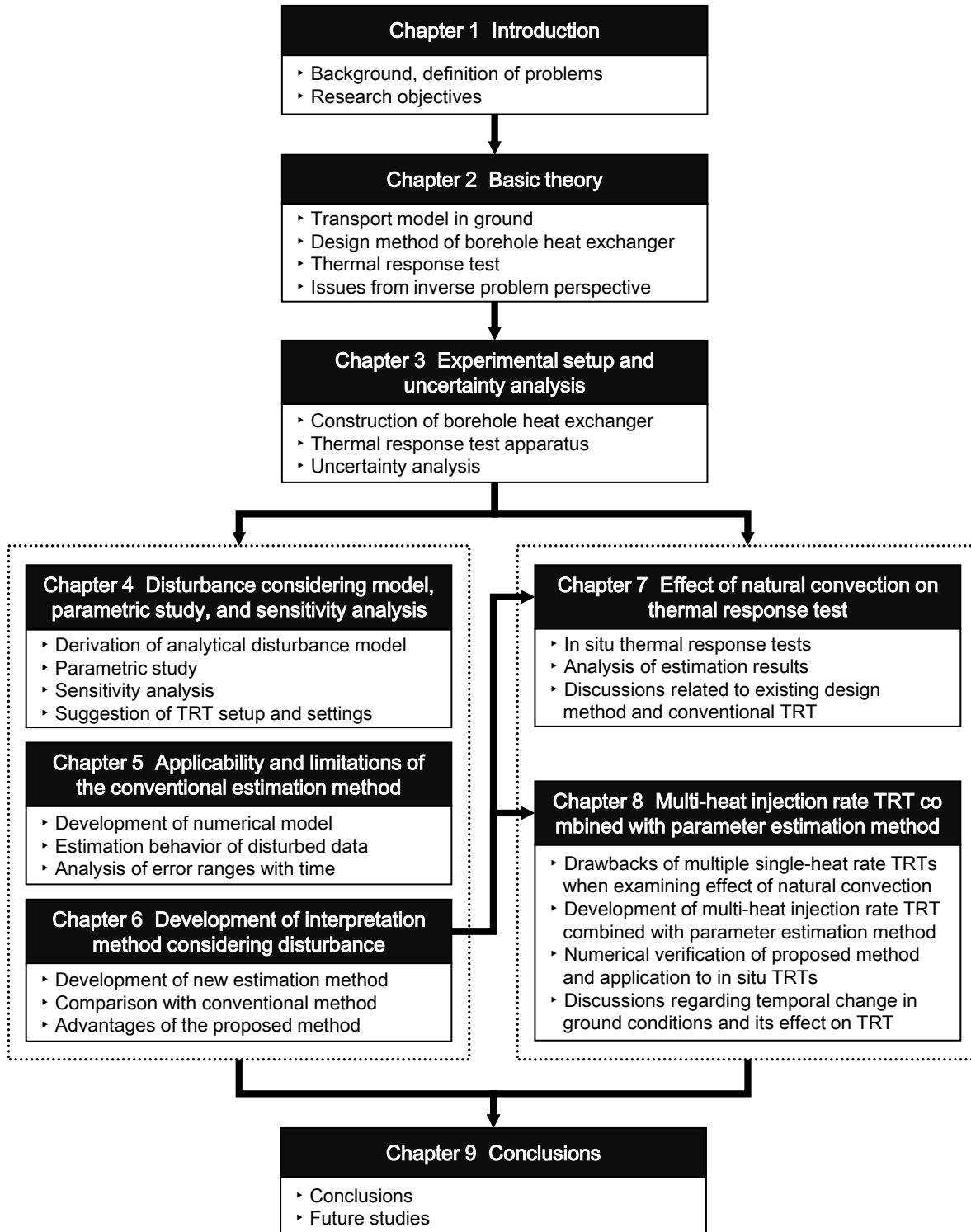


**Fig. 1.5** Research flow and structure of thesis.

Chapter 7 and 8 discuss the effect of natural convection on TRTs and the development of an estimation method to examine the heat rate dependence of a TRT in a saturated porous formation.

Chapter 7 presents TRTs using different heat injection rates to examine the performance dependence of the BHE and dependences of the TRT. The existing design method and conventional TRT method are discussed.

Chapter 8 describes the proposed multi-heat injection rate TRT combined with the parameter estimation method, which is the modified version of the method presented in Chapter 4, to successfully treat a multi-heat injection rate TRT. The effectiveness of the proposed method was verified with numerical TRT data, and the method was then applied to in situ multi-heat injection rate TRTs. The temporal change in the ground conditions and its effect were considered using the results of TRTs conducted at the same site.

Chapter 9 summarizes the achievements and key findings of this work. Future studies are also suggested.

CHAPTER 2  
BASIC THEORY

## 2.1 Transport model in ground

This chapter describes the fluid flow and heat transport in porous media and their mathematical modeling. Some basic concepts in modeling and the physical background are provided. The mass, momentum, and energy conservation equations are used in the numerical model.

### 2.1.1 Continuum approach in porous media

Soil can be considered to be a porous medium that is composed of three phases: liquid, solid, and gas. At the microscopic scale, the spatial distribution of the porous medium's properties changes drastically. This microscopic variation is very complex and almost impossible to describe. Therefore, describing the transport process in porous media at the microscopic level is impractical.

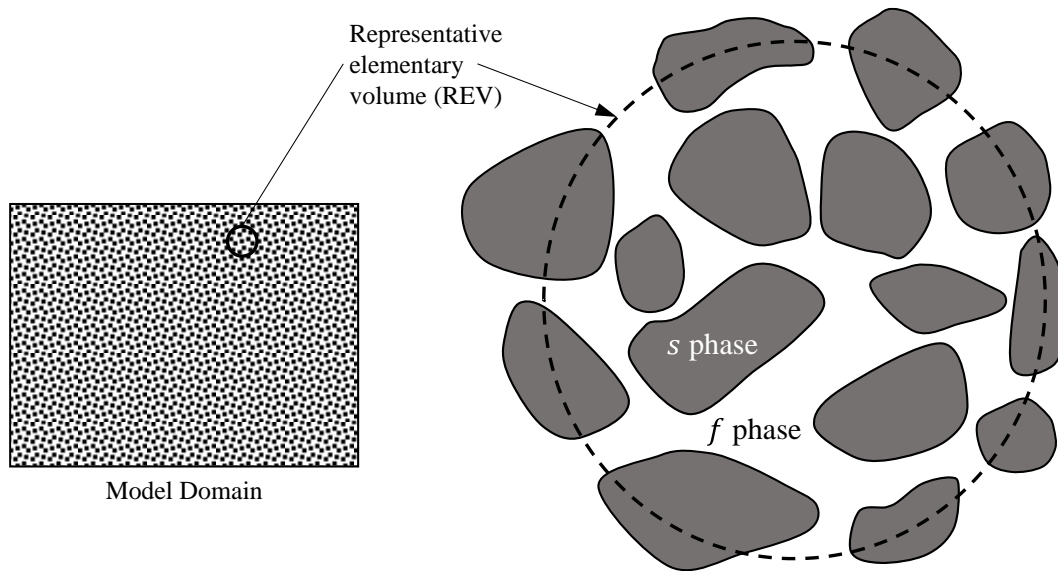


**Fig. 2.1** Schematic of representative elementary volume (REV), *s*: solid, *f*: fluid (= liquid).

The most general and successful way to describe the transport of flow, mass, and heat is to use a continuum approach at the macroscopic level. The transport processes are described in the form of partial differential equations. To describe the transport processes in a porous medium based on the continuum approach, a sample of the porous medium is assumed to represent the properties of the medium as a whole. All of the properties are treated as bulk properties, and a spatial average is applied. This is called the representative elementary volume (REV) concept. Fig. 2.1 shows a schematic that depicts the REV of a saturated porous medium. The size of the REV is arbitrary, but it should be sufficiently large that

fluctuations in the spatially averaged properties can be neglected. At the same time, the REV should be small enough that local variations in the bulk properties can be considered. Fig. 2.2 shows the variation in porosity with the size of the REV.

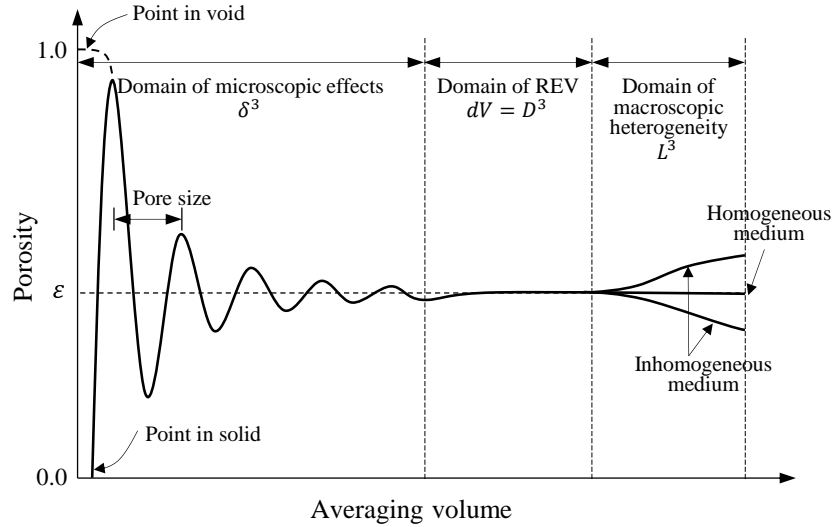


**Fig. 2.2** Porosity as function of averaging volume.  $\delta$ : microscopic length scale,  $D$ : macroscopic length scale, and  $L$ : length scale of gross inhomogeneities.

When the size of the REV has been determined, the porosity  $\varepsilon$  can be defined as the ratio of the total REV to the void space in the REV. In a saturated porous medium, the void space is filled with a fluid, denoted by  $dV_f$ .

$$\varepsilon = \frac{dV_f}{dV} \quad (2.1)$$

The flow path of the fluid is made up of connected pores. In a porous medium, not all of the pores are connected; some are isolated, or the flow path has a dead end. These parts cannot contribute to the fluid flow. The porosity can be corrected by using the effective porosity  $\varepsilon_{eff}$  to represent the fluid flow.  $\varepsilon_{eff}$  is defined as the ratio of the pore volume that contributes to the fluid flow and the total REV.

$$\varepsilon_{eff} = \frac{dV_{eff}}{dV} \quad (2.2)$$

In this thesis, the effective porosity is not considered. All of the porosities used here are based on the ratio between the pore volume and total REV.

In the REV, each phase's volume fraction is denoted by  $\varepsilon_\alpha$ . For a saturated porous medium, the fluid volume fraction is  $\varepsilon_f$ , and the soil volume fraction is  $\varepsilon_s$ . The sum of each phase's volume fraction becomes 1.

$$\sum_{\alpha} \varepsilon_{\alpha} = 1, \quad 0 \leq \varepsilon_{\alpha} \leq 1 \quad (2.3)$$

If an REV property is considered to be a bulk property, the volume-averaged property for the scalar quantity  $\psi$  is defined by using the porosity as follows:

$$\psi_b = \varepsilon(\psi_f) + (1 - \varepsilon)(\psi_s) \quad (2.4)$$

### 2.1.2 Momentum conservation (Darcy's law)

The hydraulic process in the ground is important for advective heat transport. Darcy's law is used to consider a slow fluid flow in a porous medium. This is a very simplified momentum equation.

First, the momentum conservation of the liquid phase in the porous medium can be described by using the Navier–Stokes equation. When the porous medium is saturated, the aquifer-averaged (vertically integrated over the depth  $B$ ) momentum conservation can be described as follows:

$$\frac{\partial}{\partial t} B \varepsilon \rho_f \mathbf{v} + (B \varepsilon \rho_f \mathbf{v} \nabla) \mathbf{v} = -B \varepsilon (\nabla p - \rho_f \mathbf{g}) + B \mu \nabla^2 \varepsilon \mathbf{v} + B \varepsilon (\boldsymbol{\sigma}^{int} + \boldsymbol{\sigma}^T + \boldsymbol{\sigma}^B) \quad (2.5)$$

where  $\boldsymbol{\sigma}^{int}$  represents the momentum exchange that occurs at the interface between the solid and liquid (Fig. 2.1). If the porosity is 1 (i.e., free flow), then this term can be eliminated.  $\boldsymbol{\sigma}^T$  and  $\boldsymbol{\sigma}^B$  are the momentum exchanges at the top and bottom interfaces, respectively, of the aquifer. If Eq. (2.5) is not vertically integrated, those two terms are dropped.

The velocity in the ground is generally very slow. The Reynolds number based on the typical pore diameter  $Re_p$  is less than 1. Consequently, in this case, the inertial effects can generally be neglected in relation to the viscous term.

$$\frac{\partial \mathbf{v}}{\partial t} \approx 0 \quad \text{and} \quad \mathbf{v}(\nabla \mathbf{v}) \approx 0 \quad (2.6)$$

If Eq. (2.5) is written in non-integrated form with  $B \equiv 1$ , then the top and bottom viscous stress terms are dropped. By applying the above assumption, the Navier–Stokes equation can be reduced to Eq. (2.7),

which contains only the pressure gradient, viscous drag, and interfacial viscous drag terms.

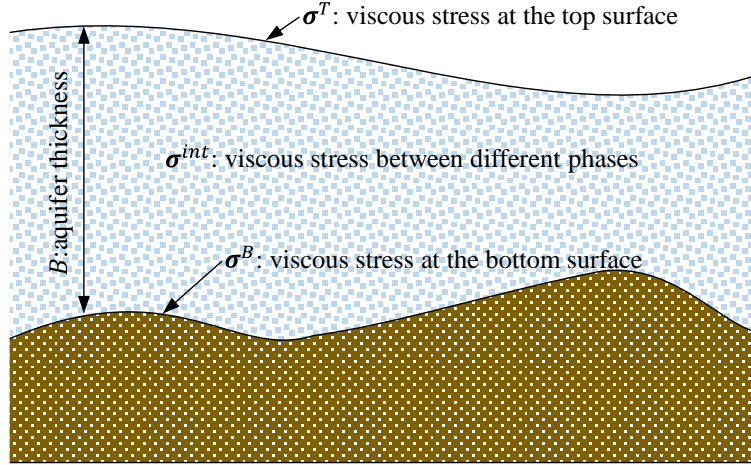


**Fig. 2.3** Schematic of aquifer and different types of viscous stress terms.

$$\varepsilon(\nabla p - \rho_f \mathbf{g}) = \varepsilon \mu \nabla^2 \mathbf{v} + \varepsilon \boldsymbol{\sigma}^{int} \quad (2.7)$$

The viscous shear stress (i.e., Brinkman term) can also be neglected compared to the interfacial drag term of the momentum exchange. That is,  $\varepsilon \mu \nabla^2 \mathbf{v} \approx 0$ . Then Eq. (2.7) is reduced to Eq. (2.8):

$$\nabla p - \rho_f \mathbf{g} = \boldsymbol{\sigma}^{int} \quad (2.8)$$

The interfacial drag term of the fluid momentum exchange can be expressed as follows:

$$\boldsymbol{\sigma}^{int} = -\frac{\mu}{k} \mathbf{q} \quad (2.9)$$

By substituting Eq. (2.9) in Eq. (2.8), the Darcy equation is finally obtained in its pressure form:

$$\mathbf{q} = -\frac{k}{\mu} (\nabla p - \rho_f \mathbf{g}) \quad (2.10)$$

The intrinsic permeability  $k$  solely depends on the geometric configuration (shape and arrangement of grains) of the porous medium. Note that this is different from the hydraulic conductivity  $K$ . The hydraulic conductivity also considers the property of the fluid and represents how easily a fluid can flow through a porous medium.

$$\mathbf{K} = \frac{\mathbf{k}\rho_f g}{\mu} \quad (2.11)$$

The pressure  $p$  can be rewritten using the hydraulic head:

$$h = \frac{p}{\rho_f g} + z \quad (2.12)$$

Eqs. (2.11) and (2.12) can be used to rewrite the equation of the Darcy velocity as follows:

$$\mathbf{q} = -\mathbf{K}\nabla h \quad (2.13)$$

The Darcy velocity has units of meters per second, but it does not mean the actual velocity. The definition of  $\mathbf{q}$  is the volumetric flow rate per unit area of REV (i.e.,  $\text{m}^3/\text{m}^2/\text{s} = \text{m}/\text{s}$ ).

Darcy's law is only valid when the averaged velocity in the porous medium is very slow, so the friction between the flowing fluid and pore wall is dominant in the system. If the pore-scale Reynolds number is greater than 1, the transition and turbulent flows should be considered. The nonlinear drag from the inertia effect and viscous drag force should be considered with Forchheimer's law and Brinkman's law, respectively. Further details are given in [41,42]. Most groundwater flows can be expressed with the Darcy equation.

The above expression is for an incompressible flow, which has constant properties. When a temperature gradient exists, the hydraulic conductivity is variable because the density and viscosity are functions of the temperature. To consider the flow caused by a temperature difference, the reference temperature  $T_0$  and the density  $\rho_0$  and viscosity  $\mu_0$  at that temperature are introduced. The Darcy equation can be expressed as follows:

$$\mathbf{q} = -\mathbf{K}f_\mu(\nabla h + \chi\mathbf{e}) \quad (2.14)$$

where

$$\mathbf{K} = \mathbf{k}\rho_{f,0}g/\mu_0 \quad (2.15)$$

$$f_\mu = \mu_0/\mu(T)$$

$$\chi = \frac{\rho_f - \rho_{f,0}}{\rho_{f,0}} = -\beta(T)(T - T_0)$$

$$h = \frac{p}{\rho_{f,0}g} + z$$

Although the variation in the air density with temperature can be approximated with a linear function over a wide range of temperatures, the valid temperature range for linear approximation is much narrower in the case of the water density. Therefore, applying the Boussinesq approximation can be an oversimplification. The range of the Boussinesq approximation is validated in Ref. [43]. Perrochet and Tacher's equation [44] can be used to consider the nonlinear change in the water density with temperature.

### 2.1.3 Mass conservation

The mass balance in a porous medium can also be described on the basis of the continuum approach through the introduction of the REV concept. The basic idea of the balance equation for a certain quantity is simple. In the unit control volume and during the unit time, the balance equation can be described on the basis of the following relation:

$$\left\{ \begin{array}{l} \text{Accumulation of} \\ \text{quantity in the} \\ \text{control volume} \end{array} \right\} = \left\{ \begin{array}{l} \text{Net quantity} \\ \text{entering rate} \\ \text{in the control volume} \end{array} \right\} + \left\{ \begin{array}{l} \text{Net source and sink rate} \\ \text{of quantity} \\ \text{in the control volume} \end{array} \right\} \quad (2.16)$$

Based on this idea, the mass conservation in the porous medium can be described as follows:

$$S_o \frac{\partial h}{\partial t} + \nabla \mathbf{q} = Q_\rho + Q_B(T) \quad (2.17)$$

where

$$Q_B(T) = -\mathbf{q} \left( \frac{S_o}{\varepsilon} \nabla h - \beta^* \nabla T \right) + \varepsilon \left( -\beta^* \frac{\partial T}{\partial t} \right) \quad (2.18)$$

$$\beta^* = \frac{\beta(T) + \frac{\partial \beta(T)}{\partial T} (T - T_0)}{1 - \beta(T)(T - T_0)} \quad (2.19)$$

The above equation is valid for a saturated porous medium. The specific storativity  $S_o$  represents the change in the water volume with a change in the hydraulic head  $h$ . The explicit expression of  $S_o$  is as follows:

$$S_o = \rho_0 g (\varepsilon \bar{\gamma} + (1 - \varepsilon) \gamma) \quad (2.20)$$

### 2.1.4 Energy conservation

The equation of energy conservation considers the conduction, advection, and dispersion effects in a

porous medium. This is also based on the REV concept. The arithmetic average using the porosity is applied to the thermal properties. The balance equation of energy in the control volume is expressed as follows:

$$(\rho c)_b \frac{\partial T}{\partial t} + (\rho c)_f \mathbf{q} \nabla T - \nabla \{ (\lambda_b + \lambda_{disp}) \nabla T \} = Q_T \quad (2.21)$$

where

$$\lambda_b = \varepsilon \lambda_f + (1 - \varepsilon) \lambda_s \quad (2.22)$$

$$\lambda_{disp} = (\rho c)_f \left\{ \alpha_T \|\mathbf{q}\| \delta + (\alpha_L - \alpha_T) \frac{\mathbf{q} \otimes \mathbf{q}}{\|\mathbf{q}\|} \right\} \quad (2.23)$$

In a porous medium, the mechanical dispersion effect becomes important when the advection effect is strong. This effect considers the variation in velocity in the microscopic velocity field and the resulting diffusion caused by the various scales of the flow path. At the pore scale, the longitudinal dispersion (in the direction of flow) describes the phenomenon where a fluid particle in the center of the pore has a higher velocity than a water particle near the interface of a solid. This causes significant dispersion in the flow direction, especially when the flow velocity is high. The transverse dispersion (in the direction perpendicular to the flow direction) describes the lateral dispersion by the detoured flow caused by the solid blocking the flow. The longitudinal and lateral dispersions are added to the thermal diffusion term.

The dispersivity is obtained from field tracer experiments or laboratory tests, but obtaining it is difficult because the dispersion is scale-dependent. In a laboratory experiment, the order is a few centimeters, while it can be up to several hundreds of meters in a field experiment. This difference is caused by the much greater heterogeneity of a porous medium in a field experiment. The dispersivity is one of the most unreliable parameters in a simulation.

## 2.2 Design method of borehole heat exchanger

Before the thermal response test (TRT), which is the main subject of this thesis, is explained, a review on current design practices will help demonstrate why the TRT is important. There are two design methods: a simulation-based method that resorts to a dimensionless response function (i.e., g-function) and the ASHRAE method. This section describes each method and related issues.

### 2.2.1 Simulation-based design method

In the simulation-based design method, the temperature of the fluid entering the heat pump (e.g., outlet temperature of the BHE) is set as a constraint, and the length, components, and geometry of the BHE and the arrangement of the borefield are determined by iterative calculations until the constraint is satisfied. Most simulation-based design methods are based on the g-function concept, which represents the dimensionless temperature response of a borehole wall as first suggested by Eskilson [11].

The g-function is generated by using a combination of analytical and numerical solutions. The basic response of single BHE from a step pulse is obtained with a 2-D (radial-axial coordinates) numerical model. The ground properties are assumed to be homogeneous, isotropic, and constant. A constant initial temperature is assigned to the whole model domain. The heat flux along the finite length of the heat source has the same flux per unit length (W/m). The top layer and bottom end of the BHE have different boundary conditions. The long-term average ambient temperature is assigned to the top ( $z = 0$ ). The bottom end ( $z = H$ ) has the undisturbed ground temperature as the boundary condition. The borehole elements and its geometry are not considered.

$$\frac{1}{\alpha_s} \frac{\partial T}{\partial t} = \frac{\partial^2 T}{\partial r^2} + \frac{1}{r} \frac{\partial T}{\partial r} + \frac{\partial^2 T}{\partial z^2} \quad (2.24)$$

Initial condition

$$T(r, z, 0) = T_0$$

Boundary condition

$$T(r, 0, t) = T_{amb}$$

$$T(r, z = H, t) = T_0$$

$$\text{at } r = r_b, \quad q_0(t) = \frac{1}{H} \int_D^{D+H} 2\pi r \lambda_s \frac{\partial T}{\partial r} dz$$

Eskilson solved the above heat conduction problem by using the finite difference method. The temperature response of the BHE wall with respect to the unit step pulse can be expressed as a function of  $t/t_s$  and  $r_b/H$ . The temperature response of a single BHE can be described in the following form:

$$T_{b,1} = T_0 + \frac{q_0}{2\pi\lambda_s} \underbrace{g_1\left(\frac{t}{t_s}, \frac{r_b}{H}\right)}_{g\text{-function}} \quad (2.25)$$

where  $t_s = H^2/9\alpha_s$  is a steady-state time scale and  $g_1$  is the g-function representing the dimensionless response factor of a single BHE.

The g-function can be defined by rearranging Eq. (2.25) with respect to  $g_1$  as follows:

$$g_1\left(\frac{t}{t_s}, \frac{r_b}{H}\right) = (T_{b,1} - T_0) \frac{2\pi\lambda_s}{q_0} \quad (2.26)$$

Eq. (2.25) is the temperature response with the unit heat pulse. Applying the temporal superposition technique allows the temperature response from the variable heat rate to be obtained.

$$T_{b,1} - T_0 = \sum_{n=1}^N \frac{q_n - q_{n-1}}{2\pi\lambda_s} g_1\left(\frac{t - t_n}{t_s}, \frac{r_b}{H}\right) \quad (2.27)$$

For the temperature of a borefield comprising  $n$  boreholes, additional factors should be considered: the horizontal distance between boreholes  $B$ , length of a BHE  $H$ , and borehole arrangement of the borefield. The averaged temperature response with respect to  $n$  BHEs  $T_{b,n}$  can be expressed as follows:

$$T_{b,n} = T_0 + \frac{q_0}{2\pi\lambda_s} g_n\left(\frac{t}{t_s}, \frac{r_b}{H}, \frac{B}{H}, \text{borefield geometry}\right) \quad (2.28)$$

If information about the temperature response at a certain time and distance from a BHE can be obtained, the g-function can be extended to a borefield using spatial superposition:

$$T_i(r_b, t) = \frac{1}{N} \sum_{j=1}^N (T_j(r_j - r_i, t) - T_g) + T_g \quad (2.29)$$

where  $r_j - r_i$  is the distance between boreholes  $i$  and  $j$ . If  $i = j$ , this refers to the location of borehole  $i$ . Note that this g-function is described at the borehole radius  $r_b$ .

Regarding Eq. (2.29), as an example, if there are nine boreholes arranged in a borefield, the temperature should be calculated nine times at each borehole. In total, 81 temperature responses are required to obtain the average borefield temperature response.

$$T_{bf}(r_b, t) = \frac{1}{N} \sum_{i=1}^N T_i(r_b, t) \quad (2.30)$$

The borehole wall temperature can be obtained with Eq. (2.30). However, the temperature of the fluid entering the heat pump is required as the constraint of the design. Introducing the borehole thermal resistance allows the average fluid temperature of the BHE to be obtained:

$$\bar{T}_{cf}(t) = T_{bf}(t) + q(t) \cdot R_b \quad (2.31)$$

Note that the thermal capacity of a BHE is neglected, and this resistance based on the steady state.  $R_b$  considers the convective thermal resistance of the U-tube's inner surface, conductive resistance of the U-tube, conductive resistance of the grout, and thermal short-circuiting between U-tube legs. Many models are available with different levels of complexity and accuracy. Please refer to the literature [45–57].

After the average fluid temperature is obtained, the outlet temperature of a borefield can be obtained as follows:

$$T_{cf,out}(t) = \frac{q_{hp}}{2\rho_{cf}c_{cf}\dot{V}_{cf}} + \bar{T}_{cf}(t) \quad (2.32)$$

The outlet temperature  $T_{cf,out}(t)$  should meet the operation temperature limit of the heat pump. Many parameters of the BHE or the length of the borefield can be changed until this condition is met.

The g-function concept has gained popularity since it was first suggested. However, its biggest disadvantage is the lack of flexibility and resulting large amount of computation time. If the geometry of a BHE or the arrangement of the borefield is changed, the g-function should be newly calculated. This drawback makes it difficult to directly incorporate into building energy simulation programs. Consequently, many pre-calculated g-functions for various geometries are saved in a massive database and incorporated into building simulation programs. If the considered geometry of a BHE and the arrangement are not pre-defined in the g-function database, then they need to be interpolated, which can generate some errors. If the BHEs in a borefield have different geometries and the borefield arrangement is irregular, then the g-function should be calculated from the beginning through a numerical approach.

To overcome this flexibility issue of the conventional g-function, a recent trend has been to analytically develop a g-function by using the finite line source (FLS) model [12,13,50,58]. When the FLS model is used to generate a g-function, differences in accuracy are caused by how the model assigns the boundary condition at the heat source; this has become a recent topic of active debate [59–61]. However, such issues are beyond the scope of this thesis and thus are discussed no further.

## 2.2.2 ASHRAE design method

Another well-known BHE design method is the ASHRAE method [62], which is based on the infinite cylindrical source (ICS) model [9,10].

The ICS model assumes that the ground properties are homogeneous, isotropic, and constant. A constant initial temperature is assigned to the whole model domain. The infinite cylindrical heat source located at

the center of the domain has a constant heat flux. Note that the heat flux boundary condition is imposed at the contact surface area between the BHE and soil (e.g.,  $r = r_b$ ), not the center of the BHE. The governing partial differential equation of the ICS model is the transient 1-D thermal diffusion equation as described in a cylindrical coordinate system. The governing equation, initial condition, and boundary conditions can be described with respect to  $u$ , which represents the temperature change relative to the initial temperature  $u(r, t) = T(r, t) - T_0$ .

$$\frac{1}{\alpha_s} \frac{\partial u}{\partial t} = \frac{\partial^2 u}{\partial r^2} + \frac{1}{r} \frac{\partial u}{\partial r} \quad (2.33)$$

Initial condition

$$u(r, 0) = T_0$$

Boundary conditions

$$u(r \rightarrow \infty, t) = T_0$$

$$\text{at } r = r_b, \quad -\lambda_s \frac{\partial u}{\partial r} 2\pi r_b = q_0$$

Under the described initial and boundary conditions, the following ICS solution can be obtained by using the Laplace transform as follows:

$$T(\text{Fo}, P) - T_0 = \frac{q_0}{\lambda_s} \frac{1}{\pi^2} \int_0^\infty \frac{e^{-\beta^2 \text{Fo}} - 1}{J_1^2(\beta) + Y_1^2(\beta)} \underbrace{[J_0(P\beta)Y_1(\beta) - J_1(\beta)Y_0(P\beta)]}_{G\text{-factor}} \frac{d\beta}{\beta^2} \quad (2.34)$$

where  $J_0$  and  $J_1$  are Bessel functions of the first kind of the zeroth and first orders, respectively;  $Y_0$  and  $Y_1$  are Bessel functions of the second kind of the zeroth and first orders, respectively;  $\text{Fo}$  is the Fourier number ( $\text{Fo} = \alpha_s t / r_b^2$ ); and  $P$  is a dimensionless distance based on the radius of the BHE ( $P = r / r_b$ )

The above solution can be rewritten by using the G-factor as follows:

$$\Delta T_g = T(\text{Fo}, P) - T_0 = \frac{q_0}{\lambda_s} G(\text{Fo}, P) \quad (2.35)$$

In fact, most response models have this general form shown as the g-function of the FLS. Based on the form of the equation, the thermal conductivity of soil  $\lambda_s$  and the heat load  $q_0$  have significant impacts on the temperature response. Note that the dimensionless response of the ICS is denoted by an uppercase ‘‘G,’’ and that of the FLS is denoted by a lowercase ‘‘g’’.

The ASHRAE method was first suggested by Kavanaugh and Rafferty [63]. Recently, the necessity of

revising the method has been actively discussed because of the overestimation problem caused by the lack of consideration for the axial effect of the ICS model and some ambiguous parameters. This is described later. If the required information is sufficiently prepared, the ASHRAE method is faster and simpler than the simulation-based design method, which requires iterative computations. Based on the work of Bernier [64,65], the following revised form has been suggested:

$$L = \frac{q_h R_b + q_y R_{10y} + q_m R_{1m} + q_h R_{6h}}{\bar{T}_{cf,lim} - (T_g + T_p)} \quad (2.36)$$

This design equation is simple, but it is not that straightforward because it has many uncertainties. In addition, the method to obtain some parameters is also somewhat ambiguous except for the maximum and minimum limits of the average fluid temperature  $\bar{T}_{cf,lim}$ , which are specified by the heat pump manufacturer. This is the most important drawback of ASHRAE method. Therefore, each parameter should be explained.

In Eq. (2.36),  $L$  is the required borehole length. Generally, more than 70% of the total length of the BHE is required to handle the peak load [3].  $T_g$  is the undisturbed ground temperature. The thermal interaction between BHEs can be considered by introducing the temperature penalty  $T_p$ . In terms of the heat transfer between a single borehole and surrounding ground, the thermal interaction refers to the increase in the undisturbed ground temperature. When a building has a large load imbalance between heating and cooling, the gradual increase or decrease in the temperature of the surrounding ground and the resulting temperature penalty are significant. This also affects the long-term effective thermal resistance of the ground  $R_y$ . An example of this calculation can be found in [66].

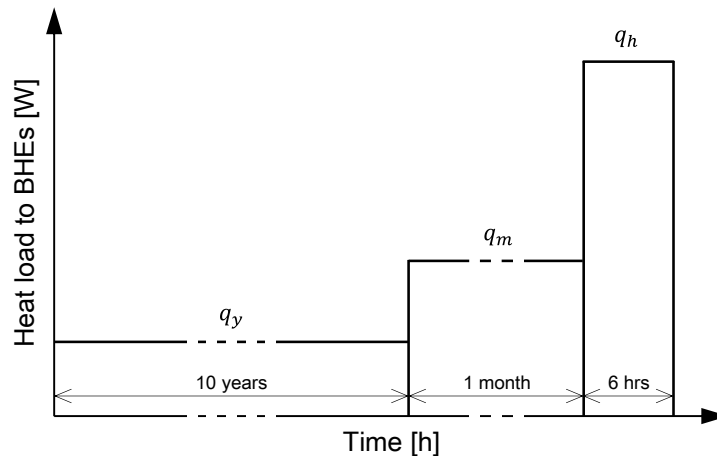


**Fig. 2.4** Three load pulses of different lengths.

$q_h$ ,  $q_m$ , and  $q_y$  are the hourly peak heat load, monthly average heat load of the peak month (total load of a month/720 h), and yearly average heat load (total load sum of yearly load/8760 h), respectively. In general, a positive  $q$  means heat extraction (heating load), and a negative  $q$  means heat rejection (cooling load). Note that these are loads for a BHE where the heat pump's coefficient of performance (COP) is considered. Therefore,  $q$  can be defined as follows:

$$q = q_{load} \left(1 \pm \frac{1}{COP}\right) \quad (2.37)$$

As noted previously, although this method was first suggested on the basis of the ICS model, other models and approaches such as the FLS and numerical methods can also be used. In fact, this makes the method more ambiguous. The method to obtain the temperature penalty  $T_p$  and different  $R$  values significantly vary depending on the model or approach used to obtain them. Even if the g-function is used, the designer experiences the same problems caused by the lack of flexibility as previously described for the simulation-based design method [61].

The ICS model can significantly overestimate the size of a borefield because it cannot consider the axial heat transfer effect, which is very important in long-term predictions. This problem has been pointed out in many studies, which is why many recent studies have focused on the FLS model. Ahmadfard and Bernier [67] claimed that the temperature penalty  $T_p$  does not need to be considered because it is already considered in the effective thermal resistance.

Two design methods and their related issues were reviewed in this section. Regardless of which design method is selected, obtaining accurate and reliable parameters is important. In both methods, the thermal conductivity of the soil and borehole thermal resistance are very important because they directly change many parameters in the design equations and thus affect the design accuracy. Therefore, reliable information about the soil and BHE properties should be obtained before a design method is chosen. This is why the accuracy of the TRT needs to be considered.

### 2.3 Thermal response test and infinite line source model

Outline of the TRT was described in Section 1.1. This section describes in more detail the TRT and infinite line source model, which is the most frequently used to interpret TRTs.

The idea of the TRT was first proposed by Mogensen [4]. Pioneering studies were conducted on in situ TRTs with mobile test rigs in the mid-1990s [5,6]. Two representative guidelines regarding TRTs were

published by the IEA [40,68,69] and ASHRAE [39,70].

Because a BHE has extremely slender geometry, it can be approximated as a line heat source/sink embedded in infinite ground. Generally, the TRT method is based on the boundary condition assumed in the ILS model [9,10], where a constant heat flux from the source is assumed.

Similar to the ICS model, the ILS model is derived from the one-dimensional thermal diffusion equation, which describes the transient temperature change of an infinite homogeneous and isotropic medium with reference to the infinite line source/sink. The heat source is assumed to reject the constant heat flux. Eqs. (2.38)–(2.40) describe this one-dimensional thermal diffusion equation in cylindrical coordinates and its initial and boundary conditions. Note that the heat flux is imposed at the center of the ground (e.g.,  $r = 0$ ).

$$\frac{1}{\alpha_s} \frac{\partial u}{\partial t} = \frac{\partial^2 u}{\partial r^2} + \frac{1}{r} \frac{\partial u}{\partial r} \quad (2.38)$$

Initial condition:

$$u(r, 0) = 0 \quad (2.39)$$

Boundary condition:

$$u(r \rightarrow \infty, t) = 0 \quad (2.40)$$

$$\text{at } r = 0, \quad -\lambda_s \frac{\partial u}{\partial r} 2\pi r = q_0$$

where  $u$  is the temperature change with respect to the initial temperature  $u(r, t) = T(r, t) - T_0$ .

Under the above described initial and boundary conditions, the ILS solution can be obtained by using the Laplace transform as follows:

$$T(r, t) - T_0 = \frac{q_0}{4\pi\lambda} \text{Ei} \left( \frac{C_s r^2}{4\lambda_s t} \right) \quad (2.41)$$

The temperature at the borehole wall ( $r = r_b$ ) is denoted by  $T_r$ , such that Eq. (2.41) can be rewritten in terms of  $T_r$ :

$$T_r(t) = \frac{q_0}{4\pi\lambda_s} \text{Ei} \left( \frac{C_s r_b^2}{4\lambda_s t} \right) + T_0 \quad (2.42)$$

where  $T_r$  is the temperature at the borehole wall and  $c_s$  is the volumetric thermal capacity of the soil.

If the heat transfer between the circulating fluid and borehole wall is assumed to be at a steady state, the borehole thermal resistance  $R_b$  can be defined as follows:

$$\frac{\bar{T}_{cf}(t) - T_r(t)}{q_0} = R_b \quad (2.43)$$

where  $\bar{T}_{cf}(t)$  is the average temperature of the circulating fluid and  $\bar{T}_{cf}(t) = 0.5 (T_{cf,in}(t) + T_{cf,out}(t))$ .

By substituting  $T_r$  into Eq. (2.42) according to Eq. (2.43), the ILS solution with respect to the temperature of the heat carrier fluid can be obtained as follows:

$$\bar{T}_{cf}(t) = \frac{q_0}{4\pi\lambda_s} \text{Ei}\left(\frac{C_s r_b^2}{4\lambda_s t}\right) + R_b \cdot q_0 + T_0 \quad (2.44)$$

The most commonly used method to estimate the effective thermal conductivity of the soil and the borehole thermal resistance involves using the exponential integral approximated ILS model. The exponential integral can be described as the sum of the infinite series as follows [71]:

$$\text{Ei}(x) = \int_x^\infty \frac{e^{-v}}{v} dv = -\gamma - \ln x + \sum_{m=1}^{\infty} \frac{(-1)^{m+1} x^m}{m \cdot m!} \quad (2.45)$$

where  $\gamma$  is the Euler–Mascheroni constant ( $\cong 0.5772$ ).

For practical use, only the first two terms in Eq. (2.45) can be considered to obtain the following approximated form:

$$\bar{T}_{cf}(t) = \underbrace{\frac{q_0}{4\pi\lambda_s}}_k \ln(t) + \frac{q_0}{4\pi\lambda_s} \left\{ \ln\left(\frac{4\lambda_s}{C_s r_b^2}\right) - \gamma \right\} + R_b \cdot q_0 + T_0 \quad (2.46)$$

According to Eq. (2.46), the average temperature of the heat carrier fluid  $\bar{T}_{cf}$  varies linearly with the natural logarithm of time. Therefore, the effective thermal conductivity of the soil  $\lambda_{eff}$  can be estimated from the gradient  $k$  of the temperature response curve versus the natural logarithm of time by linear regression (e.g., the least-squares method) using the following relation:

$$\lambda_{eff} = \frac{q_{avg}}{4\pi k} \quad (2.47)$$

Note that the constant heat flux from the source  $q_0$  and the soil's thermal conductivity  $\lambda_s$  change to  $q_{avg}$  and  $\lambda_{eff}$ , respectively.  $q_{avg}$  is the averaged heat rate over the heat injection period, and  $\lambda_{eff}$  is a parameter that represents the average thermal conductivities of the soil in the vicinity of the BHE.

After  $\lambda_{eff}$  is estimated, the effective borehole thermal resistance can be estimated by rearranging Eq.

(2.46) with respect to  $R_b$  as follows:

$$R_b = \frac{1}{q_{avg}} (\bar{T}_{cf}(t) - T_0) - \frac{1}{4\pi\lambda_{eff}} \left[ \ln \left( \frac{4t\lambda_{eff}}{C_s r_b^2} \right) - \gamma \right] \quad (2.48)$$

The accuracy of the initial temperature response from the ILS model is not reliable because it cannot consider the thermal capacity of the borehole itself. Therefore, the temperature response of the early period is generally neglected. Previous studies have discussed the appropriate starting time for estimation [18,72]. Generally, the time criterion  $t \geq 5r_b^2/\alpha_s$  which guarantees the accuracy of approximation of the exponential integral (Eq. (2.45)) is applied for regressive estimation.

Many analytical models such as the ILS, ICS, and FLS can be used to reproduce the temperature response of a BHE. Any one of them can be used to interpret TRT data if the heat transfer in the ground is dominated by conduction. For analytical models, the main issue is the range of validity for each model. Most models cannot consider the short-term response when the response from the BHE itself is dominant. After the heat transfer inside the BHE reaches a quasi-steady state, this problem becomes negligible. This is why any of the above models can be used to interpret a TRT, which is usually conducted for 50–70 h. In terms of usability, the ILS model has the advantage over the ICS and FLS models because the former does not contain the integration of Bessel functions or complementary error functions; if the exponential integration is approximated, the response can be calculated with a simple algebraic expression. Note that, if a TRT is conducted for a long time, the axial effect should be considered. In this case, the FLS model should be used to interpret a TRT. A detailed comparison between the ILS and FLS is given in [73]. The importance of the axial effect to long-term predictions is considered in [74–77].

If the boundary conditions assumed in an analytical model are not violated, the estimation accuracy of the TRT is guaranteed. However, as noted in Chapter 1, there are some problems that should be considered when conducting and estimating TRTs from the perspective of the inverse problem.

## 2.4 Thermal response test as inverse problem

When a TRT is interpreted with a parameter estimation technique rather than the conventional linear regression method, better accuracy and faster convergence can be achieved. At the same time, however, some problems arise that are not a concern with the conventional estimation method. This section describes the basic theory of the inverse parameter estimation, the problems expected when dealing with a TRT as an inverse problem, and what should be considered in an inverse problem.

### 2.4.1 Inverse parameter estimation

To simulate the behavior of a certain physical system, thermo-fluid scientists construct a mathematical model based on their knowledge. This leads to the development of a numerical or analytical model. The following transient heat diffusion equation can be used for the heat conduction problem:

$$\rho c_s \frac{\partial T}{\partial t} = \lambda_s \nabla^2 T \quad (2.49)$$

Generally, Eq. (2.49) is used to obtain the distribution of the temperature  $T$ , which is a dependent variable of the model under the given initial and boundary conditions and known model parameters (physical quantities such as the thermal conductivity, density, and heat capacity). This is called the direct problem.

In contrast, if the model parameters are already known, the purpose of the inverse problem is to estimate the boundary or initial conditions by observing the dependent variable  $T$ . Of course, when the initial and boundary conditions are known, the inverse problem can be used to estimate the model parameters. This is called parameter estimation, and TRT belongs to this category.

The difference between the inverse and direct problems is not only the direction of how a problem is dealt with. The two problems can also be characterized by their posedness. A direct problem is a well-posed problem that should satisfy the following conditions: (1) a solution must exist, (2) the solution must be unique, and (3) the solution must be stable against small changes to the input data.

If one of these conditions is not satisfied, the problem is ill-posed. In parameter estimation, there is more than one combination of parameters for the same dependent variable, and a small error in the observation would make the problem very unstable. This is an intrinsic characteristic of inverse problems and makes them challenging and computationally intensive to solve. Many stabilization techniques have been proposed to alleviate these characteristics in order to successfully solve inverse problems, such as Tikhonov's regularization procedure [78–81], Alifanov's iterative regularization techniques [82–84], and Beck's function estimation approach [85,86]. Further details about inverse heat transfer problems can be found in [85,87].

Most inverse problems can be solved by minimizing the least-squares norm; this is known as the least-squares method. If errors in observation are not considered, the objective function can be expressed as follows:

$$\min f_{obj} = (\mathbf{Y} - \mathbf{T})^T (\mathbf{Y} - \mathbf{T}) \quad (2.50)$$

where  $\mathbf{Y}$  and  $\mathbf{T}$  are the measured and estimated temperature vectors, respectively.

Although the approach to solving an inverse problem is very similar to that for optimization problems, the two are not the same. In an optimization problem, if multiple solutions show the same value, then they can be the solutions to the problem. However, in an inverse parameter estimation problem, only one solution is close to the absolute truth. Therefore, alleviating the ill-posedness is very important to inverse parameter estimation.

### 2.4.2 Issues with thermal response test from inverse problem perspective

The first step of inverse parameter estimation is the construction of a mathematical model (e.g., model of the direct problem) that describes the physical phenomena involved, such as the conservation, exchange, and transfer of the mass, energy, and momentum. This can be described by partial differential equations; if the geometry is simple and the initial and boundary conditions are known, an analytical solution can be obtained and used. If the latter is possible, it should be used because doing so can significantly reduce the computation time and cost of an inverse problem.

In parameter estimation for a TRT, the first issue is “whether the model can reflect actual physical phenomena.” The first step of inverse parameter estimation is the construction of a mathematical model that corresponds to physical phenomena, and this can be challenging with a TRT because the physical phenomena of the subsurface are difficult to determine. In terms of the accuracy of the estimated parameters, selecting an appropriate model is very important; however, most analytical response models assume that the heat is transferred by conduction alone. If other physical phenomena such as advection by groundwater flow or natural convection in a porous formation are not negligible, a conduction-only model cannot provide accurate and stable results. In inverse parameter estimation, just adding the momentum equation (Eq. (2.14)) and advection term (Eq. (2.21)) cannot be the solution to such a situation because doing so requires additional information about the initial and boundary conditions and model parameters such as the effective porosity, permeability, hydraulic head, and Darcy velocity. This makes inverse problems extremely difficult and sometimes impossible to solve.

The second issue is “whether the assumptions made in the physical model (e.g., analytical or numerical model) used for the inverse estimation and the experimental conditions are consistent.” This concerns the disturbances in a TRT and the resulting inconsistency between the assumptions of the physical model and the experiment. If an analytical model is selected for the parameter estimation, the experimental conditions should match the assumptions in the analytical model. For instance, if the ILS model is used, the TRT should be conducted under the following conditions: the ground surface is adiabatic, and the heat flux from the source is constant. However, at an actual TRT site that is fully exposed to the outdoor environment, those assumptions are violated most of the time. As shown in Fig. 1.3, the temperature

response is perturbed by the heat transfer between the outdoor environment and aboveground TRT setup. Moreover, the unstable heat generation caused by fluctuation in the supply voltage also causes a fluctuating temperature response. These violations cause disagreement between the ILS and experimental data and results in an estimation error. Developing a method to consider them in TRT analysis would lead to better estimation accuracy.

The third issue is “which algorithm should be used for parameter estimation.” If the conventional TRT method and regressive estimation using the ILS model are used, then this issue does not need to be considered. However, if a TRT is conducted with a new method and a parameter estimation technique (i.e., optimization method) is introduced to evaluate the objective function, then the appropriate optimization algorithm needs to be selected because different methods have different search methods and speeds (computation time). Optimization methods can be classified into two groups: heuristic (including stochastic) and gradient methods. The heuristic method has the advantage of finding the global optimum. However, it requires high computation costs, and the obtained solution sometimes cannot be reproduced. The gradient-based method has the advantages of a fast convergence speed and reproducibility. Because of the different advantages and disadvantages of each method, it is important to select the appropriate algorithm according to the objective.

# CHAPTER 3

## EXPERIMENTAL SETUP AND UNCERTAINTY ANALYSIS

This chapter describes the two borehole heat exchangers (BHEs), thermal response test (TRT) apparatus, and uncertainty of the TRT according to the regressive estimation method based on the infinite line source (ILS) model.

### 3.1 Borehole heat exchangers

The experimental system was constructed at Chiba Experimental Station at the University of Tokyo (Inage Ward, Chiba, Japan) in 2014. Fig. 3.1 shows a picture of the test setup, and Fig. 3.2 shows schematic diagrams of the drill log and experimental setup. The site was stratigraphically divided into a top layer of loam and clay down to 8 m; this was followed by fine sand (8–25 m), silt (25–31 m), and fine sand (31–60 m) (Fig. 3.2(a)). The groundwater level fluctuated around a depth of 10–12 m. Table 3.1 describes the hydrogeological parameters of the fine sand, which was the dominant soil type at the site. Hydrogeological parameters such as the porosity and hydraulic conductivity were obtained from previous pumping and boring tests conducted at the same site in 2005 [88].

**Table 3.1** Detailed parameters of borehole heat exchanger (BHE) setup and soil.

Parameter [units]	Value
Borehole heat exchanger	
Borehole depth [m]	50
Borehole diameter [mm]	165
U-tube: High-density polyethylene	
Outer diameter [mm]	34
Inner diameter [mm]	27
Shank spacing [mm]	50
Thermal conductivity [W/(m·K)]	0.38
Volumetric thermal capacity [MJ/(m <sup>3</sup> ·K)]	1.81
Heat carrier fluid: Water	
Thermal conductivity [W/(m·K)]	0.6
Volumetric thermal capacity [MJ/(m <sup>3</sup> ·K)]	4.2
Soil: Fine sand	
Porosity [–]	0.35
Hydraulic conductivity [m/s]	2.1E–04

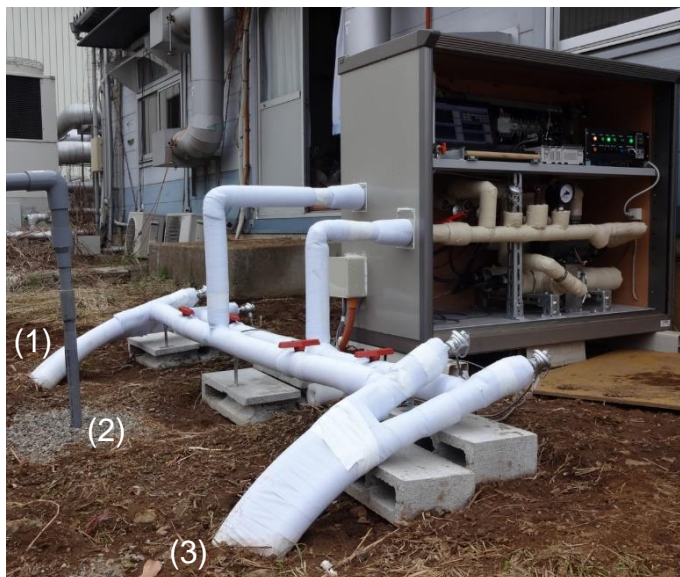


**Fig. 3.1** TRT setup at site: (1) gravel-backfilled BHE, (2) observation well, and (3) cement-grouted BHE.

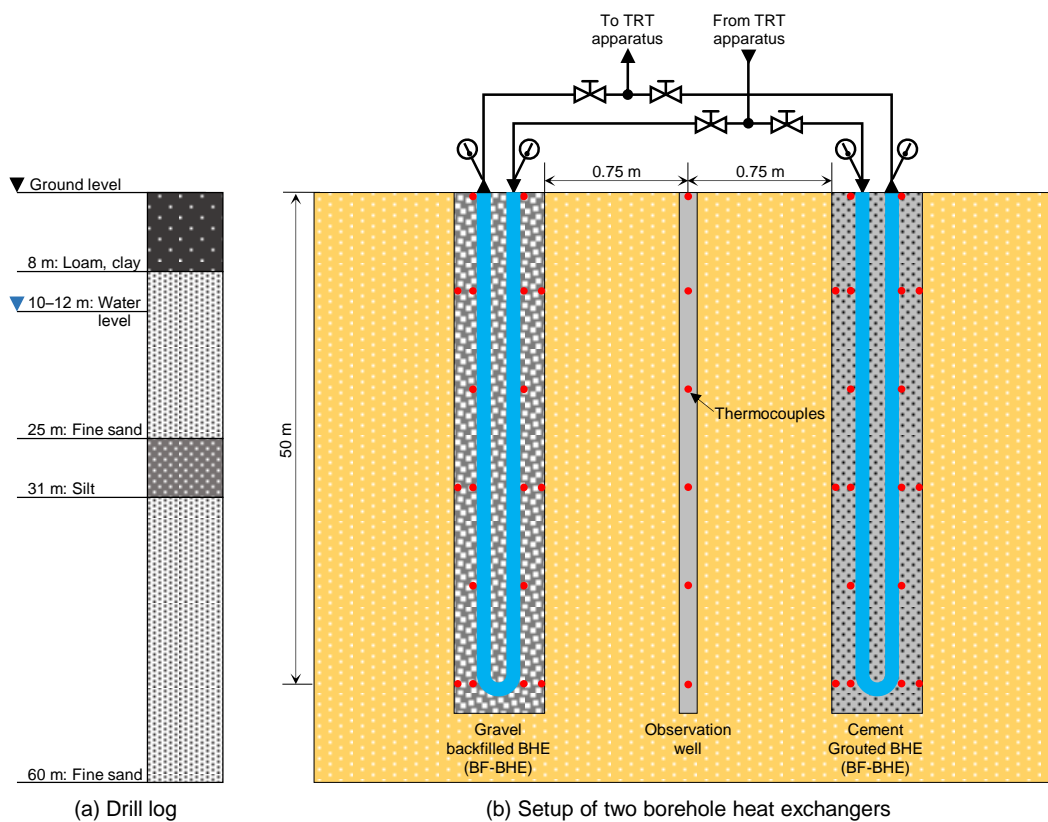


**Fig. 3.2** Schematic illustration of (a) drill log of the experiment site and (b) experimental setup.



**Fig. 3.3** Spacer used to maintain shank space of U-tube (units of ruler: cm).



**Fig. 3.4** Grain size of the gravel used in backfilled BHE (units of ruler: cm).

Two vertical closed loop BHEs were installed 1.5 m apart from each other with an observation well drilled between them (Fig. 3.2 (b)). The effective depth and diameter of the boreholes were 50 m and 165 mm, respectively. After the drilling, a single high-density polyethylene (HDPE) U-tube was inserted in each borehole with spacers. The spacers were placed between the U-tube legs at 10-m intervals to maintain a shank spacing of 50 mm (Fig. 3.3). The outer and inner diameters of the pipe legs were 34 and 27 mm, respectively. The BHE on the right side of the observation well was grouted with Portland cement mixed with 20% silica sand (GR-BHE), and the BHE located on the left was backfilled with gravel (BF-BHE) with grain sizes of 8–15 mm (Fig. 3.4). The measured porosity of the gravel was 38%. T-type thermocouples were installed at 10-m intervals in both boreholes and the observation well to obtain additional information regarding the thermal behavior of the soil (Fig. 3.5). To reduce the exchange of heat between the circulating fluid and external environment and thus reducing the effect of diurnal

variations in factors such as the temperature, radiation, wind, and precipitation, both the hydraulic circuit located above the ground and the TRT apparatus were insulated. Water was used as the heat carrier fluid.



**Fig. 3.5** T-type thermocouples installed on surface of U-tube.

## 3.2 Thermal response test apparatus

The TRT apparatus (Fig. 3.6) that was designed and constructed in 2014 comprised a heating unit, constant rate pump, hydraulic circuit, electrical circuit, control circuit, and measuring system.

The heating unit consisted of three different heaters with power outputs of 2, 4, and 6 kW. The output could thus be increased to up to 12 kW at 2-kW intervals by using different on/off combinations of the three heaters. The power consumption of the heating unit was measured with a wattmeter. A magnetic drive pump was used to circulate the heat carrier fluid, and it was operated at a constant flow rate and a power consumption of 0.36 kW. The flow rate was controlled with the bypass loop and measured with an electromagnetic flowmeter. Platinum resistance temperature sensors (Pt-100) were installed in both the BHE and the TRT apparatus loops (Fig. 3.2 and Fig. 3.6). Their use allowed for the measurement of the actual heat injection rate to the BHE and the heat loss or gain in the hydraulic circuit above the ground. In addition, the temperature inside the TRT apparatus, dry-bulb temperature, relative humidity, global insolation, and precipitation were measured. Data were recorded every 2 or 5 s. Table 3.2 summarizes the specifications and accuracy of the sensors and components.

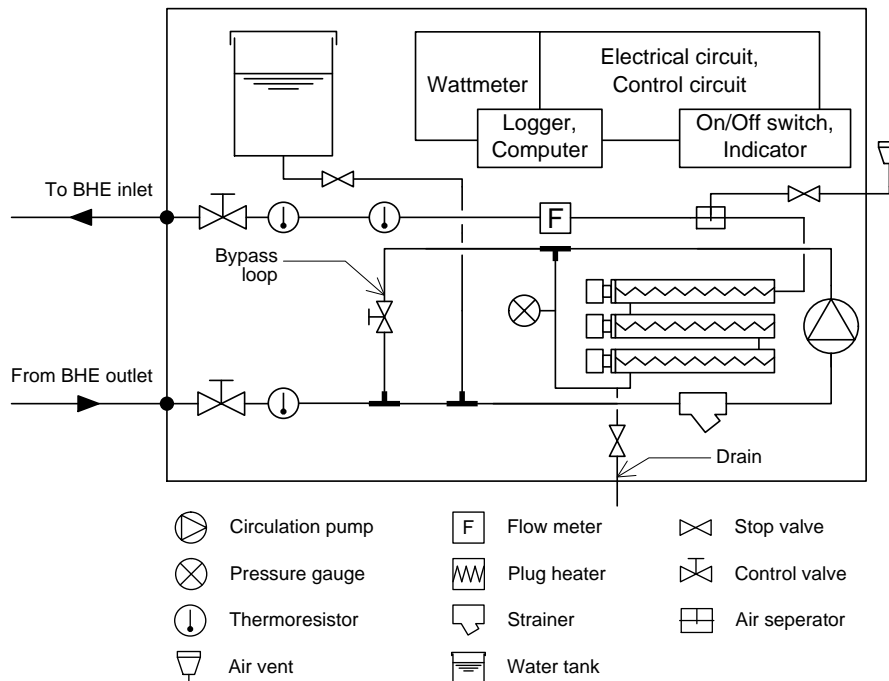


**Fig. 3.6** Schematic diagram of thermal response test apparatus.

**Table 3.2** Details of components used in the TRT apparatus.

Component	Manufacturer	Specifications, Accuracy
Heater	Izumi Dennetsu	2, 4, 6 kW plug heater
Pump	Iwaki Pump	Magnetic drive pump Power consumption: 364 W Max. flow rate: 135 l/min, Head: 11.7 m
Flow meter	Keyence	Range: 5–100 L/min at 1 s interval $\pm 3.5\%$ at 2.5 s interval $\pm 2.5\%$ at 5 s interval $\pm 1.6\%$ at 10 s interval $\pm 1.0\%$
Pt-100	Netsushin	Class A, $\pm(0.15 + 0.002 \times T)$ °C
Thermocouples	Netsushin	Class A, $\pm(0.5 + 0.004 \times T)$ °C
Data logger	Keyence	$\pm 0.05\%$ (T-type) $\pm 0.1\%$ (Pt-100) Flow rate: $\pm 0.03\%$
Temperature controller	Azbil	Sampling interval: 0.1 s $\pm 0.15\%$ (Pt-100) Current output: $\pm 0.1\%$

The roles of the control circuit were to control the heater output as intended by the experimenter, ensure operation under safe conditions, and prevent damage to the apparatus from abnormal operation. Fig. 3.7 shows a schematic of the control sequence. This control sequence can be performed by combining the electrical and control circuits, which are shown in Fig. 3.8 and Fig. 3.9, respectively. Table 3.3 explains the abbreviations used in Fig. 3.8 and Fig. 3.9.

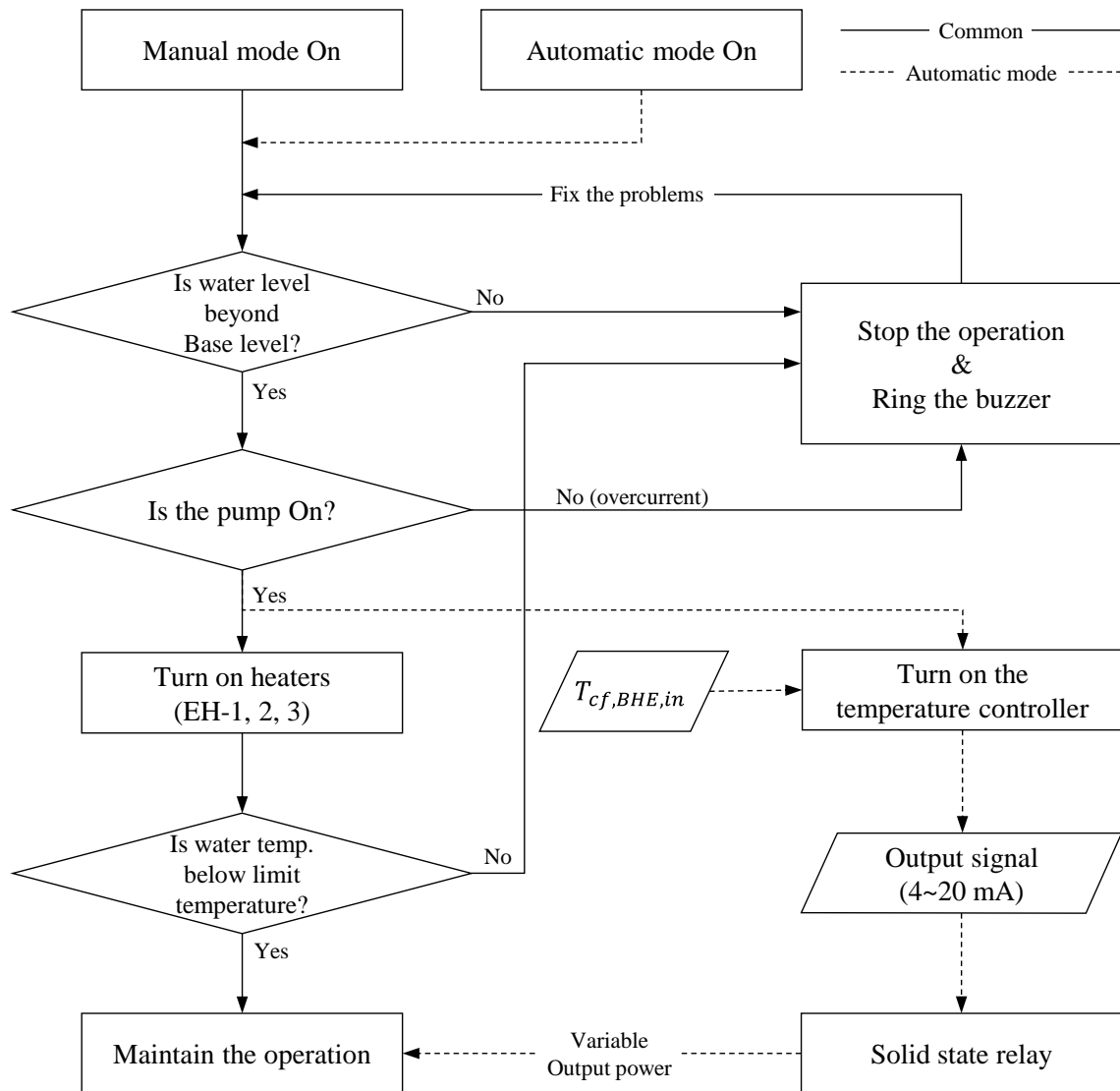


**Fig. 3.7** Control sequence of TRT apparatus.

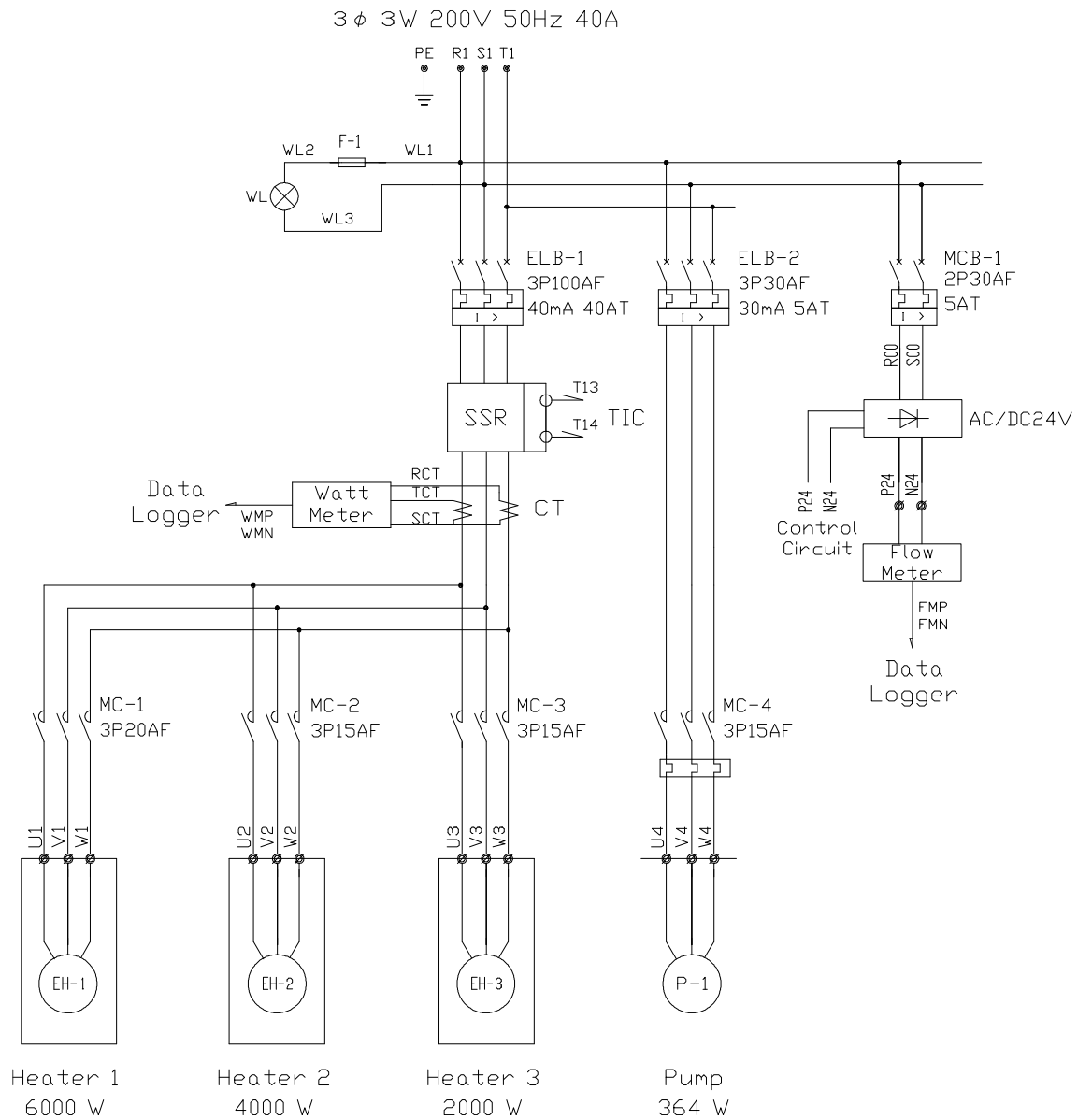


**Fig. 3.8** Schematic of electrical circuit of TRT apparatus.

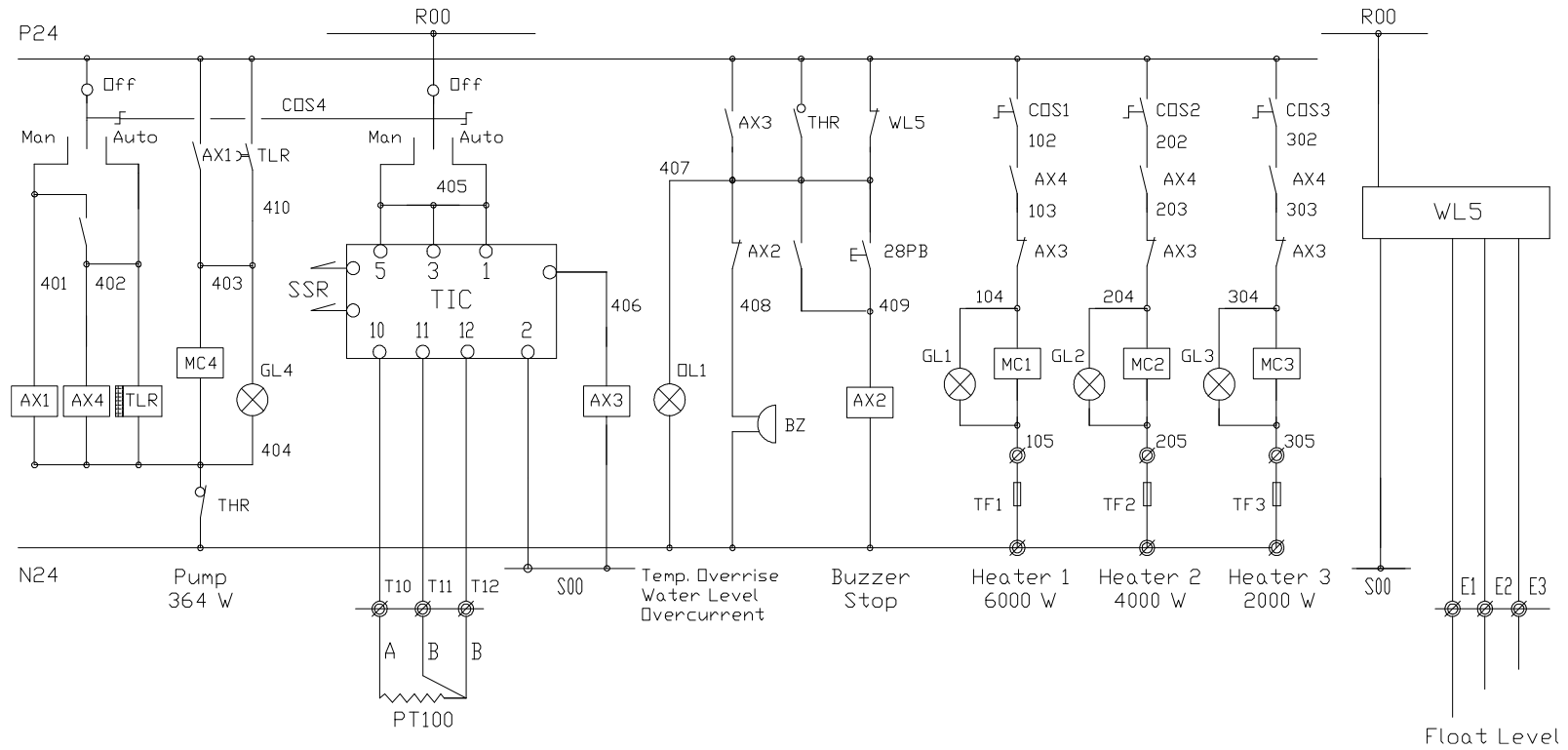


Fig. 3.9 Schematic of control circuit of TRT apparatus.

**Table 3.3** Abbreviations used in Fig. 3.8 and Fig. 3.9 for electrical and control circuits.

Abbreviation	Original form	Note
AX	Auxiliary Relay	
BZ	Buzzer	Buzzer for warnings
COS	Change Over Switch	On/off of pump, and heaters
CT	Current Transformer	Used to adjust input of wattmeter
EH	Electric Heater	2, 4, 6 kW plug heaters
ELB	Electrical Leakage Circuit Breaker	Circuit breaker for the main
F	Fuse	Fuses used for three heaters
GL	Green Lamp	Status light for operation of heaters and pump
MC	Magnetic Contactor	Circuit breaker for pump and heaters
MCB (=NFB)	Molded Case Circuit Breaker (No Fuse Breaker)	Circuit breaker for over-current and short circuiting
N	N/A	Neutral connection
OL	Orange Lamp	Status light for warnings
P	Pump	Constant flow rate pump
PB	Push Button	Buzzer stop button
PE	N/A	Earth connection
P, N	N/A	Direct current output
R, S	N/A	Direct current input
R, S, T	N/A	Three phase alternating current input
SSR	Solid State Relay	SSR is a non-contact semiconductor relay that has an advantage over the electromagnetic relay in terms of speed, accuracy, and noise. The heater output was controlled by combining the SSR with the temperature controller. Voltage signal from TIC → On / Off control Current signal from TIC → Cycle control
TF	Temperature Fuse	Used for overheating of heaters
THR	Thermal Relay	Relay for over-current flow
TIC	Temperature Indicator Controller	Sends a voltage or current signal to the SSR. The proportional-integral-derivative (PID) control algorithm is used to control the heater output.
TLR	Time Lag Relay	To prevent overheating of the circulating water, the pump turns off 5 s after the heaters turn off.
U, V, W	N/A	Three phase alternating current output
WL5	Water Level Relay	Relay for makeup water level
WL	White Lamp	Status light for power supply
3P	3 Phase	Supply power
30mA 40AT	30 mA–40 Ampere Trip	A circuit breaker allows a current flow of 30 mA–40 A and trips out of the allowed current range. The lower bound (30 mA) is referred to as the sensitivity of the breaker. A lower value better protects against an electric shock. The upper bound (40 A) is referred as the rated breaking current. A breaker was configured to trip at a current beyond 40 A.
40AF	40 Ampere Frame	Mechanical frame size of circuit breaker. Among the materials constituting the circuit breaker, the non-conducting frame part had the maximum rated current capacity of 40 A. AF is related to the life of the circuit breaker, which is shortened by internal heat generation. AF is always greater than AT.

The TRT apparatus could be operated in two modes: manual and automatic. In the manual mode, the output of the heaters was not controlled. Constant heat generation at 2 kW intervals up to 12 kW was possible with manual combination of the three heaters. The heater output was only controlled by the temperature controller when the fluid temperature was over the safety limit. In contrast, the automatic mode could control the heat output to meet a set temperature value by using the solid state relay (SSR), transducer, and temperature controller. When combined, these components allowed cycle control for an alternating current of 50 Hz. The solid line in Fig. 3.7 represents the control logic used in both manual and automatic modes, and the dotted line represents the control logic used only in automatic mode.

In both the manual and automatic modes, the beginning of the control sequence is the same. First, when power is supplied, the water level of the makeup water tank is sensed. If the water is above the base level, the pump operates. If the water level is below the reference level, the pump does not operate, and a buzzer rings. The buzzer stops ringing and the pump starts to operate when the water rises above the base level. When the pump still does not work even if the water is above the base level, this indicates that there is a problem due to an overcurrent. In this case, the circuit breakers should be checked. If the pump is not in operation, the heaters cannot operate because the AX4 is opened when the pump is operating. This control logic prevents the fluid from overheating without circulation. Safe operation of the TRT apparatus is guaranteed by the control sequence and by monitoring the fluid temperature, current, and makeup water level.

### 3.3 Uncertainty analysis

Uncertainty refers to doubt about the measured results. In a broad sense, this is the uncertainty of the measurement and doubt about the validity of the measured result. In this study, the quantitative evaluation of the uncertainty was based on the Guide to the Expression of Uncertainty in Measurement (GUM) suggested by ISO [89]. This is an evaluation method based on mathematical and statistical principles. The GUM provides a general method for evaluating and expressing uncertainty.

Uncertainty is evaluated by considering the error of all components that is known or suspected. It refers to doubt about how well the measured results represent the true value. The term “true value” is not used in uncertainty analysis because the absolute true measured value cannot be known. This is because the uncertainty is caused by various factors. Traditionally, these effects are divided into random and systematic errors. Random error represents the scatter of measurements caused by unknown reasons, and systematic error is due to biases in the measurement system. Therefore, measurement uncertainty is caused by imperfections in the correction of systematic errors and the effect of random error, which is not

controllable. The final form of the measurement uncertainty is expressed by using the measured values with an uncertainty range to characterize the degree of scattering. In the GUM of ISO, the uncertainty is expressed as Type A or B rather than the terms “random” and “bias” errors that are used in conventional uncertainty analysis. Types A and B are defined as follows.

- Type A: The uncertainty component is obtained from a statistical analysis using a series of observations. In general, the normal distribution (Gaussian distribution) is assumed in an analysis.
- Type B: The uncertainty obtained using any methods except for the uncertainty determined statistically from repeated observations (e.g., the method of Type A). All available information about the uncertainty of each component is used to evaluate uncertainty. Scientific judgment based on past experience or knowledge can also be used. The error range of a measuring instrument given by the manufacturer’s specifications and certificate can also be used. For the provided error range, the shape of the probability distribution, standard uncertainty, and degree of freedom should be determined.

Uncertainty analysis is conducted in two stages: (1) obtaining the uncertainties related to the measurement of individual variables, and (2) determining the uncertainty in the final result from the propagation of individual measurement uncertainties.

### 3.3.1 Standard uncertainty

#### • Type A uncertainty

First, the method to determine Type A uncertainty is explained. The quantity  $Y$  is measured and defined as the measurand. This is not directly measured but determined from  $N$  other measured quantities (input variables). The input quantities are expressed as  $X_1, X_2, \dots, X_N$ , and the measurement equation is

$$Y = f(X_1, X_2, \dots, X_N) \quad (3.1)$$

If it is possible to obtain the observed value without an error, the uncertainty analysis simply becomes a mathematical problem, and there is no need to use a statistical method. However, the observed variables always contain errors from the measurement calibration, differing times when observations are made, and different observers. Thus, Eq. (3.1) should be expressed as a measurement process that contains all of the factors that can contribute to errors in the measurement results.

The estimate of the measurand (output quantity)  $Y$  is denoted by  $y$  and is obtained from Eq. (3.1) by using the input estimates  $x_1, x_2, \dots, x_n$  for the values of the  $N$  quantities  $X_1, X_2, \dots, X_N$ . The output estimate  $y$  obtained from the measurement is expressed as

$$y = f(x_1, x_2, \dots, x_n) \quad (3.2)$$

Type A uncertainty is evaluated by calculating the standard deviation from a series of independent observations under the same conditions. The expected value of a quantity  $q$  that changes randomly can be obtained by using the following arithmetic mean equation:

$$\bar{q} = (1/n) \sum_{k=1}^n q_k \quad (3.3)$$

By using a series of observed input quantities  $X_i$  that are described in Eq. (3.3), the arithmetic mean can be expressed as  $\bar{X}_i$ .  $\bar{X}_i$  is used as the input estimate  $x_i$  in Eq. (3.2) to calculate the measurement result  $y$ , that is,  $x_i = \bar{X}_i$ .

The individual observation  $q_k$  has different values because each measured value is affected by random variation or random errors of the data acquisition system. The degree of variability can be quantified by evaluating the variance of the probability distribution for  $q_k$ :

$$s^2(q_k) = \left(\frac{1}{n-1}\right) \sum_{k=1}^n (q_k - \bar{q})^2 \quad (3.4)$$

where  $s^2$  is the variance of the probability distribution and its positive square root  $s$  denotes the experimental standard deviation. In the GUM, the standard deviation  $s$  is defined as the experimental uncertainty  $u$  as follows:

$$u(q_k) = s(q_k) = \sqrt{\left(\frac{1}{n-1}\right) \sum_{k=1}^n (q_k - \bar{q})^2} \quad (3.5)$$

The uncertainty from Eq. (3.5) is referred to as Type A uncertainty. This uncertainty only indicates how much the data is distributed with respect to the average value and cannot be used to evaluate the bias of the data, as can be inferred from Eq. (3.5).

**• Type B uncertainty**

Type B uncertainty is evaluated by a scientific method based on all of the related information, such as the calibration uncertainty, operation procedure, resolution of instruments, environmental changes, different operators, and reading drift of the instrument. The following information can be used to determine Type B uncertainty:

- (1) The prior measured data
- (2) The knowledge or experience related to using the instrument
- (3) The specifications of the instrument from the manufacturer
- (4) The calibration certificate from the manufacturer
- (5) The data from a handbook

If the calibration certificate or manufacturer's specifications about the error range of the instrument are available, Type B uncertainty is reliable and easy to estimate. If the upper and lower bounds of the distribution are denoted by  $\pm a_i$ , then the geometric shape of the distribution that should be used is the only issue. Well-known distribution shapes are rectangular (uniform), normal (Gaussian), triangular, and asymmetric (Table 3.4). Selecting the appropriate distribution shape depends on the available information.

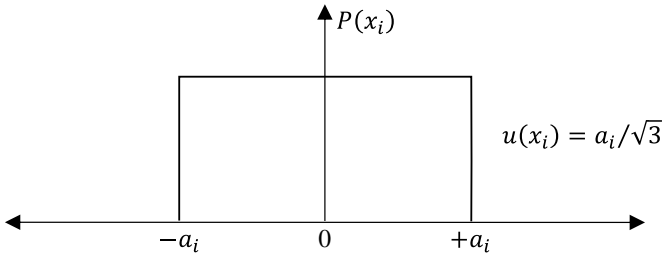
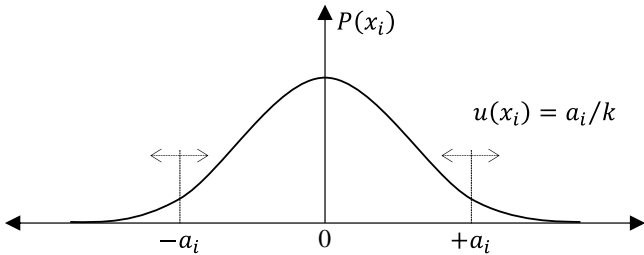
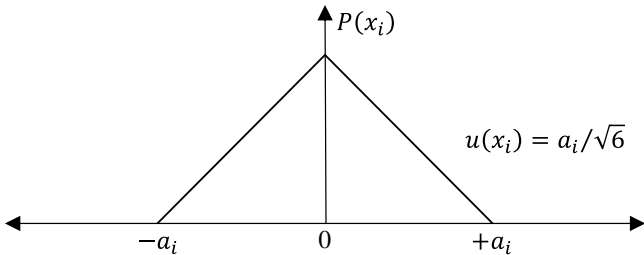
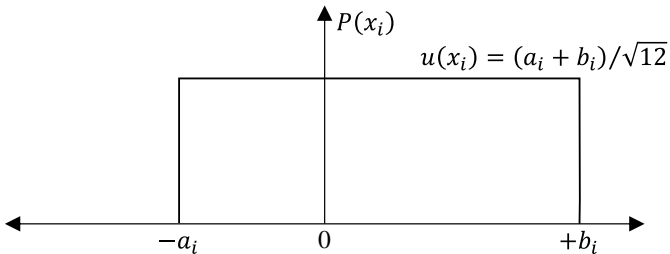
(1) Rectangular distribution: The input quantity lies in the interval  $\pm a_i$  with a probability of 100% (i.e., without an exception). The quantity is treated as if it is equally probable for uniform probability distribution.

(2) Normal distribution: By using the provided uncertainty level and the coverage factor, which represents the confidence interval, the uncertainty quoted in a calibration certificate, manufacturer's specifications, etc. can be converted into the standard uncertainty with the normal distribution. In general, two confidence intervals are used: 95% and 99%. Their coverage factors  $k$  are 1.96 and 2.576, respectively.

(3) Triangular distribution: This distribution shape is used in the absence of any information other than the upper and lower bounds.

(4) Asymmetric distribution: When the upper and lower bounds are not symmetric because of reasons such as the drift of the measuring instrument, an asymmetric distribution can be used to estimate the standard uncertainty.

**Table 3.4** Schematic of probability distribution shapes.

Distribution	Standard uncertainty of measured value $x_i$
Rectangular	
Normal (Gaussian)	
Triangular	
Asymmetric	

### 3.3.2 Combined standard uncertainty

After the uncertainty of individual variables is evaluated, the second stage of uncertainty analysis is evaluating the combined standard uncertainty  $u_c$ , which represents the uncertainty of the final result. This process involves analyzing how those individual uncertainties propagate to the final result. The combined uncertainty with respect to  $y$  is calculated from the following equation:

$$u_c^2(y) = \sum_{i=1}^N c_i^2 u^2(x_i) + 2 \sum_{i=1}^{N-1} \sum_{j=i+1}^N c_i c_j u(x_i) u(x_j) r(x_i, x_j) \quad (3.6)$$

where  $N$  is the number of measurements and  $c$  is the sensitivity coefficient, which is expressed by the first derivative with respect to each variable:

$$c_i = \partial f / \partial x_i \quad (3.7)$$

The sensitivity coefficient can be estimated numerically by using the finite difference method.

$$\frac{\partial f}{\partial x_i} = \frac{\Delta f}{\Delta x_i} = \frac{f(x_i + \Delta x_i) - f(x_i)}{\Delta x_i} \quad (3.8)$$

Typically, 0.1–1% of  $x_i$  for  $\Delta x_i$  is sufficient for numerical approximation of the first derivative.

In Eq. (3.6),  $r$  is the correlation coefficient and represents how much two quantities are inter-correlated.

This is expressed as

$$r(x_i, x_j) = \frac{u(x_i, x_j)}{[u(x_i)u(x_j)]} \quad (3.9)$$

where  $u(x_i, x_j)$  is the covariance between  $x_i$  and  $x_j$ .

The range of  $r$  is -1 to +1. If the variables are independent, then  $r(x_i, x_j) = 0$ . In this case, the second term of the right-hand side of Eq. (3.6) becomes 0, and the equation for the combined uncertainty reduces to

$$u_c^2(y) = \sum_{i=1}^N c_i^2 u^2(x_i) \quad (3.10)$$

Eq. (3.10) is a formulation to evaluate the combined uncertainty using the independent variables.

If the input variables are perfectly inter-correlated, then  $r(x_i, x_j) = 1$ . In this case, the combined uncertainty is simply the sum of the standard uncertainty of each variable.

$$u_c(y) = \sum_{i=1}^N c_i u(x_i) \quad (3.11)$$

### 3.3.3 Uncertainty analysis of TRT interpretation

To evaluate the estimation error range of TRT, uncertainty analysis was conducted to estimate the effective thermal conductivity with the ILS model. The ILS model (Eq. (2.46)) was rewritten using the heat injection rate  $Q_{BHE}$  and length of BHE  $H$  as follows:

$$\bar{T}_{cf}(t) = \frac{Q_{BHE}}{\underbrace{4\pi H \lambda_{eff}}_k} \ln(t) + \frac{Q_{BHE}}{4\pi H \lambda_{eff}} \left\{ \ln\left(\frac{4\lambda_{eff}}{C_s r_b^2}\right) - \gamma \right\} + R_b \cdot \frac{Q_{BHE}}{H} + T_0 \quad (3.12)$$

Although  $Q_{BHE}$ , which is a very important parameter in this thesis, is constantly fluctuating and has a significant impact on the estimation, it was assumed to be constant to consider the estimation error caused solely by the intrinsic error of the sensors.

The relationship between the average fluid temperature and logarithmic elapsed time Eq. (3.12) is given by the effective thermal conductivity  $\lambda_{eff}$  and can be estimated by using the gradient of the semi-log plot:

$$\lambda_{eff} = \frac{Q_{BHE}}{4\pi H k} \quad (3.13)$$

The gradient of the semi-log plot  $k$ , length of BHE  $H$ , and heat injection rate  $Q_{BHE}$  were assumed to be 2.2, 50 m, and 2.5 kW, respectively. Under these assumptions, the estimated  $\lambda_{eff}$  was 1.81 W/(m·K). If there is no error in the regression process for obtaining  $k$ ,  $\lambda_{eff}$  and the related input variables can be expressed as follows:

$$\lambda_{eff} = f(Q_{BHE}, H) \quad (3.14)$$

However,  $Q_{BHE}$  cannot be obtained directly in an experiment and is obtained using  $Q_{BHE} = (T_{cf,in} - T_{cf,out})\rho_{cf}c_{cf}\dot{V}_{cf}$ . Therefore, the explicit expression of Eq. (3.14) is:

$$\lambda_{eff} = f(\rho_{cf}, \dot{V}_{cf}, c_{cf}, T_{cf,in}, T_{cf,out}, H) \quad (3.15)$$

To evaluate the combined uncertainty of the estimated  $\lambda_{eff}$ , the individual uncertainties of input variables should be known. The error ranges for the thermal properties of the circulating fluid were assumed to be  $\pm 0.5\%$ . For the input variables obtained from sensors, Type B uncertainty was used based on the provided error ranges from the sensor manufacturers. The Gaussian distribution and the coverage factor  $k = 1.96$  corresponding to a confidence interval of 95% were used (Table 3.5).

**Table 3.5** Specified and assumed error range and used uncertainty of individual input quantities.

Input variable	Measured value	Specified or assumed error range	Error range	Uncertainty
$\dot{V}_{cf}$ [m <sup>3</sup> /s]	3.4 E-04	$\pm(1.6 \times \dot{V}_{cf})\%$	$\pm 5.4$ E-06	2.8 E-06
$T_{cf,in}$ [°C]	35.0	$\pm(0.15 + 0.002 \times T)$ °C	$\pm 0.22$	0.112
$T_{cf,out}$ [°C]	33.25	$\pm(0.15 + 0.002 \times T)$ °C	$\pm 0.217$	0.111
$\rho_{cf}$ [kg/m <sup>3</sup> ]	1000	$\pm 0.5\%$ (assumed)	$\pm 5$	2.55
$c_{cf}$ [J/kg·K]	4200	$\pm 0.5\%$ (assumed)	$\pm 21$	10.71
$H$ [m]	50	$\pm 0.1\%$ of reading	$\pm 0.05$	0.026

Because the input quantities are independent of each other, the combined uncertainty can be obtained by using Eq. (3.10). The explicit expression of Eq. (3.10) is as follows:

$$\begin{aligned}
 u_c(\lambda_{eff}) &= \sqrt{\sum_{i=1}^N c_i^2 u^2(x_i)} \quad (3.16) \\
 &= [c^2(\dot{V}_{cf})u^2(\dot{V}_{cf}) + c^2(T_{cf,in})u^2(T_{cf,in}) + c^2(T_{cf,out})u^2(T_{cf,out}) \\
 &\quad + 2c^2(\rho_{cf})u^2(\rho_{cf}) + c^2(c_{cf})u^2(c_{cf}) + c^2(H)u^2(H)]^{1/2}
 \end{aligned}$$

The combined uncertainty of  $\pm 0.163$  W/(m·K) was obtained using the values in Table 3.5 and this corresponds to 9.04% of the estimated  $\lambda_{eff}$  (=1.81 W/(m·K)).

Knowing which input variable has the largest impact on the combined uncertainty is important for improving the experiment design. The error contribution of the input parameter  $\epsilon_i$  for a certain parameter is defined as follows:

$$\epsilon_i = c_i^2 u^2(x_i) / \sum_{i=1}^n c_i^2 u^2(x_i) \quad (3.17)$$

Table 3.6 summarizes the calculated  $\epsilon_i$  of each parameter. The error of the temperature sensors had the most significant impact on the combined uncertainty of  $\lambda_{eff}$ . This means that the accuracy of the temperature sensors is extremely important to reducing the uncertainty in a TRT. Therefore, for better accuracy, special care should be taken with the temperature sensors when designing the setup for a TRT.

**Table 3.6** Calculated results and error contribution of each input variable.

Component	$\dot{V}_{cf}$	$T_{cf,in}$	$T_{cf,out}$	$\rho_{cf}$	$c_{cf}$	$H$
$c_i \approx \Delta f / \Delta x_i$	3111.1	0.605	-0.605	0.0011	0.0003	-0.021
$u(x_i)$	2.8 E-06	0.112	0.111	2.55	10.71	0.026
$c_i^2 u^2(x_i)$	7.5.E-05	4.6.E-03	4.5.E-03	7.3.E-06	7.3.E-06	2.9.E-07
$\epsilon_i$ [%]	0.81	50.31	48.72	0.08	0.08	0.00

### 3.3.4 Expanded uncertainty of TRT

Although the standard combined uncertainty  $u_c$  can be widely used to quantitatively express the uncertainty of the measurement results, it is often necessary to provide a measure of uncertainty that defines the interval of the measured result. That is, the interval may be expected to encompass a large fraction of the distribution of values that could reasonably be attributed to the measurand, which is the measurement target. The expanded uncertainty  $U$  can be used to represent this interval.  $U$  is calculated by multiplying  $u_c$  with the coverage factor  $k$ , which represents the broadness of the range being covered:

$$U = k u_c(y) \quad (3.18)$$

When  $k$  is 1.96, it corresponds to a confidence interval of 95% for the normal distribution. This means that the measurements were conducted 20 times, and 19 of the 20 measurements lay in the interval.

The result of a measurement is expressed as  $Y = y \pm U$ , and the coverage factor and confidence interval should also be described with the expanded uncertainty. For example, when using the calculated  $u_c(\lambda_{eff}) = \pm 0.163 \text{ W}/(\text{m}\cdot\text{K})$  and  $k = 1.96$ , the following description should be provided:

$$\lambda_{eff} = 1.81 \pm 0.267 \text{ (confidence interval 95\%)}$$

In general, the coverage factor follows Student's t-distribution.



CHAPTER 4  
DEVELOPEMENT OF ANALYTICAL DISTURBANCE  
MODEL, PARAMETRIC STUDY, AND SENSITIVITY  
ANALYSIS

## 4.1 Introduction

Many analytical and numerical response models have been used to solve the inverse problem using TRT data. Specifically, the infinite line source (ILS) model [9], the infinite cylindrical source model [10], the finite line source model [11], the composite model [90], and the numerical method with a parameter estimation technique [14,18,22,53,91–94] have been used to estimate the thermal properties of the ground and to predict the temperature response of the ground. Among all of the estimation methods available, one of the most frequently used methods is regression estimation using the exponential integral approximated ILS model [5,9]. This is primarily because of the ILS model's simplicity and wide applicability. It becomes more attractive when combined with the sequential plot method [20,95] because the estimation behavior and the convergence of the test can be known.

For the boundary conditions, as described in Section 2.3, the ILS model assumes the adiabatic condition on the ground surface and the constant heat flux from the heat source. However, in reality, these assumptions are violated in most cases. Regarding the adiabatic surface condition, the assumption is violated by the heat exchange between ground surface and atmosphere. The effect of heat flux from the ground surface would be small for a TRT of a relatively long BHE. Additionally, the TRT rig, which includes the hydraulic circuit that connects the TRT rig and BHE loop, can also be affected by changes in the external environment. Moreover, voltage fluctuations from the power grid can affect the heat output from the TRT rig. Therefore, the constant heat rate assumption is also violated. These violations of the boundary conditions cause estimation errors when the ILS model is used for the inverse estimation.

The above-mentioned disturbances have been recognized by many researchers [7,14–22], and the effects can even be found in some response curves from studies that did not account for the influence of the disturbances [8,23–27].

Power fluctuations of the heater caused by unstable supply voltage from the power grid were clearly captured in the TRT results conducted by Sharqawy et al. [19]. They observed increases in the heating power during the night time and decreases during the day time. The electrical power swing was directly connected to temperature fluctuations in the circulating fluid.

Florides and Kalogirou [17] stated that TRT data are affected by two factors. One is the heat flux from the ground surface, which changes the temperature of the top layer of the ground. The second factor is the change of the heat injection rate caused by voltage fluctuations from the power grid. In their study [17], the output of the heater increased by about 300 W at night time. The authors said that the disturbance effects from multiple factors can be neglected during 280–400 h of the TRT when the fluid temperature increment becomes stable. However, in practice, a TRT of such a long duration might not be conducted

because of cost and time limitations. Accordingly, many researchers have been trying to determine the appropriate minimum test period to obtain reliable results [18,70,90,96–100].

Austin [14] also found that temperature changes in the heat carrier fluid can occur as a result of unstable power supplies and that the results of a TRT can be altered by diurnal temperature variations. Notably, Austin [14] observed disturbance effects even when the test period was long. Other researchers [7,72] have also pointed out this same problem.

Signorelli et al. [18] presented the relation between estimated thermal conductivity and the temperature difference between the outdoor air temperature and heat carrier fluid. The estimated ground thermal conductivity was oscillating within the range of 3.5 to 3.9 W/(m·K) because of the heat exchange between the outdoor air and heat carrier fluid. The authors stated that insufficient insulation of the test device and piping above the ground can affect the test results considerably. Raymond et al. [34] showed that there was a strong influence of surface temperature variations, which varied between day and night, on a TRT conducted in a short BHE installed in a mine waste dump. This disturbance created different estimated thermal conductivities between the numerical analysis and ILS model results. Roth et al. [15] found that the fluid temperature was affected by the outdoor environment even when the hydraulic circuit was insulated. Bandos et al. [16] also pointed out effects from the varying external environment.

Power fluctuations of the heater caused by unstable supply voltage from the power grid were clearly captured in the TRT results conducted by Sharqawy et al. [19]. They observed increases in the heating power during the night time and decreases during the day time. The electrical power swing was directly connected to temperature fluctuations in the circulating fluid.

To consider the variable heat rate, some other methods are used. For example, recursive curve matching estimation using a temporal superposition-applied analytical model [5,8,21,57,101–103] and estimation using a numerical model combined with the parameter estimation technique [14,18,22,34,53,91–94] were employed to account for the variable heat rate in a TRT. However, before considering the disturbed variable heat rate, consideration must be given to how an experimenter can obtain quality data, i.e., data that can be interpreted using an analytical model that assumes constant heat flux. In other words, insights into the factors that affect the quality of TRT data and the extent of their influence are important. In this respect, a systematic analysis of disturbance effects in TRTs is necessary. Because most TRTs, except for special-purpose experiments conducted in laboratories [104], are conducted in outdoor environments, which are not fully controllable, many factors affect the quality of the TRT data and some of them vary continuously. These factors include weather conditions (wind velocity, ambient temperature, and solar irradiation), settings of the TRT rig (heat injection rate and flow rate), and the properties and geometry (thickness of insulation, radiation absorptivity of surface, and length) of the hydraulic circuit that connects

the BHE and the TRT rig. Insights into which among these parameters should be controlled first and how a TRT should be conducted have practical significance, and they can be gained through quantitative estimation of the disturbance effect in the TRT setup.

The objective this chapter is to provide insights into conducting TRTs and designing TRT setup to obtain quality data. For this, a quasi-steady state analytical model that considers the disturbance in an aboveground TRT setup was derived. Using this model and six different typical weather conditions, parameters related to the disturbance effect were analyzed in a systematic and qualitative manner. To elucidate the importance of each parameter intuitively, a sensitivity analysis was conducted. Some general conclusions were drawn on the basis of the results to obtain less-disturbed TRT data.

## 4.2 Analytical Model considering disturbance in thermal response test

### 4.2.1 Derivation of disturbance model

This section describes the derivation of a theoretical model that represents the disturbance in a TRT setup above the ground. The general setup of the TRT, which includes the TRT rig and a connecting hydraulic circuit, is shown in Fig. 4.1.

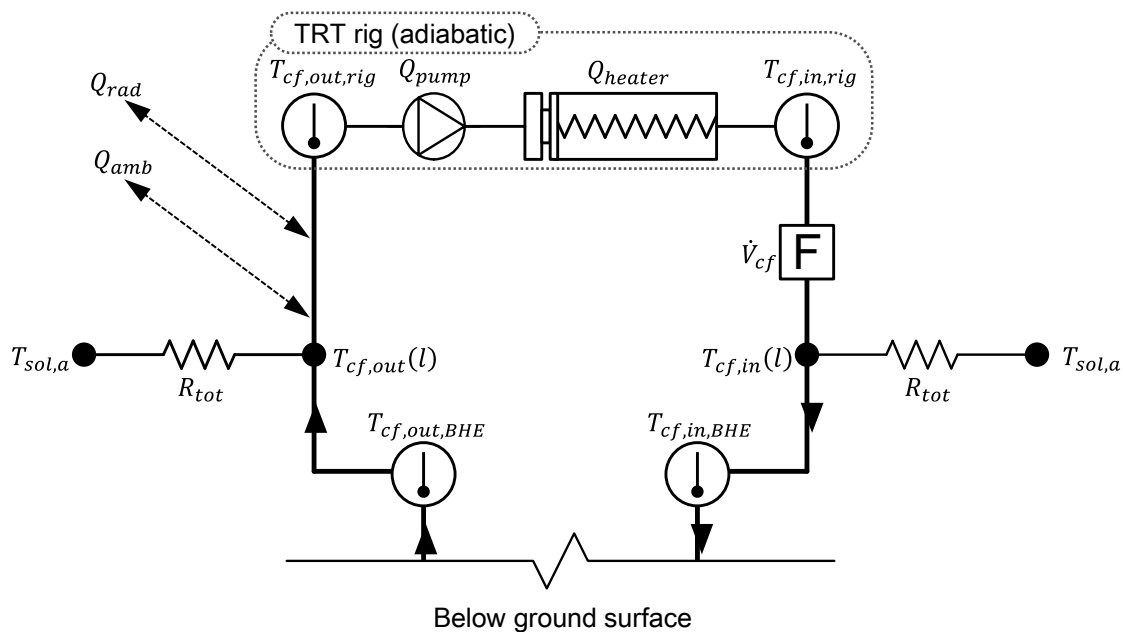


**Fig. 4.1** Schematic of aboveground thermal response test (TRT) setup.

The heat injection rate is typically assumed to be constant in analytical models such as the ILS [9] and ICS [10] models. The heat injection rate comprises heat generation from heaters  $Q_{heater}$  and pump  $Q_{pump}$  in the TRT rig, and the sum of them is denoted by  $Q_{rig}$ . This value is proportional to the square of the voltage from the electric grid. Even without considering the heat exchange with the outdoor environment,  $Q_{rig}$  is not constant in reality because of voltage fluctuation from the electric grid. The voltage fluctuation can be stabilized to some extent by installing a voltage regulator, however, the cost for a high capacity regulator is expensive and perfect stabilization is hard to achieve. The voltage fluctuation can be measured using a wattmeter, it is not predictable or fully controllable. Therefore, voltage fluctuation was not considered in this study.

Besides the voltage fluctuation, heat transfer that occurs in the hydraulic circuit is a significant cause of temperature perturbation (Fig. 4.1). The total disturbance heat exchange rate is denoted by  $Q_{d,tot}$ , which is the sum of  $Q_{amb}$ ,  $Q_{rad}$ , and  $Q_{lat}$ .  $Q_{amb}$  is the heat exchange rate between the circulating fluid and the outdoor air that is influenced by conduction and convection processes.  $Q_{rad}$  and  $Q_{lat}$  are the heat exchange rates caused by radiation and evaporative processes (latent heat), respectively. Among these disturbance components,  $Q_{lat}$  has very little effect if the hydraulic circuit is not wet. Therefore, only  $Q_{amb}$  and  $Q_{rad}$  are considered here for a clear and simple analysis. Then, the actual heat injection rate to the ground,  $Q_{BHE}$ , can be written as the following equation:

$$Q_{BHE} = Q_{rig} + \frac{Q_{amb} + Q_{rad}}{Q_{d,tot}} \quad (4.1)$$

Assuming that the length of the hydraulic circuit in the rig is relatively very short compared with the connecting circuit and that the effect of the outdoor environment in the TRT rig is negligible (i.e., adiabatic condition), the heat generated from the heaters and pump is the only heat transferred to the circulating fluid. Under these conditions, four fluid temperature nodes with different values can be obtained: the inlet and outlet temperature nodes of the BHE and TRT rig. The length of pipe from the BHE outlet to the inlet of the TRT rig and that from the outlet of the TRT rig to the BHE inlet are assumed to be the same. The  $L$  denotes one half of the length of the pipe, and points on the pipe are denoted by  $l$  ( $0 \leq l \leq L$ ).  $l = 0$  refers to the start location of the inflow and outflow circuits ( $T_{cf,out}(l = 0) = T_{f,out,BHE}$ ,  $T_{cf,in}(l = 0) = T_{cf,in,rig}$ ), and  $l = L$  refers to the end location of the inflow and outflow circuits ( $T_{cf,out}(l = L) = T_{cf,out,rig}$ ,  $T_{cf,in}(l = L) = T_{cf,in,BHE}$ ). The subscript *out* denotes the outflow from the BHE outlet to the TRT rig's inlet, and *in* denotes the inflow from the TRT rig's outlet to the BHE inlet. Therefore, starting from the BHE's outlet, the flow direction is  $T_{cf,out,BHE} \rightarrow T_{cf,out,rig} \rightarrow T_{cf,in,rig} \rightarrow T_{cf,in,BHE}$ .

A disturbance model is derived to estimate the temperature perturbation in the three nodes based on  $T_{cf,out,BHE}$ , which is already known. As described in Eq. (4.1), the heat transfer in the hydraulic circuit occurs in different modes. To combine the heat transfer components  $Q_{amb}$  and  $Q_{rad}$  in Eq. (4.1), the solar air temperature  $T_{sol,a}$  and the overall thermal resistance per unit circuit length  $R_{tot}$  are introduced.  $R_{tot}$  is the resistance of serial connection of four different resistances (internal fluid's convective, pipe's conductive, insulation's conductive and combined radiative and convective).  $T_{sol,a}$  and  $R_{tot}$  will be described in detail in the next section. In a quasi-steady state, change in the temperature of the circulating fluid in the outflow circuit above the ground can be described by following equations:

$$\frac{dT_{cf,out}(l,t)}{dl} = \frac{1}{\rho_{cf}c_{cf}\dot{V}_{cf}R_{tot}(t)}(T_{sol,a}(t) - T_{cf,out}(l,t)) \quad (4.2)$$

To solve Eq. (4.2), it is integrated in the interval  $[0, L]$ :

$$\int_{T_{cf,out}(l=0)}^{T_{cf,out}(l=L)} \frac{1}{T_{sol,a}(t) - T_{cf,out}(l,t)} dT_{cf,out}(l,t) = \int_0^L \frac{1}{\rho_{cf}c_{cf}\dot{V}_{cf}R_{tot}(t)} dl \quad (4.3)$$

Because  $T_{cf,out}(l=0,t) = T_{cf,out,BHE}(t)$  and  $T_{cf,out}(l=L,t) = T_{cf,out,rig}(t)$ , Eq. (4.3) can be rewritten as

$$\ln\left(\frac{T_{sol,a}(t) - T_{cf,out,rig}(t)}{T_{sol,a}(t) - T_{cf,out,BHE}(t)}\right) = -\frac{L}{\rho_{cf}c_{cf}\dot{V}_{cf}R_{tot}(t)} \quad (4.4)$$

Then a dimensionless parameter  $\kappa$  is introduced:

$$\frac{L}{\rho_{cf}c_{cf}\dot{V}_{cf}R_{tot}(t)} = \kappa(t) \quad (4.5)$$

By substituting Eq. (4.5) into Eq. (4.4) and using an expression with respect to  $T_{cf,out,rig}(t)$  in Eq. (4.4), following equation is obtained.

$$T_{cf,out,rig}(t) = T_{cf,out,BHE}(t)e^{-\kappa_{out}(t)} + T_{sol,a}(t)(1 - e^{-\kappa_{out}(t)}) \quad (4.6)$$

Eq. (4.6) describes the temperature perturbation when the fluid flows from the BHE outlet to the TRT rig inlet.  $R_{tot}$  varies according to the starting node temperature of the inflow and outflow circuits ( $T_{cf,out,BHE}$  and  $T_{cf,in,rig}$ ). Therefore,  $\kappa$  is also different between inflow and outflow circuits.

Using the known rate of heat generation from the heater and pump in the TRT rig  $Q_{rig}$ , the volumetric flow rate  $\dot{V}_{cf}$ , and the inlet temperature of the TRT rig  $T_{cf,in,rig}$ , the outlet temperature of the TRT rig  $T_{cf,out,rig}$  can be determined:

$$T_{cf,in,rig}(t) = T_{cf,out,rig}(t) + \frac{Q_{rig}}{\rho_{cf}c_{cf}\dot{V}_{cf}} \quad (4.7)$$

Using the derivation process for the outflow circuit described in Eqs. (4.2)–(4.5), the temperature perturbation in the inflow circuit can be obtained:

$$T_{cf,in,BHE}(t) = T_{cf,in,rig}(t)e^{-\kappa_{in}(t)} + T_{sol,a}(t)(1 - e^{-\kappa_{in}(t)}) \quad (4.8)$$

Using Eqs. (4.6)–(4.8), the temperature perturbation and the disturbed heat rate in the aboveground hydraulic circuit can be quantitatively estimated. The temperature changes in the outflow and inflow circuits are estimated using Eqs. (4.9) and (4.10), respectively:

$$\Delta T_{cf,out}(t) = T_{cf,out,BHE}(t) - T_{cf,out,rig}(t) \quad (4.9)$$

$$\Delta T_{cf,in}(t) = T_{cf,in,rig}(t) - T_{cf,in,BHE}(t) \quad (4.10)$$

The total temperature change in the circuit is the sum of Eq. (4.9) and Eq. (4.10):

$$\Delta T_{cf,tot} = \Delta T_{cf,out}(t) + \Delta T_{cf,in}(t) \quad (4.11)$$

Changes in the rate of heat exchange in the outflow and inflow circuits are estimated using Eq. (4.12) and Eq. (4.13), respectively, and the total heat exchange rate can be estimated using Eq. (4.14):

$$Q_{d,out}(t) = \rho_{cf}c_{cf}\dot{V}_{cf} \cdot \Delta T_{cf,out}(t) \quad (4.12)$$

$$Q_{d,in}(t) = \rho_{cf}c_{cf}\dot{V}_{cf} \cdot \Delta T_{cf,in}(t) \quad (4.13)$$

$$Q_{d,tot}(t) = Q_{d,out}(t) + Q_{d,in}(t) \quad (4.14)$$

## 4.2.2 Description of parameters in derived model

### • Sol-air temperature, $T_{sol,a}$

The sol-air temperature  $T_{sol,a}$  is frequently used in dynamic building simulations to consider convective and radiative heat transfer simultaneously. The general form of  $T_{sol,a}$  is:

$$T_{sol,a} = T_{amb} + \frac{a_{ins}I_{sol}}{h_o} - \frac{\varepsilon\Delta R}{h_o} \quad (4.15)$$

$$\Delta R = \sigma(T_{amb}^4 - T_{surr}^4) \quad (4.16)$$

where  $a_{ins}$  is the absorptivity of surface,  $I_{sol}$  is the intensity of global solar irradiation,  $h_o$  is the overall heat transfer coefficient,  $\varepsilon$  is the emissivity of surface, and  $\Delta R$  is the difference between longwave radiation incident on surface from sky and surroundings and radiation emitted by blackbody at outdoor air temperature.

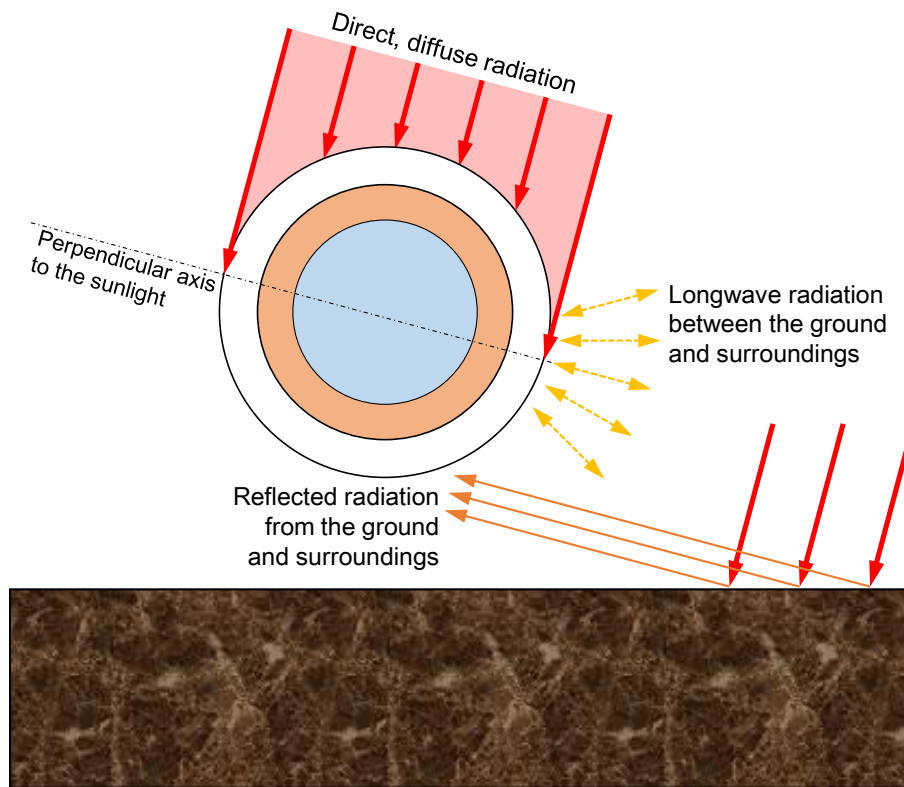


**Fig. 4.2** Radiative heat transfer on surface of aboveground hydraulic circuit.

To apply  $T_{sol,a}$  to the heat transfer in aboveground TRT setup, some correction should be made. First, the second term on the right-hand side of Eq. (4.15) considers the radiative and convective heat transfer on the outer surface of a building. However, the geometry of the aboveground hydraulic circuit is different from a building façade, which is generally flat and fully facing the sun. As depicted in Fig. 4.2, assuming that the hydraulic circuit is set up at the same height above the ground as the TRT rig's inlet and outlet

and that the altitude of the sun is sufficiently high, the upper half of the circuit's circumference would be directly affected by the direct and diffuse radiation. The lower and side parts of the circuit would be affected by the reflected radiation and the longwave radiation from the ground surface and the surroundings. Therefore, a correction factor,  $F_{cor}$ , should be introduced to consider the differences in the radiative heat transfer between the flat surface of building and the circular surface. Assuming that the mean albedo of the ground surface is 0.3, at least 65% of the global radiation and the reflected radiation would be incident on the surface of the circuit compared with a flat wall that has the same length as the circuit's circumference. According to this assumption,  $F_{cor}$  was set to 0.65 in this study.

The third term on the right-hand side of Eq. (4.15) is the correction term to account for the longwave radiation between the surroundings and the sky. For horizontal roofs, the only longwave radiation is from the sky. In this case, the appropriate  $\Delta R$  is approximately  $63 \text{ W/m}^2$  [105]. Therefore, if  $\varepsilon = 1$  and  $h_o = 17 \text{ W/(m}^2\cdot\text{K)}$ , the value of the correction term is approximately  $4 \text{ K}$  [106]. For vertical surfaces, they receive longwave radiation from the surrounding buildings, ground, and sky. When the intensity of the solar irradiation is high, the surfaces of terrestrial objects have higher temperature than the ambient air. Therefore, the longwave radiation from the surroundings compensates, to some extent, for the low emittance from the sky. This makes accurate estimation of  $\Delta R$  very difficult, and assuming  $\varepsilon\Delta R = 0$  for vertical surfaces of a building is a common practice [105]. For the aboveground hydraulic circuit, the consideration of longwave radiation is more complex. The upper side circumference of the circuit exchanges heat with the sky, and the lower and side circumferences of the circuit exchange heat with the ground surface and surroundings. Consequently, the third term on the right-hand side of Eq. (4.15) would be much less than  $4 \text{ K}$ , the value for the flat roof of a building. Explicit consideration of the third term is a complex task and varies with the location of the TRT. Hence, the third term in Eq. (4.15) was neglected in this study, which was reasonable for the daytime during clear skies and cloudy days. Experimental validation of omitting this term was conducted in Ref. [107].

As stated previously, after neglecting the third term in Eq. (4.15) and applying the correction factor, the following form of sol-air temperature, which is similar to the form suggested by Mackey and Wright [108] who first introduced the sol-air temperature, can be obtained.

$$T_{sol,a} = T_{amb} + F_{cor} \frac{a_{ins} I_{sol}}{h_o} \quad (4.17)$$

In this study, the environmental temperature  $T_{env}$  was used to represent the outdoor temperature during both day and night. During daytime affected by the solar irradiation,  $T_{env}$  equals  $T_{sol,a}$ , and during night,  $T_{env}$  equals  $T_{amb}$ .

To obtain the overall heat transfer coefficient  $h_o$ , McAdams's formula [109], which is based on Jürges's formula [110], was used. Related to  $h_o$ , Ouzzane et al. [111] predicted the ground temperature using three different heat transfer coefficient models [109,112,113] and verified their accuracy by comparing with measured data. They [111] verified that McAdams's formula [109] can be applied to a wide range of weather conditions and gives better results than other models. The formula suggested by Jürges [110], generally called the Nusselt–Jürges correlation, is based on wind tunnel experiments:

$$h_o = 5.678 \left\{ m + n \left[ \left( \frac{294.26}{273.16 + T_{amb}} \right) v_w / 0.3048 \right]^p \right\} \quad (4.18)$$

where  $m, n, p$  are constants that depend on the roughness of surface and the range of wind velocity.

McAdams [109] approximated the Jürges model [110] as a function of wind velocity. Under a wind velocity of 5 m/s, it is approximated as a linear function:

$$h_o = 5.7 + 3.8v_w \quad (v_w \leq 5 \text{ m/s}) \quad (4.19)$$

When estimating the overall heat transfer coefficient, the wind velocity near the ground is generally not available because the measurement height at a weather station is much higher than near the ground surface. Therefore, a correction for the wind velocity is required when estimating  $h_o$  using general velocity data measured at a weather station. The general power-law wind profile of the boundary layer is expressed as follows:

$$v_w = v_{w,m} \left( \frac{z}{z_m} \right)^{\alpha_m} \quad (4.20)$$

where  $z$  is the height above ground, subscript  $m$  is the site condition or the value of the measurements, and  $\alpha_m$  is the exponent of power law, which can be found in Ref. [105].

It should be noted that the wind velocity near the ground surface is generally very low. Consequently,  $h_o$  would be low near the ground surface. Assuming a wind velocity of 0.5 m/s,  $h_o$  is 7.6 W/m<sup>2</sup> according to Eq. (4.19). This value was used as the reference condition for the analysis in this study.

#### • Overall thermal resistance of hydraulic circuit, $R_{tot}$

$R_{tot}$  is the overall thermal resistance of the hydraulic circuit. This can be described by a serial connection of four resistances (Fig. 4.3): convective resistance at the inner surface of the pipe, conductive resistance of the pipe layer, conductive resistance of the insulation layer, and the combined convective

and radiative resistance on the surface of the insulation.

$$R_{tot} = R_{c,i} + R_p + R_{ins} + R_o \quad (4.21)$$

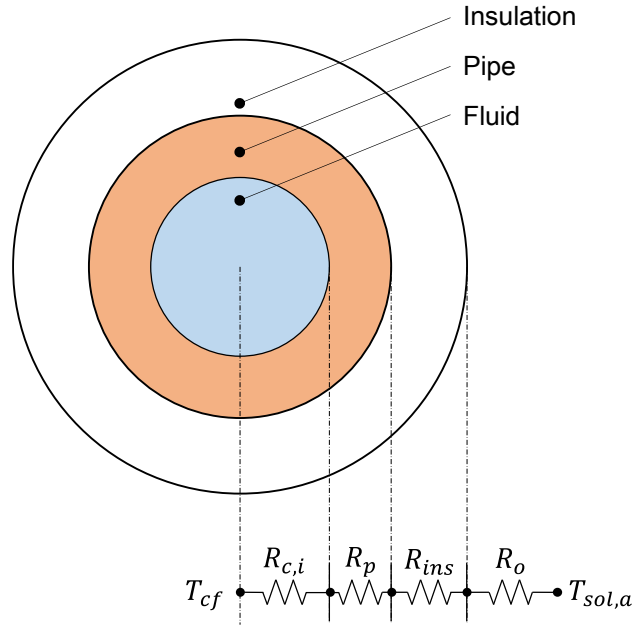


**Fig. 4.3** Thermal resistance network for heat transfer between circulating fluid and outdoor environment.

The internal convective thermal resistance  $R_{c,i}$  has different values in the inflow and outflow circuits because it refers to the starting node temperature of each circuit, which are  $T_{cf,out,BHE}$  and  $T_{cf,in,rig}$ . For the sake of brevity, the subscripts *in* and *out* are not specified for  $R_{c,i}$  and  $R_{tot}$ . Eq. (4.21) can be rewritten as the following explicit form:

$$R_{tot} = \frac{1}{2\pi r_{p,i} h_i} + \frac{\ln(r_{p,o}/r_{p,i})}{2\pi \lambda_p} + \frac{\ln(1 + \tau_{ins}/r_{p,o})}{2\pi \lambda_{ins}} + \frac{1}{2\pi r_{ins,o} h_o} \quad (4.22)$$

The convective heat transfer coefficient at the inner surface of the pipe,  $h_i$  can be estimated using the Nusselt number (Nu):

$$h_i = \frac{Nu \lambda_{cf}}{2r_{p,i}} \quad (4.23)$$

Nu is a function of the roughness of surface and the flow velocity. Using Gnielinski's formula [114],

$$\text{Nu} = \frac{(f/8)(\text{Re} - 1000)\text{Pr}}{1 + 12.7(f/8)^{0.5}(\text{Pr}^{2/3} - 1)} \quad (4.24)$$

This relation is valid for  $(0.5 \leq \text{Pr} \leq 2000, \quad 3 \times 10^3 < \text{Re} < 5 \times 10^6)$ , where Pr is the Prandtl number and Re is the Reynolds number.

Re and Pr are defined as Eq. (4.25) and Eq. (4.26), respectively:

$$\text{Re} = \rho_{cf} v_{cf} 2r_{p,i} / \mu_{cf} = v_{cf} 2r_{p,i} / \nu_{cf} \quad (4.25)$$

$$\text{Pr} = \mu_{cf} c_{cf} / \lambda_{cf} \quad (4.26)$$

The dynamic viscosity  $\mu_{cf}$  is approximated by the following formula:

$$\mu_{cf} = 2.414 \times 10^{-5} \times 10^{274.8/(273.15+T_{cf}-140)} \quad (4.27)$$

As stated previously,  $\mu_{cf}$  has different values in the inflow and outflow circuits because the outflow refers to the outlet temperature of BHE,  $T_{cf,out,BHE}$ , and the inflow refers to the outlet temperature of TRT rig,  $T_{cf,in,rig}$ .

The Darcy friction factor  $f$  can be estimated from the Moody diagram or the following formula [115] in the case of a smooth surface:

$$f = (0.79 \ln \text{Re} - 1.64)^{-2} \quad (4.28)$$

This relation is valid for  $3 \times 10^3 < \text{Re} < 5 \times 10^6$ .

The validation of derived theoretical model using in situ TRT data will be presented in Section 5.3.

### 4.3 Parametric study using disturbance model

A parametric study was conducted on the basis of the derived theoretical model. The reference conditions and parameters for the study are listed in Table 4.1. These conditions were used for both the analyses using reference weather conditions (Table 4.2) and the parametric study. Some parameters in Table 4.1 and the weather conditions in Table 4.2 were selected on the basis of the real conditions in Tokyo. In general, the undisturbed ground temperature of Tokyo is 16–17 °C [116], and assuming that the

effective thermal conductivity of the ground is approximately 1.5–2.0 W/(m·K) and the heat transfer is dominated by conduction, the outlet temperature of the circulating fluid 24 h after a heat injection of 50 W/m would be above 30 °C. Therefore, the outlet temperature of BHE is set to 30 °C in Table 4.1.

**Table 4.1** Reference conditions and parameters for analysis.

Parameter [units]	Value
Borehole heat exchanger	
Borehole depth [m]	50
U-tube: High-density polyethylene	
Outer radius [mm]	17
Inner radius [mm]	13.5
Thermal conductivity [W/(m·K)]	0.38
Insulation: Polyethylene foam	
Thickness [mm]	10
Radiation absorptivity [–]	0.6
Thermal conductivity [W/(m·K)]	0.04
Heat carrier fluid: Water	
Thermal conductivity [W/(m·K)]	0.6
Volumetric thermal capacity [MJ/(m <sup>3</sup> ·K)]	4.2
Outlet temperature of BHE [°C]	30
TRT rig and connecting hydraulic circuit	
Heat rate [kW] ([W/m])	2.5 (50)
Volumetric flow rate [L/min]	15
Hydraulic circuit length [m]	2

#### 4.3.1 Reference conditions

The six weather conditions listed in Table 4.2 are based on the upper and lower bound conditions (around 12:00 PM and 05:00 AM) of a clear day in summer, intermediate season, and winter. The results of the disturbed temperature  $\Delta T_{cf,tot}$ , disturbed heat exchange rate  $Q_{d,tot}$ , and disturbance ratio  $Q_{d,tot}/Q_{rig}$  (disturbed heat exchange rate/heat injection rate) based on the six weather conditions are also summarized in Table 4.2.

The highest heat gain and heat loss occurred during the daytime of summer (Sum-day) and the nighttime of winter (Win-night), respectively, when the differences between the environmental temperature and BHE outlet temperature were the highest. The heat loss occurred even during the nighttime of summer

because the BHE outlet temperature of fluid, 30 °C (Table 4.1), was higher than the environmental temperature of 27 °C. For the daytime, the results show that the fluid gained heat from the outdoor environment even in winter because the environmental temperature ( $T_{sol,a}$ ) was higher than the temperature of fluid. However, heat gain during daytime of winter occurs for a very short period of the day when the intensity of global solar irradiation is strong or during the very early period of the test when the fluid temperature is low, because the fluid temperature rapidly increases as the test progresses. Therefore, most of the TRT period in winter was dominated by heat loss. The parametric studies described in the following section were conducted for the case of daytime of intermediate season (Int-day) unless otherwise stated.

**Table 4.2** Reference weather conditions and resulting disturbance (positive: heat gain from environment to fluid, negative: heat loss from fluid to environment).

Season	Case	$T_{amb}$ ( $T_{sol,a}$ ) [°C]	$I_{sol}$ [W/m <sup>2</sup> ]	$v_w$ [m/s]	$\Delta T_{cf,tot}$ [°C]	$Q_{d,tot}$ [W]	$Q_{d,tot}/Q_{rig}$ [%]
Summer	Sum-day	34 (85.3)	1000	0.5	0.076	79.60	3.18
	Sum-night	27	0	0.5	-0.006	-6.16	-0.25
Intermediate -season	Int-day	21 (64.6)	850	0.5	0.047	49.16	1.97
	Int-night	10	0	0.5	-0.030	-31.17	-1.25
Winter	Win-day	7 (42.9)	700	0.5	0.016	17.25	0.69
	Win-night	-1	0	0.5	-0.045	-47.34	-1.89

Sum-day: daytime of summer; Sum-night: nighttime of summer; Int-day: daytime of intermediate season; Int-night: nighttime of intermediate season; Win-day: daytime of winter; Win-night: nighttime of winter

#### 4.3.2 Settings of TRT rig and temperature of circulating fluid

The settings of TRT rig are the heat injection rate and flow rate. The outlet temperature of BHE is also related to the heat injection rate. The parametric study of these parameters is described in the following subsections.

##### • Heat injection rate, $Q_{rig}$

There are few standards or guidelines on the settings of TRTs. For the heat injection rate  $Q_{rig}$ , ASHRAE [39] suggests 50–80 W/m. In the cases of Int-day and Win-night, the change in the disturbed heat rate in the inflow circuit  $Q_{d,in}$  with the change in  $Q_{rig}$  is shown in Fig. 4.4. The amount of disturbance in the outflow circuit remains constant if the BHE outlet temperature is constant, because the disturbance in the outflow circuit is not affected by changes in the generated heat in the TRT rig. Therefore, data of changes in the disturbance in the outflow circuit  $Q_{d,out}$  are not presented in this paper. In the case of Int-day, as

$Q_{rig}$  increased, the difference between the sol-air temperature and fluid temperature decreased. This yielded a decreasing trend of  $Q_{d,in}$  in Fig. 4.4 and of  $Q_{d,tot}/Q_{rig}$  in Fig. 4.5. Following the general practice stated in ASHRAE fundamentals [39], the heat injection rate  $Q_{rig}$  was divided by the length of BHE (50 m) and is plotted on the horizontal axis of Fig. 4.4 and Fig. 4.5. In the case of Win-night, when the ambient temperature was lower than the fluid temperature,  $Q_{d,in}$  increased with  $Q_{rig}$  because the difference between the ambient temperature and fluid temperature increased with  $Q_{rig}$  (Fig. 4.4). However, the disturbance ratio  $Q_{d,tot}/Q_{rig}$  in Fig. 4.5 shows a decreasing trend because the amount of increase in  $Q_{d,in}$  was much smaller than the increase in  $Q_{rig}$ . As shown in Fig. 4.4, in the case of Win-night, when  $Q_{rig}$  increased by 500 W (10 W/m) from 2500 W (50 W/m) to 3000 W (60 W/m), heat loss in the inflow circuit increased by 0.35 W. The ratio of the increased  $Q_{rig}$  to the increased  $Q_{d,in}$  is approximately 0.07%. Therefore, in a general setup of TRT, an increase in  $Q_{rig}$  always works toward reducing  $Q_{d,tot}/Q_{rig}$ . This means that the influence of disturbance on the actual heat injection rate  $Q_{BHE}$  becomes small as  $Q_{rig}$  increases.

Therefore, in general, a large heat injection rate results in a stable estimation behavior, and this is confirmed by the sequential plots of two TRTs, conducted in [116], using 2 kW and 4 kW heaters. However, care should be taken because accuracy is guaranteed only when the TRT is conducted in conduction-dominated conditions. In the case of groundwater-filled BHE or saturated porous formation, estimation results can be dependent on the amount of heat injection rate [116–122].

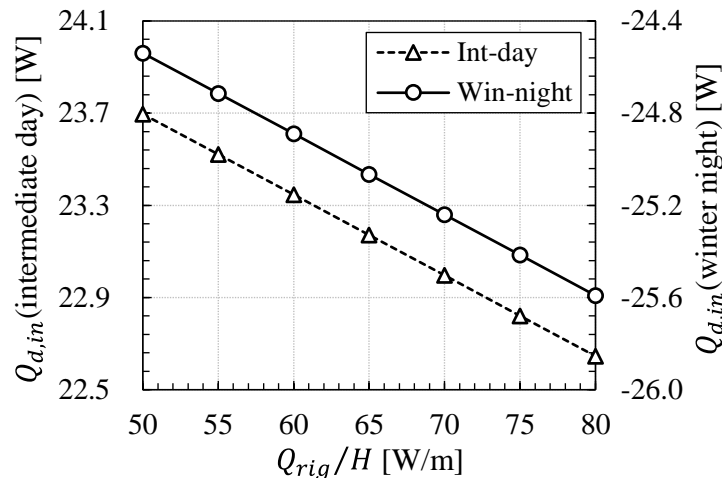


**Fig. 4.4** Change in disturbed heat rate in inflow circuit due to changes in heat injection rate per unit length of borehole heat exchanger (left vertical axis: daytime of intermediate season; right vertical axis: nighttime of winter).

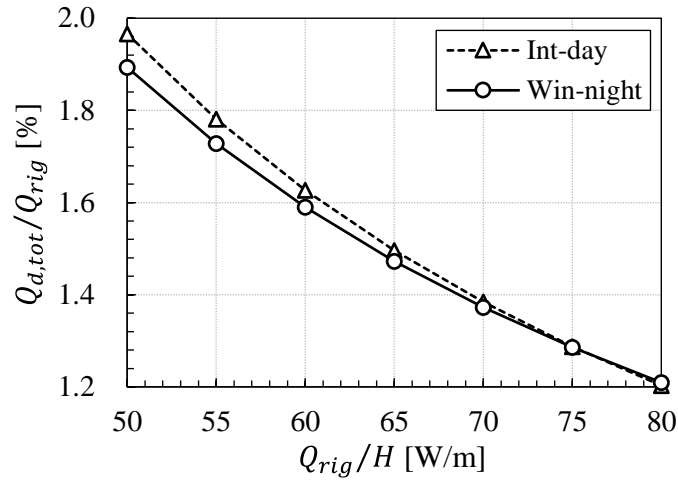


**Fig. 4.5** Changes in disturbed heat rate ratio with changes in heat injection rate per unit length of borehole heat exchanger ( $Q_{d,tot}$ : total disturbed heat rate;  $Q_{rig}$ : heat injection rate; Int-day: daytime of intermediate season; Win-night: nighttime of winter).

▪ **Outlet temperature of BHE,  $T_{cf,out,BHE}$**

The increase in heat injection rate and lapse of TRT time are directly related to the increasing temperature of the circulating fluid. Therefore, changes in the disturbance effect caused by increasing fluid temperature should be examined. For this, the Sum-day and Win-night cases were selected. The total perturbed temperature in the aboveground circuit  $\Delta T_{cf,tot}$  and the disturbance ratio  $Q_{d,tot}/Q_{rig}$  with changing BHE outlet temperature  $T_{cf,out,BHE}$  are shown in Fig. 4.6 and Fig. 4.7, respectively. These results are easily predictable because the amount of disturbance is solely dependent on the difference between the environmental temperature  $T_{env}$  and the fluid temperature. In general, in the case of Sum-day, which has a high sol-air temperature, the amount of disturbed heat rate decreased as the  $T_{cf,out,BHE}$  increased. Conversely, in the case of Win-night, which has a low ambient temperature, the disturbance increased as the  $T_{cf,out,BHE}$  increased. When the diurnal change in the environmental temperature during the TRT ranges beyond the initial ground (fluid) temperature and the maximum fluid temperature, as was the case of Sum-night, both heat gain and heat loss can occur. As shown in Fig. 4.6 and Fig. 4.7, the transition from heat gain to heat loss occurred when  $T_{cf,out,BHE}$  was near 27 °C, which is the ambient temperature of Sum-night. In other words, the disturbance ratio decreased (heat gain) as  $T_{cf,out,BHE}$  increased to 27 °C and increased (heat loss) as  $T_{cf,out,BHE}$  increased above 27 °C. In the summer and intermediate seasons, heat gain and heat loss would occur alternately during the TRT. However, the zero-sum of heat gain and heat loss does not mean a stable interpretation of the TRT; a sequential estimation will elicit fluctuating behavior.

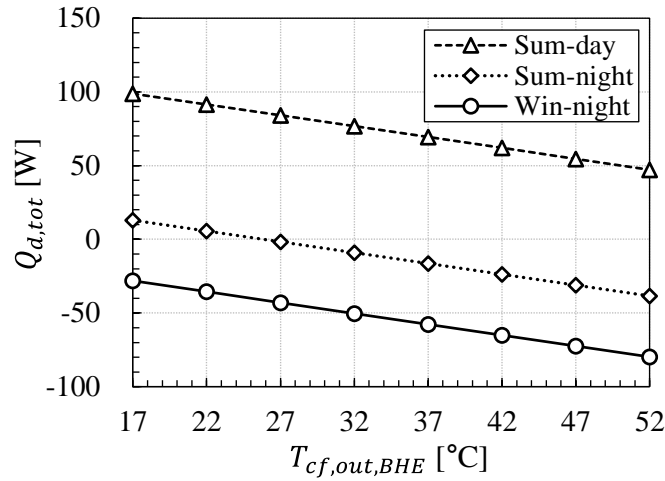


**Fig. 4.6** Changes in the disturbed heat rate in aboveground hydraulic circuit with changes in outlet fluid temperature of borehole heat exchanger,  $T_{cf,out,BHE}$  (Sum-day: daytime of summer; Sum-night: nighttime of summer; Win-night: nighttime of winter).

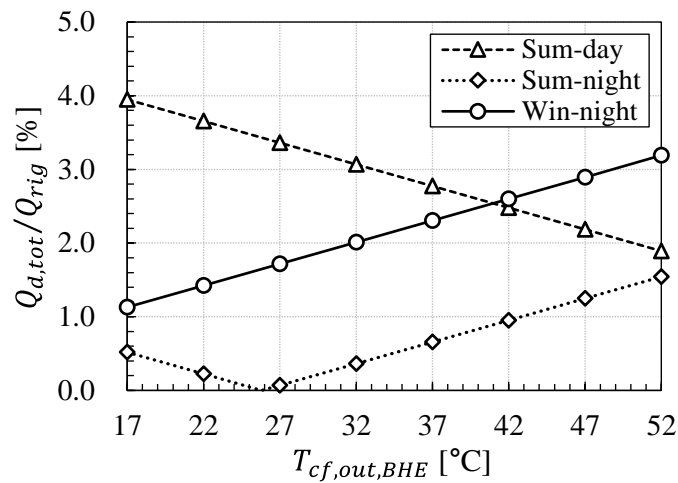


**Fig. 4.7** Changes in disturbance ratio with changes in outlet fluid temperature of borehole heat exchanger,  $T_{cf,out,BHE}$ .

#### • Circulation flow rate, $\dot{V}_{cf}$

Similar to the heat injection rate, the standards and guidelines on the settings of flow rate are also few. It is customary to conduct TRTs using heat injection rate and flow rate values that are close to the actual operation conditions of GSHPs. In general, a flow rate of 10–25 L/min is used, which can be found in many past studies [7,18,23,37,123–127]. However, lower [16,17,128] and higher [129,130] flow rates have also been employed.

When the dimensionless parameter  $\kappa$ , defined in Eq. (4.5), is low, the temperature difference between two consecutive nodes in the outflow and inflow becomes small. In Eq. (4.5),  $\kappa$  becomes smaller as the flow rate  $\dot{V}_{cf}$  increases, and the effect of disturbance can be expected to decrease. However, this is an incorrect interpretation because the amount of disturbance should be decided by the disturbed heat rate, defined in Eqs. (4.12)–(4.14). Another parameter related to  $\dot{V}_{cf}$  is the internal convective resistance  $R_{c,i}$ , which is a component of the overall thermal resistance  $R_{tot}$ . As the flow rate increases, the convective heat transfer coefficient  $h_i$  increases and consequently  $R_{c,i}$  decreases. The change rate of  $R_{tot}$  is particularly high at low flow rates (Fig. 4.8). Therefore, at a given BHE outlet fluid temperature and environmental temperature, the disturbed heat rate increases as  $\dot{V}_{cf}$  increases. However, as can be seen in Fig. 4.8, the change in  $R_{tot}$  is very small because the contribution of  $R_{c,i}$  to  $R_{tot}$  is small.

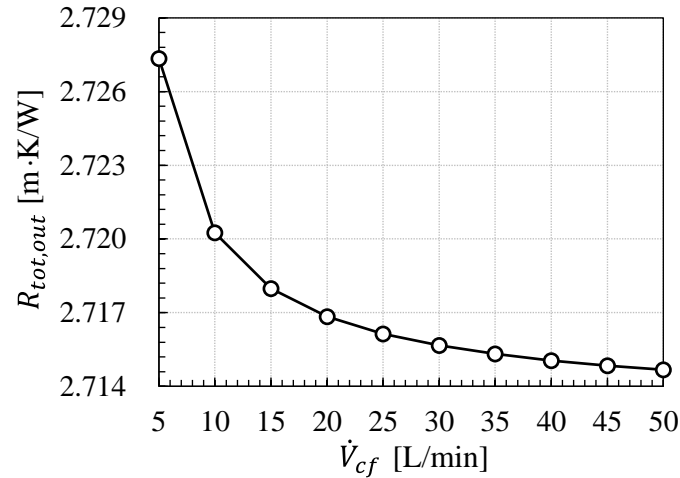


**Fig. 4.8** Changes in overall thermal resistance of outflow circuit with changes in volumetric flow rate.

With the changes in  $\dot{V}_{cf}$ , the disturbance in the inflow circuit showed more complex behavior than that in the outflow circuit because it depends on not only  $R_{c,i}$  but also the relationship between the outlet fluid temperature of TRT rig  $T_{cf,in,rig}$  and the environmental temperature  $T_{env}$ . In the outflow circuit, regardless of  $T_{env}$ , an increase in  $\dot{V}_{cf}$  always resulted in an increase in  $Q_{d,out}$ . For the inflow circuit, the results were the same as for the outflow circuit when  $T_{env}$  was higher than  $T_{cf,in,rig}$  (Fig. 4.9 (a)). When  $T_{env}$  was lower than  $T_{cf,in,rig}$ , however,  $Q_{d,in}$  decreased with increasing  $\dot{V}_{cf}$  (Fig. 4.9 (b)) because the increase in temperature from  $T_{cf,out,rig}$  to  $T_{cf,in,rig}$  was strongly dependent on  $\dot{V}_{cf}$ , as described in Eq. (4.7). With decreasing  $\dot{V}_{cf}$ , the difference between  $T_{cf,in,rig}$  and  $T_{env}$  increased and so did the disturbance, even though  $R_{c,i}$  increased.

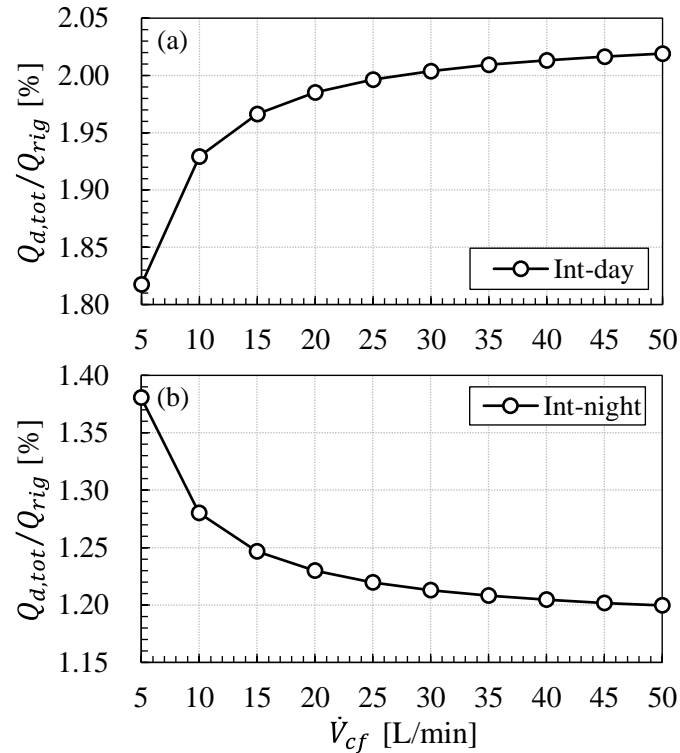


**Fig. 4.9** Changes in disturbed heat rate ratio with changes in volumetric flow rate; (a) daytime of intermediate season and (b) nighttime of intermediate season.

In the actual operation of a GSHP, a relatively high flow rate would be helpful for heat transfer in the ground because it lowers the borehole thermal resistance. However, in a TRT, it can have an adverse effect in the aboveground circuit, as can be seen in Fig. 4.9. Therefore, it is difficult to say what flow rate should be used in the TRT. Although the selection of flow rate requires careful analysis, a suggestion can be made on the basis of the measurement errors of flow and temperature sensors.

If a low flow rate is chosen, then it should be beyond the level where the measurement uncertainty caused by the intrinsic error of sensors becomes sufficiently small compared with the measured values. In contrast, relatively accurate measurement of the flow rate can be obtained when its values are high. However, as the flow rate increases, the difference between the outlet and inlet temperatures of BHE decreases. In general, the typical measurement error of temperature sensors used in TRTs is approximately  $\pm 0.15$  K. A smaller temperature difference results in a higher uncertainty in the measured heat injection rate. If high heat injection rates are chosen, then higher flow rates can be chosen because the higher heat injection rates increase the temperature difference between the inlet and outlet of BHE. Related to the measurement error in TRT, Witte [131] conducted an extensive study and pointed out the same problem in choosing the flow rate.

### 4.3.3 Aboveground hydraulic circuit

The parameters related to the aboveground hydraulic circuit are the length of the hydraulic circuit, thickness of the insulation layer, and the radiation absorptivity of the circuit's surface.

- **Length of aboveground hydraulic circuit,  $L$**

As the circuit length  $L$  increases, the dimensionless parameter  $\kappa$  and, therefore, the temperature perturbation and the disturbed heat rate increase. The increase rate (sensitivity) of  $Q_{d,tot}/Q_{rig}$  is dependent on the temperature difference between  $T_{env}$  and  $T_{cf,out,BHE}$ .  $Q_{d,tot}/Q_{rig}$  increased by 1% per meter in the Int-day condition (Fig. 4.10). The sensitivity of  $Q_{d,tot}/Q_{rig}$  is especially high when the difference between  $T_{env}$  and  $T_{cf,out,BHE}$  is high. Therefore, the circuit length should be as small as possible, especially when the TRT is conducted in summer or winter. The sensitivity of the parameters is described in more detail in Section 4.4.

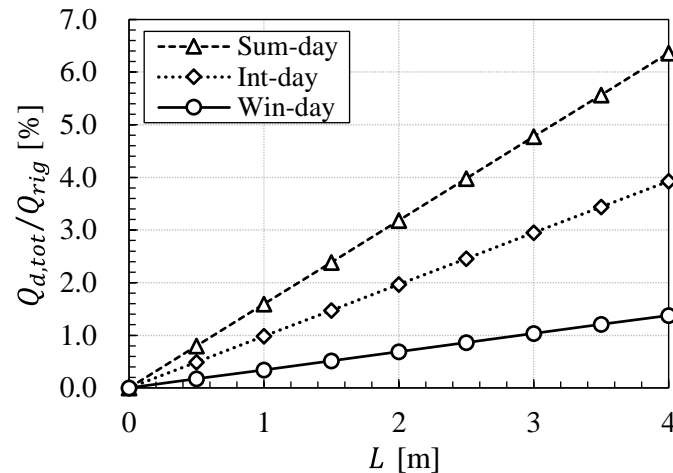


**Fig. 4.10** Changes in disturbed heat rate ratio with changes in length of hydraulic circuit,  $L$ .

- **Thickness of insulation,  $\tau_{ins}$**

The thickness of the insulation  $\tau_{ins}$  affects the thermal resistance of insulation layer  $R_{ins}$ , overall thermal resistance  $R_{tot}$ , and the dimensionless parameter  $\kappa$ . The typical thermal conductivity of pipe insulation made of polyethylene foam is approximately 0.04 W/(m·K). The changes in  $R_{ins}$  and  $Q_{d,tot}/Q_{rig}$  with changes in thickness of the insulation layer are shown in Fig. 4.11 and Fig. 4.12, respectively. The radiation absorptivity of the pipe surface was assumed to be the same ( $a_{ins} = 0.6$ ) as that of the insulation surface when the thickness was 0 mm. The decrease rate of the disturbance ratio was

high for low insulation thicknesses (Fig. 4.12). An insulation of 10 mm thickness reduced the amount of disturbance by 50% compared with the non-insulated circuit. Therefore, insulation is an important factor in reducing the disturbance effect and a thickness of at least 10 mm is required if polyethylene foam is used for the insulation of aboveground hydraulic circuit.

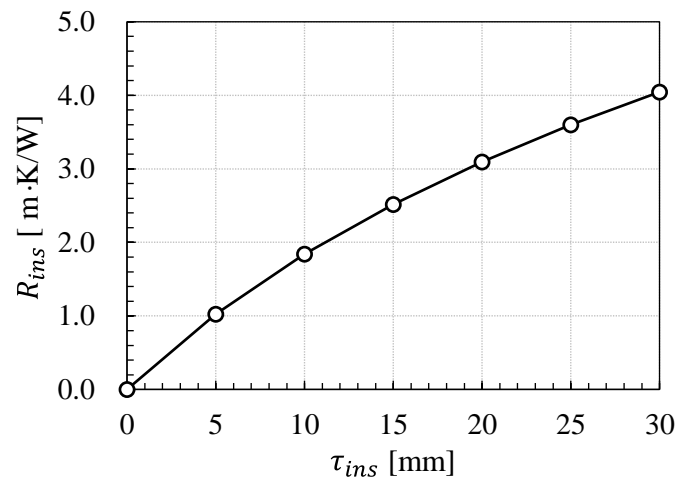


**Fig. 4.11** Changes in thermal resistance of insulation layer with changes in thickness of insulation,  $\tau_{ins}$ .

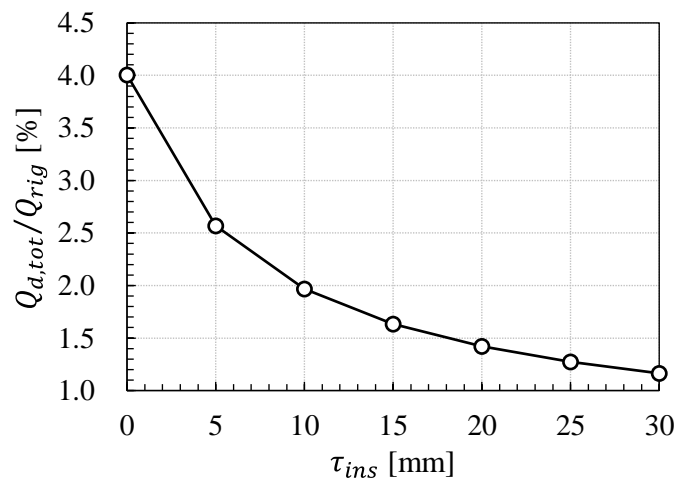


**Fig. 4.12** Changes in disturbed heat rate ratio with changes in insulation thickness,  $\tau_{ins}$ .

▪ **Radiation absorptivity of the insulation surface,  $a_{ins}$**

Although many researchers have pointed out that the insulation of aboveground hydraulic circuit is important for obtaining quality data [7,15–19,22,26,96,101,104,132–135], sometimes only the ambient temperature is considered. However, to effectively control the influence of outdoor environment, the radiation effect must be considered. In particular, the radiation absorptivity of the insulation surface  $a_{ins}$  is critical to deciding the sol-air temperature. Because this important factor is not recognized widely, dark-colored insulation or finishing material for the hydraulic circuit is sometimes used in TRT setups.

The changes in disturbance ratio with  $a_{ins}$  are shown in Fig. 4.13. In the Sum-day case, the total heat gain  $Q_{d,tot}$  increased by 25.16 W when  $a_{ins}$  increased by 0.2. This result was for a BHE outlet temperature of 30 °C. Therefore, in the early period of TRT when the fluid temperature is low, the impact of  $a_{ins}$  would be stronger than in later periods of TRT. Moreover, as the amount of global solar irradiation decreases, the impact of  $a_{ins}$  also decreases.

In the cases of Int-day and Win-day when the ambient temperature is lower than the BHE outlet temperature, the trends of disturbance ratio in Fig. 4.13 are different from those observed for Sum-day. The nature of these trends (increasing or decreasing) depends on the relationship between the sol-air temperature and the fluid temperature. For example, if the sol-air temperature is lower than the fluid temperature, an increase in  $a_{ins}$  decreases the temperature difference and yields a decreasing trend of the disturbance ratio as shown in Fig. 4.13. However, the outdoor environment continuously changes. In most situations, a high  $a_{ins}$  causes a high amplitude of fluctuation in the response curve. Therefore, a lower  $a_{ins}$  elicits better quality of TRT data, on all occasions.

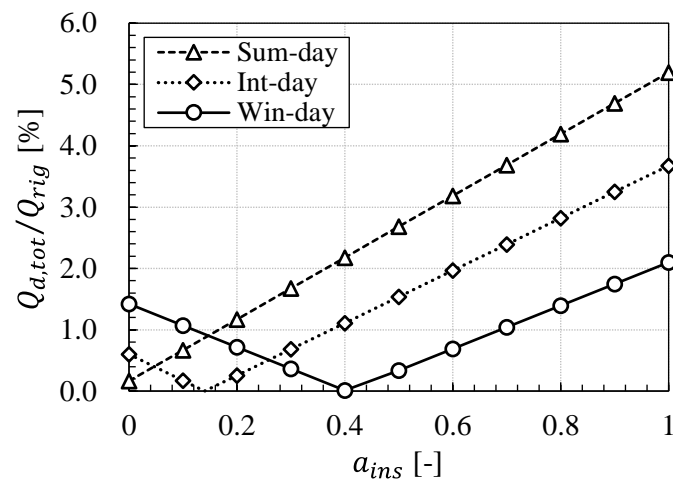


**Fig. 4.13** Changes in disturbed heat rate ratio with changes in radiation absorptivity of insulation surface,  $a_{ins}$ .

### 4.3.4 Weather conditions

When latent heat exchange is not considered, the weather parameters related to the heat exchange between the fluid and outdoor environment are the wind velocity, global solar irradiation, and ambient temperature.

#### • Wind velocity, $v_w$

The wind velocity  $v_w$  affects the overall heat transfer coefficient of the outer surface  $h_0$  and the sol-air temperature  $T_{sol,a}$ . The changes in the overall thermal resistance of the outflow circuit  $R_{tot,out}$  and  $T_{sol,a}$  with changes in  $v_w$  are shown in Fig. 4.14. As defined in Eq. (4.22) and Eq. (4.17),  $R_{tot}$  and  $T_{sol,a}$  are inversely proportional to  $h_0$ . Therefore, in the Sum-day condition when the ambient temperature  $T_{amb}$  is higher than the fluid temperature, an increase in  $v_w$  reduces the disturbed heat rate, as shown in Fig. 4.15. However, in the Win-day case when  $T_{sol,a}$  decreases below the fluid temperature, the heat gain transitions to heat loss (Fig. 4.15). During nighttime when  $T_{amb}$  is lower than the fluid temperature, an increase in  $v_w$  stimulates convective heat transfer and consequently heat loss increases. The Win-night case in Fig. 4.15 is an example of such a situation. However, the sensitivity of  $v_w$  during nighttime is very low compared with daytime (Fig. 4.15).

As shown in Fig. 4.15, changes in  $v_w$  can affect both heat loss and heat gain. In this parametric study,  $v_w$  was varied up to 5 m/s, although in general  $v_w$  near the ground surface much lower.

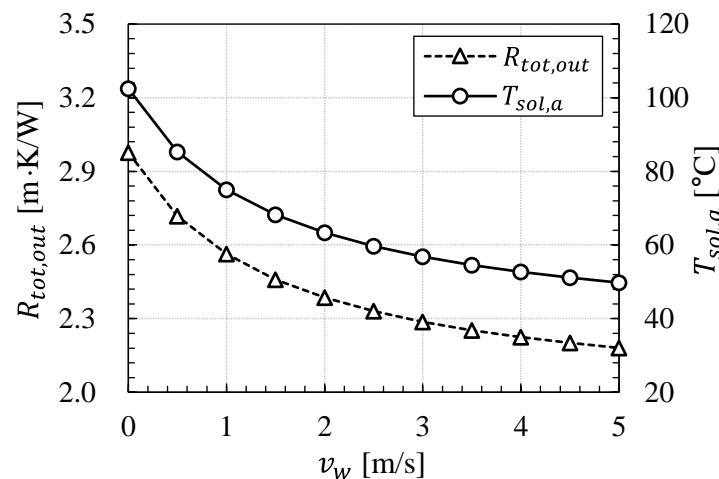


**Fig. 4.14** Changes in overall thermal resistance  $R_{tot,out}$  of outflow circuit and sol-air temperature  $T_{sol,a}$  with changes in wind velocity (daytime of summer).

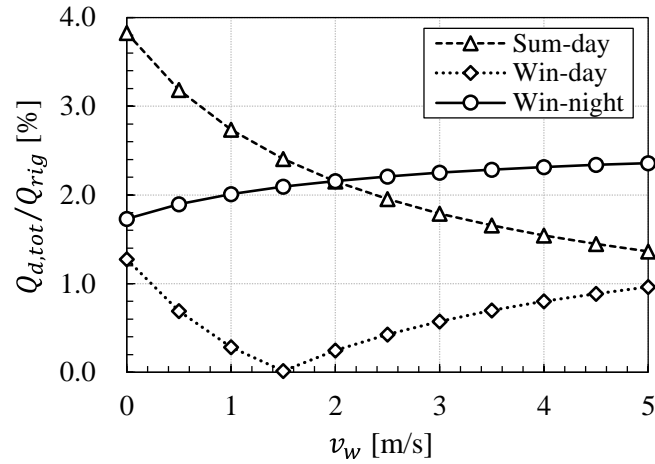


**Fig. 4.15** Changes in disturbed heat rate ratio with changes of wind velocity,  $v_w$ .

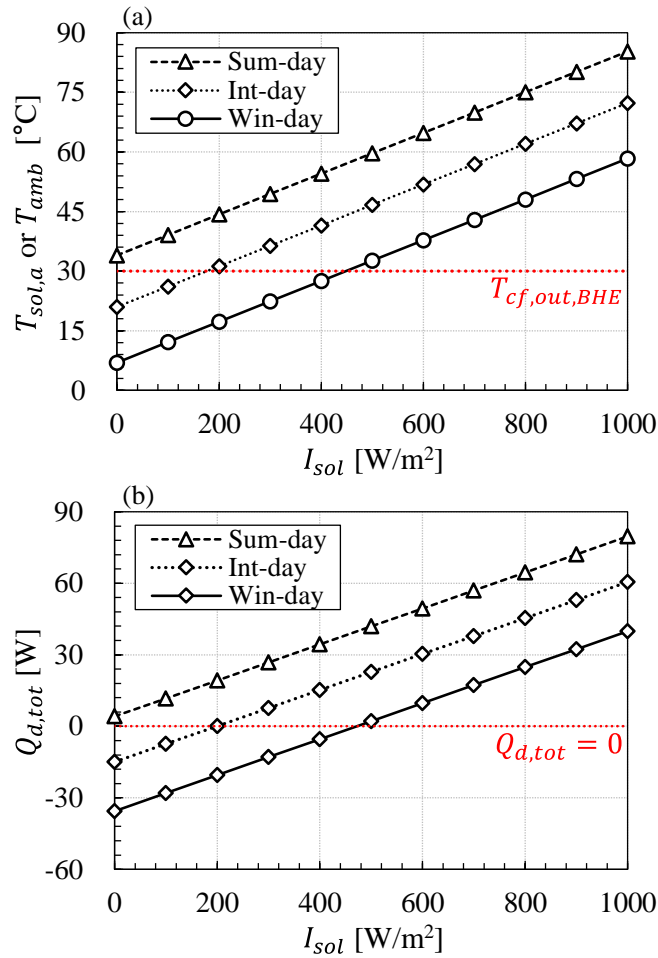


**Fig. 4.16** Changes in global solar irradiation,  $I_{sol}$ , and resulting changes in (a) environmental temperature,  $T_{sol,a}$  or  $T_{amb}$ , and (b) total disturbed heat rate,  $Q_{d,tot}$ .

• **Global solar irradiation  $I_{sol}$  and sol-air temperature  $T_{sol,a}$  or ambient temperature  $T_{amb}$**

The global solar irradiation  $I_{sol}$  is related to the sol-air temperature  $T_{sol,a}$ , and heat gain and heat loss depend on the relationship between the fluid temperature  $T_{cf,out,BHE}$  and  $T_{sol,a}$ . Fig. 4.16 (a) and Fig. 4.16 (b) show the changes in  $T_{sol,a}$  with changing  $I_{sol}$  and the resulting disturbed heat exchange rate, respectively. As shown in Fig. 4.16, depending on the relationship between  $T_{cf,out,BHE}$  and  $T_{sol,a}$ , both heat loss and heat gain can occur. This temperature difference is related to the amount of disturbance ratio shown in Fig. 4.17. A TRT setup should be designed to reduce the amplitude of fluctuation related to  $a_{ins}$ , as stated previously, because a changing  $I_{sol}$  also affects both heat gain and heat loss, as shown in Fig. 4.16 and Fig. 4.17.

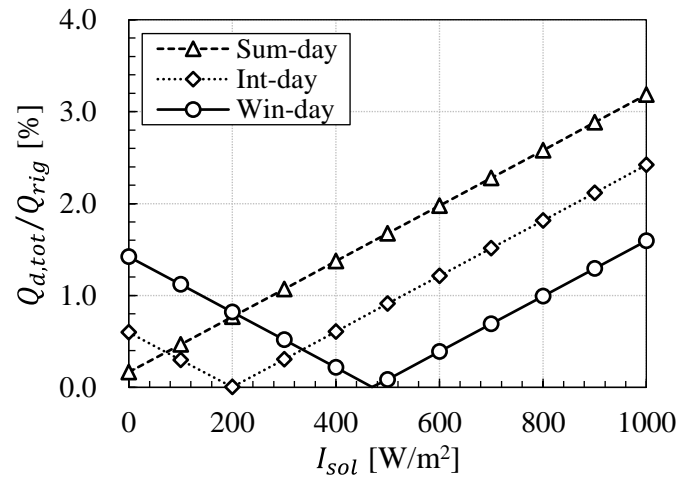


**Fig. 4.17** Changes in disturbed heat rate ratio with changes in global solar irradiation,  $I_{sol}$ .

#### 4.4 Sensitivity analysis

Through the parametric studies, changes in disturbance were examined in various conditions according to changes in certain parameters. To compare the relative impact of each parameter on disturbance, however, a sensitivity analysis using sensitivity coefficients is very useful. The sensitivity coefficient describes how the output varies with changes in the input. In this study, the output was the total disturbed heat rate  $Q_{d,tot}$  and the input was parameter  $P_i$ . The sensitivity coefficients can be defined using the first partial derivative of the dependent variable  $Q_{d,tot}$  with respect to parameter  $P_i$  as

$$SC_i = \frac{\partial Q_{d,tot}(P_1, P_2, \dots, P_i, \dots, P_N)}{\partial P_i} \quad (4.29)$$

In the case of an analytical solution, equations for the sensitivity coefficients can be obtained explicitly, but they may have complex forms. The partial derivative of Eq. (4.6) and Eq. (4.8) with respect to certain parameters also shows a complex form. As an alternative, the sensitivity coefficients can be obtained by numerical approximation of the partial derivatives. Using the forward difference, Eq. (4.29) can be rewritten as:

$$SC_i \approx \lim_{\Delta P_i \rightarrow 0} \frac{Q_{d,tot}(P_1, P_2, \dots, P_i + \Delta P_i, \dots, P_N) - Q_{d,tot}(P_1, P_2, \dots, P_i, \dots, P_N)}{\Delta P_i} \quad (4.30)$$

where  $SC_i$  is the sensitivity coefficient with respect to the  $i$ -th parameter and  $P_i$  is the parameters related to  $Q_{d,tot}$ :  $Q_{rig}$ ,  $\dot{V}_{cf}$ ,  $T_{cf,out,BHE}$ ,  $\tau_{ins}$ ,  $L$ ,  $a_{ins}$ ,  $I_{sol}$ ,  $v_w$ , and  $T_{amb}$ .

The results of Eq. (4.30) have different units and orders of magnitude for each parameter. Therefore, the comparison of these coefficients is difficult. By multiplying a parameter with its sensitivity coefficient, the resulting relative sensitivity coefficient,  $RSC$ , makes it possible to compare different sensitivity coefficients:

$$RSC_i = SC_i \cdot P_i \quad (4.31)$$

For an intuitive comparison, the relative sensitivity coefficients were normalized by the maximum relative sensitivity coefficients  $RSC_{max}$  of each season.

$$RSC_i^* = RSC_i / RSC_{max} \quad (4.32)$$

The maximum normalized relative sensitivity coefficient  $RSC_i^*$  in a given weather condition was taken as 1. Then, the calculated  $RSC_i^*$  of six different weather conditions and the difference between the environmental temperature  $T_{env}$  and the fluid temperature  $T_{cf}$  are summarized in Table 4.3. The negative values in the table indicate that small increases in the corresponding parameters reduce the disturbance, whereas the positive values increase it.  $RSC_i^*$  is treated as high or low based on its absolute value.

**Table 4.3** Differences between environmental temperature and borehole heat exchanger outlet temperature of circulating fluid, and normalized relative sensitivity coefficients of each parameter in six weather conditions.

Case	$T_{env} - T_{cf}$ [°C]	$Q_{rig}$	$\dot{V}_{cf}$	$T_{cf,out,BHE}$	$\tau_{ins}$	$L$	$a_{ins}$	$I_{sol}$	$T_{amb}$	$v_w$
Sum-day	55.3	-0.02	0.02	-0.55	-0.44	1.00	0.95	0.95	0.63	-0.17
Sum-night	-3	0.04	-0.04	1.00	-0.06	0.14	N/A	N/A	-0.90	0.01
Int-day	34.6	-0.03	0.03	-0.69	-0.33	0.76	1.00	1.00	0.48	-0.20
Int-night	-20	0.04	-0.04	1.00	-0.31	0.71	N/A	N/A	-0.33	0.05
Win-day	12.9	-0.03	0.03	-0.83	-0.14	0.33	1.00	1.00	0.19	-0.23
Win-night	-31	0.04	-0.03	0.93	-0.44	1.00	N/A	N/A	-0.03	0.07

N/A: not applicable ; Sum-day: daytime of summer; Sum-night: nighttime of summer; Int-day: daytime of intermediate season; Int-night: nighttime of intermediate season; Win-day: daytime of winter; Win-night: nighttime of winter

$Q_{rig}$  and  $\dot{V}_{cf}$ , which were the settings of the experiment, have relatively low  $RSC^*$ , and as stated in Section 4.3.2, they both can reduce or increase the disturbance depending on the nature of the temperature difference (positive or negative) between the environment and fluid. The decrease trend for the Win-night case with increasing  $Q_{rig}$  observed in Fig. 4.5 is different from the  $RSC^*$  of  $Q_{rig}$  in Table 4.3 because the  $RSC^*$  is related to the amount of disturbance  $Q_{d,tot}$ , not the disturbance ratio  $Q_{d,tot}/Q_{rig}$ .

The BHE outlet temperature  $T_{cf,out,BHE}$ , which represents the temperature of the circulating fluid, has a relatively high  $RSC^*$  but varies in a wide range. The absolute magnitude of  $RSC^*$  increases with decreasing difference between  $T_{env}$  and  $T_{cf}$ . Therefore, the  $RSC^*$  of  $T_{cf,out,BHE}$  continuously changes during a TRT.

The thickness of insulation layer  $\tau_{ins}$  and the length of aboveground hydraulic circuit  $L$  also have varying  $RSC^*$  depending on the magnitude of the difference between  $T_{env}$  and  $T_{cf}$ . Unlike  $T_{cf,out,BHE}$ , they both show higher  $RSC^*$  when the temperature difference increases, and as can be seen in Table 4.3, the  $RSC^*$  of  $L$  varies in a very wide range. In the Sum-night case, the  $RSC^*$  of  $L$  is 0.14, but in the Sum-day and Win-night cases, it has the highest  $RSC^*$  among the parameters. Therefore, the length aboveground hydraulic circuit must be as small as possible. In all cases,  $\tau_{ins}$  has negative  $RSC^*$  and  $L$  has positive  $RSC^*$ .

The radiation absorptivity of hydraulic circuit's surface  $a_{ins}$  has high  $RSC^*$  in all daytime cases. Its magnitude is one of the highest, along with those for  $I_{sol}$  and  $L$ . Clearly,  $a_{ins}$  only has an impact during daytime.

Among the weather parameters, the global solar irradiation  $I_{sol}$  has the highest  $RSC^*$ . In addition to having high  $RSC^*$ , the parameter varies in a wide range. In summer,  $I_{sol}$  increases up to 1000 W/m<sup>2</sup>;

therefore, it has a high impact on the fluctuation of temperature response in TRT. Because  $a_{ins}$  also has high  $RSC^*$ , in all circumstances, care should be taken for the parameters related to the radiative heat transfer.

The  $RSC^*$  of the ambient temperature  $T_{amb}$  also varies in wide range, and its behavior is slightly different between day and night. Whereas it increases during both day and night as  $T_{amb}$  increases, during daytime,  $I_{sol}$  also affects the  $RSC^*$  of  $T_{amb}$ . The magnitude of  $RSC^*$  increases as  $I_{sol}$  decreases.

$v_w$  has higher  $RSC^*$  during the day than night because it has an impact on both the overall heat transfer coefficient  $h_o$  and the sol-air temperature  $T_{sol,a}$  during daytime. The magnitude of  $RSC^*$  is affected by existence of  $I_{sol}$ ,  $T_{amb}$ , and the relationship between  $T_{env}$  and  $T_{cf}$ . During the night when there is no solar irradiation, the  $RSC^*$  increases as the temperature difference increases and its sign is positive. The magnitude of  $RSC^*$  is very small, and the variation range is also very narrow. The maximum  $RSC^*$  is 0.07 in the Win-night case, and the minimum is 0.01 in the Sum-night case. However, during the daytime when solar irradiation exists, the magnitude of  $RSC^*$  is higher and the behavior of  $RSC^*$  is more complex than during the night. For a given  $I_{sol}$ ,  $RSC^*$  decreases as  $T_{amb}$  increases, and for a given  $T_{amb}$ ,  $RSC^*$  increases as  $I_{sol}$  increases. In most situations, the sign of  $RSC^*$  is negative during daytime. However, there is an exception in the Win-day case. Even when  $I_{sol}$  exists, if  $T_{env}$  is lower than  $T_{cf}$ , the sign of  $RSC^*$  is positive and its magnitude increases as  $I_{sol}$  increases. After  $T_{env}$  increases above  $T_{cf}$  as  $I_{sol}$  increases, the sign of  $RSC^*$  changes to negative. As shown in Table 4.3, the maximum magnitude of  $RSC^*$  of  $v_w$  is 0.23 and the variation range is as narrow as for the night cases.

Low  $RSC^*$  of a parameter does not mean that it is insignificant because the variation range of each parameter is different and some parameters are intercorrelated with each other. For example, the  $RSC^*$  of  $Q_{rig}$  is one of the lowest but  $Q_{rig}$  can be easily varied in much wider range than other parameters that have high  $RSC^*$ , such as  $\tau_{ins}$  and  $L$ . Moreover,  $Q_{rig}$  is intercorrelated with  $T_{cf,out,BHE}$ , which has a much higher  $RSC^*$  than  $Q_{rig}$ . In the summer condition when  $T_{env}$  is generally much higher than the initial temperature of fluid and the  $RSC^*$  of  $Q_{rig}$  and  $T_{cf,out,BHE}$  have negative values, a high  $Q_{rig}$  can significantly alleviate the magnitude of disturbance because the temperature difference between the fluid and outdoor environment can be narrowed in a short time by a rapid rise of fluid temperature in the early period response. Moreover, as shown in Fig. 4.4 and Fig. 4.5, an increasing  $Q_{rig}$  results in a decreasing contribution of disturbance effect in all cases.

The insights into TRT presented in this paper can be helpful in the design of TRTs and more stable and faster convergence of estimation can be achieved.

## 4.5 Conclusions

In this study, on the basis of a theoretical model that considers the heat exchange between the circulating fluid and the outdoor environment, a parametric study and sensitivity analysis were conducted in a systematic manner. For some parameters, no general conclusion could be drawn because the weather conditions and the relationship between the environmental temperature and the fluid temperature continuously change. Therefore, the conclusions that can be drawn from this study are limited, but if a constant heat flux model such as the ILS model is chosen by the experimenter to interpret TRT data, then the following conclusions should be considered and applied in the design of TRT setup and conducting a TRT.

### ▪ Settings of TRT

The heat injection rate and the flow rate are chosen by the experimenter. If the experimenter knows that the subsurface heat transfer is conduction dominated, then more stable estimation can be expected by applying a high heat injection rate because the disturbance has low impact with increasing heat injection rate. In particular, in a situation where the environmental temperature is much higher than the initial fluid temperature and the diurnal amplitude of the environmental temperature is significant, this measure would be effective. Even in a situation where the environmental temperature is lower than the initial fluid temperature, which means the temperature difference increases as TRT proceeds, the disturbance ratio is lowered, as shown in Fig. 4.5. Therefore, if the conduction-dominated condition is guaranteed, a high heat injection rate is good measure for stable estimation.

For the flow rate, it is difficult to draw a general conclusion. Regardless, the flow rate should be chosen to minimize the measurement uncertainty caused by the intrinsic error of the sensors because the flow rate has little impact on the disturbed heat rate compared with other parameters. Note that not only the error of the flow rate sensors but also the error of temperature sensors should be considered. When a high heat injection rate is used, the flow rate can also be higher because the temperature difference between inlet and outlet of BHE increases.

### ▪ Connecting hydraulic circuit

A clear conclusion can be drawn for the parameters related to the connecting hydraulic circuit: the circuit length should be as short as possible, particularly when a TRT is conducted in the condition where the temperature difference between the environment and fluid is large.

A thicker insulation is better for a TRT. As shown in Fig. 4.12, compared with the no-insulation circuit, an insulation of 10 mm thickness reduced the disturbance by half. If the material of insulation is

polyethylene foam, an insulation thickness more than 10 mm is recommended.

The radiation absorptivity of the circuit's surface is a parameter that should be controlled. As shown in Fig. 4.13 and Table 4.3, the parameters related to the radiative heat transfer showed the highest impact on the disturbance. Nevertheless, the importance of radiation absorptivity and impact of radiative heat transfer on the disturbance is not recognized widely. An experimenter may apply dark-colored insulation or finishing material in a TRT setup. The color of insulation or finishing material should be bright to ensure low absorptivity. If possible, a reflecting material should be applied to the circuit and a canopy tent should be installed covering the entire TRT setup to significantly reduce the temperature fluctuation due to radiation.

In Chapter 5, using a numerical model combined with the disturbance analytical model developed in this study, the applicability and limitations of the ILS model in interpreting disturbed TRT data are examined.

CHAPTER 5  
APPLICABILITY AND LIMITATIONS OF INFINITE LINE  
SOURCE MODEL FOR INTERPRETATION OF DISTURBED  
RESPONSE DATA

## 5.1 Introduction

The objective of this chapter is qualitative examination of errors in interpreting TRT data using the ILS model when the data are disturbed by the heat exchange between the outdoor environment and the fluid. A numerical model was developed and combined it with the analytical model developed in Section 4.2, which considers the heat exchange in the aboveground connecting circuit with the outdoor environment. By combining these two models, the disturbance effect from the outdoor environment can be taken into account. The developed model was validated with in situ TRT data. Three types of synthetic weather data, representing clear days of three different seasons (summer, intermediate season, and winter), were generated and used to identify general characteristics of the disturbance and the estimation error. Then, 36 cases of disturbed numerical TRTs were conducted using measured weather data. Through this study, some characteristic estimation behavior related to the weather conditions was described and changes in error range with testing duration were analyzed to clarify the applicability and limitation of the ILS model for interpretation. On the basis of the results, some practical suggestions regarding conducting and interpreting TRTs using the ILS model are provided.

## 5.2 Description of numerical model

A numerical BHE model was developed in the FEFLOW [136] environment, which is based on the finite element method. The model is three-dimensional, and the geometry of the BHE, which is 50 m long, is fully discretized. The model considers conduction heat transfer only. The thermal properties of the BHE components and soil are isotropic, homogeneous, and constant (i.e., no temperature dependence). The following is a detailed description of the numerical model.

### 5.2.1 Governing equation

The saturated ground consists of two phases: solid and fluid. In general, the ground is modeled from a macroscopic view using the porosity. In this study, except for the fluid flow in the U-tube, the model considers neither the advective heat transfer nor the natural convection in the porous medium. Therefore, all properties of elements are considered as bulk properties denoted by subscript  $b$ :

$$(\rho c)_b = \varepsilon(\rho c)_f + (1 - \varepsilon)(\rho c)_s \quad (5.1)$$

The fluid flow in the U-tube was modeled using one-dimensional (1D) flow elements and pseudo-fluid elements. A description of this modeling scheme will be provided in the next section. Except for the 1D flow element in the U-tube, the entire model domain is governed by the following equation of energy conservation:

$$(\rho c)_b \frac{\partial T}{\partial t} - \nabla \lambda_b \nabla T = Q_T \quad (5.2)$$

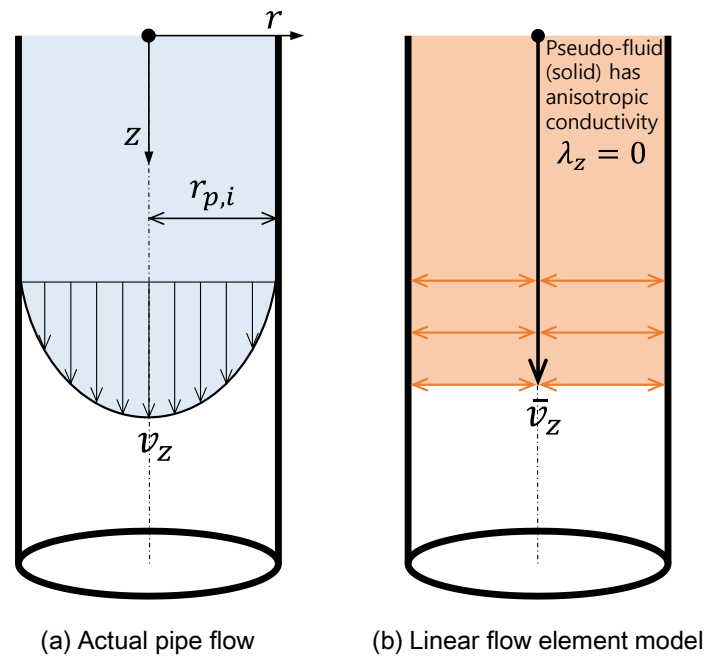


**Fig. 5.1** Schematic of simplified flow and heat transfer in the U-tube; (a) actual pipe flow and (b) simplified flow model using linear flow element based on the Hagen–Poiseuille law and a solid with anisotropic thermal conductivity.

### 5.2.2 1-D representation of flow in U-tube and governing equations of linear element

The fluid flow in the U-tube was modeled as a 1D flow element on the basis of the law of Hagen–Poiseuille flow [137–139]. This element is located in the center of pipe, and pseudo-fluid elements are used for the radial heat transfer between the linear element and pipe element. The pseudo-fluid elements have low thermal capacity ( $1 \text{ J}/(\text{m}^3\text{K})$ ) and very high anisotropic thermal conductivity ( $1000 \text{ W}/(\text{m}\cdot\text{K})$ ) to mimic the heat transfer in turbulent flow (Table 5.1). Because the pseudo-fluid has zero thermal conductivity in the vertical direction ( $\lambda_z = 0$ ), the heat transfer from the linear element to pipe occurs only in the radial direction. By using this modeling scheme (Fig. 5.1), heat transfer characteristics in turbulent

flow, which is dominant in the radial direction, can be efficiently modeled. Similar modeling approaches have been used and can be found in Refs. [140–142].

If the inertial term in the Navier–Stokes equation is not considered and the flow field has constant velocity only in the  $z$  direction along the axisymmetric pathline ( $v_r = 0$ ,  $v_\phi = 0$ ), the momentum equation can be simplified to a 1D, steady-state flow equation:

$$\frac{dp}{dz} - \rho g = \frac{\mu}{r} \left[ \frac{\partial}{\partial r} \left( r \frac{\partial v_z}{\partial r} \right) \right] \quad (5.3)$$

Two assumptions are applied to derive the momentum equation for the  $z$  direction: no velocity change at  $r = 0$  ( $dv_z/dr = 0$ ) and velocity is zero at the inner surface of pipe ( $v_z(r_{p,i}) = 0$ ). Using these two assumptions and integrating Eq. (5.3) twice with respect to  $r$ , the following equation is obtained:

$$v_z = -\frac{1}{4\mu} \left( \frac{dp}{dz} - \rho g \right) (r_{p,i}^2 - r^2) \quad (5.4)$$

The average velocity for the Hagen–Poiseuille flow in the pipe can be obtained by double integration of Eq. (5.4):

$$\bar{v}_z = -\frac{1}{\pi r_{p,i}^2} \int_{\phi=0}^{2\pi} \int_{r=0}^{r_{p,i}} v_z r dr d\phi = -\frac{r_{p,i}^2}{8\mu} \left( \frac{dp}{dz} - \rho g \right) \quad (5.5)$$

The discharge flow rate in the pipe can be defined as

$$Q = \pi r_{p,i}^2 \bar{v}_z = -\frac{\pi r_{p,i}^4}{8\mu} \left( \frac{dp}{dz} - \rho g \right) \quad (5.6)$$

The hydraulic radius  $r_{hydr}$  is defined as the flow area divided by the wetted perimeter. In the case of tubular geometry, it can be expressed as

$$r_{hydr} = \frac{\pi r_{p,i}^2}{2\pi r_{p,i}} = \frac{r_{p,i}}{2} \quad (5.7)$$

Using the hydraulic radius, Eq. (5.5) can be re-written as

$$\bar{v}_z = -\frac{r_{hydr}^2}{2\mu} \left( \frac{dp}{dz} - \rho g \right) \quad (5.8)$$

Eq. (5.8) is the momentum equation for the linear flow element in the U-tube.

The mass conservation for the linear element can be written as

$$\pi r_{p,i}^2 \left( \rho_0 g \gamma_f + \frac{1}{B} \right) \frac{\partial h}{\partial t} - \nabla \left( \pi r_{p,i}^2 \frac{r_{hydr}^2 \rho_0 g}{2\mu_0} \delta f_\mu \nabla h \right) = \pi r_{p,i}^2 B Q_\rho \quad (5.9)$$

The energy conservation for the linear element can be written as

$$\pi r_{p,i}^2 (\rho c)_f \frac{\partial T}{\partial t} - \pi r_{p,i}^2 (\rho c)_f \mathbf{v} \nabla T - \nabla (\pi r_{p,i}^2 \lambda_f \nabla T) + \pi r_{p,i}^2 (\rho c)_f Q_\rho (T - T_0) = \pi r_{p,i}^2 Q_T \quad (5.10)$$

### 5.2.3 Effective pipe thermal conductivity

If the flow in the pipe is modeled using the linear flow element and pseudo-fluid element, the convective thermal resistance on the inner pipe wall cannot be considered. Therefore, the concept of effective thermal conductivity is introduced for the pipe element. The thermal resistance of pipe can be expressed as

$$R_p = \frac{\ln(r_{p,o}/r_{p,i})}{2\pi\lambda_p} \quad (5.11)$$

This is a 1D resistance expression that neglects the vertical ( $z$ ) direction.

The convective thermal resistance on the inner pipe wall can be written as:

$$R_{c,i} = \frac{1}{2\pi r_{p,i} h_i} \quad (5.12)$$

The convective heat transfer coefficient is determined on the basis of the Nusselt number (Nu):

$$h_i = \frac{\text{Nu} \lambda_{cf}}{2r_{p,i}} \quad (5.13)$$

Nu is a function of flow velocity and the roughness of the inner surface of pipe. It can be estimated using Gnielinski's formula [114]:

$$\text{Nu} = \frac{(f/8)(\text{Re} - 1000)\text{Pr}}{1 + 12.7(f/8)^{0.5}(\text{Pr}^{2/3} - 1)} \quad (5.14)$$

This relation is valid for ( $0.5 \leq \text{Pr} \leq 2000$ ,  $3 \times 10^3 < \text{Re} < 5 \times 10^6$ ), where Pr is the Prandtl number and Re is the Reynolds number. Re and Pr are defined as

$$\text{Re} = \rho_{cf} v_{cf} 2r_{p,i} / \mu_{cf} = v_{cf} 2r_{p,i} / \nu_{cf} \quad (5.15)$$

$$\text{Pr} = \frac{\nu_{cf}}{\alpha_{cf}} = \mu_{cf} c_{cf} / \lambda_{cf} \quad (5.16)$$

The dynamic viscosity is approximated by following equation:

$$\mu_{cf} = 2.414 \times 10^{-5} \times 10^{274.8 / (273.15 + T_{cf} - 140)} \quad (5.17)$$

The Darcy friction factor  $f$  can be obtained from the Moody diagram, or in the case of a smooth pipe, the following formula [115] can be used:

$$f = (0.79 \ln \text{Re} - 1.64)^{-2} \quad (5.18)$$

This relation is valid for  $3 \times 10^3 < \text{Re} < 5 \times 10^6$ .

The convective and pipe thermal resistances form a serial connection. If the sum of the two resistances is assumed to be equal to the effective pipe resistance, it can be expressed as

$$R_{p,eff} = R_{c,i} + R_p \quad (5.19)$$

By substituting Eq. (5.11) and Eq. (5.12) into Eq. (5.19),

$$\frac{\ln(r_{p,o}/r_{p,i})}{2\pi\lambda_{p,eff}} = \frac{1}{2\pi r_{p,i} h_i} + \frac{\ln(r_{p,o}/r_{p,i})}{2\pi\lambda_p} \quad (5.20)$$

Rearranging Eq. (5.20) with respect to  $\lambda_{p,eff}$  yields

$$\lambda_{p,eff} = \frac{\ln(r_{p,o}/r_{p,i})}{1/r_{p,i} h_i + \ln(r_{p,o}/r_{p,i})/\lambda_p} \quad (5.21)$$

Because the thermal conductivity of pipe is constant,  $\lambda_{p,eff}$  is a function of flow velocity and dynamic viscosity  $\mu_{cf}$ . Based on the calculations, in general for a TRT,  $\lambda_{p,eff}$  is approximately 0.01–0.05 W/(m·K) lower than  $\lambda_p$ .

#### 5.2.4 Discretized model and element properties

The discretized model is illustrated in Fig. 5.2, and the geometry of the BHE and thermal properties of each component are summarized in Table 5.1. The calculation domain has dimensions of  $15 \times 15 \times 80$  m

(length  $\times$  width  $\times$  depth). From a series of trial calculations with an adiabatic lateral boundary condition, it was found that the length of temperature plume did not reach 3 m from the center of the borehole before the 120th hour of heat injection. Therefore, the size of calculation domain is sufficiently large without being affected by the lateral boundary. The entire domain has an initial temperature of 17 °C. The top, bottom, and lateral boundary conditions are adiabatic. The boundary condition of BHE will be explained in the next section.

The horizontal mesh is generated by a triangular mesh generator [143]. The size of finite elements is varied spatially to consider the temperature gradient. The smallest element size of 0.7 mm is used for the U-tube heat exchanger where the steepest temperature gradient is expected. The element size is gradually increased toward the lateral boundaries. The number of elements per slice is 7467. In the vertical direction, the calculation model has 76 slices and the vertical distance between slices is varied from 0.02 to 5 m to appropriately consider different vertical temperature gradients. The finest discretization is made around the bottom of the BHE (around  $z = -50$  m) to consider the steepest temperature gradient.

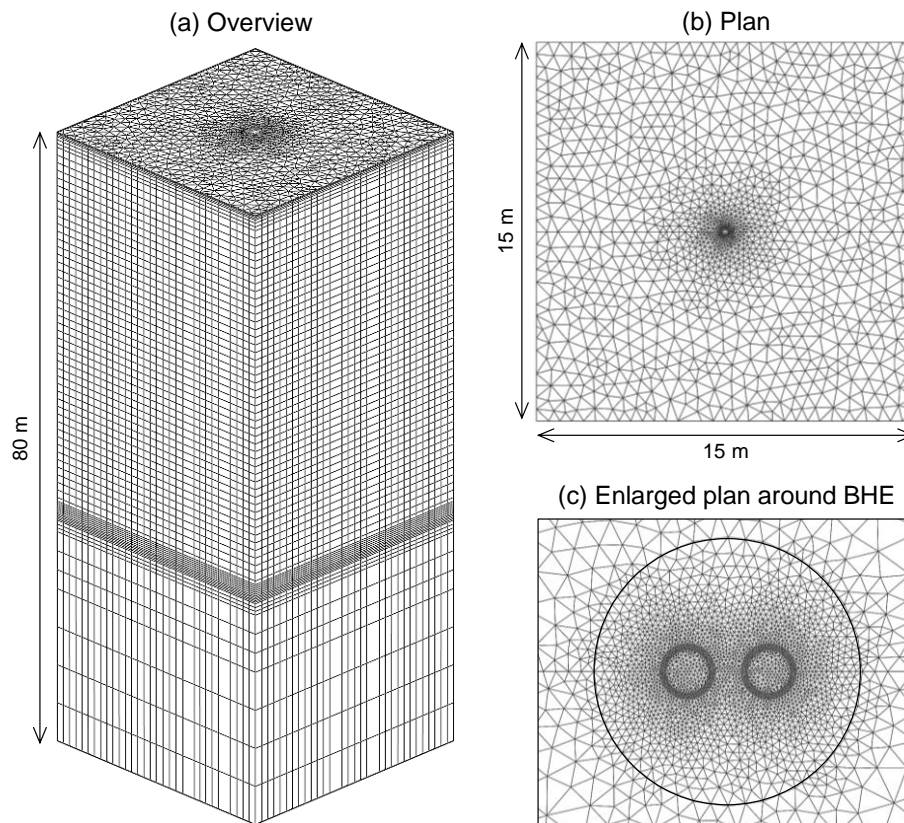


**Fig. 5.2** Details of discretized numerical model (not to scale); (a) overview of model, (b) plan, and (c) enlarged plan around BHE.

**Table 5.1** Parameters of borehole heat exchanger (BHE), thermal response test (TRT) setup, soil, and settings of test.

Parameter [units]	Value
Linear flow element: Water	
Thermal conductivity [W/(m·K)]	0.6
Volumetric thermal capacity [MJ/(m <sup>3</sup> ·K)]	4.2
Pseudo-fluid in U-tube	
Thermal conductivity [W/(m·K)]	1000
Volumetric thermal capacity [MJ/(m <sup>3</sup> ·K)]	1×10 <sup>-6</sup>
U-tube: High density polyethylene	
Outer diameter [mm]	34
Inner diameter [mm]	27
Shank spacing [mm]	60
Effective thermal conductivity [W/(m·K)]	0.36
Volumetric thermal capacity [MJ/(m <sup>3</sup> ·K)]	1.8
Borehole heat exchanger	
Borehole depth [m]	50
Borehole diameter [mm]	165
Grout	
Thermal conductivity [W/(m·K)]	1.4
Volumetric thermal capacity [MJ/(m <sup>3</sup> ·K)]	2.0
Soil	
Thermal conductivity [W/(m·K)]	1.8
Volumetric thermal capacity [MJ/(m <sup>3</sup> ·K)]	2.5
Connecting hydraulic circuit	
Length of connecting circuit [m]	2.0
Thickness of insulation [m]	0.01
Thermal conductivity of insulation [W/(m·K)]	0.04
Radiation absorptivity of circuit surface (insulation) [-]	0.6
TRT setting	
Heat injection rate [kW]	2.5
Volumetric flow rate [L/min]	15

### 5.2.5 Disturbance model combined as boundary condition of BHE

In Section 4.2, the analytical model for the heat transfer in the aboveground hydraulic circuit was derived. Here, the analytical model is integrated into the numerical model as the boundary condition of the BHE inlet to consider the heat exchange in the aboveground hydraulic circuit and the resulting temperature perturbation in the circulating fluid. In this section, the BHE's boundary condition is described in detail.

Heat exchange between the circulating fluid and the outdoor environment occurs in the aboveground

hydraulic circuit, which connects the BHE and the TRT rig. As described in Chapter 4, the flow directions in the hydraulic circuit are defined on the basis of the BHE and TRT rig. The outflow from the BHE outlet to TRT rig's inlet is denoted by subscript *out*, and the inflow from the TRT rig's outlet to BHE inlet is denoted by subscript *in*. The derived analytical model which considers the conductive, convective, and radiative heat exchanges between the outdoor environment and the circulating fluid in the outflow circuit is described in Eq. (4.6). For the better readability, the related equations obtained in Section 4.2 are provided in this section again.

In the outflow circuit, the temperature perturbation is expressed as:

$$T_{cf,out,rig}(t) = T_{cf,out,BHE}(t)e^{-\kappa_{out}(t)} + T_{sol,a}(t)(1 - e^{-\kappa_{out}(t)}) \quad (4.6)$$

where

$$\kappa(t) = \frac{L}{\rho_{cf}c_{cf}\dot{V}_{cf}R_{tot}(t)} \quad (4.5)$$

$$T_{sol,a}(t) = T_{amb}(t) + F_{cor} \frac{a_{ins}I_{sol}(t)}{h_o(t)} \quad (4.15)$$

$$R_{tot} = \frac{1}{2\pi r_{p,i}h_i} + \frac{\ln(r_{p,o}/r_{p,i})}{2\pi\lambda_p} + \frac{\ln(1 + \tau_{ins}/r_{p,o})}{2\pi\lambda_{ins}} + \frac{1}{2\pi r_{ins,o}h_o} \quad (4.21)$$

where correction factor is required for the sol-air temperature  $F_{cor}$  is set to 0.65. For details of the parameters used in above equations, please refer to Section 4.2.

A certain volumetric flow rate  $\dot{V}_{cf}$  is assigned to the inlet and outlet of the BHE as inflow and outflow boundary conditions, respectively (Table 5.1).

After estimating the inlet temperature of the TRT rig using Eq. (4.6), assuming that there is no heat exchange in the TRT rig except for the heat power  $Q_{rig}$  generated from the pump and heater, the outlet temperature of the TRT rig can be determined by Eq. (4.7):

$$T_{cf,in,rig}(t) = T_{cf,out,rig}(t) + \frac{Q_{rig}}{\rho_{cf}c_{cf}\dot{V}_{cf}} \quad (4.7)$$

Similar to Eq. (4.6), which describes the temperature perturbation in the outflow circuit, the temperature perturbation in the inflow circuit can be calculated using Eq. (4.8).

$$T_{cf,in,BHE}(t) = T_{cf,in,rig}(t)e^{-\kappa_{in}(t)} + T_{sol,a}(t)(1 - e^{-\kappa_{in}(t)}) \quad (4.8)$$

Using Eqs. (4.6) and (4.7), the total temperature perturbation in the aboveground hydraulic circuit can be estimated. The temperature differences between two nodes of the inflow and outflow circuits are estimated using Eqs. (4.9) and (4.10), respectively, and their sum is the total temperature change in the hydraulic circuit, defined by Eq. (4.11):

$$\Delta T_{cf,out}(t) = T_{cf,out,BHE}(t) - T_{cf,out,rig}(t) \quad (4.9)$$

$$\Delta T_{cf,in}(t) = T_{cf,in,rig}(t) - T_{cf,in,BHE}(t) \quad (4.10)$$

$$\Delta T_{cf,tot}(t) = \Delta T_{cf,out}(t) + \Delta T_{cf,in}(t) \quad (4.11)$$

The rate of heat exchange between the circulating fluid and outdoor environment in the outflow and inflow circuits can be quantified using Eq. (4.12) and Eq. (4.13), respectively, with their sum being the total heat exchange rate in the hydraulic circuit expressed by Eq. (4.14):

$$Q_{d,out}(t) = \rho_{cf} c_{cf} \dot{V}_{cf} \cdot \Delta T_{cf,out}(t) \quad (4.12)$$

$$Q_{d,in}(t) = \rho_{cf} c_{cf} \dot{V}_{cf} \cdot \Delta T_{cf,in}(t) \quad (4.13)$$

$$Q_{d,tot}(t) = Q_{d,out}(t) + Q_{d,in}(t) \quad (4.14)$$

Therefore, the time-varying Dirichlet boundary condition of the BHE inlet that considers the disturbance effect from the outdoor environment can be written as the following time-discretized form:

$$T_{cf,in,BHE}(t_i) = T_{cf,out,BHE}(t_{i-1}) + \frac{Q_{rig}(t_i)}{\rho_{cf} c_{cf} \dot{V}_{cf}(t_i)} + \Delta T_{cf,tot}(t_i) \quad (5.22)$$

The second and third terms on the right-hand side of Eq. (5.22) account for the temperature change due to the generated heat power in the TRT rig and the temperature perturbation in the aboveground hydraulic circuit, respectively. This boundary condition is based on Eq. (4.7) and Eq. (4.11) and changes at every time step. The entire calculation process described in this section was developed using the C++ and incorporated into FEFLOW as a subroutine. The developed subroutine code is attached in Appendix A. This subroutine is called at every time step.

## 5.3 Validation of numerical model

### 5.3.1 Validation against infinite line source model

Initially, the numerical model is validated against the ILS model. This result is referred to as the reference case. Subsequently, the model is validated against in-situ TRT data, and a comparison in terms of the average fluid temperature and estimated thermal conductivity and borehole thermal resistance is made. In this study, the average heat injection rate  $q_{avg}$  was used instead of the unit heat pulse  $q_0$  in Eq. (2.46). Then the approximated ILS model (Eq. (2.46)) can be rewritten as follows:

$$\bar{T}_{cf}(t) = \frac{q_{avg}}{\underbrace{4\pi\lambda_{eff}}_k} \ln(t) + \frac{q_{avg}}{4\pi\lambda_{eff}} \left\{ \ln\left(\frac{4\lambda_{eff}}{C_s r_b^2}\right) - \gamma \right\} + R_b \cdot q_{avg} + T_0 \quad (5.23)$$

By using the linear relationship between the average temperature of the circulating fluid with the natural logarithm of time, the effective thermal conductivity was obtained using linear regression (e.g., the least-squares method).

The response values before 13 h of TRT were not included in the estimation because the ILS model does not consider the response of the BHE itself. After estimating the effective thermal conductivity of the ground, the effective borehole thermal resistance  $R_b$  was estimated by substituting the estimated effective thermal conductivity into Eq. (5.23).

As the boundary conditions of the BHE in the numerical model, a flow rate of 15 L/min and heat injection rate of 2.5 kW ( $\cong 50$  W/m) are assigned (Table 5.1). The TRT duration is 96 h, and the time step of the calculation is 6 min. As given in Table 5.1, the thermal conductivities of the grout and soil are 1.4 W/(m·K) and 1.8 W/(m·K), respectively. The parameters in Table 5.1 are also used in Section 5.4.

For the borehole thermal resistance  $R_b$  in the ILS model, Eq. (5.24) was used. To obtain  $R_g$ , Bennet et al.'s model [48] was used (Eq. (5.26) and Eq. (5.27)), and an  $R_b$  of 0.162 m·K/W was obtained.

$$R_b = R_{c,i} + R_p + R_g \quad (5.24)$$

where

$$R_{c,i} = \frac{1}{2\pi r_{p,i} h_i}, \quad R_p = \frac{\ln(r_{p,o}/r_{p,i})}{2\pi\lambda_p} \quad (5.25)$$

$$R_g = \frac{1}{4\pi\lambda_g} \left[ \ln\left(\frac{\chi_1 \chi_2^{1+4\omega}}{2(\chi_2^4 - 1)\omega}\right) - \frac{\chi_3^2 (1 - (4\omega/(\chi_2^4 - 1)))^2}{1 + \chi_3^2 (1 + (16\omega/(\chi_2^2 - 1/\chi_2^2))^2)} \right] \quad (5.26)$$

$$\chi_1 = r_b/r_{p,o}, \quad \chi_2 = r_b/s, \quad \chi_3 = r_{p,o}/2s, \quad \omega = (\lambda_g - \lambda_s)/(\lambda_g + \lambda_s) \quad (5.27)$$

A comparison of the ILS and numerical models and the sequential estimation plot are shown in Fig. 5.3. The absolute relative error, which is plotted on the right-side vertical axis in Fig. 5.3 (a), is defined as

$$\epsilon_{rel} = \frac{|\bar{T}_{cf,num} - \bar{T}_{cf,ILS}|}{\bar{T}_{cf,num}} \times 100 \quad (5.28)$$

In Fig. 5.3, except during the early period when the response is mainly affected by the BHE itself, the relative error between the two response curves after 13 h is less than 0.3%. This error is caused by the relatively low thermal conductivity of the grout compared with that of the soil. The estimated thermal conductivity and borehole thermal resistance based on the numerical model were 1.785 W/(m·K) and 0.162 m·K/W, respectively, which are very close to the values used in the ILS model, 1.8 W/(m·K) and 0.162 m·K/W, respectively.

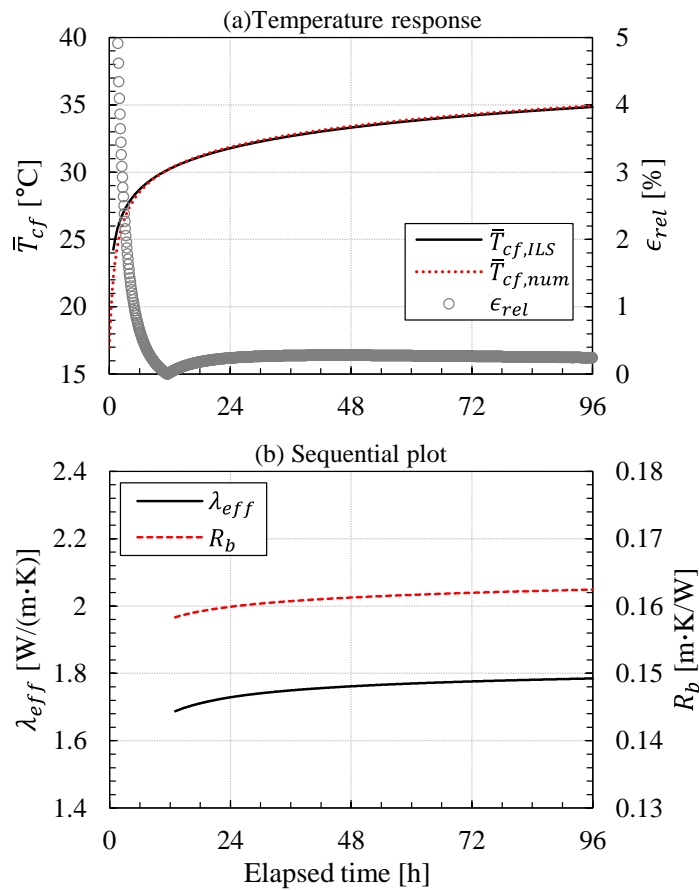


**Fig. 5.3** Comparison of the numerical model and ILS model; (a) temperature response of the two models and (b) sequential estimation using the temperature data from the numerical model.

### 5.3.2 Validation using in-situ TRT data

The second validation is for the developed disturbance model combined with the numerical model as the boundary condition of the BHE. In the TRT setup of this study, from the measured inlet and outlet temperatures of the BHE and flow rate, the actual heat injection rate, which includes all disturbance factors (voltage fluctuation and heat exchange with outdoor environment), can be determined. The actual heat injection rate was regarded as piecewise constant square pulses of 3 min intervals. Using these heat pulses, parameter estimation was conducted to obtain the thermal conductivity and volumetric heat capacity of the grout (1.43 W/(m·K) and 1.9 MJ/m<sup>3</sup>K) and soil (1.86 W/(m·K) and 2.9 MJ/m<sup>3</sup>K). However, the reliability of the estimated volumetric heat capacities is much lower than for the thermal conductivities because the sensitivity coefficient of the volumetric heat capacity is much lower [20,37,53,92,101,132,144]. A comparison of the experimental and numerical temperature responses is shown in Fig. 5.4. Except during the very early period, the two response curves show very good agreement. After 2 h, the maximum difference between the experiment and simulation is approximately 0.29 K, and the maximum relative error is less than 0.92%.

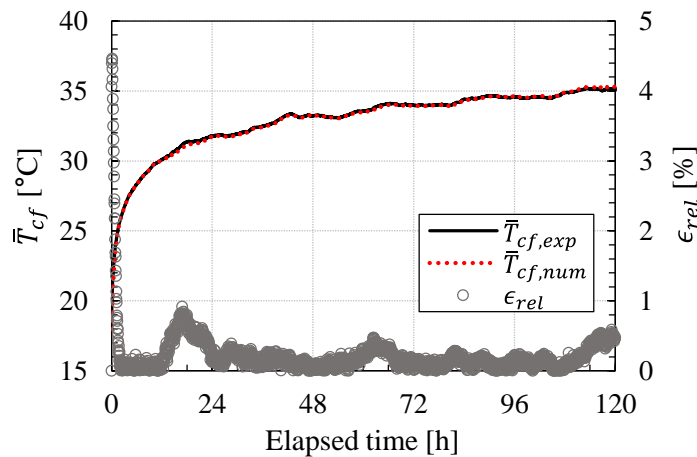


**Fig. 5.4** Comparison of the experimental and numerical temperature responses using actual heat injection rate (the heat injection rate was calculated from the measured inlet and outlet temperatures and the volumetric flow rate).

After obtaining the thermal properties of all components, the developed disturbance model was validated using the ambient temperature, global irradiation, wind velocity, and supplied wattage for the heater and pump, which does not contain disturbance from the outdoor environment. From the wattmeter installed in the TRT rig, the supplied wattage could be known, and weather data could be obtained from a weather station installed at the site. The measured weather data during the TRT are shown in Fig. 5.5. The ambient temperatures were measured for both the TRT apparatus and the weather station. Although a

small unstable fluctuation was observed, only the data for the TRT apparatus were used owing to a sensor failure at the weather station; this fluctuation was larger than that at the weather station but was due to the intrinsic error of the T-type thermocouple and thus not significant for this study. For the wind velocity, the following power-law is used to correct the wind velocity near the ground.

$$v_w = v_{w,m} \left( \frac{z}{z_m} \right)^{\alpha_m} \quad (5.29)$$

where  $z$  is the height above ground (0.1 m), subscript  $m$  is the site condition or the value of the measurements, and  $\alpha_m$  is the exponent of power law (0.3), which can be found in Ref. [105].

The parameters related to the aboveground hydraulic circuit installed at the TRT site are summarized in Table 5.2. The time step for the numerical simulation was 6 min, and the measured wattage values were also regarded as 6 min-averaged square pulses.

The numerical simulation was first conducted using the heat rate measured from the wattmeter without the disturbance model applied. This result is shown in Fig. 5.6(a) where the deviation between the experiment and numerical simulation continuously increases with time. The variation in the error exhibits an oscillating behavior that reflects the diurnal cycle of the outdoor environment. Overall, the average fluid temperature from the numerical simulation is higher than the experimental temperature. This signifies that heat loss from the circulating fluid to the outdoor environment was dominant during the TRT period.

Using the same supplied wattage values, the numerical simulation was repeated, but this time with the disturbance model applied as the boundary condition. With the model, the increasing trend of the error evident in Fig. 5.6(a) disappears in Fig. 5.6(b). Although a small fluctuation can be seen compared with Fig. 5.4, which is the result using the actual heat injection rate, the agreement between the experiment and numerical simulation is very good. The maximum difference between the experiment and simulation is approximately 0.2 K, and the maximum relative error is less than 0.8%. Therefore, it is clear that the developed model can reflect the actual disturbance effect in the aboveground hydraulic circuit with good accuracy.

**Table 5.2** Parameters of aboveground hydraulic circuit used for validation of the numerical model.

Parameter [units]	Value
Length of connecting circuit [m]	2.5
Thickness of insulation [m]	0.01
Thermal conductivity of insulation [W/(m·K)]	0.04
Radiation absorptivity of circuit surface (insulation) [-]	0.6

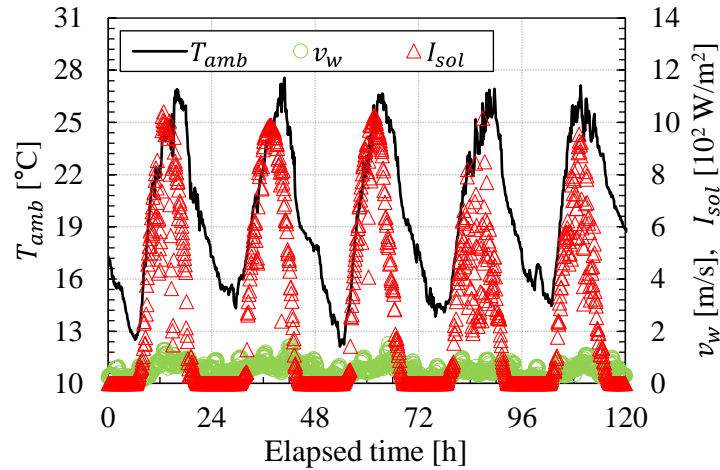


**Fig. 5.5** Weather data measured from the start of heat injection during the thermal response test (from May 15, 2014 at 22:00).

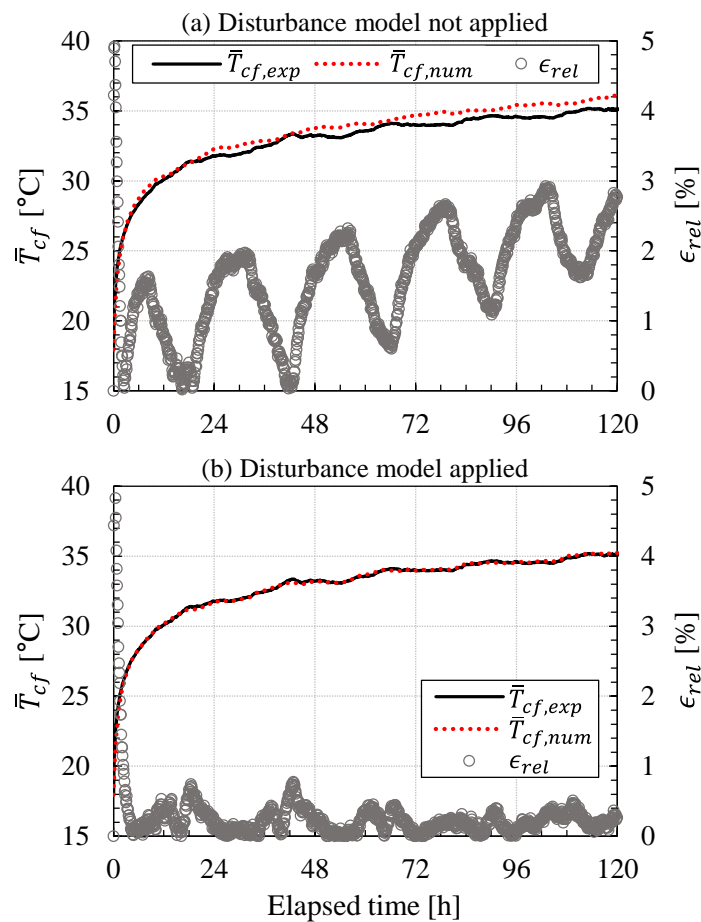


**Fig. 5.6** Comparison of the experimental and numerical temperature responses using the heat injection rate from the wattmeter; (a) disturbance model not applied and (b) disturbance model applied.

## 5.4 Analysis of disturbance effect

### 5.4.1 Effect of outdoor environment: using synthetic weather data

To calculate temperature perturbation in the aboveground hydraulic circuit, data of global solar irradiation, ambient temperature, and wind velocity are required. Typical weather data of a clear day in three different seasons (summer, intermediate season, and winter) were generated to examine the characteristics of disturbance in each season and the resulting fluctuation and error in estimation. From the weather data of Tokyo, which were generated by the expanded AMeDAS (EA) method [145], five clear days of each season were selected. Based on these days, synthetic weather models for one day were developed using the Fourier transform. Eq. (5.26) expresses the ambient temperature, and Eq. (5.27) and Eq. (5.28) express the global solar irradiation. The coefficients in Eq. (5.30) and Eq. (5.31) are summarized in Table 5.3 and Table 5.4, respectively, and the generated weather data are shown in Fig. 5.7. The wind velocity was assumed to be constant at 0.5 m/s in the simulations.

$$T_{amb}(t) = a + b \cos(t \cdot w) + c \sin(t \cdot w) + d \cos(2t \cdot w) + e \sin(2t \cdot w) \quad (5.30)$$

$$I_{sol}(t) = [a + b \cos(t \cdot w) + c \sin(t \cdot w)](H(t - p_1) - H(t - p_2)) \quad (5.31)$$

$$H(n) = \begin{cases} 0, & n < 0 \\ 1, & n \geq 0 \end{cases} \quad (5.32)$$

where  $H$  is the Heaviside step function.

**Table 5.3** Coefficients for the synthetic ambient temperature (Eq. (5.30)).

Season	$a$	$b$	$c$	$d$	$e$	$w$
Summer	30.1	-3.2	-1.5	-0.86	0.22	0.26
Intermediate	15.1	-4.4	-3.1	0.94	0.44	0.26
Winter	2.8	-1.8	-2.9	0.69	0.35	0.26

**Table 5.4** Coefficients for the synthetic global solar irradiation (Eq. (5.31)).

Season	$a$	$b$	$c$	$w$	$p_1$	$p_2$
Summer	470	-250	-460	0.36	4.3	19.1
Intermediate	390	-100	-460	0.40	5.1	18.0
Winter	360	390	22	0.53	6.8	17.1

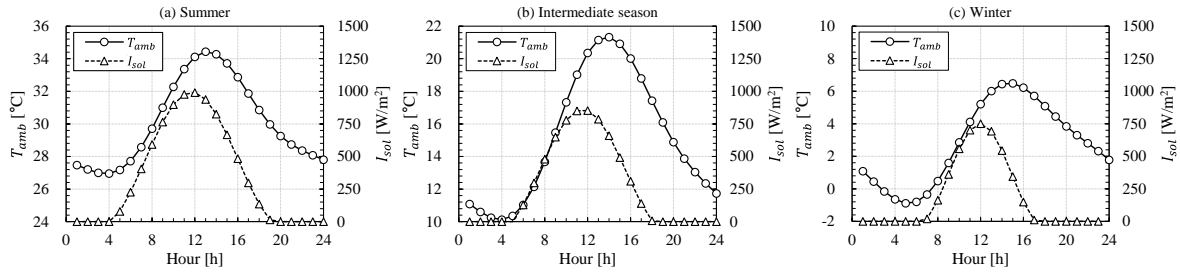


**Fig. 5.7** Generated synthetic weather data using Eq. (5.30) and Eq. (5.31); (a) summer, (b) intermediate season, and (c) winter.

Using the three synthetic weather data, a numerical TRT was simulated for 96 h, which is the same as for the reference case (Fig. 5.3), for comparison (the second column of Table 5.5). For each season, the 24 h synthetic weather data (Fig. 5.7) were used for all four days of the simulation. The calculated results of temperature response, heat exchange rate, and the disturbance ratio and the sequential estimations using the average fluid temperature from the numerical simulation are shown in Figs. 5.8–5.10. In these figures, a positive disturbed heat rate  $Q_d$  value indicates heat gain from the outdoor environment to the circulating fluid and a negative  $Q_d$  indicates heat loss from the circulating fluid to the outdoor environment. The disturbance ratio  $Q_{d,ratio}$  is defined as  $Q_{d,tot}/Q_{rig}$  (total disturbed heat rate/generated heat in the TRT rig). In summer, heat gain is dominant, whereas winter shows the opposite result.

In every case, the sequential plot shows fluctuating behavior. The amplitude of fluctuation is significant in the early-period estimations because the regression method (e.g., sequential estimation) is very vulnerable when the number of data points is small. Therefore, the amplitude of fluctuation is attenuated with time. The fluctuating behavior reflects the diurnal change of outdoor environment, and the magnitude of fluctuation depends on the amount of disturbed heat exchange rate. This result can be confirmed by the early-period estimation and the disturbance ratio in subfigures (b) and (c) in Figs. 5.8–5.10 and the maximum values during the estimation in Table 5.5. The summer case showed the largest disturbance and a resulting maximum  $\lambda_{eff}$  of 2.757 W/(m·K) and  $R_b$  of 0.194 m·K/W.

The characteristics of each estimation are quantified using the final estimated values, the maximum and minimum values, and the standard deviations based on the final estimated values (Table 5.5). As can be seen in Figs. 5.8–5.10 and the standard deviations in Table 5.5, compared with the reference case (i.e., no disturbance) shown in Fig. 5.3, the three disturbance cases show approximately 6–9 times larger  $\sigma$  of  $\lambda_{eff}$  and 5–7 times larger  $\sigma$  of  $R_b$ . Nevertheless, the final estimated values at 96 h are close to those of the reference case. The maximum deviations of  $\lambda_{eff}$  and  $R_b$  for the reference case were approximately 0.035 W/(m·K) and 0.002 m·K/W, respectively. However, the estimated values can vary depending on when the

TRT is terminated. When the disturbed heat rate changes rapidly during daytime, the estimation behavior also changes rapidly. However, when the change in the disturbed heat rate is gradual, as such at night, the estimation shows relatively stable behavior. In the summer case, although the largest heat exchange rate and fluctuation existed, values closest to the reference case can also be observed because the disturbance ratio was the smallest at night when the TRT was terminated. Therefore, assuming that other disturbances such as unstable heat generation are not involved, the TRT should be terminated at times such as right before the sunrise when the outdoor conditions are not changing rapidly. However, the estimation will still have uncertainty if the disturbance is not controlled effectively.

**Table 5.5** Simulated results using synthetic weather data; averaged heat rate, final estimated results, maximum and minimum values, and standard deviations based on the final estimated values.

Parameters	Reference TRT (No disturbance)	Summer (Synthetic data)	Intermediate (Synthetic data)	Winter (Synthetic data)
Averaged heat rate, $q_{avg}$ [W/m]	50	50.50	49.81	49.20
Final $\lambda_{eff}$ [W/(m·K)]	1.785	1.816	1.817	1.818
Final $R_b$ [m·K/W]	0.162	0.162	0.163	0.163
Max, min of $\lambda_{eff}$ [W/(m·K)]	1.785, 1.687	2.757, 1.603	2.630, 1.614	2.451, 1.565
Max, min of $R_b$ [m·K/W]	0.162, 0.158	0.194, 0.161	0.191, 0.161	0.186, 0.158
$\sigma$ of $\lambda_{eff}$ [W/(m·K)]	0.035	0.329	0.288	0.210
$\sigma$ of $R_b$ [m·K/W]	0.002	0.014	0.012	0.010

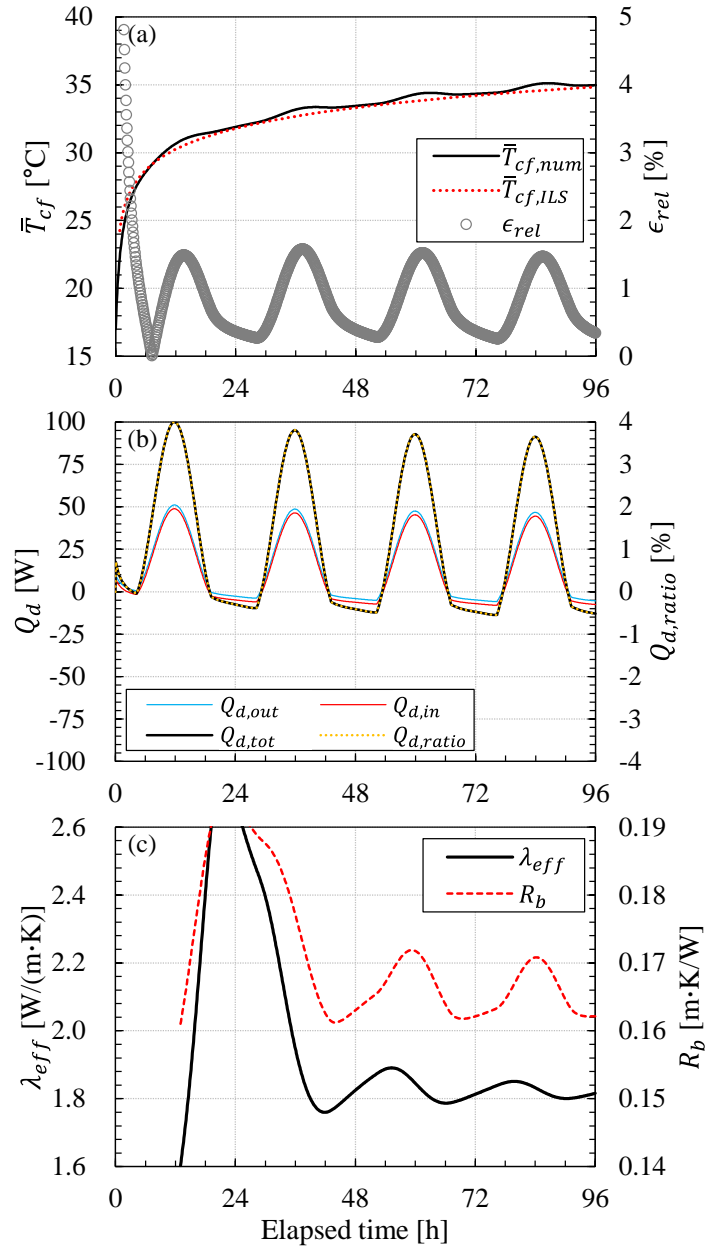


**Fig. 5.8** Numerical thermal response test using synthetic weather data of summer and the estimated results; (a) temperature response and absolute relative error compared with the ILS model, (b) disturbed heat rate and its ratio, and (c) sequential plot.

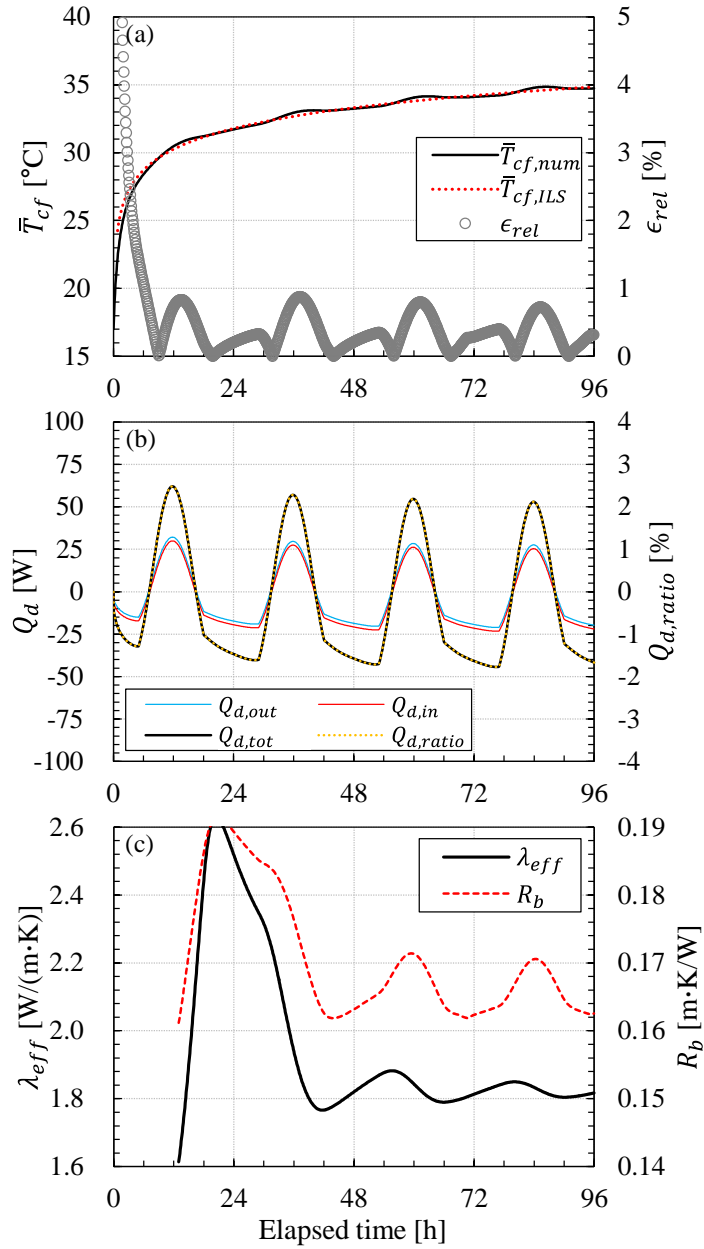


**Fig. 5.9** Numerical thermal response test using synthetic weather data of intermediate season and the estimated results; (a) temperature response and absolute relative error compared with the ILS model, (b) disturbed heat rate and its ratio, and (c) sequential plot.

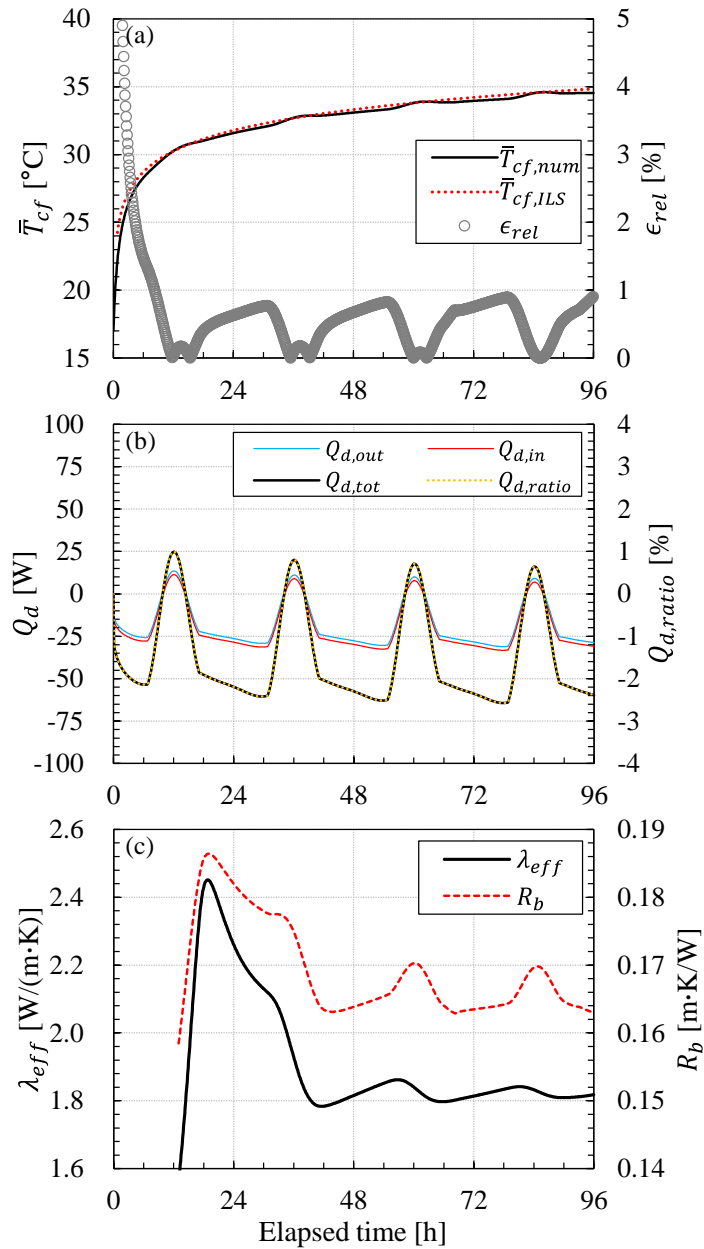


**Fig. 5.10** Numerical thermal response test using synthetic weather data of winter and the estimated results; (a) temperature response and absolute relative error compared with the ILS model, (b) disturbed heat rate and its ratio, and (c) sequential plot.

### 5.4.2 Effect of outdoor environment: using measured weather data

Although simulation using smooth synthetic weather data is helpful in examining the characteristics of disturbance and the resulting estimation behavior, it cannot represent the disturbance of a TRT conducted in real weather conditions. The actual weather conditions vary daily and sometimes even on a minute scale. To examine the effect of various weather conditions, 36 numerical TRTs were conducted using measured weather data. The ambient temperature, global solar irradiation, and wind velocity were collected at the weather station described in Section 5.3. The data were recorded from June 2013 to February 2015 at 1–5 s intervals, and data averaged across 6 min were used in the numerical model. For each season, 12 numerical TRTs were conducted and the results are summarized in Table 5.6. Among the 36 cases, four cases (TRT7, TRT18, TRT23, and TRT25) that showed different estimation behaviors were chosen and are depicted in Figs. 5.11–5.14. In these figures, subfigure (a) shows the measured weather data at 6 min intervals, (b) shows a comparison of the numerical temperature response and the reference ILS model using  $\lambda_{eff} = 1.8 \text{ W}/(\text{m}\cdot\text{K})$  and  $R_b = 0.162 \text{ m}\cdot\text{K}/\text{W}$ , (c) shows the disturbed heat rate and the disturbance ratio compared with the heat injection rate, and (d) shows the sequential estimation of  $\lambda_{eff}$  and  $R_b$ . Along with the reference case (Fig. 5.3), the final estimated values, maximum and minimum values, and standard deviations based on the final estimated values of the four TRTs are summarized in Table 5.6.

**Table 5.6** Simulated results using measured weather data; averaged heat rate, final estimated results, maximum and minimum values, and standard deviations based on the final estimated values.

Parameters	Reference TRT (No disturbance)	TRT7 (2013-06-27)	TRT18 (2014-10-03)	TRT23 (2014-11-08)	TRT25 (2015-01-21)
Averaged heat rate, $q_{avg}$ [W/m]	50	49.96	49.70	49.42	49.05
Final $\lambda_{eff}$ [W/(m·K)]	1.785	1.845	1.893	1.787	1.766
Final $R_b$ [m·K/W]	0.162	0.165	0.168	0.158	0.153
Max, min of $\lambda_{eff}$ [W/(m·K)]	1.785, 1.687	2.657, 1.257	2.372, 1.452	1.789, 1.634	1.872, 1.524
Max, min of $R_b$ [m·K/W]	0.162, 0.158	0.193, 0.145	0.184, 0.153	0.161, 0.154	0.161, 0.148
$\sigma$ of $\lambda_{eff}$ [W/(m·K)]	0.035	0.298	0.164	0.038	0.041
$\sigma$ of $R_b$ [m·K/W]	0.002	0.012	0.006	0.002	0.003

**Table 5.7** Summary of 36 numerical thermal response tests (TRTs).

	Season	Duration [yyyy-mm-dd]	$q_{avg}$ [W/m]	Final $\lambda_{eff}$ [W/m·K]	Final $R_b$ [m·K/W]	Max $\lambda_{eff}$ [W/m·K]	Min $\lambda_{eff}$ [W/m·K]	Max $R_b$ [m·K/W]	Min $R_b$ [m·K/W]	$\sigma$ of $\lambda_{eff}$ [W/m·K]	$\sigma$ of $R_b$ [m·K/W]
TRT1	Summer	2013-06-17– 2013-06-20	49.859	1.894	0.168	2.325	0.821	0.183	0.116	0.165	0.007
TRT2		2013-06-18– 2013-06-21	49.761	1.893	0.168	2.665	1.344	0.190	0.148	0.153	0.006
TRT3		2013-06-20– 2013-06-23	49.790	1.741	0.156	1.861	1.707	0.165	0.155	0.055	0.005
TRT4		2013-06-21– 2013-06-24	49.856	1.767	0.158	1.900	1.221	0.166	0.137	0.082	0.004
TRT5		2013-06-25– 2013-06-28	49.860	1.756	0.158	3.035	1.718	0.194	0.157	0.212	0.009
TRT6		2013-06-26– 2013-06-29	49.881	1.759	0.158	1.849	1.560	0.165	0.148	0.079	0.005
TRT7		2013-06-27– 2013-06-30	49.964	1.845	0.165	2.657	1.257	0.193	0.145	0.298	0.012
TRT8		2013-06-29– 2013-07-02	49.934	1.808	0.162	5.377	1.560	0.222	0.158	0.275	0.010
TRT9		2013-07-12– 2013-07-15	50.222	1.839	0.165	2.559	1.611	0.192	0.163	0.263	0.012
TRT10		2013-07-14– 2013-07-17	50.068	1.862	0.167	2.968	1.537	0.198	0.161	0.272	0.023
TRT11		2013-07-18– 2013-07-21	50.101	1.863	0.167	2.570	1.429	0.192	0.154	0.254	0.017
TRT12		2013-07-22– 2013-07-25	49.993	1.863	0.167	2.229	1.310	0.181	0.146	0.138	0.006
TRT13	Inter- mediate	2014-04-18– 2014-04-21	49.396	1.801	0.159	2.081	1.586	0.169	0.147	0.092	0.005
TRT14		2014-04-19– 2014-04-22	49.463	1.835	0.162	2.894	1.267	0.194	0.144	0.335	0.013
TRT15		2014-09-11– 2014-09-14	49.879	1.757	0.157	1.892	1.571	0.165	0.150	0.068	0.004
TRT16		2014-10-01– 2014-10-04	49.744	1.768	0.158	1.947	1.619	0.167	0.155	0.054	0.004
TRT17		2014-10-02– 2014-10-05	49.082	1.779	0.155	1.825	1.652	0.160	0.152	0.034	0.002

TRT18		2014-10-03– 2014-10-06	49.697	1.893	0.168	2.372	1.452	0.184	0.153	0.164	0.006
TRT19		2014-10-05– 2014-10-08	49.647	1.745	0.155	1.769	1.611	0.161	0.153	0.031	0.002
TRT20		2014-10-13– 2014-10-16	49.082	1.779	0.155	1.825	1.652	0.160	0.152	0.034	0.002
TRT21		2014-10-14– 2014-10-17	49.662	1.836	0.163	2.654	1.402	0.191	0.151	0.271	0.012
TRT22		2014-11-06– 2014-11-09	49.465	1.840	0.162	2.093	1.572	0.172	0.154	0.085	0.004
TRT23		2014-11-08– 2014-11-11	49.422	1.787	0.158	1.789	1.634	0.161	0.154	0.038	0.002
TRT24		2014-11-09– 2014-11-12	49.424	1.836	0.161	2.051	1.571	0.170	0.154	0.087	0.004
TRT25	Winter	2015-01-21– 2015-01-24	49.052	1.766	0.153	1.872	1.524	0.161	0.148	0.041	0.003
TRT26		2015-01-23– 2015-01-26	49.234	1.804	0.158	2.419	1.486	0.181	0.151	0.206	0.009
TRT27		2015-01-26– 2015-01-29	49.233	1.847	0.160	2.129	1.458	0.173	0.149	0.096	0.005
TRT28		2015-01-27– 2015-01-30	49.132	1.874	0.162	2.283	1.589	0.175	0.160	0.108	0.021
TRT29		2015-02-04– 2015-02-07	49.111	1.804	0.157	3.213	1.488	0.195	0.151	0.277	0.011
TRT30		2015-02-05– 2015-02-08	49.071	1.791	0.155	1.814	1.588	0.159	0.148	0.064	0.003
TRT31		2015-02-06– 2015-02-09	49.105	1.845	0.159	2.287	1.465	0.177	0.149	0.160	0.008
TRT32		2015-02-08– 2015-02-11	49.130	1.764	0.154	1.871	1.718	0.161	0.153	0.037	0.003
TRT33		2015-02-09– 2015-02-12	49.210	1.772	0.155	2.136	1.285	0.172	0.138	0.150	0.008
TRT34		2015-02-13– 2015-02-16	49.252	1.791	0.156	6.438	1.720	0.223	0.154	0.305	0.010
TRT35		2015-02-14– 2015-02-17	49.200	1.855	0.161	2.440	1.484	0.182	0.151	0.199	0.008
TRT36		2015-02-23– 2015-02-27	49.281	1.865	0.162	2.292	1.602	0.179	0.157	0.149	0.007

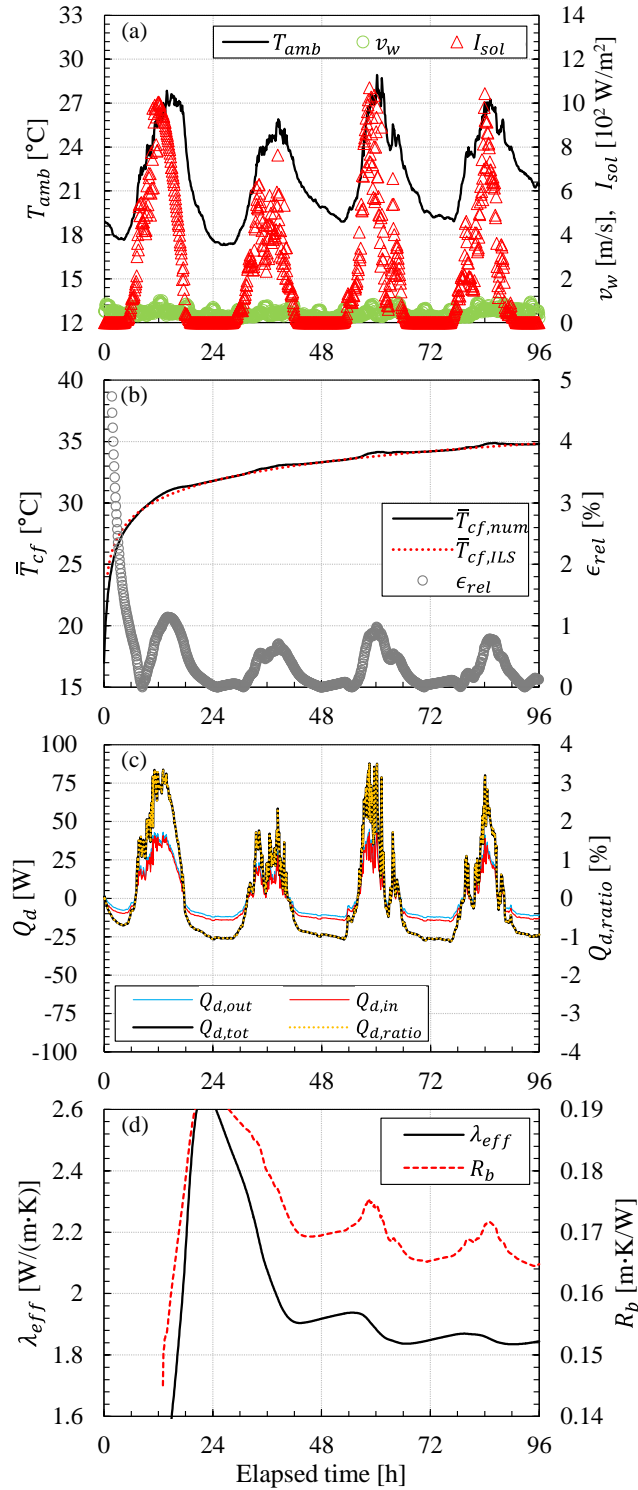


**Fig. 5.11** Numerical thermal response test (TRT7) using measured weather data (from Jun. 27, 2013, 00:00) and the estimated results; (a) weather data, (b) temperature response and absolute relative error compared with the ILS model, (c) disturbed heat rate and its ratio, and (d) sequential plot.

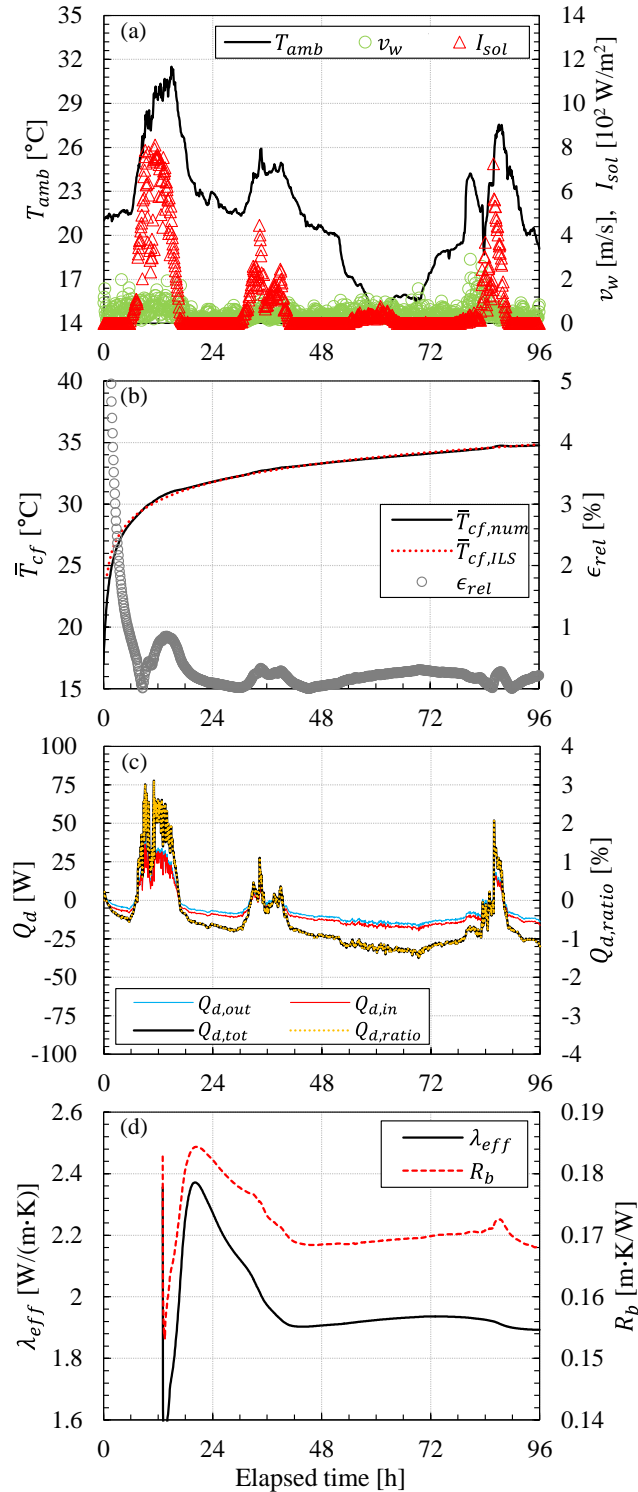


**Fig. 5.12** Numerical thermal response test (TRT18) using measured weather data (from Oct. 03, 2014, 00:00) and the estimated results; (a) weather data, (b) temperature response and absolute relative error compared with the ILS model, (c) disturbed heat rate and its ratio, and (d) sequential plot.

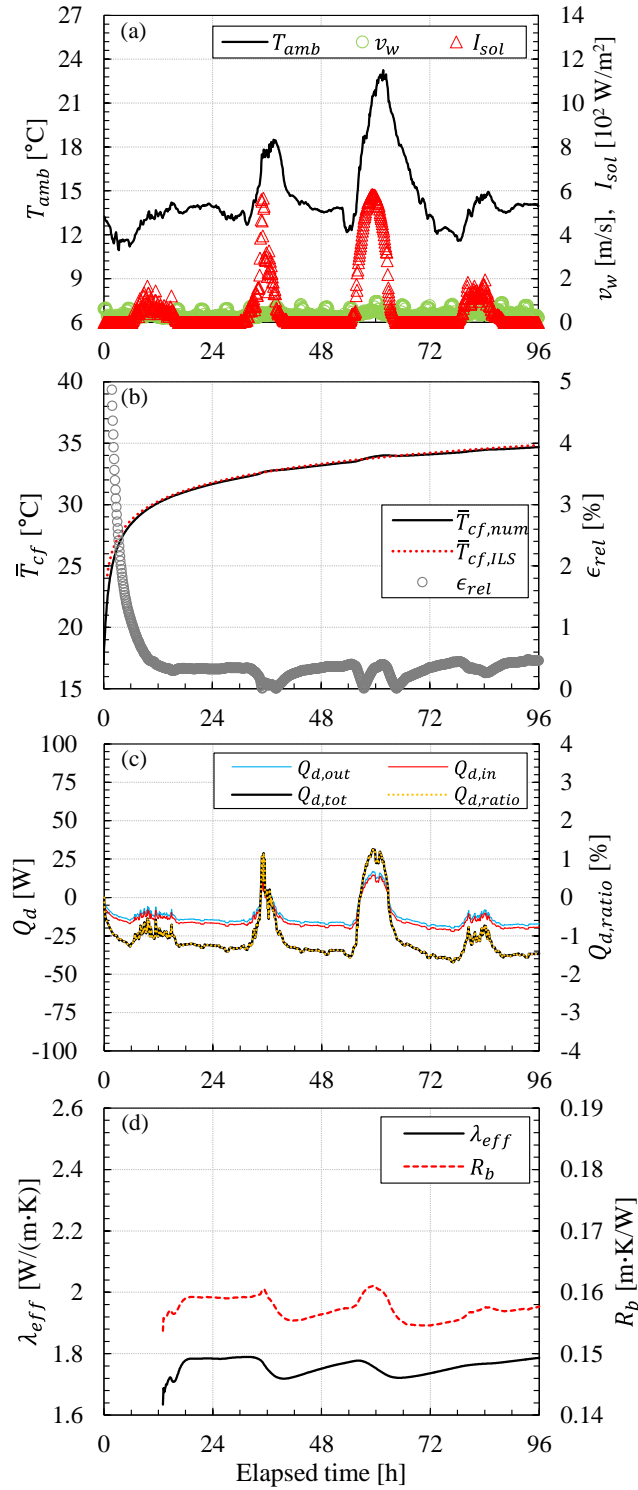


**Fig. 5.13** Numerical thermal response test (TRT23) using measured weather data (from Nov. 08, 2014, 00:00) and the estimated results; (a) weather data, (b) temperature response and absolute relative error compared with the ILS model, (c) disturbed heat rate and its ratio, and (d) sequential plot.

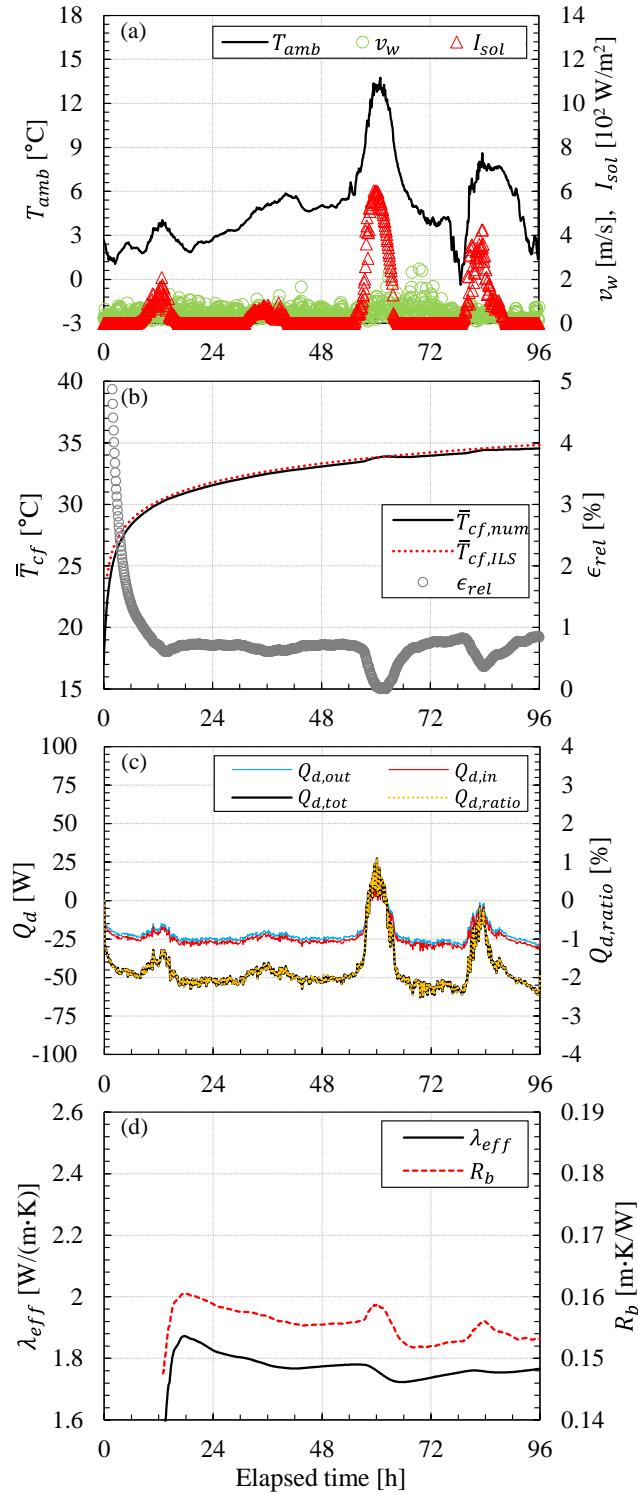


**Fig. 5.14** Numerical thermal response test (TRT25) using measured weather data (from Jan. 21, 2015, 00:00) and the estimated results; (a) weather data, (b) temperature response and absolute relative error compared with the ILS model, (c) disturbed heat rate and its ratio, and (d) sequential plot.

Both TRT7 and TRT18 showed a rapidly rising behavior in the early period of estimation (Fig. 5.11(d) and Fig. 5.12(d)). As shown in the results using synthetic weather data, TRT7, which used the weather data of summer, showed larger fluctuation in the early period than TRT18, which used the weather data of intermediate season, because the amount of solar irradiation in TRT7 was larger (Fig. 5.11(a) and Fig. 5.12(a)). The resulting rapid increase in disturbed heat rate  $Q_{d,tot}$  (Fig. 5.11(c) and Fig. 5.12(c)) also supports the strong fluctuation in the early-period estimation. Compared with TRT7 and TRT18, there are no rapid increases in the early-period estimation in TRT23 and TRT25 (Fig. 5.13(d) and Fig. 5.14(d)). These estimation behaviors are similar to that of the reference TRT shown in Fig. 5.3(b) and more stable than those of TRT7 and TRT18 because solar irradiation was very weak on the first day of TRT (Fig. 5.13(a) and Fig. 5.14(a)), which resulted in a gradual change in the disturbed heat rate (Fig. 5.13(c) and Fig. 5.14(c)). Although the overall amount of disturbed heat rate of TRT25 (approximately  $-50$  W) was much larger than those of TRT7 and TRT18, except during the daytime, TRT25 showed more stable estimation behavior. Therefore, the main cause of the fluctuating estimation behavior in the early period is the rapid change in environmental temperature due to solar irradiation. In all 36 cases summarized in Table 5.7, there is no strong fluctuation during the early-period estimation if the first day of TRT was cloudy.

Although the third or fourth day of the TRT was relatively clear sky in all four chosen cases, this was not related to the strong fluctuation in the estimation that can be seen in the early-period estimations because the abrupt deviation from the least squares has a much smaller impact as time lapses (i.e., data points used for the regression increase). The impact of the rapid change in the disturbance is not as strong after the early-period, but it still causes small fluctuation. The heat gain from solar irradiation is related to the momentary decrease in  $\lambda_{eff}$  and the increase in  $R_b$  ((c) and (d) in Figs. 5.11–5.14).

The accuracy of the final estimated values was difficult to predict. Relatively stable estimation behavior does not necessarily mean more accurate estimation. Although TRT7 showed much larger fluctuation in the early-period estimation than TRT18 (Fig. 5.11(d) and Fig. 5.12(d)), the final estimated values at 96 h were closer to the reference values (Table 5.7). Moreover, both TRT23 and TRT25 showed relatively stable estimation behavior in the early period, and TRT25 showed the largest deviation of final  $R_b$  from the reference case (Table 5.6).

Because the estimated values of the 36 cases at different times are distributed in a wide range, a meaningful conclusion cannot be drawn from the individual results. Therefore, a statistical analysis based on the 36 results was conducted to examine the change in estimation range with testing duration. The maximum, minimum, average, and the range of standard deviation at different estimation times are shown in Fig. 5.15, and those of  $\lambda_{eff}$  and  $R_b$  are summarized in Table 5.8 and Table 5.9, respectively. The initial

estimated results at 13 h, which used only two data points, are not depicted in Fig. 5.15 for the sake of clarity and are summarized in Table 5.8 and Table 5.9 only. As shown in Fig. 5.15, within the early period, the estimation ranges of  $\lambda_{eff}$  and  $R_b$  were very large but narrowed rapidly with time. After 48 h of TRT, the estimation range stabilized, the decrease in estimation range narrowed slowly, and the magnitude of standard deviations decreased to within  $\pm 5\%$  of the final estimated values of the reference case ( $\pm 0.089$  W/(m·K) and  $\pm 0.008$  m·K/W). However, this TRT duration was for when considering only the magnitude of standard deviation at a certain time. If estimation accuracy, which is represented by the average values, of  $\pm 5\%$  was to be achieved in addition to the standard deviation, the required duration of TRT increased. This duration was approximately 60 h; here, the estimated values were 1.696–1.874 W/(m·K) and 0.154–0.170 m·K/W, which were within  $\pm 5\%$  of the final estimated values of the reference case (1.785 W/(m·K) and 0.162 m·K/W). However, the error range could not be decreased to within  $\pm 2.5\%$  during the entire TRT, i.e., 96 h.

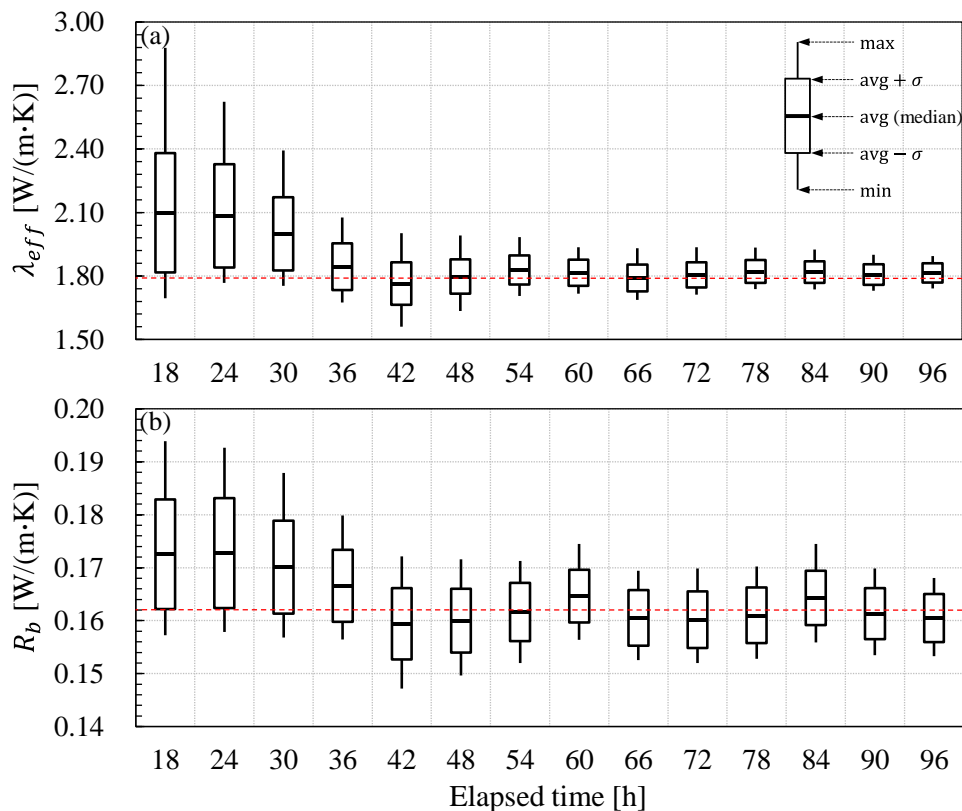


**Fig. 5.15** Maximum, minimum, average, and standard deviations at different estimation times based on data of 36 numerical thermal response tests; (a) effective thermal conductivity and (b) borehole thermal resistance.

**Table 5.8** Average, minimum, maximum, and standard deviations of the effective thermal conductivity at different estimation times based on 36 numerical thermal response tests (unit: W/(m·K)).

Elapsed time [h]	Avg	Min	Max	$\sigma$	Avg $- \sigma$	Avg $+ \sigma$
14	1.861	1.285	3.159	0.405	1.456	2.266
18	2.099	1.695	2.878	0.282	1.817	2.380
24	2.085	1.768	2.622	0.244	1.841	2.328
30	1.999	1.753	2.394	0.173	1.826	2.172
36	1.844	1.674	2.076	0.111	1.734	1.955
42	1.765	1.561	2.003	0.100	1.665	1.865
48	1.798	1.634	1.992	0.082	1.716	1.879
54	1.829	1.706	1.983	0.069	1.760	1.898
60	1.816	1.716	1.936	0.061	1.754	1.877
66	1.790	1.687	1.932	0.064	1.727	1.854
72	1.805	1.712	1.936	0.060	1.746	1.865
78	1.822	1.738	1.934	0.055	1.767	1.876
84	1.819	1.736	1.926	0.051	1.768	1.870
90	1.806	1.731	1.900	0.049	1.758	1.855
96	1.815	1.741	1.894	0.046	1.768	1.861

**Table 5.9** Average, minimum, maximum, and standard deviations of the borehole thermal resistance at different estimation times based on 36 numerical thermal response tests (unit: m·K/W).

Elapsed time [h]	Avg	Min	Max	$\sigma$	Avg $- \sigma$	Avg $+ \sigma$
14	0.164	0.138	0.197	0.012	0.152	0.176
18	0.173	0.157	0.194	0.010	0.162	0.183
24	0.173	0.158	0.193	0.010	0.162	0.183
30	0.170	0.157	0.188	0.009	0.161	0.179
36	0.167	0.156	0.180	0.007	0.160	0.173
42	0.159	0.147	0.172	0.007	0.153	0.166
48	0.160	0.150	0.172	0.006	0.154	0.166
54	0.162	0.152	0.171	0.005	0.156	0.167
60	0.165	0.156	0.174	0.005	0.160	0.170
66	0.161	0.153	0.169	0.005	0.155	0.166
72	0.160	0.152	0.170	0.005	0.155	0.166
78	0.161	0.153	0.170	0.005	0.156	0.166
84	0.164	0.156	0.174	0.005	0.159	0.169
90	0.161	0.153	0.170	0.005	0.157	0.166
96	0.160	0.153	0.168	0.005	0.156	0.165

The results described above are based on statistical analysis, and actual results can deviate more than the standard deviation (i.e., the error can be beyond the range of standard deviation) at each different time which are specified in Fig. 5.15, and Tables 5.8 and 5.9. Many researchers have discussed the minimum TRT duration required to obtain accurate estimates of the thermal properties of soil [18,90,96,98–100,146], but the results obtained in this study demonstrate that when disturbance is involved and TRT data are interpreted by a model such as the ILS model that assumes constant heat flux, the required minimum duration would increase and so would the uncertainty in estimation. Therefore, if disturbance is involved in a TRT, a longer TRT duration is highly desirable to decrease the estimation uncertainty.

## 5.5 Discussion and conclusion

In this study, a numerical model that considers disturbance in aboveground TRT setups was developed. Based on the developed numerical model, numerical TRTs were conducted using synthetic typical weather data and measured weather data and temperature response was interpreted by the ILS model, which assumes constant heat flux from the source. The results provide some suggestions on conducting TRTs and their interpretation using the ILS model.

The first suggestion is about the duration of a TRT. The early-period estimation is very unstable, and the estimation behavior becomes stable as time lapses because of the characteristics of regressive estimation. It took approximately 60 h to obtain estimated values that were within  $\pm 5\%$  of the reference case values. Therefore, if the ILS model is used for the interpretation, at least 60 h of TRT is recommended for accurate estimation.

The second suggestion is about the decision of the interpretation method to be used. If a TRT can be conducted for more than 3 days, assuming that other disturbance factors such as voltage fluctuation and accuracy of the sensors do not affect the result, the accuracy of estimation would be adequate to some extent regardless of the weather conditions. However, TRTs conducted for less than 50 h can be found in the literature and other reports. As shown in Fig. 5.11 and Fig. 5.12, if the first day of TRT is clear and strongly affected by solar irradiation, the effective thermal conductivity and borehole thermal resistance show higher values than the actual values at 50 h. In this case, interpretation using the ILS model can lead to a large amount of error. Therefore, if the first day of TRT is clear and the allowed duration of the TRT is short, an interpretation method that considers disturbance, such as the numerical model combined with the parameter estimation technique and an analytical model that considers variable heat rate, should be used.

This study also provides suggestions on the effectiveness of sequential plots generated using the ILS

model. If the disturbance effect is small, the convergence of estimation and additional information about the characteristics of heat transfer in the subsurface can be presumed from the estimation behavior of the sequential plot. However, as shown in this study, under the influence of rapidly changing disturbed heat rate, such as in the case of a clear day, those advantages cannot be utilized. To make use of the advantages of the sequential estimation using the ILS model, the disturbance should be fully controlled or, as an alternative, the interpretation method using temporal superposition-applied analytical model combined with the parameter estimation technique [116] can be used.

This study has a limitation in that some disturbance factors such as the random error of sensors and voltage fluctuation were not considered. Moreover, the impact of disturbance from the outdoor environment can vary depending on the geometry and properties of the TRT setup (circuit length, thermal conductivity of the insulation, thickness of the insulation, and radiation absorptivity) and the TRT settings (heat injection rate and flow rate); a systematic study of the sensitivity of each of these parameters was done in Section 4.4. However, the combined effect of the unaccounted disturbance factors and the disturbance from outdoor environment should be investigated in a future study as it can have a large influence on the interpretation of a TRT.



CHAPTER 6  
DEVELOPMENT OF INTERPRETATION METHOD  
CONSIDERING DISTURBANCE

## 6.1 Introduction

In Chapter 5 the disturbance effect from the outdoor environment and the resulting errors in the regressive estimations using the ILS model were examined. As shown in Chapter 5, the sequential estimation using the ILS model is very vulnerable to disturbance effects. In the early-period estimation, the disturbed temperature response showed considerable fluctuation in estimation behavior.

Other approaches can be used to deal with the variable heat rate problems in TRTs. Using the numerical method combined with the parameter estimation technique, the variable heat rate problems have been successfully dealt with in many studies [14,18,22,34,53,91–94]. The main advantage of numerical methods over analytical models is that there are fewer assumptions that need to be met to obtain results (e.g., assumptions regarding the geometry of the BHE and boundary conditions). Therefore, one can expect results with high accuracies; however, the application of numerical methods for parameter estimation incurs high computational costs because the smallest size of a cell or an element needs to be smaller than the thickness of the U-tube (generally around 3 mm). From a practical point of view, the numerical method is not an option that is always available for in-situ test conditions and during the design phase. Analytical models have an advantage over numerical methods in this regard, and that is the main reason why conventional estimation using the ILS model is still the most commonly used technique.

To consider variable heat injection rates using an analytical model, a temporal superposition applied analytical models [5] can be used. Estimation using a temporal superposition model requires recursive curve matching procedures [7,8,57,101,102,147,148] because the conventional gradient method is not applicable here. If the ground is conduction dominated, the estimated values over the TRT time can be trusted. However, if there is no a priori information about the test site or the allowed test duration is short, there is a possibility that the estimation would not be accurate because the estimating behavior cannot be known. The additional information can be provided by the stepwise sequential plot method [20,149] with the approximated ILS model. From the behavior of the sequential plot, a field engineer can know whether the estimation has converged or not and what is the dominant heat transfer process in the ground. For example, if the estimated thermal conductivity increases with time, one can infer that heat transfer is dominated by the advection effect. Because of those advantages for the conventional method, in-situ estimation using a superposition applied analytical model is not the preferred approach, although it can consider disturbance effects without high computational costs such as those associated with the numerical approach.

However, the reliability and stability of the stepwise estimation using the ILS model holds only if the constant heat injection rate assumption is met by heat rate fluctuations that are small enough to be ignored.

Therefore, to make use of the advantages of the sequential estimation using the ILS model, the constant heat rate assumption of the ILS model should be met. For stable estimation using the ILS model, some studies have approached the problem from mechanical and numerical perspectives [15,16,22]. Witte et al. [22] developed a TRT apparatus equipped with a water-to-air heat pump and a control system to maintain a constant temperature difference and flow rate. Some research groups [15,16] tried to correct disturbed heat injection rate by the inverse estimation of heat exchange rate from the outdoor environment. Their results showed a reduced difference between the measured and predicted fluid temperatures [15] and attenuated the oscillation amplitude of the sequential plot to some extent [16]. However, the effect of disturbance was still noticeable because voltage fluctuation and radiative heat transfer were not considered.

In contrast to their methods [15,16], a proposed interpretation method in this chapter considers the disturbance effects should be included as important factors for accurate estimations on the basis of a theoretical analysis of the TRT process using the analytical model, which is derived in Section 4.2. Specifically, the proposed method uses a temporal superposition applied ILS model combined with the quasi-Newton optimization method to take advantage of both the sequential estimation method and recursive estimation using superposition applied analytical models. This estimation method does not require complicated pre-processing of the TRT data, which had to be done in the previous studies [15,16]. Additionally, the proposed method can capture the behavior of the estimated values accurately, which is very important when inferring the subsurface conditions and the finish times of tests. Moreover, the proposed method significantly reduces the convergence time of estimations as compared to the conventional method. Therefore, estimations can be obtained in a very stable and fast manner.

## 6.2 Theoretical analysis: why disturbance effect should be included

A theoretical analysis was used to evaluate the disturbance factors that can impact TRT results and to obtain insight into appropriate interpretation methods that can enhance estimation accuracy. The analysis in this section is based on the disturbance-considering analytical model (Eqs. (4.6) and (4.8)) which was derived in Section 4.2. The derived analytical equations are provided here again for the analysis.

The temperature perturbation in the outflow circuit is described in Eq. (4.6).

$$T_{cf,out,rig}(t) = T_{cf,out,BHE}(t)e^{-\kappa_{out}(t)} + T_{sol,a}(t)(1 - e^{-\kappa_{out}(t)}) \quad (4.6)$$

The temperature perturbation in the inflow circuit is described in Eq. (4.8).

$$T_{cf,in,BHE}(t) = T_{cf,in,rig}(t)e^{-\kappa_{in}(t)} + T_{sol,a}(t)(1 - e^{-\kappa_{in}(t)}) \quad (4.8)$$

where

$$\frac{L}{\rho_{cf}c_{cf}\dot{V}_{cf}R_{tot}(t)} = \kappa(t) \quad (4.5)$$

When the dimensionless parameter  $\kappa$  converges to 0, there is no heat exchange in the hydraulic circuit above the ground. This means  $T_{cf,out,BHE}(t) = T_{cf,out,rig}(t)$  and  $T_{cf,in,rig}(t) = T_{cf,in,BHE}(t)$  (refer to Fig. 4.1). The conditions for  $\kappa = 0$  are: (1) the length of hydraulic circuit  $L \rightarrow 0$ , (2) the volumetric flow rate  $\dot{V}_{cf} \rightarrow \infty$ , and (3) the overall thermal resistance  $R_{tot} \rightarrow \infty$ . However, meeting these conditions is almost impossible.

The derived form of analytical model is very similar to the models used in two other studies [15,16] where the researchers tried to eliminate the influence from the outdoor environment. Those studies estimated  $R_{tot}$  and used these values to eliminate the disturbed heat exchange rate from the measured heat injection rate. However, explicit and accurate estimation of  $R_{tot}$  is a very hard task. As described in Section 4.2, there is heat conduction through the pipe and insulating material, and heat convection depends on the continuously varying wind speed, short and long wave radiation, and evaporative latent heat exchange. For the calculation of  $R_{tot}$ , the information about the many continuously varying parameters related to each heat transfer process should be known. Because of this difficulty, the authors of the two studies [15,16] estimated  $R_{tot}$  through the iterative regression method, and this should be estimated at the time of each TRT. In addition, there are drawbacks to the method used in the previous studies [15,16]. Specifically, their model cannot consider the effect from voltage fluctuations, which is not predictable, and their model does not consider radiative heat transfer, which can be the most critical factor during day time fluctuations of the fluid temperature. Moreover,  $R_{tot}$  is considered as a constant coefficient even though it is continuously changing over the TRT period. Consequently, the oscillation amplitude of the sequential plot [20,149], which is also known as the stepwise interval plot from the work of Bandos et al. [16] (see Fig. 4 in [16]), is attenuated but still oscillating in the range of 0.2 W/(m·K). In the work of Roth et al. [15], the disturbance corrected temperature response curve (see Fig. 8 in [15]) does not overlap neatly with the measured temperature data.

In fact, the actual heat injection rate  $Q_{BHE}$  can be measured using Eq. (6.1) if the temperature sensor is close to the ground surface level.

$$Q_{BHE} = \rho_{cf} c_{cf} \dot{V}_{cf} (T_{cf,in,BHE} - T_{cf,out,BHE}) \quad (6.1)$$

This is also important to reduce disturbance effects from the external environment, as some researchers have suggested [22,72,149].  $Q_{BHE}$  contains all the disturbance factors  $Q_{d,tot}$  and the voltage fluctuation from the electrical grid. This means the temperature response corresponding to the variable heat injection rate  $Q_{BHE}$  can be known. Therefore, the simpler but more accurate way of estimation is to use a temperature response model that can consider the variable heat injection rate, not via excluding the disturbance effects by use of a model that assumes a constant heat injection rate. The temporal superposition applied analytical models can be used to consider the disturbance factors in this manner. As described in Section 6.1, to obtain the estimation behavior, a temporal superposition applied ILS model combined with the quasi-Newton method was used. This is described in further detail in the next section.

## 6.3 Development of disturbance-considered interpretation method

### 6.3.1 Infinite line source model with temporal superposition principle

In this study, the TRT data were interpreted on the basis of the ILS model [9]. The ILS model was already provided in Eq. (2.44) with respect to the average temperature of the circulating fluid. By substituting  $q_{avg}$  and  $\lambda_{eff}$  into  $q_0$  and  $\lambda_s$ , respectively, following form is obtained.

$$\bar{T}_{cf}(t) = \frac{q_{avg}}{4\pi\lambda_{eff}} \text{Ei}\left(\frac{C_s r_b^2}{4\lambda_{eff} t}\right) + R_b \cdot q_{avg} + T_0 \quad (6.2)$$

The exponential approximated ILS model was provided in Eqs. (2.46) and (5.23). It is provided here again:

$$\bar{T}_{cf}(t) = \frac{q_{avg}}{4\pi\lambda_{eff}} \ln(t) + \frac{q_{avg}}{4\pi\lambda_{eff}} \left\{ \ln\left(\frac{4\lambda_{eff}}{C_s r_b^2}\right) - \gamma \right\} + R_b \cdot q_{avg} + T_0 \quad (6.3)$$

The Eq. (6.3) was used to conduct stepwise regressive estimations using the least squares method, as did in Chapter 5. The first 15 h of temperature response data were not included in the estimation on the basis of the time criterion  $t \geq 5r_b^2/\alpha_s$ . After estimating the effective thermal conductivity of the ground, the effective borehole thermal resistance  $R_b$  was estimated from Eq. (6.3).

In conventional estimations using the ILS model, it has been customary to adopt the averaged heat injection rate  $q_{avg}$  as an input parameter for the estimation using the ILS model (Eq. (6.3)); however, this method cannot eliminate or account for disturbance effects. To overcome this drawback, with practical and applicability issues in mind as stated in Chapter 6.1, the temporal superposition applied ILS model [5] was selected to conduct parameter estimations.

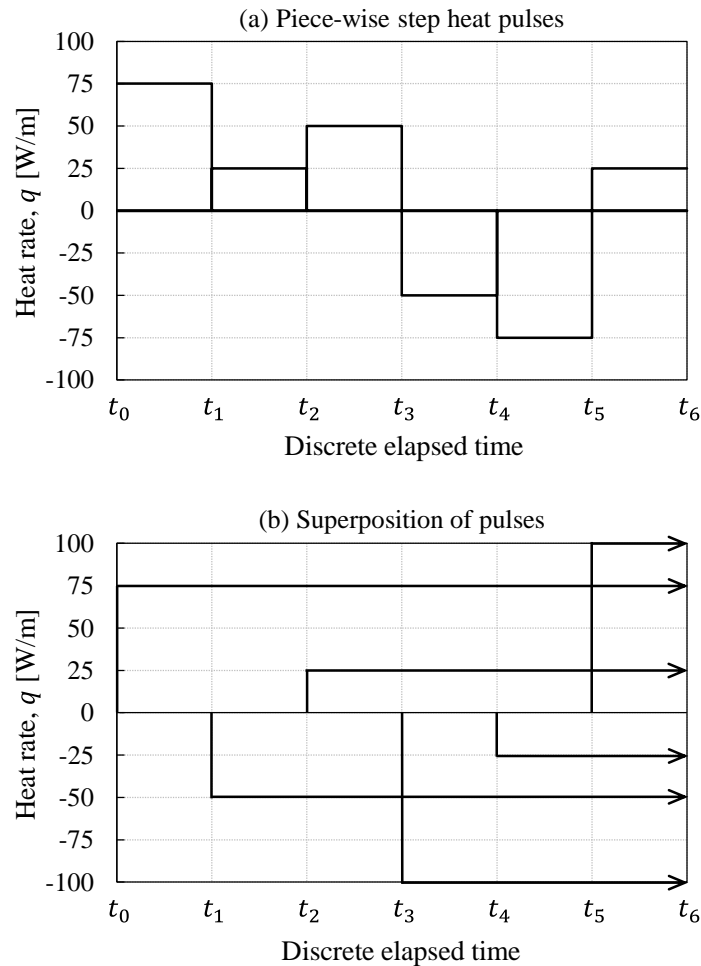


**Fig. 6.1** Temporal superposition of heat pulses.

The temporal superposition technique has been used in similar engineering fields such as in geothermal power plant applications to determine the true formation temperature or in well tests for the petroleum industry [150,151]. For shallow geothermal applications, Eskilson [11] was the first who considered applying a temporal superposition based on Duhamel's theorem [152] to consider variable heat injection rates. Eklöf and Gehlin [5] and other research groups [65,153] also referred to Eskilson's methodology

when handling variable heat injection rates. The same methodology was used to handle the variable heat injection rate in the ILS model. In particular, the variable heat injection rate was regarded as piece-wise constant square pulses. Then, the heat pulses, which were subdivided into  $N$  different intervals, were superimposed to obtain a temperature response corresponding to the variable heat rate (Fig. 6.1). The ILS solution for considering a variable heat rate is as follows:

$$\bar{T}_{cf,cal}(t) = \sum_{n=1}^N \frac{q_n - q_{n-1}}{4\pi\lambda_{eff}} \text{Ei}\left(\frac{C_s r_b^2}{4\lambda_{eff}(t_N - t_{n-1})}\right) + R_b \cdot q_N + T_0 \quad (6.4)$$

### 6.3.2 Parameter estimation using quasi-Newton method

Many previous studies [7,14,154] used the downhill Simplex (hereafter Simplex) algorithm [155] for parameter estimation. Simplex is a sort of heuristic based optimization algorithm that is numerically very simple and free to adapt to any optimization landscape; it can even be applied for rugged and discontinuous functions. However, Simplex is not the appropriate algorithm for this study, and this will be discussed further in the end of this section.

#### • The quasi-Newton method

In this study, the quasi-Newton optimization method was used to inversely estimate the borehole thermal resistance  $R_b$  and the effective thermal conductivity of the soil  $\lambda_{eff}$ . This method approximates the Hessian (i.e., second derivatives of the objective function) at each iteration to determine the search direction using only the gradient of the objective function, rather than solving the Hessian precisely. Although the quasi-Newton method approximates the Hessian, which can sometimes involve cumbersome and expensive computations, it mimics the true properties of the true Hessian and yet still attains a superlinear rate of convergence [156]. In particular, the Broyden–Fletcher–Goldfarb–Shanno (BFGS) method [157–160] was used to approximate the Hessian. Detailed information about the quasi-Newton method can be found in [156].

The first step of an inverse problem is the definition of an objective function. This function should then be minimized in the inverse problem:

$$f_{obj} = f(\mathbf{P}); \quad \mathbf{P} = \{P_1, P_2, \dots, P_N\} \quad (6.5)$$

where  $\mathbf{P}$  is the parameter vector of the problem. Although, in this study, the parameter vector  $\mathbf{P}$  is composed of only two elements,  $\lambda_{eff}$  and  $R_b$ , the following description assumes a general form such as

$\mathbf{P} = \{P_1, P_2, \dots, P_N\}$ . The objective function  $f_{obj}$  in this study is the minimization of fluid temperature difference between the experimentally obtained temperature  $\bar{T}_{cf,exp}$  and the calculated temperature  $\bar{T}_{cf,cal}$  which is given by Eq. (6.4).

One can explain the quasi-Newton method in a simple manner by beginning with the Newton–Raphson method. If the objective function  $f(\mathbf{P})$  is smooth and at least twice differentiable, then the second-order Taylor expansion of  $f(\mathbf{P})$  around  $d$  is given by

$$f(\mathbf{P} + d) \approx f(\mathbf{P}) + \nabla f(\mathbf{P})^T d + \frac{1}{2} (d)^T \mathbf{H}(\mathbf{P}) d \quad (6.6)$$

where  $(\cdot)^T$  is the transpose and  $\mathbf{H}$  is the Hessian matrix defined as the second derivatives of  $f(\mathbf{P})$ :

$$\mathbf{H}(P_i) = \nabla^2 f(P_i) = \begin{pmatrix} \frac{\partial^2 f}{\partial P_1^2} & \dots & \frac{\partial^2 f}{\partial P_1 \partial P_n} \\ \vdots & \ddots & \vdots \\ \frac{\partial^2 f}{\partial P_n \partial P_1} & \dots & \frac{\partial^2 f}{\partial P_n^2} \end{pmatrix} \quad (6.7)$$

If the Hessian is positive definite, then the Newton direction can be found. By taking the gradient of Eq. (6.7) with respect to  $d$ , the following equation is obtained:

$$\nabla f(\mathbf{P} + d) \approx \nabla f(\mathbf{P}) + \mathbf{H}(\mathbf{P}) d \quad (6.8)$$

The optimum can be obtained when the left-hand side of Eq. (6.8) is equal to zero. Based on this, Eq. (6.8) is re-written with respect to  $d$  as follows:

$$d = -[\mathbf{H}(\mathbf{P})]^{-1} \nabla f(\mathbf{P}) \quad (6.9)$$

where  $d$  is known as the Newton direction.

The nonlinear minimization problem using the iterative search procedure can be written in the general form as:

$$\mathbf{P}^{k+1} = \mathbf{P}^k + \alpha^k \mathbf{d}^k \quad (6.10)$$

where  $k$  is the iteration index and  $\alpha$  is the search step size chosen to satisfy the Wolfe conditions [156,161,162].

Eq. (6.9) can be re-written in the following iterative form:

$$\mathbf{d}^{k+1} = -[\mathbf{H}(\mathbf{P}^k)]^{-1}\nabla f(\mathbf{P}^k) \quad (6.11)$$

The quasi-Newton method is very similar to the Newton method, but the former approximates the Hessian only using first-order derivatives. Now a new matrix  $\mathbf{B}$ , which is inverse of the Hessian is defined:

$$\mathbf{B}^k = [\nabla^2 f(\mathbf{P}^k)]^{-1} \quad (6.12)$$

Eq. (6.11), which describes the search direction, can be re-written using Eq. (6.12) as

$$\mathbf{d}^{k+1} = -\mathbf{B}^k \nabla f(\mathbf{P}^k) \quad (6.13)$$

Matrix  $\mathbf{B}$  is iteratively calculated as

$$\mathbf{B}^k = \mathbf{B}^{k-1} + \mathbf{M}^{k-1} + \mathbf{N}^{k-1} \quad (6.14)$$

At the first iteration ( $k=0$ ),  $\mathbf{B}^0$  is the identity matrix (e.g.,  $\mathbf{B}^0 = \mathbf{I}$ ). Therefore, the quasi-Newton method is exactly the same as the steepest descent method at its first iteration.

One of the most frequently used methods for the approximation of the Hessian is the BFGS method [157–160], which is defined by

$$\mathbf{M}^{k-1} = \left( \frac{1 + (\mathbf{Y}^{k-1})^T \mathbf{B}^{k-1} \mathbf{Y}^{k-1}}{(\mathbf{Y}^{k-1})^T \mathbf{d}^{k-1}} \right) \frac{\mathbf{d}^{k-1} (\mathbf{d}^{k-1})^T}{(\mathbf{d}^{k-1})^T \mathbf{Y}^{k-1}} \quad (6.15)$$

$$\mathbf{N}^{k-1} = \frac{\mathbf{d}^{k-1} (\mathbf{Y}^{k-1})^T \mathbf{B}^{k-1} + \mathbf{B}^{k-1} \mathbf{Y}^{k-1} (\mathbf{d}^{k-1})^T}{(\mathbf{Y}^{k-1})^T \mathbf{d}^{k-1}} \quad (6.16)$$

$$\mathbf{Y}^{k-1} = \nabla f(\mathbf{P}^k) - \nabla f(\mathbf{P}^{k-1}) \quad (6.17)$$

The iteration procedure is continued until the convergence criteria are satisfied. The following three conditions are generally used for the convergence criteria: (1) Does the iteration reach the maximum number of the iterations? (2) Does  $f(\mathbf{P}^k)$  reach the pre-defined tolerance? (3) Does  $\nabla f(\mathbf{P}^k)$  reach the pre-defined value? In this work, the following convergence criteria were used: (1) maximum iterations of 1000 and (2)  $f(\mathbf{P}^k) < 10^{-5}$  (Eq. (6.18)). However, criterion (1) was never used because in most of the estimations, the number of iterations was less than 10.

The calculation flow of the quasi-Newton method is described in Fig. 6.2.

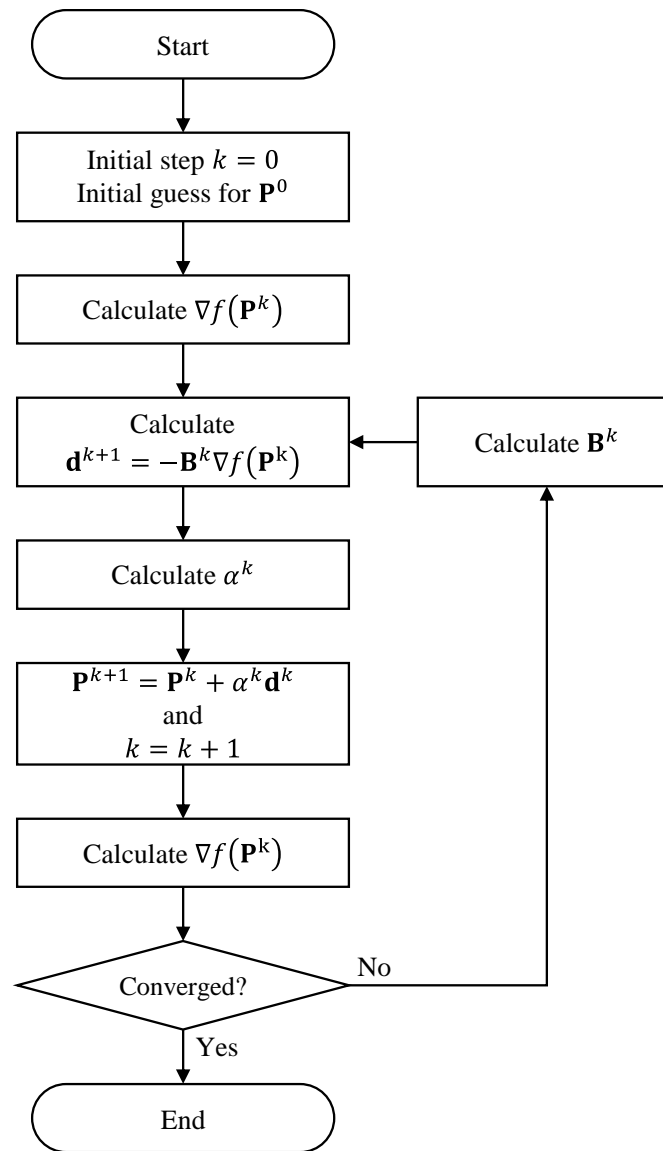


**Fig. 6.2** Calculation flow of the quasi-Newton method.

#### • Comparison between the quasi-Newton method and Nelder-Mead Simplex method

Unlike the recursive curve fitting method used for the whole test period for only one solution, or sequential estimation involving the addition of one measurement after another, the developed estimation program was executed for each time step using only measured temperature data at a particular time step and given history of heat fluxes. This method is pure estimation; as such, each result is not affected by the error from the previous result, which is the case for the linear regression method. Therefore, the behavior of the estimated parameters caused by the formation conditions (e.g., increasing in the presence of

groundwater flow or natural convection) could be more accurately and instantly reflected in the estimation results than in the sequential estimation.

The logic of the parameter estimation is described in Fig. 6.3. The estimation stopped when the squared difference between the calculated temperature  $\bar{T}_{cf,cal}$  and the experimental temperature  $\bar{T}_{cf,exp}$  became less than  $10^{-5}$  for each discrete time step. The objective function is defined as follows:

$$\min f_{obj}(\lambda_{eff}, R_b) = \left( \bar{T}_{cf,exp} - \bar{T}_{cf,cal}(\lambda_{eff}, R_b) \right)^2 \leq 10^{-5} \quad (6.18)$$

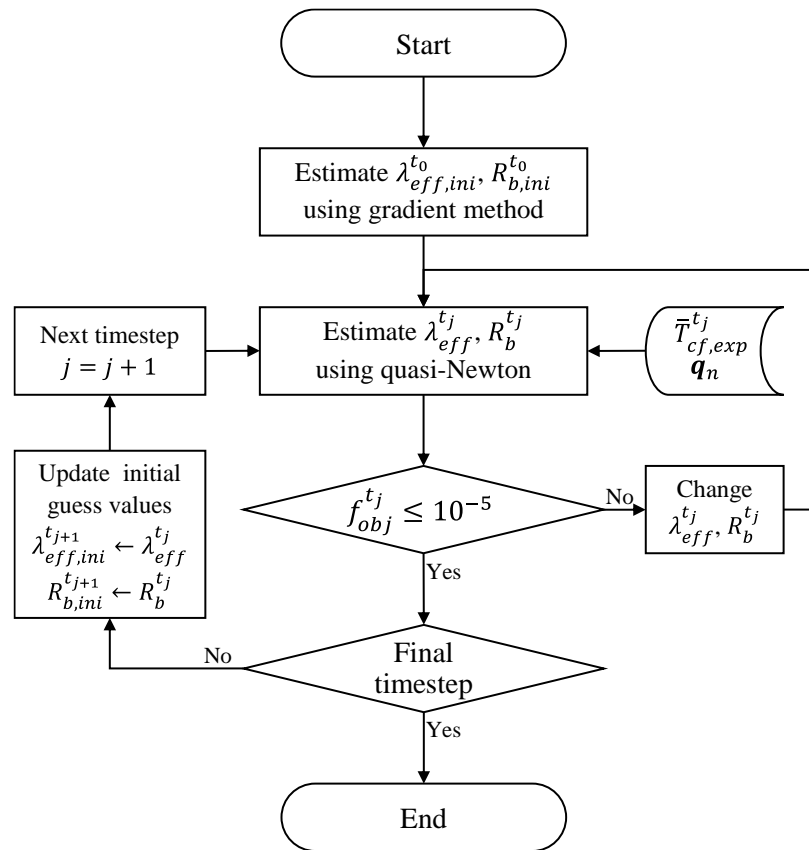


**Fig. 6.3** Flow chart of the parameter estimation.

The rate of convergence and estimated values are dependent on the initial guess values because the parameter estimation is an ill-posed inverse problem that has non-unique solutions. To start searching with good initial values, the estimated values from the conventional gradient method were implemented as the initial values. These values were used only for the first search. From the second time step on, the initial guess values were updated from the estimated values for the previous time step (Fig. 6.3). The lower and upper bounds for the searching were also varied with each time step based on the previous estimated values

as follows:  $[\lambda_{eff} \pm 0.5 \text{ W}/(\text{m}\cdot\text{K})]$  and  $[R_b \pm 0.05 \text{ m}\cdot\text{K}/\text{W}]$ . The first 15 h of experimental data were not included for the estimation because the ILS solution cannot accurately predict the temperature response during this early period.

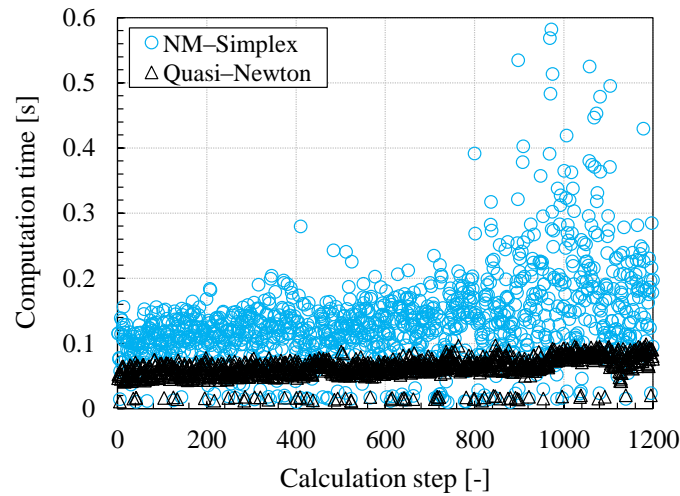


**Fig. 6.4** Comparison of the computation time between the downhill Simplex method and quasi-Newton method.

Returning to the Simplex algorithm, there are several reasons why this is not an appropriate method for this estimation method. First, the randomness of the initial values is an issue. In Simplex, three vertices should be assigned. One vertex can be fixed exactly in the same manner as applied to the quasi-Newton method described above. However, the other two vertices are assigned randomly. Because the inverse estimation is highly ill-posed, this randomness results in oscillating estimation behavior for many combinations. Considering that one important objective of this study is to provide additional information from the sequential estimation, this is a critical drawback. This matter can be resolved by using the quasi-Newton method with simple modifications, that is, by updating the initial guess values from the previous solution as described in the above paragraph and Fig. 6.3. By using this updating scheme, the estimation behavior is stabilized and the estimation speed becomes faster because the initial guess values are already in a very close proximity to the solution.

Second, the Simplex method requires longer computation times than the quasi-Newton method because of its heuristic nature. Although the robustness is one of the advantages of Simplex, in this study, the optimization landscape of the objective function is already known. Therefore, the solution can be obtained in a very fast manner with the initial guess values close to the solution and the gradient based search method. In contrast, in the case of the Simplex method, the computation time can be very long even if the

problem is simple, and sometimes, the model will not converge because of its heuristic nature. Trial calculations of 1200 time steps (6 min intervals) were conducted using the TRT data from GR4, which is described in Section 6.4. All the calculation conditions were exactly the same as those described in this section. An initial values update scheme was also applied to the Simplex method and the number of iterations was limited to 1000. As shown in Fig. 6.4, compared to the stable and short computation time of the quasi-Newton method, the Simplex method needed a longer calculation time and the results were distributed over a wide range. Moreover, convergence was not achieved in three time steps with the Simplex method. These time steps took 10–13 s; such data are not included in Fig. 6.4 for clarity. The total computation times were 197.4 s and 76.0 s for the Simplex and quasi-Newton methods, respectively (CPU: dual core 1.8 GHz, RAM: 8 GB). Through the analysis described above, the quasi-Newton method was selected for parameter estimation.

### 6.3.3 Sensitivity analysis of parameter estimation

In an inverse problem, a sensitivity analysis provides information about whether the estimation can be performed successfully and provides a strategy for solving a problem [85,87]. For a multi-parameter estimation in particular, information on the sensitivity of each parameter provides insight into how to solve an inverse problem. In a transient heat transfer problem, the interdependence between the parameters should be examined. If a strong linear dependence exists among the sensitivity coefficients, simultaneous estimation is impossible. In this study, the sensitivity coefficients were defined using the first partial derivative of the dependent variable  $\bar{T}_{cf}$  with respect to parameter  $P_i$ , as expressed by the following general equation form:

$$SC_i = \frac{\partial \bar{T}_{cf}(\mathbf{P})}{\partial P_i} \quad (6.19)$$

In the case of an analytical solution, equations for the sensitivity coefficients can be obtained explicitly, but sometimes these can have complex forms. As an alternative, the sensitivity coefficients can be obtained by numerical approximation of the partial derivatives. Using the forward difference, Eq. (6.19) can be rewritten as follows:

$$SC_i \approx \lim_{\Delta P_i \rightarrow 0} \frac{\bar{T}_{cf}(P_1, P_2, \dots, P_i + \Delta P_i, \dots, P_N) - \bar{T}_{cf}(P_1, P_2, \dots, P_N)}{\Delta P_i} \quad (6.20)$$

where  $SC_i$  is the sensitivity coefficient of the  $i$ -th parameter  $P_i$ .

A large sensitivity coefficient is desirable in an inverse problem. A small sensitivity coefficient indicates that large changes in the parameter  $P_i$  yield small changes in the dependent variable  $\bar{T}_{cf}$ . In such a case, accurate estimation of the parameter is very difficult because almost equal values of the dependent variable can be obtained for a wide range of parameter values [87]. This means that the inverse problem is very ill-conditioned.

The results of Eq. (6.20) have different units and orders of magnitude for each parameter. Therefore, comparison of these coefficients is difficult. If each sensitivity coefficient is multiplied by its parameter, the resulting relative sensitivity coefficient  $RSC$  can be used to compare different sensitivity coefficients:

$$RSC_i = SC_i \cdot P_i \quad (6.21)$$

Substituting the values  $q_{avg} = 50 \text{ W/m}$ ,  $\lambda_{eff} = 1.8 \text{ W/(m}\cdot\text{K)}$ ,  $R_b = 0.17 \text{ m}\cdot\text{K/W}$ , and  $T_0 = 17 \text{ }^\circ\text{C}$  into the ILS model, the transient  $RSC$  values with respect to  $\lambda_{eff}$  and  $R_b$  were calculated and are shown in Fig. 6.5. The absolute magnitude of the  $RSC$  of  $\lambda_{eff}$  increases with time, whereas the  $RSC$  of  $R_b$  does not change over time. This can be intuited from the first derivative of the ILS model Eq. (6.3) with respect to  $R_b$ . Therefore, the behaviors of  $RSC$  of  $\lambda_{eff}$  and  $R_b$  are linearly independent, and therefore, simultaneous estimation of the two parameters is possible. Moreover, the increase in the magnitude of the  $RSC$  of  $\lambda_{eff}$  over time indicates that the estimation of  $\lambda_{eff}$  becomes more accurate over time. The change in the  $RSC$  also provides insight into the impact of each parameter on the heat transfer between the BHE and the ground. Compared with the  $RSC$  of  $\lambda_{eff}$ , that of  $R_b$  becomes relatively small with time, meaning that  $R_b$  has less impact than  $\lambda_{eff}$  on the long-term performance of a GSHP.

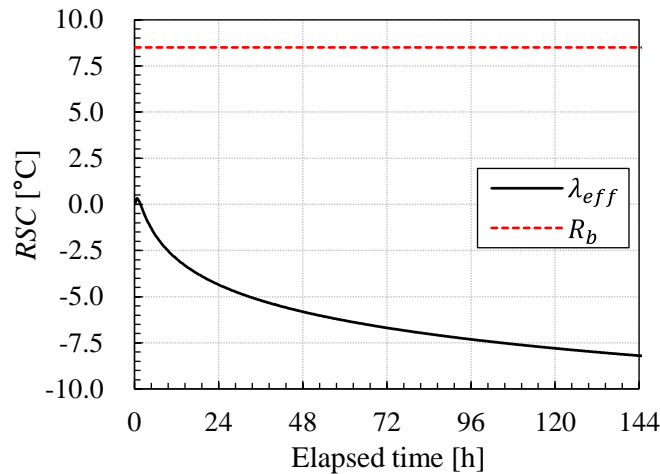


**Fig. 6.5** Relative sensitivity coefficients of effective thermal conductivity and borehole thermal resistance.

## 6.4 Thermal response test

### 6.4.1 Test conditions

The experimental conditions are described in Table 6.1. The TRTs were conducted twice using the 2 kW and 4 kW heaters. To verify the thermal behavior of the BHE and obtain reliable results, the experiments were continued for a relatively long period (140 h). The flow rate was set to about 20 L/min, but it increased as the temperature of the circulating fluid increased. The increasing flow rate was due to the decrease in the viscosity of water with increasing temperature. The maximum and minimum values of the actual heat injection rate are estimated values from 1–140 h; the heat injection rate increased gradually from near 0 kW right after the heater was turned on. Although the range of  $Q_{BHE}$  was wider in GR4 than GR2, from the standard deviation and the averaged value (Table 6.1), the relative fluctuations of GR2 were bigger than those of GR4 during the tests. The standard deviations correspond to 1.37% and 1.81% of the averaged  $Q_{BHE}$  for GR4 and GR2, respectively. The T-type thermocouples installed in the BHEs and the observation well measured an initial ground temperature in the range 16–17 °C below 10 m depth. However, there was seasonal temperature variation above 10 m depth. In this study, the initial ground temperature was set to 17 °C. The given heat injection and flow rates correspond to values averaged over the heat injection period (Table 6.1). Once a test was finished, the following test was started after confirming that the ground temperature had returned to the initial value. It took about 40 days for the ground to return to baseline values when a test was conducted for 140 hours using a 4 kW heater. For the test using a 2 kW heater, the recovery time was about 25 days.

**Table 6.1** Experimental conditions for the two thermal response tests (TRTs).

Test name [BHE-Heater]	Heat injection starting time [YYYY/MM/DD/hh:mm]	Duration [h]	$\dot{V}_{cf}$ [L/min]	$Q_{BHE}$ [kW] (W/m)	Max, min of $Q_{BHE}$ [kW]	$\sigma$ of $Q_{BHE}$ [kW]
GR4	2014/03/25/15:40	140	21.9	4.22 ( $\approx$ 84)	4.39, 4.05	0.058
GR2	2014/05/15/22:00	140	19.8	2.32 ( $\approx$ 46)	2.46, 2.22	0.042

### 6.4.2 Temperature response

The average circulating water temperature, heat injection rate, and outdoor dry-bulb temperature of the two tests are shown in Fig. 6.6(a) and Fig. 6.7(a). Please note that data for the outdoor dry-bulb temperatures around 0 h and 30 h in GR4 (in Fig. 6.6(a)) were missing because of a sensor failure. The GR4 test was conducted during winter-like conditions in March when the diurnal temperature amplitude is typically narrower and the solar irradiation is lower than other seasons. Therefore, there was little

disturbance from the external environment and the temperature response curve was smooth without distinct low frequency oscillations due to the interaction with the outdoor environment (Fig. 6.6(a)). On the contrary, the GR2 test was conducted during the spring season when the diurnal temperature amplitude is wider. In addition, as examined in Section 4.3.2, when the generated heat in the TRT apparatus  $Q_{rig}$  is small, the disturbance rate becomes larger. Hence, the effect from the external environment can be clearly seen in the temperature response and the actual heat injection rate (Fig. 6.7(a)). The distinct coupling effect from the outside environment shown in GR2 was not only caused by the weather differences but also by the relative influence of the heat exchange rate. Supposing that the heat exchange rate from the external environment was the same, the relative influence was bigger in GR2, which used a 2 kW heater, than in GR4, which used a 4 kW heater. The disturbance from the external environment is clear in the semi-logarithm plot (Fig. 6.6(b) and Fig. 6.7(b)). In GR4, the temperature response was almost perfectly overlapped with the linear regression line using the data from 15 h (red dotted line in Fig. 6.6(b)). In contrast to the good overlap in GR4, the semi-logarithm plot of GR2 fluctuated along the regression line (Fig. 6.7(b)). The effect of disturbances when using the conventional estimation method is discussed in following section.

#### 6.4.3 Developed parameter estimation method versus conventional regression method

When interpreting TRT data, the sequential plot method is frequently used [20,149] because the behavior of estimated values over time can be seen. One can therefore decide the appropriate finish time of the TRT or presume the advection effect from the groundwater flow from the trend of the estimated values. In this study, the sequential plot method was used to compare the results with those from the proposed estimation method. The sequential estimation was conducted using instantaneous temperature data at 3 min intervals and the averaged heat injection rate. The developed estimation method was conducted using the instantaneous temperature data at 6 min intervals and 6 min averaged heat pulses. In the developed method, although the effective thermal conductivity and borehole thermal resistance were obtained every 6 min, these data are shown at 1 h intervals for clarity (Fig. 6.8 and Fig. 6.9). The results are presented starting at 20 h even though both methods started estimations at 15 h because large fluctuations occurred during early-time estimations using the sequential method (to see all of the estimated data, please refer to the supplementary interactive plot data). For the conciseness of the descriptions, hereafter the abbreviations GR4-PE, GR4-Seq, GR2-PE, and GR2-Seq are used, which stand for the “experiment name-estimation method.”

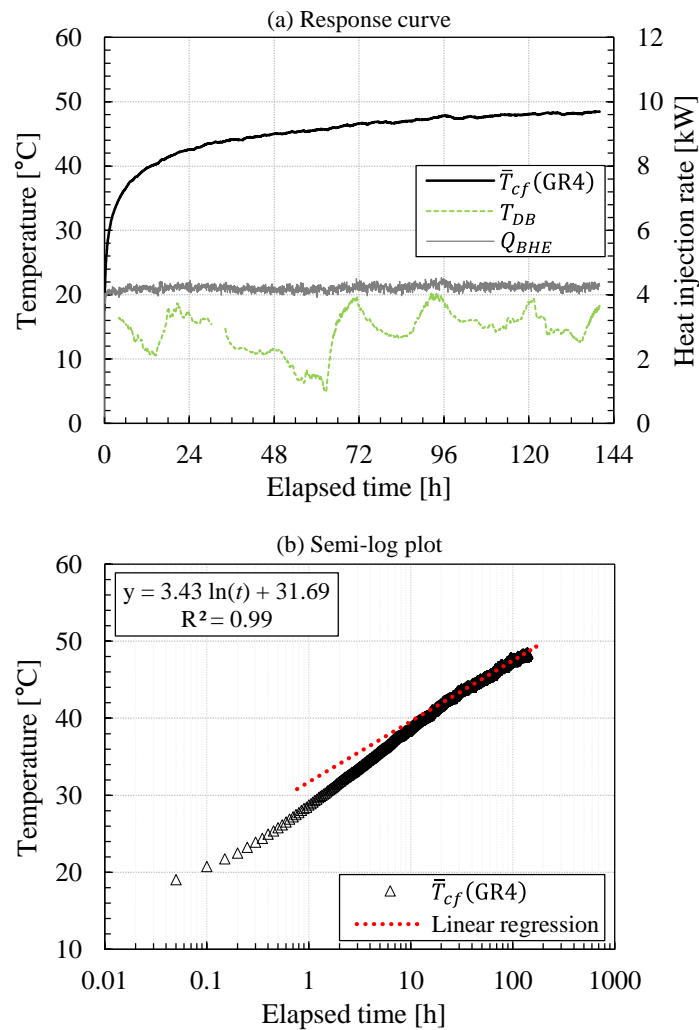


**Fig. 6.6** Temperature response from GR4 showing the (a) average fluid temperature, heat injection rate, and outdoor dry-bulb temperature and (b) semi-logarithm plot of the average water temperature.

The estimated results from the data of GR4 and GR2 are shown in Fig. 6.8 and Fig. 6.9, respectively. In GR4-Seq, the estimated  $\lambda_{eff}$  and  $R_b$  converged around  $t = 60$  h (Fig. 6.8). No distinct fluctuations in the data of GR4-Seq were observed because GR4 had little influence from the external environment. However, the results imply that at least 60 h are needed to obtain reliable estimations using the conventional method. In GR4-PE, the estimated values were already close to the final values around  $t = 20$  h. The estimated  $\lambda_{eff}$  and  $R_b$  at 20 h were 0.058 W/(m-K) lower and 0.003 m-K/W higher than those at 140 h.

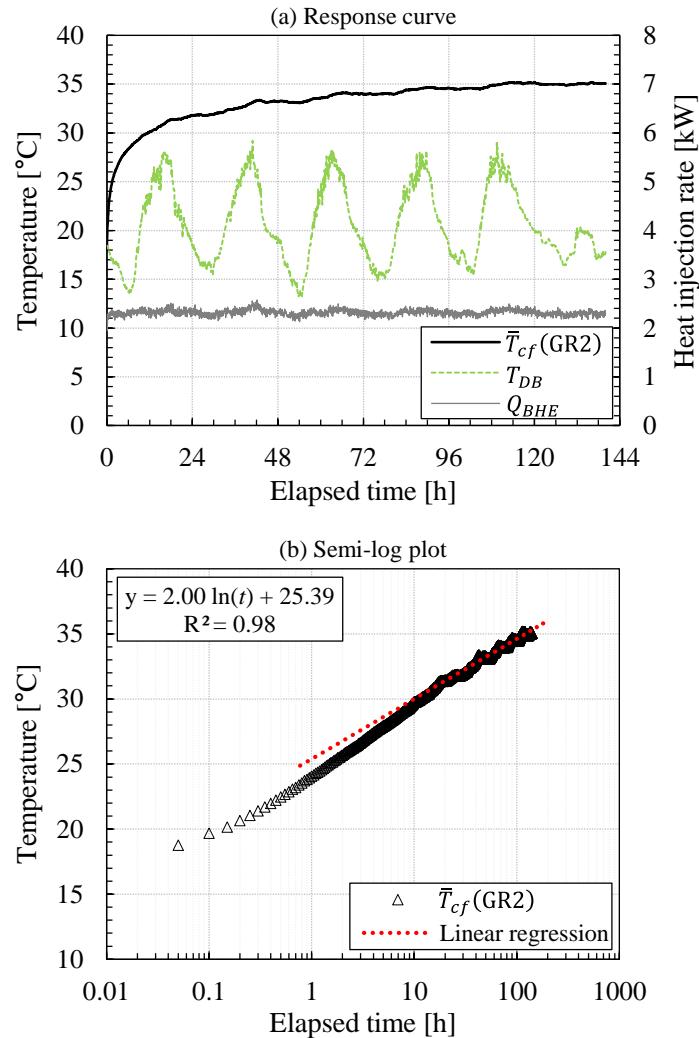


**Fig. 6.7** Temperature response from GR2 showing the (a) average fluid temperature, heat injection rate, and outdoor dry-bulb temperature and (b) semi-logarithm plot of the average water temperature.

In contrast with the stable results of GR4-Seq, the results of GR2-Seq kept oscillating constantly (Fig. 6.9). The amplitude of oscillation before 40 h was especially large and the oscillating trend was observed until the end of the test time. The main cause of this phenomenon is heat exchange with the external environment because the oscillating cycle exactly coincides with the diurnal variation cycle of the outdoor environment. When the sequential estimation does not converge with an oscillating trend, an engineer cannot confidently decide whether the test has been run long enough to finish or not. Compared to GR2-Seq, the estimating trend of GR2-PE was very stable (Fig. 6.9). As observed in GR4-PE, GR2-PE also converged during a very early time point of the test and the differences between the earlier values and the values at the final hour were marginal. The estimated  $\lambda_{eff}$  and  $R_b$  at 20 h were 0.015 W/(m·K) and 0.003

m·K/W lower than those at 140 h. Despite the large and constant fluctuation of the GR2-Seq, the absolute difference for the estimated values between GR2-Seq and GR2-PE at the final hour were small ( $\Delta\lambda_{eff} = 0.008 \text{ W}/(\text{m}\cdot\text{K})$ ,  $\Delta R_b = 0.003 \text{ m}\cdot\text{K}/\text{W}$ ). The sensitivity to the disturbance effect decreased as the test time increased. This can be seen in Fig. 6.9, which shows the attenuating amplitude of the oscillation with time. This result is similar to that obtained by Florides and Kalogirou [17] who stated that the combined disturbance effect is negligible as the increment of fluid temperature almost reaches steady state. However, it should be noted that a 140 h TRT is rarely conducted in practice.

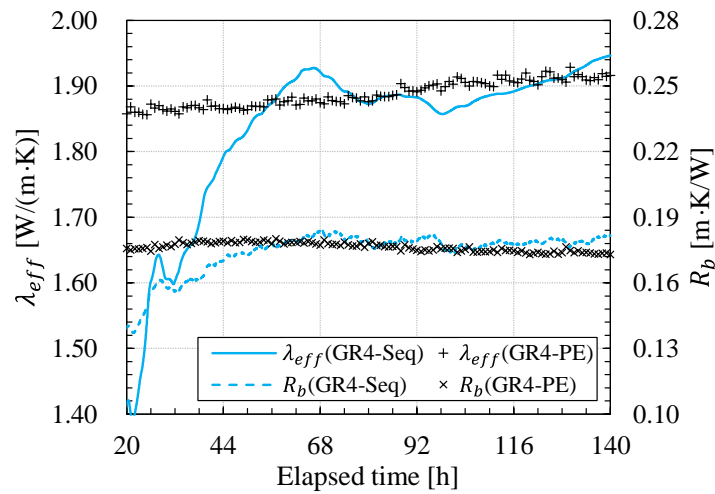


**Fig. 6.8** Estimated effective thermal conductivity and borehole thermal resistance of GR4 using the sequential method (GR4-Seq) and the developed parameter estimation method (GR4-PE).

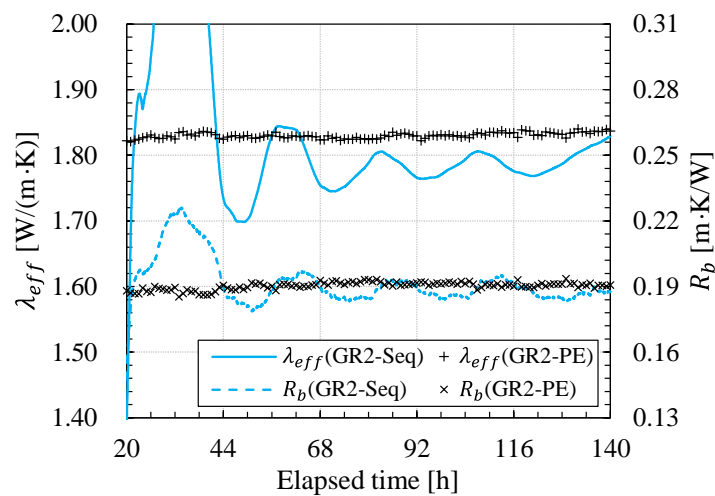


**Fig. 6.9** Estimated effective thermal conductivity and borehole thermal resistance from GR2 using the sequential method (GR2-Seq) and the developed parameter estimation method (GR2-PE).

The final estimated values, the maximum and minimum values, and the standard deviations from each of the estimation methods using the estimated values from 17–140 h are summarized in Table 6.2. Although the estimation was started at 15 h, the estimated values before 17 h were not included here because of a large fluctuation during this early timeframe that was caused by not having enough data for the regression estimation (e.g., the estimation at 17 h represents a regression using only 40 data points). Additionally, it should be noted that the standard deviations of the estimated values in Table 6.2 are based on the final estimated values (estimated at 140 h) rather than averaged values. The standard deviation used for the estimated values is defined as follows:

$$\sigma = \sqrt{\frac{1}{N-2} \sum_{j=1}^{N-1} [P_i(t_j) - P_i(t_f)]^2} \quad (6.22)$$

where  $P_i(t_j)$  is the estimated parameter at the time step  $t_j$ ,  $N$  is the number of estimations, and  $t_f$  is the final time step of the estimation.

With the maximum and minimum estimated values, the stability of the developed method can be evaluated. In the case of sequential estimation, the estimation ranges (maximum value – minimum value) of  $\lambda_{eff}$  and  $R_b$  were very wide. The  $\lambda_{eff}$  and  $R_b$  ranges were 0.74 W/(m·K) and 0.070 m·K/W for GR4-Seq, and 1.56 W/(m·K) and 0.152 m·K/W for GR2-Seq, respectively. Because of the disturbance effect, GR2-Seq showed the widest estimation range, whereas the developed method showed much narrower estimation ranges. These were 0.07 W/(m·K) and 0.007 m·K/W for GR4-PE, and 0.02 W/(m·K) and 0.009 m·K/W for GR2-PE, respectively. Of course, these differences in the estimation ranges were directly connected to the standard deviations.

The standard deviation was divided into two time intervals: 17–70 h and 17–140 h. The former would be a useful index because a TRT is conducted for three days in general practice. This is why two standard deviations of different time intervals are presented. The standard deviations from the regression method (GR4-Seq, GR2-Seq) were much larger than those from the developed method (GR4-PE, GR2-PE) because of the instability of early time estimations, which was caused by the small number of data points and the disturbance effect. As mentioned previously, the estimation instability of the regression method attenuated with time. It can be seen that the standard deviations of 17–70 h were higher than those of 17–140 h (Table 6.2). In the case of the 17–70 h interval, the standard deviations of  $\lambda_{eff}$  and  $R_b$  were beyond 14.9% and beyond 12.6% of the final estimated values for both regression estimation cases (GR4-Seq and GR2-Seq), respectively, whereas these values were within 2.5% and 2.9% for the developed estimation cases (GR4-PE and GR2-PE). In the case of the 17–140 h interval, the standard deviations of  $\lambda_{eff}$  and  $R_b$

were beyond 10.1% and beyond 8.2% of the final estimated values for both regression cases (GR4-Seq and GR2-Seq), respectively, whereas these values were within 1.8% and 2.3% for the developed estimation cases (GR4-PE and GR2-PE).

**Table 6.2** Final estimated values for each of the methods along with the maximum and minimum values, and the standard deviations that were obtained over time intervals of 17–70 h and 17–140 h (the max and min values were obtained from the estimated values at 17–140 h).

Cases	Final $\lambda_{eff}$ [W/(m·K)]	Final $R_b$ [m·K/W]	Max, min of $\lambda_{eff}$ [W/(m·K)]	Max, min of $R_b$ [m·K/W]	$\sigma$ of $\lambda_{eff}$ (17–70 h) [W/(m·K)]	$\sigma$ of $R_b$ (17–70 h) [m·K/W]	$\sigma$ of $\lambda_{eff}$ (17–140 h) [W/(m·K)]	$\sigma$ of $R_b$ (17–140 h) [m·K/W]
GR4-PE	1.92	0.173	1.93, 1.86	0.180, 0.173	0.048	0.005	0.035	0.004
GR4-Seq	1.95	0.182	1.95, 1.21	0.184, 0.114	0.290	0.023	0.196	0.015
GR2-PE	1.84	0.191	1.84, 1.82	0.194, 0.185	0.009	0.003	0.008	0.002
GR2-Seq	1.83	0.188	2.48, 0.88	0.226, 0.074	0.327	0.029	0.219	0.019

The lowered borehole thermal resistances of GR4 compared to GR2 were caused by the natural convection in the ground, which consisted of saturated porous soil. It was confirmed again that the decrease of borehole thermal resistance was more evident in the gravel backfilled BHE. However, a discussion about natural convection is not presented here because it is beyond the scope of the paper.

Additionally, the increasing estimation behavior of the thermal conductivity and the decreasing estimation behavior of the borehole thermal resistance with time can be seen in GR4 (Fig. 6.8). Because the ILS model cannot consider the natural convection, the slightly changing estimation trend is sort of signal that shows that different heat transfer processes were involved. The fact that additional information can be read from the behavior of the estimation is another advantage of the proposed method, which recursive curve matching estimation using the temporal superposition applied analytical model cannot provide.

## 6.5 Advantages of proposed method

The developed method is simple but provides very stable and fast estimations. Moreover, this method can be applied without detailed analysis of the disturbance factors and pre-processing of the measured data if the heat transfer in the ground is conduction dominated. At the same time, unlike recursive curve matching estimation using a temporal superposition applied analytical model, the proposed method can show the estimating behavior of every time step. Another benefit of this method involves the instability

of early time estimations, which can be seen in the results from the sequential method. The causes of early time instability include inaccurate early time responses of analytical models, the high sensitivity of the data to disturbance effects, and not enough data to conduct regression analyses. This can lead to slow convergences when conducting sequential regression estimations using analytical solutions. On the contrary, the developed method is not influenced by the regression errors from prior time steps because estimations at certain time steps use only one measured mean temperature of that time step and the calculated value that considers the history of the unstable heat rate. For example, when estimating parameters at 20 h, the proposed method uses only the mean temperature value at 20 h and the calculated temperature value whose history of unstable heat rate is considered using temporal superposition. However, in case of the conventional regression method, it uses 100 measured values from 15–20 h (20 points per hour) without considering the disturbance effect. This is the reason why the developed method is also stable during early time estimations (Fig. 6.8 and Fig. 6.9) and showed a narrower estimation range and smaller standard deviations than the sequential estimation (Table 6.2). Although the estimated results from 15–20 h are not presented in Fig. 6.8 and Fig. 6.9, the first estimated values (e.g., at 15 h) were very close to the final values in both GR4-PE and GR2-PE. The estimated  $\lambda_{eff}$  and  $R_b$  of the first time step were 1.86 W/(m·K) and 0.175 m·K/W for GR4-PE, and 1.82 W/(m·K) and 0.188 m·K/W for GR2-PE, respectively (please refer to the supplementary interactive plot data for the earlier time points). This convergence time of 15 h was at least four times faster than that of about 60 h for GR4-Seq. Many researchers have attempted to determine the minimum duration of a TRT needed to ensure accurate estimation. The minimum durations that have been reported are distributed over a wide range: 12–20 h [28], 30 h [90], 36–48 h [29], 50 h [96,98], 53 h [99], and 60 h [18,97]. These values are based on various estimation methods and different BHE configurations. Therefore, it is hard to compare the results from this study to others, but 15 h is quite good compared to the other results. Although the results cannot be generalized for other formations and BHE configurations at this time, the independent estimations of each time step using the parameter estimation technique can provide for much faster convergence times than the conventional regression method. If the TRT data contain few disturbance effects so the heat rate is maintained at a sufficiently constant level, this finding would be valid even when a variable heat injection rate is not considered. Therefore, use of the developed method could reduce test times and costs of a TRT, while at the same time, more accurately show the behavior of estimated values than the sequential method.

## 6.6 Conclusion

In this study, a TRT interpretation method was proposed for disturbed TRT data using a temporal superposition applied ILS model combined with the quasi-Newton method. The proposed method was validated with data from two in-situ TRTs and the estimated results were compared with those from the conventional regression method. The main results can be summarized as follows.

- The developed method showed very stable estimations even when the TRT data were influenced by external disturbance effects. Neither detailed analyses of disturbance factors nor pre-processing of measured data is needed for the use of the developed method. The proposed method yielded at least four times lower standard deviations than the sequential method. For the most accurate estimations using the proposed method, the locations of the fluid temperature measurements should be close to the ground surface level, as previous studies have suggested [22,72,149].
- The developed method has about four times faster convergence speeds than those of the conventional estimation method because it is independent of errors from the prior measured data and considers the history of the variable heat rate. It took about 15 h to obtain values close to those of final estimation values.
- When disturbance effects on TRT data were small, the estimation converged around 60 h with the conventional sequential method. In contrast, when the disturbance effects were relatively large, the sequentially estimated values fluctuated until the end of the estimation period. In this case, the proposed method can be a good alternative method for a reliable and fast estimation.



CHAPTER 7  
EFFECT OF NATURAL CONVECTION ON THERMAL  
RESPONSE TEST

## 7.1 Introduction

The borehole thermal resistance depends on the geometry of the BHE and the thermal properties of the pipes and materials (e.g., grout and backfill soil) that fill the annular space of the borehole. Not only the effective thermal conductivity of soil, but also the borehole thermal resistance has a significant impact, in the design of a GSHP.

The general practice in constructing a BHE is to fill the annular space with grout or a backfill material such as sand or gravel. This prevents collapse of the borehole and contamination of the groundwater and aquifer and enhances the thermal contact between the BHE and ground. A thermally enhanced backfill material is typically used to lower the borehole thermal resistance, as reported previously [22,24,163–167].

In northern Europe, groundwater-filled BHE is a commonly used BHE configuration. A schematic diagram of a groundwater-filled BHE is shown in Fig. 7.1 (a). Several recent studies [118–120,129,168] on these BHEs have reported that natural convection occurring in the annular space considerably lowers the borehole thermal resistance and that the results of a TRT depend on the heat injection rate. Gustafsson and Gehlin [168] reported that the borehole thermal resistance was decreased by more than 10% when the heat injection rate increased from 40 W/m to 80 W/m. They used the ILS model [9] for the interpretation of TRT data. Gustafsson and Westerlund [119] conducted multi-injection-rate TRTs of two BHEs with lengths of 75 m and 150 m. They varied the heat injection rate over the range of 21–83 W/m. The results showed that the borehole thermal resistance decreased from 0.12 m·K/W to 0.065 m·K/W. Comparing the results of these two studies [119,168], Javed et al. [120] reported that the borehole thermal resistance does not depend on the heat injection rate but that the effective thermal conductivity increases beyond 10% when the heat injection rate changes from 68 W/m to 140 W/m.

Studies of groundwater-filled BHEs have also been conducted in Japan. Fujii et al. [169] conducted TRTs in groundwater-filled BHE and interpreted the data using the Horner plot method and the infinite cylindrical source model [170]. They reported the enhancement of heat transfer by natural convection as revealed using the empirical formula for the Rayleigh number and Nusselt number suggested by MacGregor and Emery [171]. Fujii et al. [122] estimated the vertical distribution of the thermal conductivity by conducting TRTs with optical fiber sensors. The effective heat exchange length of the groundwater-filled BHE was approximately 30 m. Heat injection rates of 68, 118, and 168 W/m were used. The effective thermal conductivity increased slightly from 2.4 to 2.46 W/(m·K), and the borehole thermal resistance decreased from 0.1 to 0.089 m·K/W as the heat injection rate increased.

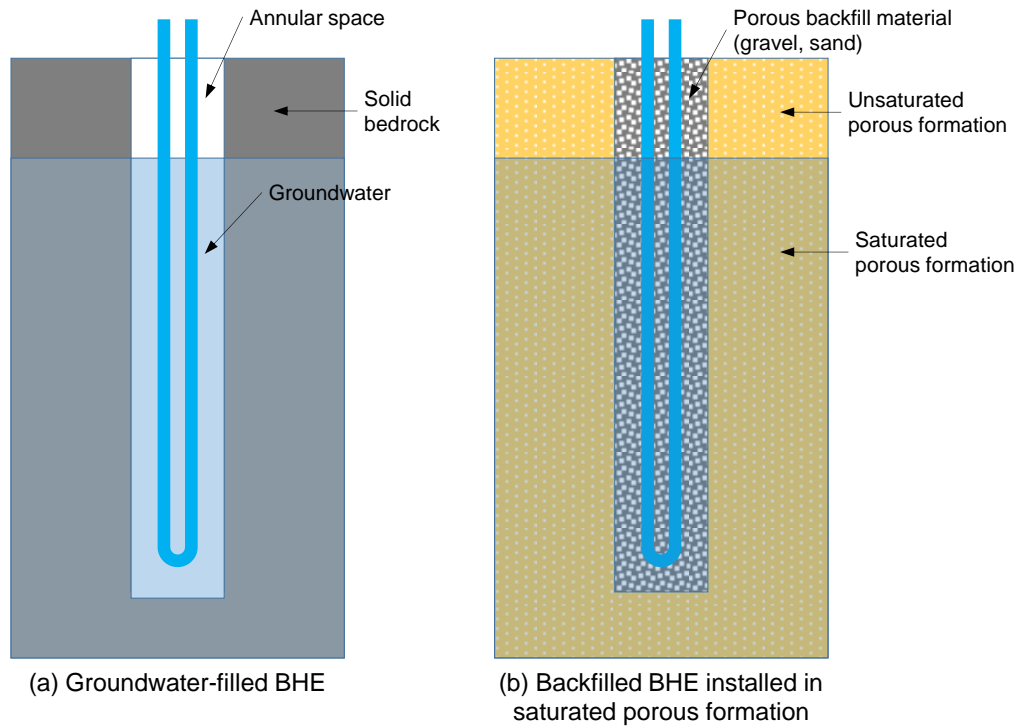


**Fig. 7.1** Schematic diagrams of two borehole heat exchanger (BHE) configurations: (a) groundwater-filled BHE and (b) backfilled BHE installed in porous formation.

From the perspectives of performance, constructability, and maintenance, a groundwater-filled BHE is a promising type of BHE. However, the applicability of groundwater-filled BHEs is limited to certain subsurface conditions. In areas with strong subsurface bedrock, where a borehole is structurally stable and can maintain its shape against lateral pressure without the need for a backfill material, a groundwater-filled configuration can be used. However, in weak subsurface conditions, the most common BHE construction method involves grouting or backfilling. In addition, groundwater-filled BHEs sometimes cannot be installed because of local regulations related to the use of groundwater.

Regarding the general backfill types of BHEs, studies have focused on the advection effect by groundwater flow in the aquifer [28–38]. Various studies have considered the Darcy velocity and flow direction [37], effect of groundwater flow in vertical fractures [31], development of moving line source models [32,172], and case studies with various combinations of the groundwater velocity, direction, and borefield arrangement [36]. Most of these studies focused on the performance enhancement by the groundwater flow.

However, if the hydraulic head difference or the hydraulic conductivity is small, the saturated formation does not always include strong groundwater flow. In this case, even in a backfilled or grouted BHE, if the ground is saturated and consists of porous medium, such as sand and gravel, the natural convection inside

and around a BHE can occur. A schematic diagram of a backfilled BHE configuration is shown in Fig. 7.1(b). The strength of natural convection depends on the difference between the temperature of heat carrier fluid in the BHE and undisturbed ground temperature, which means that the results of a TRT may depend on the heat injection rate. Therefore, when TRTs are conducted in saturated porous formations, heat rate dependence should be examined.

Although the use of backfilled BHEs in saturated porous formation is more common than the use of groundwater-filled BHEs, which is limited to strong bedrock, there are few mentions in the literature of TRTs conducted under such conditions.

Fujii et al. [173] experimentally examined the effect of natural convection in a saturated porous medium by using a reduced-scale coaxial cylinder apparatus. They used gravel with two different grain size distributions of 10–20 mm and 5–10 mm and silica sand with a grain size of less than 0.3 mm. They confirmed that the case filled with the larger gravel had a 20% higher heat exchange rate than the case filled with silica sand. In addition, they found that the borehole thermal resistance decreases as the heat exchange rate increases. Choi and Ooka [117] conducted numerical analyses to examine the effect of the heat injection rate on the results of TRTs conducted in a saturated porous formation. The numerical TRT data were interpreted using the ILS model. In comparison with the 50 W/m case, in which natural convection was not considered, in the 100 W/m case, natural convection was shown to result in an 8.5% higher effective thermal conductivity and 3.0% lower borehole thermal resistance.

In this study, the effect of natural convection on the results of TRTs conducted in saturated porous formations was examined experimentally. In situ TRTs were conducted with two BHEs with the same geometry but different backfill materials: one was grouted with a mix of Portland cement and silica sand and the other was backfilled with gravel (Section 3.1). Two TRTs were conducted for each BHE at different heat injection rates, for a total of four TRTs. To assess the effect of disturbance from the external environment and to enhance the estimation accuracy, the parameter estimation method developed in Chapter 6 was used to interpret the TRT data. On the basis of the results, the performance of the two types of BHEs is examined and discussions are presented concerning the performance and constructability of BHEs and existing design methods of BHEs related to typical practices employed in conducting TRTs.

## 7.2 Temperature response test: single-heat injection rate TRT

### 7.2.1 Test conditions

The test conditions are summarized in Table 7.1. The flow rates and heat injection rates given in Table 7.1 are values averaged over the heat injection period of the TRTs. To assess the thermal behavior of the

BHE and obtain reliable results, the experiments were conducted over 140 h, which is a relatively long for such tests. The flow rate was set to approximately 20 L/min. For each borehole, TRTs were conducted twice using the 2 kW and 4 kW heaters (equivalent to a heat rate of approximately 40 W/m and 80 W/m, which are close to the limits of ASHRAE's [39] recommended range of 50–80 W/m). Once a test was completed, the next test was begun as soon as it was confirmed that the ground temperature had returned to its initial value.

**Table 7.1** Experimental conditions for the thermal response tests.

Test name [BHE-Heater]	Duration [h]	Flow rate [L/min]	Heat injection rate [kW]
GR2	140	19.8	2.25 ( $\approx$ 45.0 W/m)
BF2	140	19.8	2.24 ( $\approx$ 44.8 W/m)
GR4	140	21.9	4.19 ( $\approx$ 83.8 W/m)
BF4	140	20.9	4.42 ( $\approx$ 88.4 W/m)

## 7.2.2 Temperature response and interpretation of TRT data

The measured heat injection rate, inlet and outlet fluid temperatures, and average fluid temperature in the TRTs conducted using the 2 kW heater (GR2, BF2) and 4 kW heater (GR4, BF4) are shown in Fig. 7.2 and Fig. 7.3, respectively. As shown in Fig. 3.2 and Fig. 3.6, the inlet and outlet fluid temperatures were measured for both of the two BHEs near the ground level and the TRT apparatus. Although Class A Pt-100 sensors (error range:  $\pm(0.15 + 0.002 \cdot T_{cf})$  K) were used in the experiments, perfect calibration over the full measurement range was difficult to achieve. If estimation is conducted using the temperature and heat rate values obtained from different sensors installed in the GR-BHE and BF-BHE, the comparison would be affected by the different characteristics of the sensors and their accuracy. Therefore, the temperature values obtained from the Pt-100 sensors installed in the TRT apparatus (Fig. 3.6), which can measure both the GR-BHE and BF-BHE cases, were used for the estimation.

If the same amount of heat is injected into two different BHEs, the BHE with the lower fluid temperature can be considered to exhibit better performance. GR2 and BF2, which used the 2 kW heater, had very close heat injection rates (Table 7.1). The final average temperature of GR2 was 35.1 °C, and that of BF2 was 34.1 °C. Therefore, the BF-BHE might be considered to have performed better than the BR-BHE. However, a direct comparison for the 4 kW TRTs was impossible because GR4 and BF4 had different heat injection rates (Table 7.1). The main reasons for these results are the voltage variation from the power grid and the heat exchange between the circulating fluid and the outdoor environment. The regulations

regarding voltage variation vary from region to region. Typically, the strictest allowable variation in the supply voltage is  $\pm 5\%$ . ANSI C84.1-2001 [174] and EN 50160 [175] specify tolerable voltage variation ranges of  $-10\%$  to  $+5\%$  and  $\pm 5\%$ , respectively. For a variation range of  $\pm 5\%$ , assuming that the resistance of the 4 kW heater is  $10 \Omega$  and the nominal supply voltage is 200 V, the output range of the heater is  $\pm 4.41$  kW. Therefore, the 4.41 kW for BF4, which includes the heat generation from the pump, is within the tolerable output range.

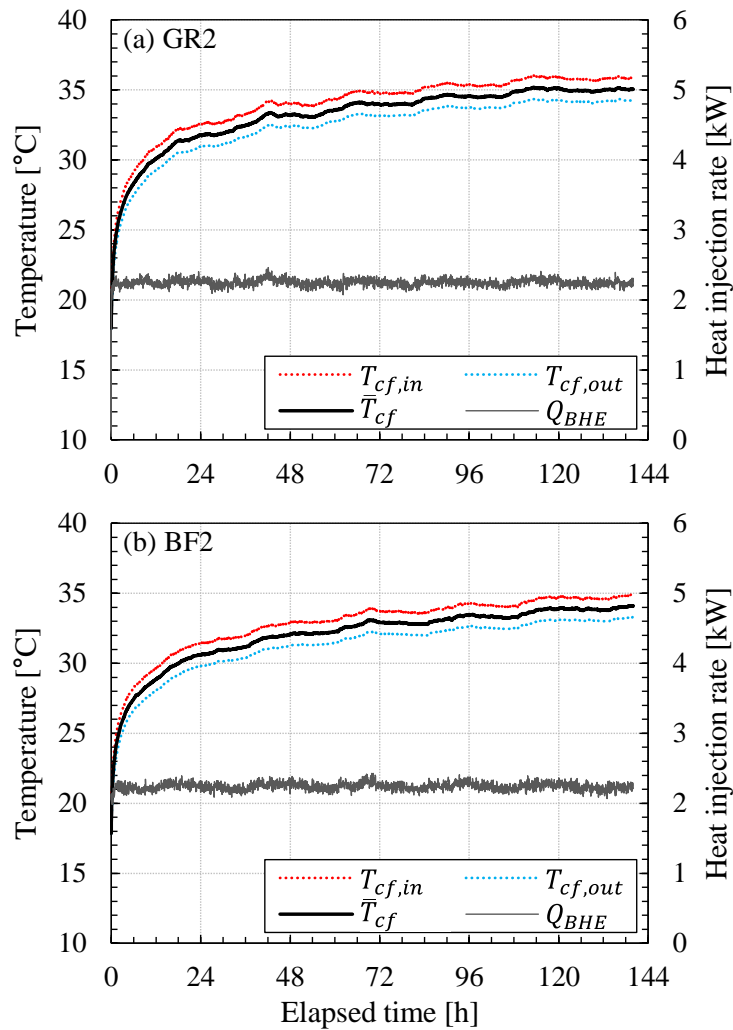


**Fig. 7.2** Temperature response curve and heat injection rate of two TRTs using 2 kW heater; (a) GR2: cement-grouted BHE using 2 kW heater and (b) BF2: gravel-backfilled BHE using 2 kW heater.

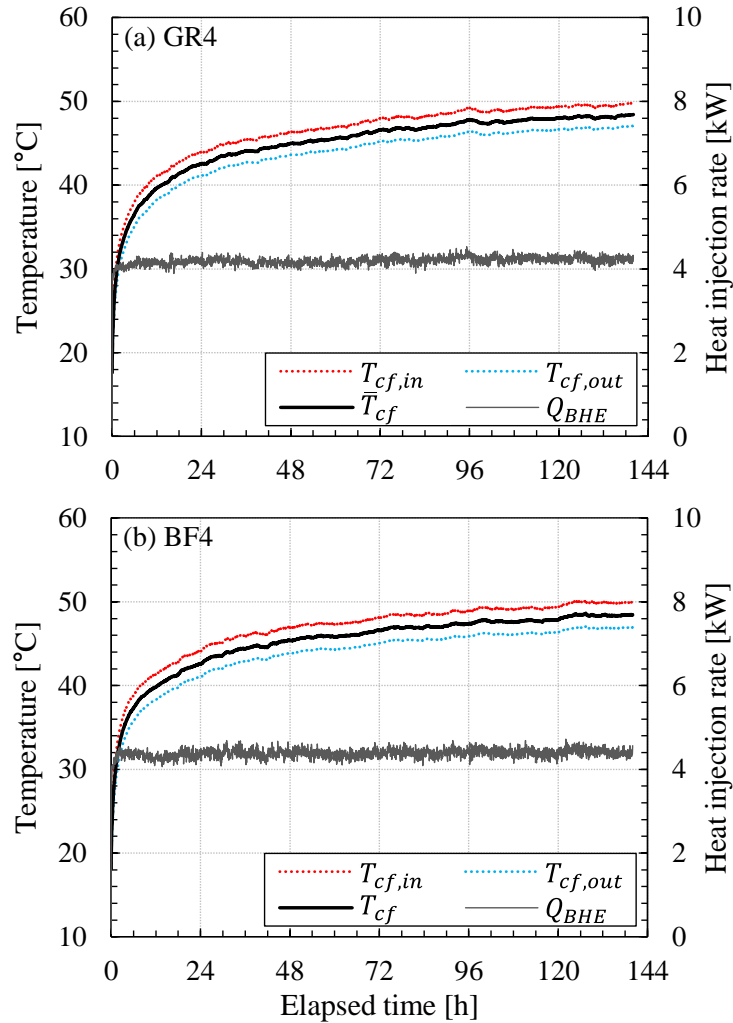


**Fig. 7.3** Temperature response curve and heat injection rate of two TRTs using 4 kW heater; (a) GR4: grouted BHE using 4 kW heater and (b) BF4: backfilled BHE using 4 kW heater.

### 7.3 Interpretation of TRT data

Before conducting estimations using the parameter estimation technique, conventional estimations using the ILS model and an assumed constant heat rate were conducted in a stepwise manner (e.g., sequential estimation) to identify initial values for use in the parameter estimation process. Because the ILS model cannot consider the early-period response, which is dominated by the BHE itself, the first 15 h of temperature data were not used for the interpretation. The estimation results for the GR-BHE and BF-BHE are shown in Fig. 7.4 and Fig. 7.5, respectively, and the final estimated values and their rates of change with increasing heat rate are summarized in Table 7.2. Because of the disturbance factors (voltage

fluctuation and heat exchange between the circulating fluid and the outdoor environment), considerable fluctuation in the estimates can be seen in the TRT results obtained using the 2 kW heater (Fig. 7.4(a) and Fig. 7.5(a)). This leads to less reliable estimation results. The applicability and limitations of the ILS model under conditions of disturbance by the outdoor environment are described in Chapter 5. At the end of GR-BHE (at 140 h), GR4 had a 9.0% larger  $\lambda_{eff}$  and 2.2% smaller  $R_b$  than GR2. However, for the BF-BHE, the trends in  $\lambda_{eff}$  and  $R_b$  with increasing heat rate were different. Compared with BF2, BF4 had a 3.4% smaller  $\lambda_{eff}$  and a 14.2% smaller  $R_b$  (Table 7.2).

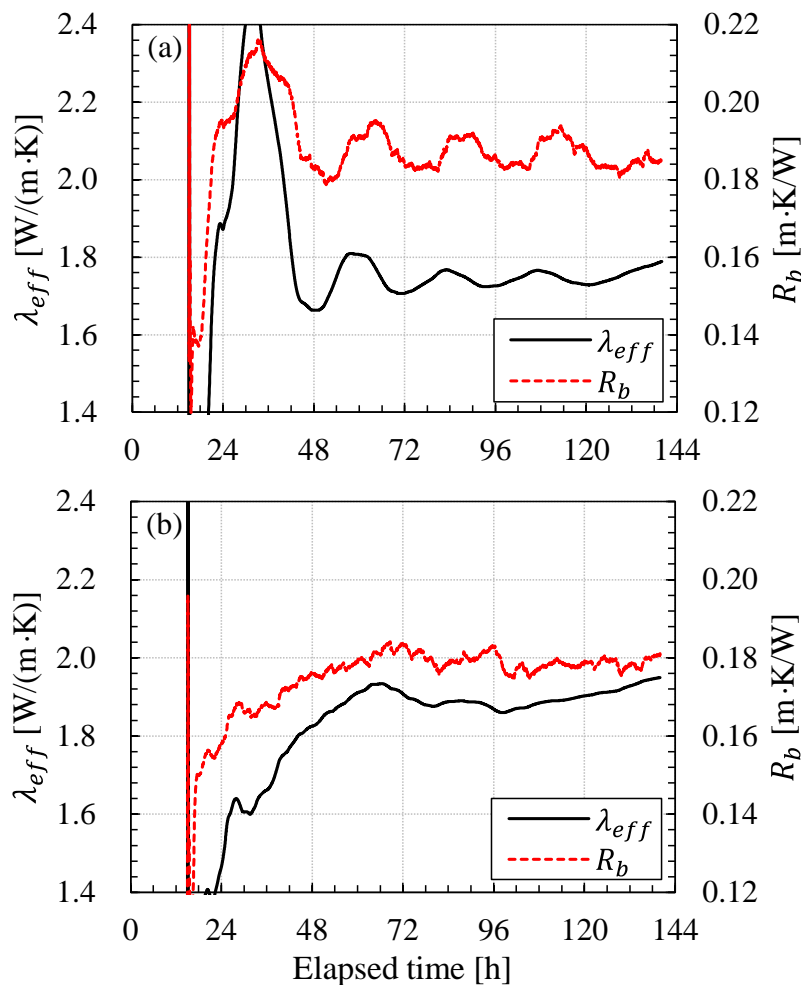


**Fig. 7.4** Sequential estimation using TRT data from GR-BHE; (a) GR2: grouted BHE using 2 kW heater and (b) GR4: grouted BHE using 4 kW heater.

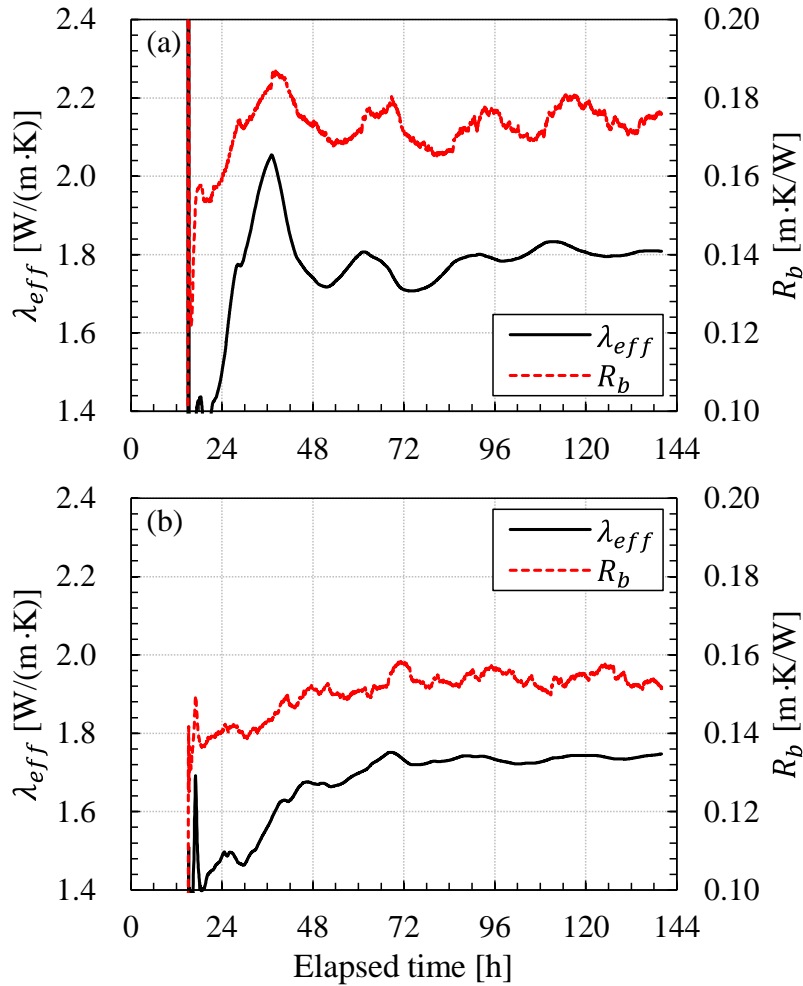


**Fig. 7.5** Sequential estimation using TRT data from BF-BHE; (a) BF2: gravel-backfilled BHE using 2 kW heater and (b) BF4: gravel-backfilled BHE using 4 kW heater.

**Table 7.2** Final values obtained by sequential estimation using the ILS model.

Test name [BHE-Heater]	$\lambda_{eff}$ [W/(m·K)]	$R_b$ [m·K/W]	Rate of change in $\lambda_{eff}$ based on 2 kW case [%]	Rate of change in $R_b$ based on 2 kW case [%]
GR2	1.789	0.185	N/A (Base case)	N/A (Base case)
GR4	1.950	0.181	9.0	-2.2
BF2	1.809	0.176	N/A (Base case)	N/A (Base case)
BF4	1.748	0.151	-3.4	-14.2

N/A: not applicable

Although the estimated results shown in Fig. 7.4 and Fig. 7.5 were influenced by the disturbances, both  $\lambda_{eff}$  and  $R_b$  can change even in the absence of a disturbance. When using a model that only considers conductive heat transfer in interpreting TRT data, which includes the effects of natural convection or advection from flowing groundwater, those effects can affect the estimates of both  $\lambda_{eff}$  and  $R_b$ . In Ref. [117], which interpreted natural convection-considered numerical TRTs using the ILS model, the results showed changes in both  $\lambda_{eff}$  and  $R_b$ . In other TRTs conducted in groundwater-filled BHEs [119,120,122,168], one or both of these parameters were found to change.

In industrial porous media applications using uniformly shaped grains, the term “effective thermal conductivity” has been used to represent the speed of thermal diffusion, which reflects both conduction and the effect of natural convection [176,177]. However, in shallow geothermal applications, this term represents the ground’s spatially averaged thermal conductivity in the vicinity of the BHE. Therefore, if the effective thermal conductivity is changed by the effect of natural convection in a TRT, not only is it different from the conventional concept of effective thermal conductivity in TRT but also comparisons become difficult because  $\lambda_{eff}$  and  $R_b$  change simultaneously.

In contrast to the regression method, which yields only one combination of  $\lambda_{eff}$  and  $R_b$ , the parameter estimation technique described in this paper yields many combinations of  $\lambda_{eff}$  and  $R_b$ . This is one of the difficulties of an inverse problem, but it can be also be an advantage, as in this study. The possibility of multiple combinations of solutions means that if the estimated  $\lambda_{eff}$  for each TRT is adjusted close to a certain value, a fair comparison using the estimated  $R_b$  values from different TRTs would be possible.

The  $\lambda_{eff}$  estimated from the 2 kW TRTs (GR2 and BF2) obtained using the parameter estimation method were regarded as the base values for comparison because the influence of natural convection in 2 kW TRTs is smaller than that in 4 kW TRTs. For the 2 kW TRTs, the final estimated  $\lambda_{eff}$  and  $R_b$  values obtained from the sequential estimation process (Table 7.2) were used as the initial values (Table 7.3). After obtaining the  $\lambda_{eff}$  and  $R_b$  values for the 2 kW TRT, parameter estimation for the 4 kW TRT (GR4 and BF4) was conducted several times with different initial values until the final estimated  $\lambda_{eff}$  was close to that obtained from the 2 kW TRT. This permitted a fair comparison of  $R_b$  values to be made.

The first 20 h of temperature data were not used because of the limitations of the ILS model. Of course, these data were used to calculate the heat injection rate, which is required to obtain  $\bar{T}_{cf,cal}$  in Eq. (6.4). The estimations were conducted at 6 min intervals using the instantaneous temperature data of a particular time step and 6 min averaged heat pulses. The estimated results for the GR-BHE and BF-BHE are shown in Fig. 7.6 and Fig. 7.7, respectively. Although the results were obtained at 0.1 h intervals (6 min), the results for 4 h intervals are shown for clarity. The estimated results of the final time step are summarized

in Table 7.3.

**Table 7.3** Estimated effective thermal conductivity and borehole thermal resistance and their rates of change based on 2 kW TRT cases.

Test name [BHE-Heater]	Initial values of $\lambda_{eff}$ and $R_b$ [W/(m·K)], [m·K/W]	$\lambda_{eff}$ [W/(m·K)]	$R_b$ [m·K/W]	Rate of change in $\lambda_{eff}$ based on 2 kW case [%]	Rate of change in $R_b$ based on 2 kW case [%]
GR2	1.80, 0.185	1.847	0.182	N/A (Base case)	N/A (Base case)
GR4	1.84, 0.169	1.849	0.168	0.1	-7.7
BF2	1.80, 0.175	1.815	0.176	N/A (Base case)	N/A (Base case)
BF4	1.81, 0.156	1.816	0.156	0.1	-11.1

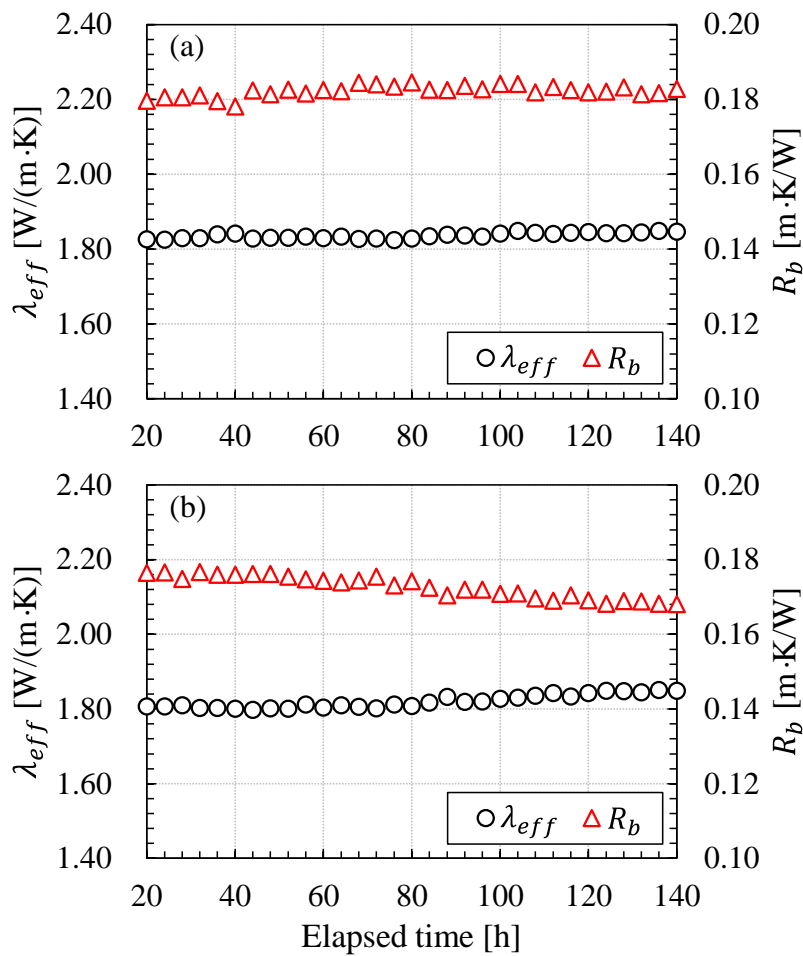


**Fig. 7.6** Results of parameter estimation using the TRT data of cement grouted BHE; (a) estimation using GR2 data and (b) estimation using GR4 data.

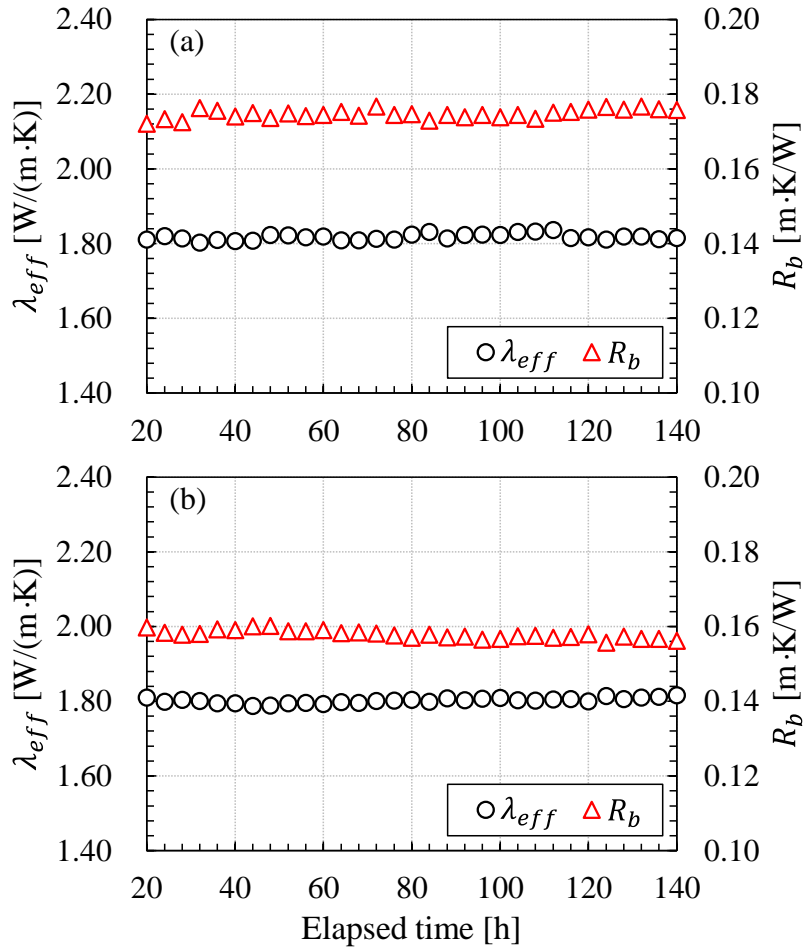


**Fig. 7.7** Results of parameter estimation using the TRT data of gravel backfilled BHE; (a) estimation using BF2 data and (b) estimation using BF4 data.

The fluctuating estimation behavior, which was clearly evident in the 2 kW TRTs (Fig. 7.4 and Fig. 7.5), disappeared because the disturbed heat rate is considered in the temporal superposition of heat pulses. As mentioned previously, based on the  $\lambda_{eff}$  value from the 2 kW TRT,  $\lambda_{eff}$  from the 4 kW TRT was estimated by iteratively changing the initial values until the estimated value was close to that of the 2 kW case. The estimated thermal conductivities were almost the same for each BHE (Table 7.3). The estimated  $\lambda_{eff}$  of the GR-BHE was approximately 0.3 W/(m.K) larger than that of the BF-BHE. The effective thermal conductivity determined from the GR-BHE can be considered more reliable than that determined from the BF-BHE. In the GR-BHE, which was filled with cement grout, the thermal contact between the U-tube and the annular space was good, as was that between the borehole wall and the soil, throughout the depth of the BHE. However, in the BF-BHE, the annular space above the groundwater level was not fully saturated. This means that air, which has low thermal conductivity, was present in the pore spaces of the

gravel backfill, and thus, the thermal contact resistance was high. However, this is not a problem in examining the effect of heat rate dependence of TRT results because the comparisons were made using TRTs conducted in the same BHE.

Because the effective thermal conductivity determined from the 4 kW TRT was adjusted to be close to the value determined from the 2 kW TRT, a comparison using the borehole thermal resistance values was possible. In the case of the GR-BHE,  $R_b$  decreased by 7.7% when the heat injection rate increased from 45.0 W/m (GR2) to 83.8 W/m (GR4). In the case of the BF-BHE, the effect of the heat injection rate was larger. When the heat injection rate increased from 44.8 W/m (BF2) to 88.4 W/m (BF4),  $R_b$  decreased by 11.1% (Table 7.3). From these results, it can be concluded that filling the annular space with a porous medium is a good choice of BHE configuration in saturated porous formations. Although the annular space was not filled with a porous medium, the GR-BHE also showed a reduction in the borehole thermal resistance. This indicates that when the geological formation is composed of a porous medium such as sand or gravel, enhancement of the thermal performance of the BHE can be expected because of natural convection around the BHE.

## 7.4 Discussion

### 7.4.1 Guidelines for consideration of heat rate dependence of TRT in testing

After Mogensen [4] first proposed the idea of TRT, pioneering studies involving in situ TRTs conducted with mobile test rigs were performed in the mid '90s [5,6]. Since then, studies pertaining to new interpretation methods [20,93,116], new test methods [7], uncertainty in the test results [131], and many factors that influence the accuracy of TRT have been conducted [72,94,133]. On the basis of the results of many studies from various perspectives, guidelines for TRTs were published by IEA [40,68,69] and ASHRAE [39,70]. However, the effect of natural convection on TRT results was not addressed in these guidelines and reports. The final report of IEA ECES Annex 21 [40], published at the end of 2013, stated that the effect of natural convection in the aquifer has not yet been examined.

The findings of this study show that the results of TRTs conducted in saturated porous formations are affected by the heat injection rate. In the case of a BHE with 76–80% of its length in contact with a saturated sandy soil, the borehole thermal resistance of the BF-BHE was reduced by 11.1% when the heat injection rate was increased from 44.8 W/m to 88.4 W/m, which is very close to the heat injection rate range of 50–80 W/m recommended in the ASHRAE Handbook [39]. This reduction in thermal resistance results in a shorter required length of the BHEs if the estimated values are considered to be constant and are used in the design of a GSHP. However, this reduction in thermal resistance also implies that if the

heat rate dependence of TRT results is overlooked, it can lead to a flawed GSHP design. In practice, the heat injection rate in a TRT corresponds to the thermal load of a building. Therefore, if the thermal load assigned to the BHE is lower than the heat rate used in a TRT, the expected performance will not be achieved.

A heat load of 50 W/m is typically used as a reference design condition [178]. However, as Kyriakis et al. [179] noted, the actual operation of a GSHP is highly dynamic and its output power can be greater than 50 W/m. They showed that for an initial ground temperature of 15 °C and a ground thermal conductivity of 1.4 W/(m·K), it takes approximately 1000 h of continuous operation to reach a heat rate of 50 W/m.

There have been few studies on the effect of natural convection on conducting TRTs. To clarify the effect of natural convection, TRTs should be conducted under various subsurface conditions in the future. In addition, studies on the dynamic performance of BHEs installed in saturated porous formations are required. Furthermore, new experimental and interpretation methods should be developed to more accurately capture the effect of natural convection on conducting TRTs because single-injection rate TRTs with different heat rates require long recovery periods between TRTs, which makes the ground conditions vary (e.g., depth-averaged initial temperature, moisture content, thermal conductivity, and groundwater level). On the basis of the aforementioned studies, the design of GSHPs and TRT methods should be refined to consider the natural convection of the ground when a BHE is installed in a saturated porous formation.

#### 7.4.2 Advantages of gravel-backfilled BHE in saturated porous formation

A gravel-backfilled BHE offers advantages in terms of not only enhanced performance but also reduced construction time and cost. When the annular space is filled with cement grout, plastic shrinkage and settlement of the grout occur. This settlement may be due to permeation of the grout into the sandy soil. The filling operation must therefore be carried out in stages to compensate for the lowering of the level of the grout. In this study, it took three days to complete the filling of the cement-grouted BHE. In contrast, the gravel-backfilled BHE only required packing of the annular space with porous medium, which took approximately 2 h. This difference represents a significant saving in terms of labor cost.

To obtain insight into the performance of backfilled BHEs, further studies on the dependence of the BHE geometry and the thermal and hydrogeological properties of both the soil and backfill material (e.g., thermal conductivity, porosity, and hydraulic conductivity) are needed. However, in locations where the geological conditions are similar to those of this study, the use of gravel-backfilled BHEs is highly recommended.

## 7.5 Conclusion

In this study, four TRTs were carried out to examine the effect of natural convection inside and around the BHE. Two different heat injection rates were applied to two different configurations of BHEs to assess the effect of the heat injection rate on performance. The data from the TRTs were interpreted using a temporal superposition-applied ILS model combined with the quasi-Newton numerical optimization method. The main results can be summarized as follows:

- When the annular space was filled with a porous medium such as gravel, the borehole thermal resistance was highly dependent on the heat injection rate: at a heat injection rate of 88.4 W/m, the borehole thermal resistance was reduced by 11.1% compared with that at 44.8 W/m.
- Even when the annular space was filled with cement grout mixed with silica sand, natural convection in the soil around the BHE enhanced its performance when a relatively high heat injection rate was used. At a heat injection rate of 83.8 W/m, the borehole thermal resistance was reduced by 7.7% compared with that at 45.0 W/m.
- The gravel-backfilled BHE also offers advantages in terms of construction time and cost savings. With the cement grout, it took 3 days to fill the annular space, whereas with the gravel backfill, it took only 2 h to fill the annular space.
- Additional research on the effect of natural convection on TRT results and on the performance of BHEs backfilled with porous medium is required to refine the design of GSHPs and TRT methods.



CHAPTER 8  
PARAMETER ESTIMATION METHOD TO DETERMINE  
HEAT INJECTION RATE DEPENDENCE IN SATURATED  
POROUS FORMATION

## 8.1 Introduction

In Chapter 7, with BHEs installed in the saturated porous formation, the performance dependence on the heat injection rate was experimentally examined. However, the TRT method used has drawbacks in terms of the actual viability and uncertainty due to temporal changes in the ground conditions. The former drawback is with regard to the time and cost of the tests. To examine the heat rate dependence, single heat rate TRTs should be conducted two or three times in the same BHE at different heat injection rates. If a TRT is conducted for 70–100 h with a heat rate of 50 W/m, then the recovery time is approximately 3–4 weeks [98,116]. The recovery time is even longer if a greater heat injection rate is used or longer TRT is conducted. This increases the cost and is rarely viable in actual situations. The latter drawback concerns the temporal changes in the moisture content, initial ground temperature, groundwater level, and local and intermittent groundwater flow (Fig. 8.1). The thermal conductivity of soil depends on the moisture content [180–184], and the groundwater level changes with time. In addition, unpredictable changes to the hydraulic head near the test site can make the groundwater flow intermittent or strong. The initial ground temperature also changes with the season. Based on the 1 year of measurement of the ground's initial temperature at the experimental site using the observation well (Fig. 3.2), the initial ground temperature averaged over a depth of 50 m fluctuated within 16–17.5 °C. If an experimenter interprets TRTs conducted on the same BHE at different times using the ILS model and the same initial ground temperature is used regardless of the actual depth-averaged temperature, then the estimated borehole thermal resistance would significantly change. Therefore, in order for the heat rate dependence to be examined accurately, a new test method needs to be developed that can be conducted in a short amount of time along with its interpretation. In short, the new method should require a single TRT with multiple heat injection rates rather than multiple TRTs with single heat injection rates.

To overcome the above problems, a new method is suggested to practically examine the heat rate dependence of TRTs while avoiding the long recovery time of the previous approach. This method uses a multi-heat injection rate and parameter estimation based on combining the ILS model with temporal superposition and the quasi-Newton method. Four multi-heat injection rate TRTs were conducted and estimated using the proposed method. The test site and BHE configurations were the same as used in Chapter 7. Two BHEs with the same geometry but different backfill materials were used: one was grouted with a mix of Portland cement and silica sand, and the other was backfilled with gravel. To examine the effectiveness of the new method, the estimated results were compared with those of single heat injection rate TRTs. The method was proven to be sufficiently fast and robust. Thus, it can be applied to the real-time interpretation of onsite TRTs.

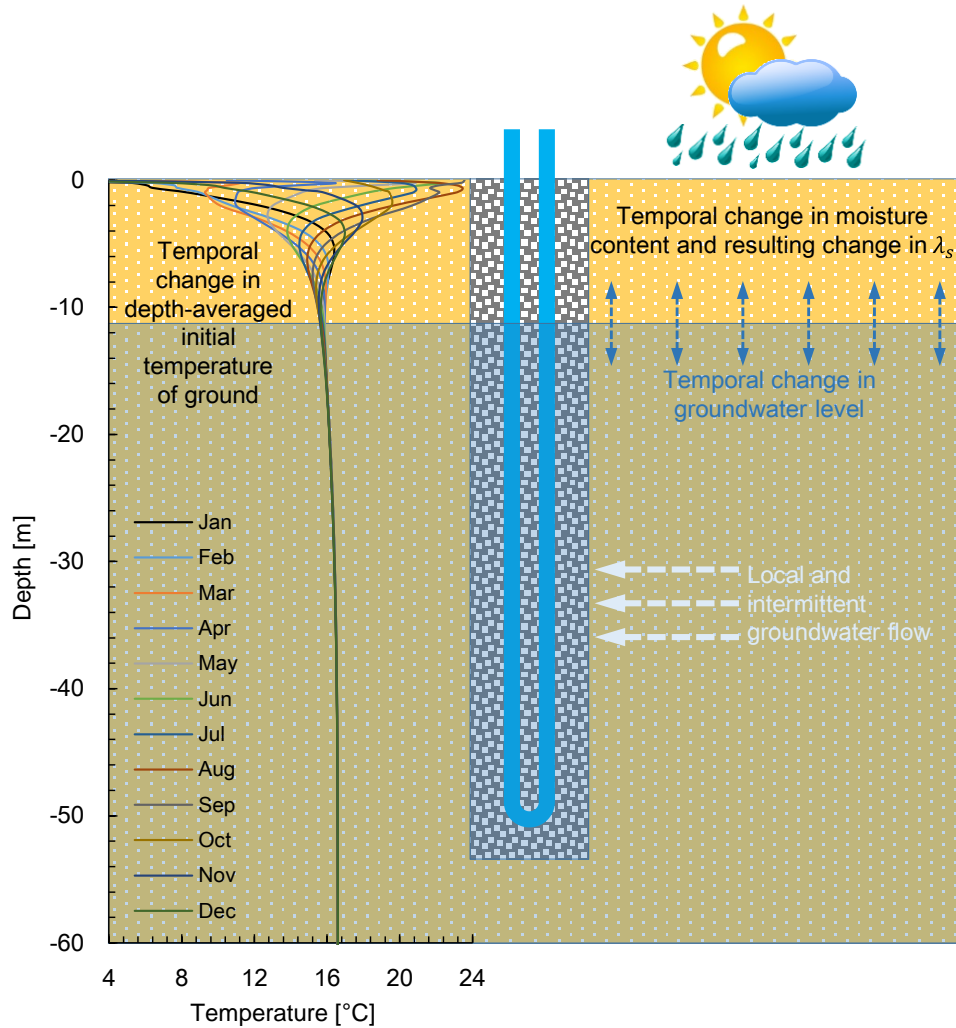


**Fig. 8.1** Schematic illustration of temporal changes in ground conditions.

## 8.2 Multi-heat injection rate TRT and parameter estimation methods

### 8.2.1 Multi-heat injection rate TRT method

The multi-heat injection rate TRT method is presented in papers on groundwater-filled BHEs [119,120,185]. The method used in this study was almost the same as those except that the first heat injection rate should be lower than 50 W/m. The reason for this measure is described below after the test procedure. The experimental procedure is as follows:

(1) Start the first injection period  $t_{p1}$  using a relatively low heat rate of 40–50 W/m. If the experimenter has a priori information on the test site, the estimation can be performed in a real-time manner with good

initial guess values. In this case, the duration of the first injection period can be less than 2 days. However, if there is no information about the test site, the first injection period should be more than 60 h to obtain reliable initial guess values for the parameter estimation through a regressive estimation method based on the exponential integral approximated ILS model.

(2) After the first injection period, the second injection period  $t_{p2}$  starts with a higher heat injection rate. The duration of the second period should be more than 1 day.

(3) If the TRT apparatus can generate a higher heat rate, the third injection period  $t_{p3}$  can be attempted. The duration of the third period should also be more than 1 day. During this period, the temperature of the circulating fluid should be less than the temperature tolerance specified by the U-tube manufacturer.

With regard to the low heat rate of the first injection period, both  $\lambda_{eff}$  and  $R_b$  can be affected if a model that only considers the conductive heat transfer is used to interpret a TRT that contains the effect of natural convection. In [117], when the numerical TRTs that considered the buoyancy effect in the porous formation were interpreted using the ILS model, both  $\lambda_{eff}$  and  $R_b$  changed. Other TRTs conducted in groundwater-filled BHEs [119,120,122,168] also showed changes in one or both parameters.

Although the term “effective thermal conductivity” is used in industrial applications using artificial porous materials to represent the speed of thermal diffusion comprising both conduction and natural convection [176,177], in shallow geothermal applications it represents the ground’s spatially averaged thermal conductivity in the vicinity of a BHE. If a high heat rate is injected during the first period, the resulting strong natural convection causes large changes in both  $\lambda_{eff}$  and  $R_b$  simultaneously. This differs from the conventional concept of effective thermal conductivity that has been used in TRTs. By using a low heat rate, the natural convection can be suppressed, and an effective thermal conductivity that is less affected by natural convection can be obtained. This is why a low heat rate should be injected in the first period. After the effective thermal conductivity is obtained in the first injection period, the estimations during the second injection period are performed using a fixed  $\lambda_{eff}$  value estimated at the end of the first period. The details are explained further in the next section.

### 8.2.2 Parameter estimation method

The parameter estimation method developed in Chapter 6 that combines the ILS model with temporal superposition and the quasi-Newton method was modified and used for interpretation [116].

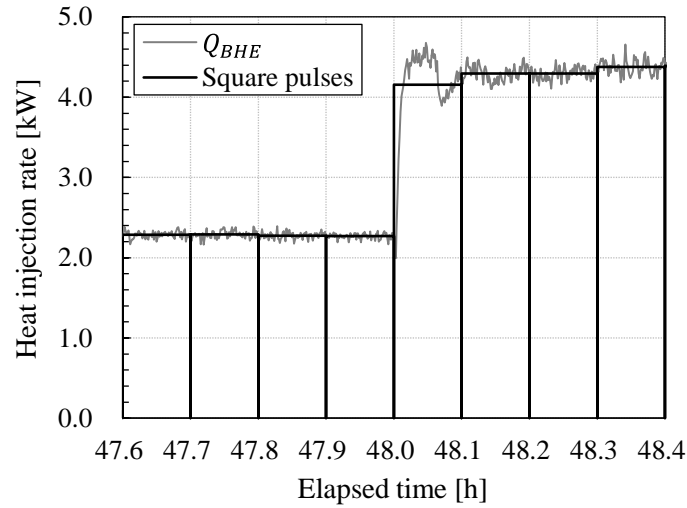


**Fig. 8.2** Example of piecewise square pulses (6 min) and measured heat injection rate. In the study, each pulse was 3 min long. However, the pulses presented here are 6 min long for clarity.

The volumetric heat capacity of soil  $C_s$  was assumed to be  $2.8 \text{ MJ/m}^3\text{K}$ . The initial ground temperature  $T_0$  was measured using T-type thermocouples installed in the BHEs and the observation well (Fig. 3.2). The depth-averaged  $T_0$  was varied in the range of  $16\text{--}17.5 \text{ }^\circ\text{C}$ . The heat rate per unit length of BHE for the given time step  $q_n$  is time-variant. It can be obtained from the actual heat injection rate  $Q_{BHE}$  ( $q = Q_{BHE}/H$ ). The heat rate  $q$  was regarded as piecewise 3-min-long square pulses, where the measured  $Q_{BHE}$  was averaged at 5 s intervals. Fig. 8.2 shows an example of a 3-min-long square pulse and the actual heat injection rate. Please note that the heat pulses actually used in the study were 3 min long, but Fig. 8.2 provides 6 min long pulses for clarity. The actual heat injection rate  $Q_{BHE}$  can be obtained from the measured flow rate  $\dot{V}_{cf}$ , inlet temperature  $T_{cf,in}$  and outlet temperature  $T_{cf,out}$ :

$$Q_{BHE} = \rho_{cf} c_{cf} \dot{V}_{cf} (T_{cf,in} - T_{cf,out}) \quad (8.1)$$

The calculated average fluid temperature  $\bar{T}_{cf,cal}$  is a function of two variables: the effective thermal conductivity  $\lambda_{eff}$  and borehole thermal resistance  $R_b$ . The two parameters  $\lambda_{eff}$  and  $R_b$  can be estimated by minimizing the objective function to less than  $10^{-5}$  for every 3 min interval of the time step described in Eq. (8.2). Starting from the second injection period,  $\lambda_{eff}$  is fixed to the final estimated value of the first injection period, which is less affected by natural convection. Therefore, the objective function Eq. (8.2) becomes Eq. (8.3), which is a function of  $R_b$  alone.

For the first injection period ( $t \leq t_{p1}$ ):

$$\min f_{obj}(\lambda_{eff}, R_b) = \left( \bar{T}_{cf,exp} - \bar{T}_{cf,cal}(\lambda_{eff}, R_b) \right)^2 \leq 10^{-5} \quad (8.2)$$

From the second injection period ( $t > t_{p1}$ ):

$$\min f_{obj}(R_b) = \left( \bar{T}_{cf,exp} - \bar{T}_{cf,cal}(R_b) \right)^2 \leq 10^{-5} \quad (8.3)$$

This objective function is minimized by using the quasi-Newton method. The same as in Chapter 6, the Broyden–Fletcher–Goldfarb–Shanno (BFGS) method [157–160] was used to approximate the Hessian. Unlike the recursive curve fitting method used for the whole test period to find only one solution, or sequential estimation involving the addition of one measurement after another, the developed estimation program was executed for each time step using only the measured temperature data at a particular time step and the given history of heat rates. The details and advantages of this estimation method are described in Chapter 6.

As were done in Chapter 6, to alleviate the ill-posedness of the parameter estimation and enhance the estimation speed, two measures were introduced: (1) from the second time step on, the initial guess values were updated using the solution of the previous time step; and (2) the search range was restricted to  $[\lambda_{eff,ini} \pm 0.5 \text{ W}/(\text{m}\cdot\text{K})]$  and  $[R_{b,ini} \pm 0.05 \text{ m}\cdot\text{K}/\text{W}]$ . The former made the estimations fast and stable because the starting point was already near the solution. The latter alleviated the ill-posed characteristics. Combining these two measures meant that the search ranges were updated each time step on the basis of the estimated values in the previous time step (initial guess values in current estimation).

Fig. 8.3 presents the flowchart of the estimation. First, the initial guess values for the estimation in the first time step should be determined. Selecting good initial guess values is important because the parameter estimation is an ill-posed inverse problem with non-unique solutions. As stated previously, this can be based on a priori information of the test site or the estimated values from the conventional regression method using the ILS model. Starting from the assumed initial guess values, the objective function is minimized by changing  $\lambda_{eff}$  and  $R_b$  until the convergence criterion (Eq. (8.2)) is satisfied using the heat flux vector  $\mathbf{q}_n$  and the average fluid temperature from the experiment  $\bar{T}_{cf,exp}$ . The solution of the current estimation is used as the initial guess values of the next estimation, as stated above. When the estimations are finished for the first period, the objective function of the estimation changes to Eq. (8.3), which has only  $R_b$  as the variable.  $\lambda_{eff}$  is fixed to the final estimated value of the first injection period.

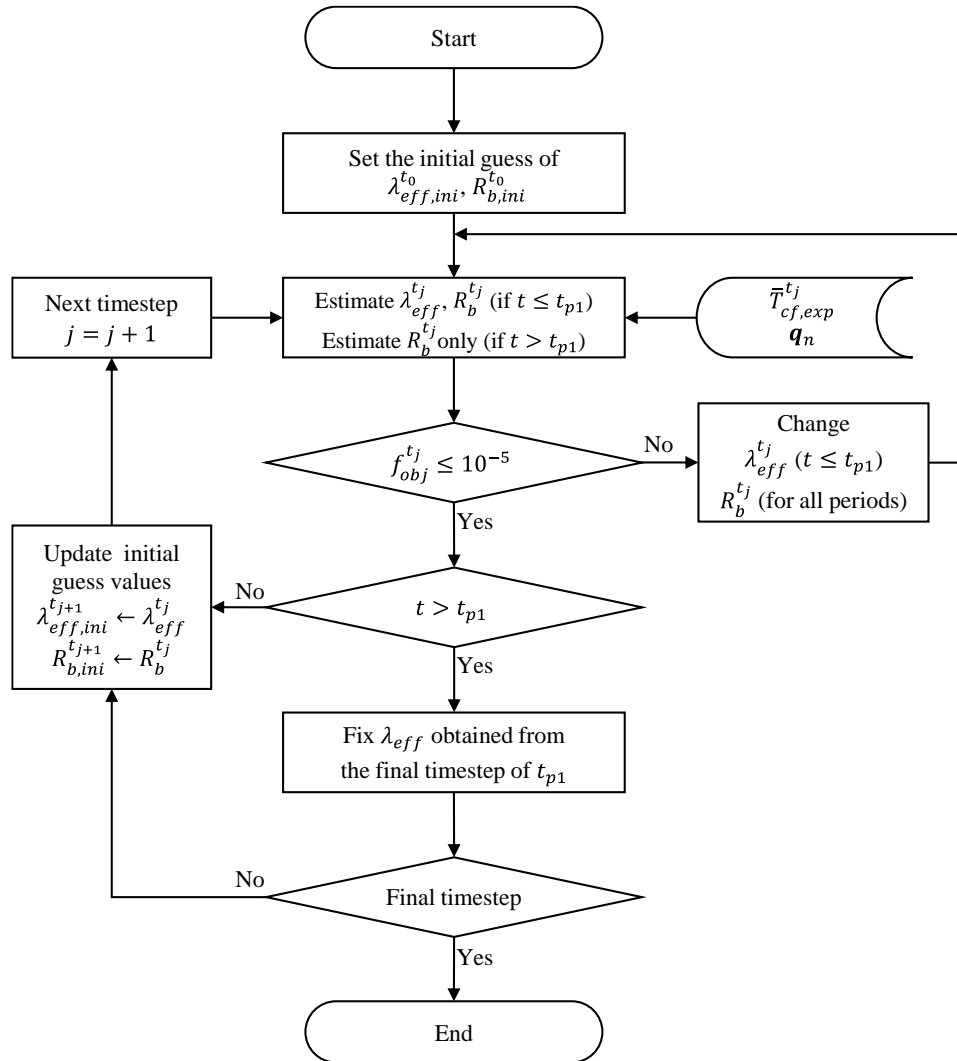


**Fig. 8.3** Flowchart of parameter estimation for multi-heat injection rate thermal response test.

### 8.2.3 Verification of proposed estimation method

To verify the effectiveness of the proposed method, numerical TRT data were generated using the finite element method. A 3-D numerical model was used, and the geometry of the BHE was fully discretized. The flow in the U-tube was modeled using 1-D linear elements. A detailed description of this modeling technique is given in Section 5.2. Except for the linear elements in the U-tube, the model only considers conductive heat transfer. The governing equation is as follows:

$$(\rho c)_s \frac{\partial T}{\partial t} - \nabla^2 \lambda_s T = 0 \quad (8.4)$$

The geometry of the BHE in the numerical model was exactly the same as that listed in Table 8.1. The calculation domain had dimensions of  $15\text{ m} \times 15\text{ m} \times 80\text{ m}$  (length  $\times$  width  $\times$  depth). The horizontal mesh was generated with a triangular mesh generator [143]. The size of the finite elements was varied spatially to consider the temperature gradient. The smallest element size of  $0.7\text{ mm}$  was used for the U-tube heat exchanger where the steepest temperature gradient was expected. The element size was gradually increased toward the lateral boundaries. The number of elements per slice was 7467. In the vertical direction, the calculation model had 76 slices, and the vertical distance between slices was varied from  $0.02$  to  $5\text{ m}$  so that different vertical temperature gradients could be considered appropriately. Fig. 8.4 shows an overview of the discretized model and the model domain. Table 8.1 lists the thermal properties of all the components, which were isotropic, homogeneous, and constant (i.e., no temperature dependence). The thermal conductivity of the soil was set to  $1.8\text{ W}/(\text{m}\cdot\text{K})$ .

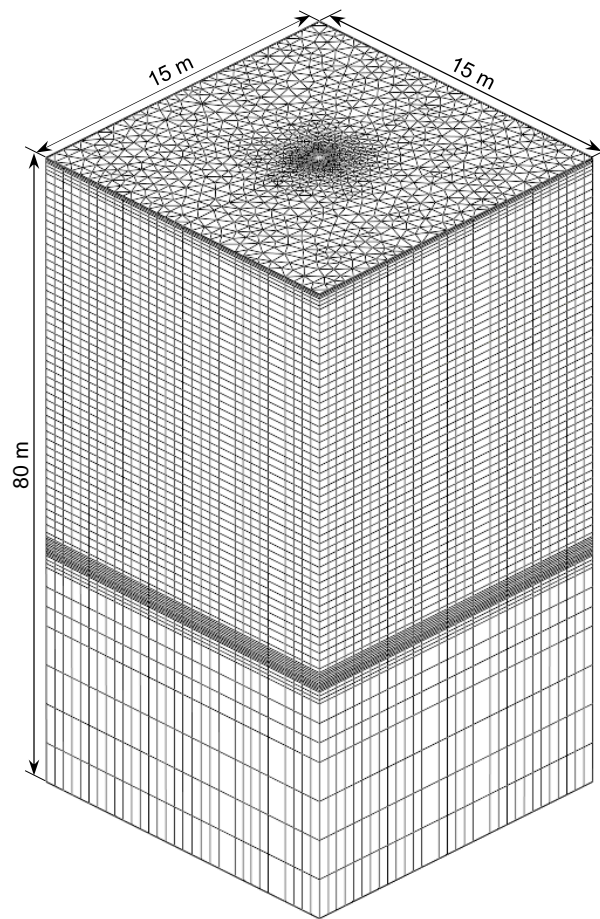


**Fig. 8.4** Overview of discretized numerical model and size of model domain (not to scale).

**Table 8.1** Thermal properties used in numerical model and settings for TRT.

Parameter [units]	Value
Grout	
Thermal conductivity [W/(m·K)]	1.4
Volumetric thermal capacity [MJ/(m <sup>3</sup> ·K)]	2.0
Soil	
Thermal conductivity [W/(m·K)]	1.8
Volumetric thermal capacity [MJ/(m <sup>3</sup> ·K)]	2.5
TRT setting	
Heat injection rate of $Q_{p1}$ , $Q_{p2}$ , and $Q_{p3}$ [kW]	2.0, 3.0, 4.0
Duration of each injection period, $t_{p1}$ , $t_{p2}$ , and $t_{p3}$ [h]	48, 24, 48
Volumetric flow rate [L/min]	15

The entire domain had an initial temperature of 17 °C. The top, bottom, and lateral boundary conditions were adiabatic. The boundary condition of the BHE was defined using time-varying Dirichlet conditions as follows:

$$T_{cf,in}(t_i) = T_{cf,out}(t_{i-1}) + \frac{Q_{BHE}(t_i)}{\rho_{cf}c_{cf}\dot{V}_{cf}(t_i)} \quad (8.5)$$

The flow rate  $\dot{V}_{cf}$  was set to 15 L/min. The first, second and third injection periods ( $t_{p1}$ ,  $t_{p2}$ , and  $t_{p3}$ ) were 48, 24, 48 h, respectively. The heat injection rates of each period ( $Q_{p1}$ ,  $Q_{p2}$ , and  $Q_{p3}$ ) were 2, 3, and 4 kW (40, 60, and 80 W/m), respectively. The time step of the calculation was 6 min.

Fig. 8.5 shows the temperature response and heat injection rate. The data from 15 h were used to conduct estimations at 6 min intervals because the ILS model cannot accurately consider the early-period temperature response. The initial guess values were  $\lambda_{eff} = 1.78$  W/(m·K) and  $R_b = 0.17$  m·K/W. Table 8.2 summarizes the final estimated  $\lambda_{eff}$  in  $t_{p1}$  and the final estimated  $R_b$  values of each period. Fig. 8.6 shows the estimated values at 1 h intervals. The relative error for a certain elapsed time is defined as follows:

$$\epsilon_{rel}(t) = \frac{|R_{b,ref} - R_b(t)|}{R_{b,ref}} \quad (8.6)$$

where  $R_{b,ref}$  is the final estimated  $R_b$  in  $t_{p1}$ , i.e.,  $R_{b,ref} = R_b(48)$ .

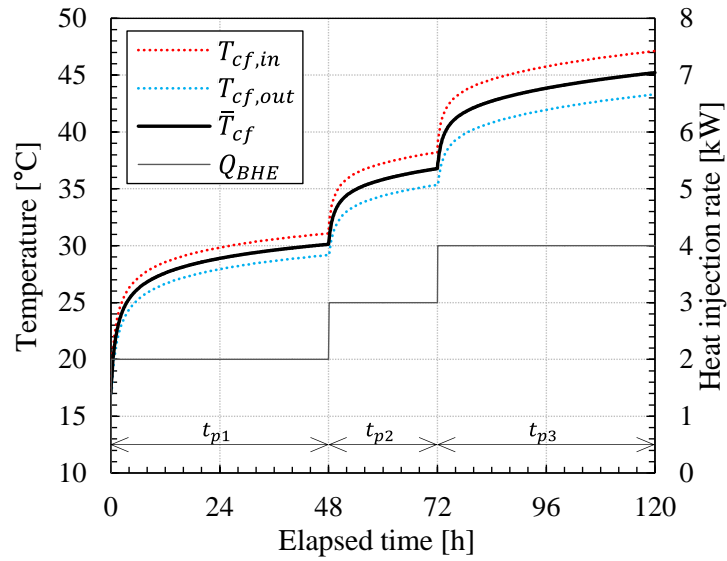


**Fig. 8.5** Temperature response curve and heat injection rate from numerical thermal response test.

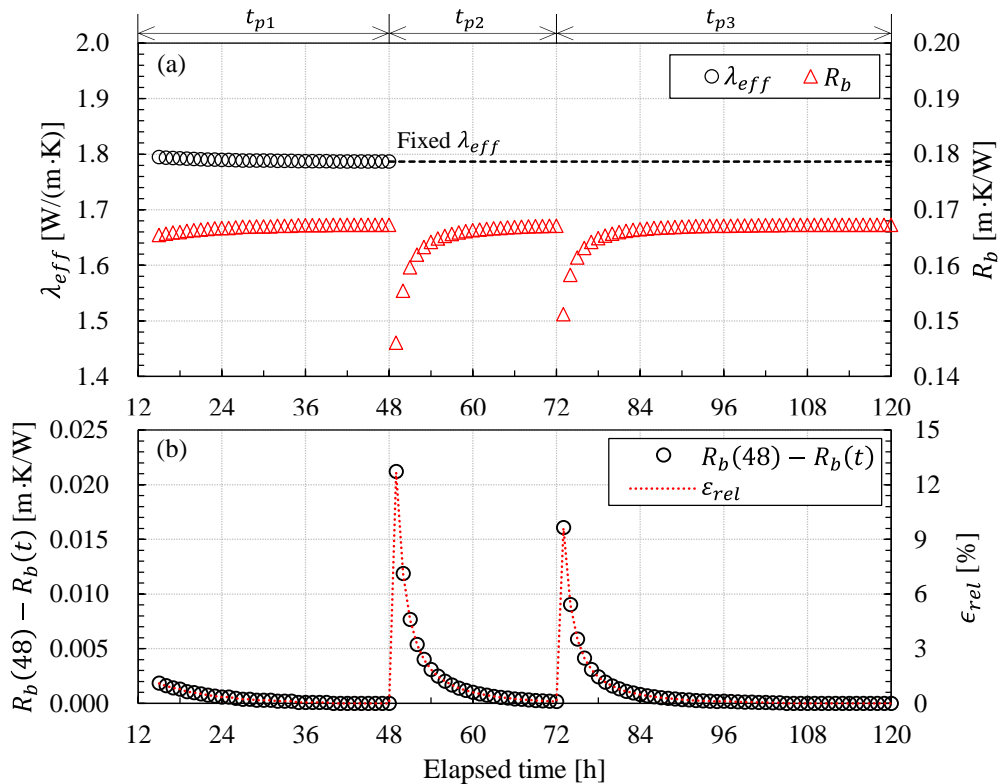


**Fig. 8.6** Estimated results and deviation of borehole thermal resistance based on final estimated value in first injection period ( $t_{p1} = 48$  h): (a) estimated effective thermal conductivity and borehole thermal resistance and (b) absolute and relative errors of borehole thermal resistance based on final estimated value in first injection period.

**Table 8.2** Initial guess values and estimated values.

Initial guess values of $\lambda_{eff}$ and $R_b$ [W/(m·K)], [m·K/W]	Final estimated $\lambda_{eff}$ in $t_{p1}$ [W/(m·K)]	Final estimated $R_b$ of each period [m·K/W]		
		$t_{p1}$	$t_{p2}$	$t_{p3}$
1.78, 0.17	1.79	0.167	0.167	0.167

The final estimated  $\lambda_{eff}$  in  $t_{p1}$  was 1.79 W/(m·K), which was very close to the set value of 1.8 W/(m·K). When the heat injection rate changed (at 48 and 72 h), the estimated  $R_b$  abruptly decreased and then gradually increased with time. This was caused by the limitations of the ILS model, which cannot accurately consider the transient temperature response when it is dominated by the BHE itself. For  $\epsilon_{rel}$  to become less than 1%,  $t_{p2}$  and  $t_{p3}$  needed to be 9 and 8 h, respectively. Although unstable behavior was observed when the heat rate changed, the final estimated  $R_b$  in  $t_{p2}$  and  $t_{p3}$  were almost the same as that in  $t_{p1}$  (Table 8.2). This means that, if the heat transfer in the ground is dominated by conduction, the  $\lambda_{eff}$  and  $R_b$  values estimated with the proposed method are independent of the heat injection rate. Therefore, if the multi-heat injection rate TRT is conducted in a saturated porous formation where the advection effect from the groundwater flow is negligible, and the estimated  $R_b$  is changed by the higher heat rate, the natural convection causes the change in  $R_b$ . Because  $\lambda_{eff}$  is fixed from  $t_{p2}$ , the effect of natural convection is fully reflected in  $R_b$  alone. Thus, the effectiveness and reliability of the proposed method were verified through this demonstration using numerical TRT data.

## 8.4 Multi-heat injection TRT and results

### 8.4.1 Test condition

Table 8.3 summarizes the test conditions. The heat injection rates and flow rates were averaged over the duration of each period. For each borehole, TRTs were conducted twice with different injection period durations: first and second periods of 48 and 24 h, respectively, or 72 and 48 h, respectively. Once a test was completed, the next test was begun when the ground temperature had returned to near the initial value (17–17.5 °C).

### 8.4.2 Temperature response

Fig. 8.7 shows the temperature responses of GR1 and BF1, and Fig. 8.8 shows the temperature responses of GR2 and BF2. When the heat injection rate and duration are the same, the BHE with the lower temperature should provide the better performance. It was difficult to control the heat injection rates of

different TRTs to be identical because of fluctuations in the voltage and the heat exchange with the outdoor environment. Fortunately, the heat injection rates for the TRTs in this study were very similar (Table 8.3). Therefore, the performance of each BHE could be intuited. At the end of each injection period, BF-BHE showed a lower temperature (Table 8.4). At the end of the first injection period, BF1 showed a 0.53 °C lower average fluid temperature than GR1, and BF2 showed a 0.94 °C lower temperature than GR2. At the end of the second injection period, BF1 showed a 0.94 °C lower average fluid temperature than GR1, and BF2 showed a 1.16 °C lower temperature than GR2. Because the TRT conditions at different times were not the same (e.g., initial ground temperature, change in moisture content and resulting change in effective thermal conductivity, and groundwater level), the direct comparison of different TRTs was somewhat unreliable. However, the temperature difference between BF-BHE and GR-BHE, which had the same injection period and heat rate, increased with time. Therefore, BF-BHE can be argued to have performed better than GR-BHE.

**Table 8.3.** Experimental conditions for four thermal response tests (averaged values during each test).

Test name [BHE-No.]	Starting time of heat injection [Date, time]	Duration [h]		$Q_{BHE}$ [kW] ([W/m])		$\dot{V}_{cf}$ [L/min]
		$t_{p1}$	$t_{p2}$	$t_{p1}$	$t_{p2}$	
GR1	Jan. 13, 2015, 12:00	48	24	2.27 (45.4)	4.49 (89.8)	21.02
BF1	Dec. 15, 2014, 14:00	48	24	2.26 (45.2)	4.47 (89.4)	20.98
GR2	Mar. 1, 2015, 13:00	72	48	2.25 (45.0)	4.51 (90.2)	19.21
BF2	Feb. 5, 2015, 13:00	72	48	2.23 (44.6)	4.49 (89.8)	19.21

**Table 8.4.** Final average temperature of each injection period.

Test name [BHE-No.]	Initial ground temp [°C]	Final $\bar{T}_{cf}$ of $t_{p1}$ [°C]	Final $\bar{T}_{cf}$ of $t_{p2}$ [°C]
GR1	17.7	32.37	44.78
BF1	17.0	31.84	43.84
GR2	17.2	31.72	45.43
BF2	16.7	30.69	44.27

### 8.4.3 Interpretation results

Before the parameter estimation was begun, the stepwise sequential estimation using the ILS model was performed to obtain the initial guess values for the parameter estimation. The stepwise regressive estimation was performed on data recorded over 5 s at intervals of 3 min. The first 15 h of temperature response data was not included in the estimation because of the limitations of the ILS model. The

sequential plots of GR1 and BF1, which had first injection periods of 48 h, had either no convergence or unknown convergence (Fig. 8.9). Compared to  $t_{p1} = 48$  h cases, convergences were confirmed for the sequential plots when  $t_{p1} = 72$  h (GR2 and BF2) (Fig. 8.10). Therefore, good initial guess values for the parameter estimation could not be obtained in the estimations of GR1 and BF1. Thus, when information about the test site is not available, the first injection period should not be less than 60 h.

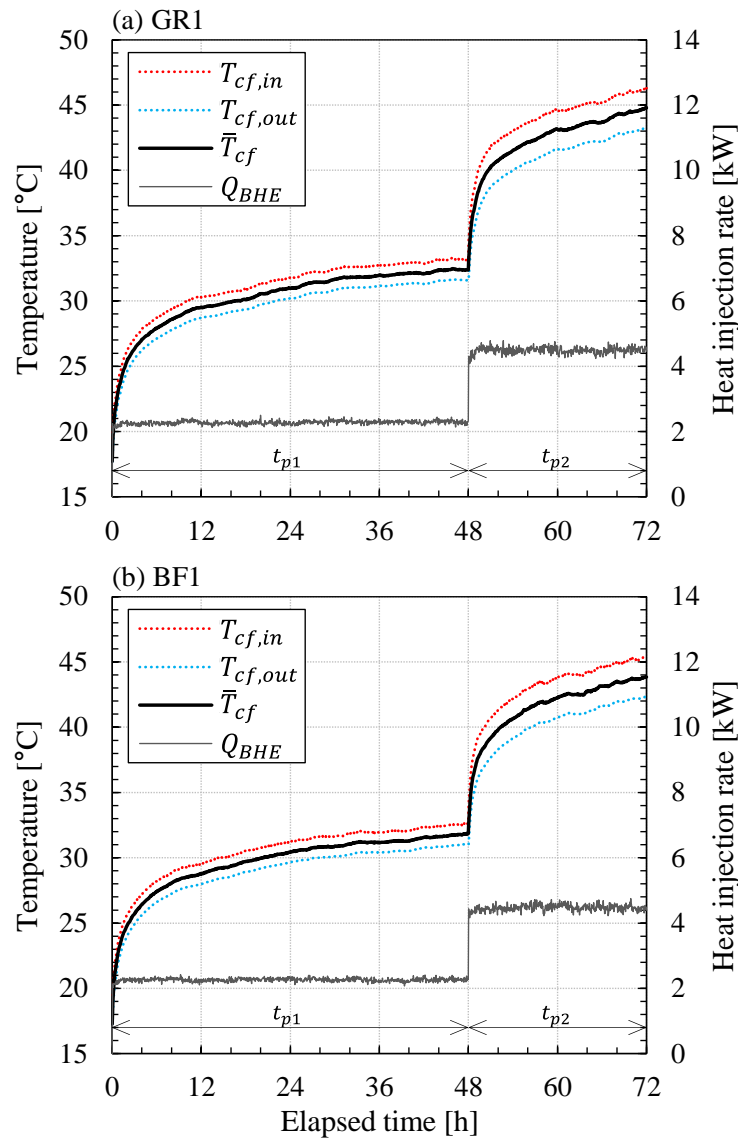


**Fig. 8.7** Temperature response curve and heat injection rate of 24–48 h cases: (a) GR1 and (b) BF1.

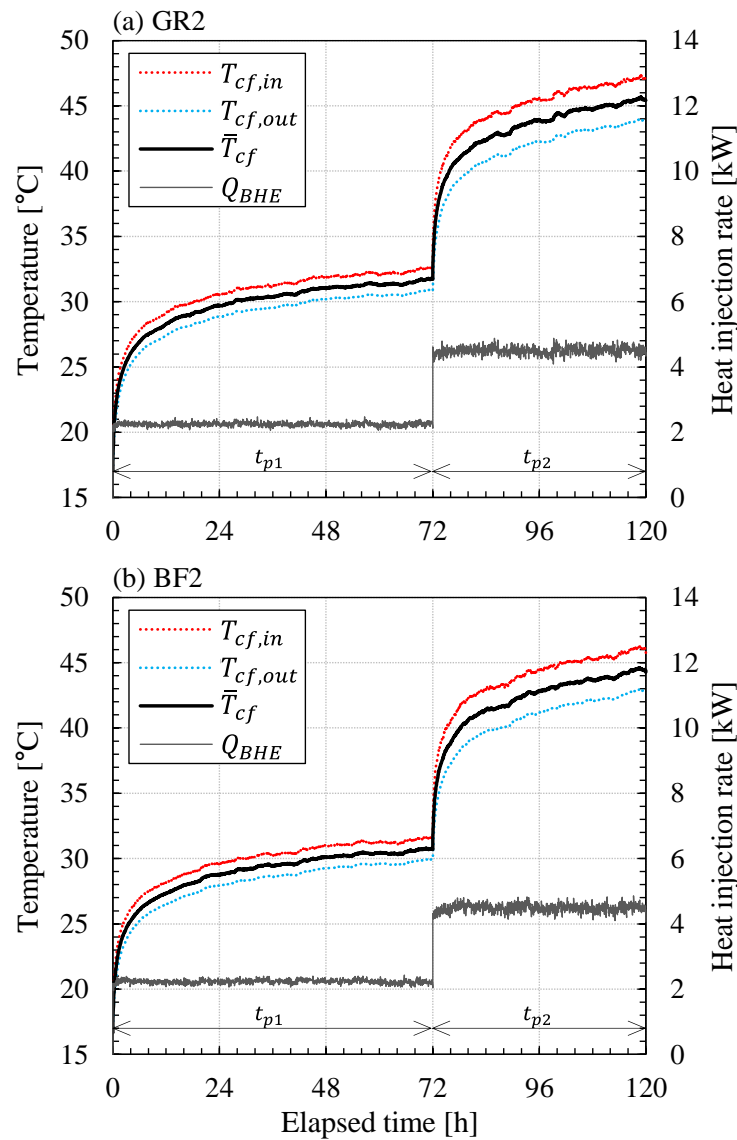


**Fig. 8.8** Temperature response curve and heat injection rate of 48–72 h cases: (a) GR2 and (b) BF2.

The proposed method was used for parameter estimation at 3 min intervals, and the results of the 48 and 24 h cases (GR1 and BF1) and 72 and 48 h cases (GR2 and BF2) are shown in Fig. 8.11 and Fig. 8.12, respectively. Although the effective thermal conductivity  $\lambda_{eff}$  and borehole thermal resistance  $R_b$  were estimated every 3 min, their values are shown at 1 and 2 h intervals in Fig. 8.11 and Fig. 8.12, respectively, for clarity. Table 8.5 summarizes the initial guess values of each estimation case, the estimated  $\lambda_{eff}$  and  $R_b$  values of each injection period, and the rate of change in  $R_b$  as the heat rate was increased.

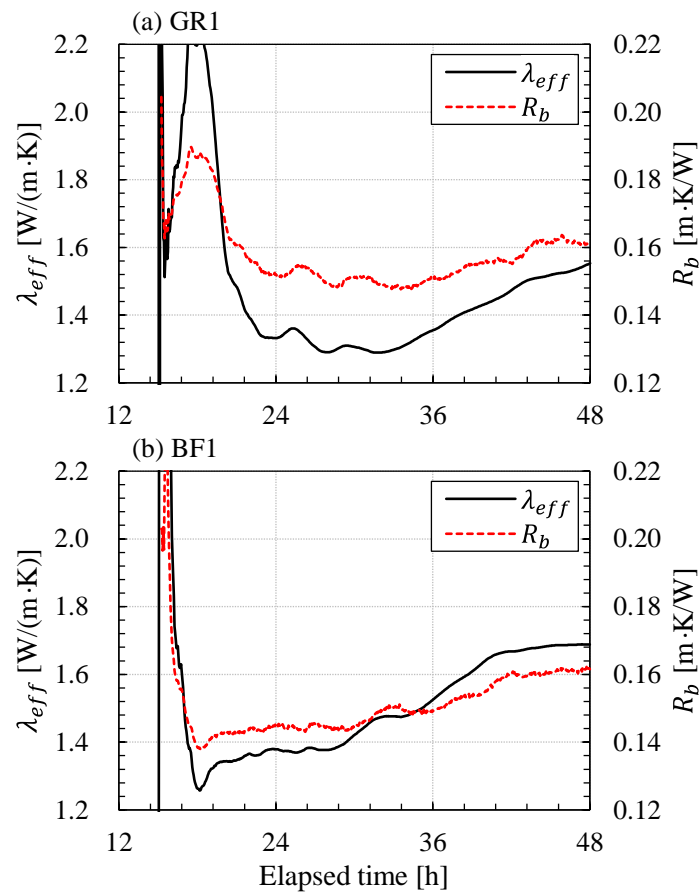


**Fig. 8.9** Sequential estimation of first injection period ( $t_{p1} = 48$  h): (a) GR1 and (b) BF1.

The initial guess values of GR1 and BF1 have uncertainty because they did not converge during the sequential estimation (Fig. 8.9). Thus, the initial guess values were decided based on the estimated values from single-heat injection rate TRTs conducted in 2014. The estimated behavior was very stable because the variation in the heat rate due to disturbances can be considered by temporal superposition. As demonstrated by the numerical verification of the proposed method, when the heat injection rate changed from  $Q_{p1}$  to  $Q_{p2}$  (at 48 h for GR1 and BF1 and at 72 h for GR2 and BF2), the estimated  $R_b$  abruptly decreased and then gradually increased with time. During this unstable early portion of the second injection period, the estimation also showed somewhat unstable behavior. As shown in Fig. 8.13, some time steps did not converge within 6 h after the second injection period was begun. The same estimation behavior was also observed in other TRT cases. This is the reason why the second and third periods should continue for at least 24 h.

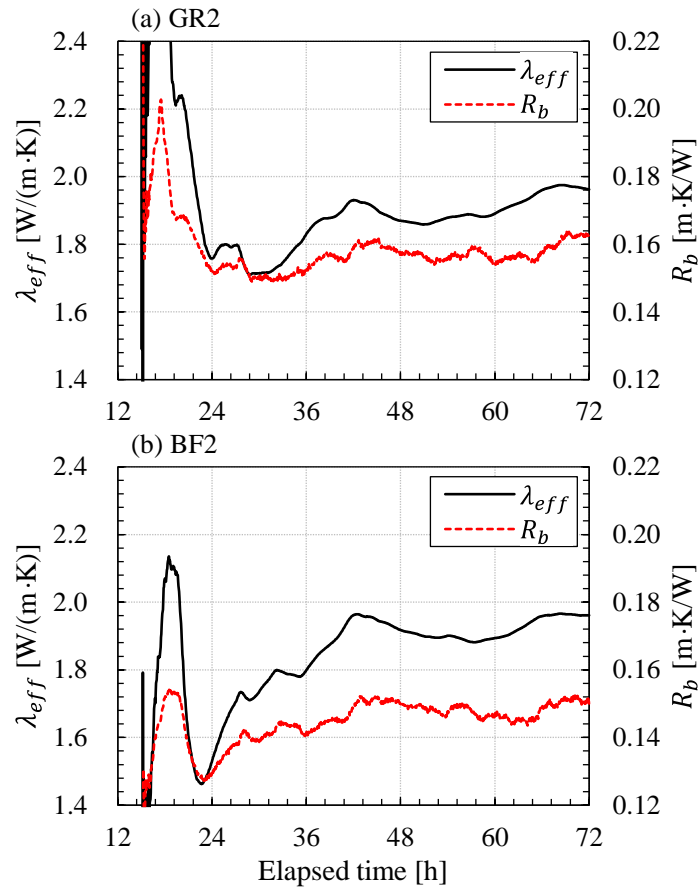


**Fig. 8.10** Sequential estimation of first injection period ( $t_{p1} = 72$  h): (a) GR2 and (b) BF2.

The estimated  $\lambda_{eff}$  and  $R_b$  values for the first injection period of the TRTs in GR-BHE (GR1 and GR2) were very close (Table 8.5). Although GR2 showed slightly superior  $\lambda_{eff}$  and  $R_b$  values compared to GR1, the rates of reduction in  $R_b$  from  $Q_{p1}$  to  $Q_{p2}$  in GR1 and GR2 were almost the same. The estimated  $\lambda_{eff}$  values for the first injection period of the TRTs in BF-BHE (BF1 and BF2) were also very close. However, the estimated  $R_b$  of BF2 was 5.5% lower than that of BF1. The rates of reduction in  $R_b$  from  $Q_{p1}$  to  $Q_{p2}$  in BF-BHE (BF1 and BF2) were greater than those in GR-BHE. While  $R_b$  decreased by 7.6% in GR-BHE, it decreased by 11.0% in BF1 and 8.7% in BF2. Similar results were obtained in Chapter 7, where two single-heat injection rate TRTs were conducted for each BHE. The rate of reduction in  $R_b$  was 7.8% for GR-BHE and 11.4% for BF-BHE. In Chapter 7, the  $\lambda_{eff}$  value of TRT that was estimated using a higher heat rate (4 kW heater) was adjusted to the  $\lambda_{eff}$  value of the lower heat rate (2 kW heater) TRT by using the ill-posed nature of the parameter estimation.

It is difficult to ascertain the reasons for the different rates of reduction in  $R_b$  between BF1 and BF2.

During the recovery time, the ground condition can vary, as described in the introduction. These temporal changes can be to the depth-averaged ground temperature, moisture content and resulting change in soil conductivity, and groundwater level. All of these can be possible causes for the different results.

**Table 8.5** Initial guess values used for the estimations, estimated effective thermal conductivity, borehole thermal resistance, and rate of change in borehole thermal resistance from first injection period to second injection period.

Test name [BHE-No.]	Initial guess values of $\lambda_{eff}$ and $R_b$ [W/(m·K)], [m·K/W]	Final estimated value of $\lambda_{eff}$ in $t_{p1}$ [W/(m·K)]	$R_b$ [m·K/W]		Rate of change in $R_b$ [%]
			$t_{p1}$	$t_{p2}$	
GR1	1.90, 0.17	1.91	0.168	0.155	-7.8
BF1	1.90, 0.16	1.88	0.165	0.147	-11.0
GR2	1.96, 0.16	1.97	0.160	0.147	-7.8
BF2	1.96, 0.15	1.93	0.156	0.142	-8.7

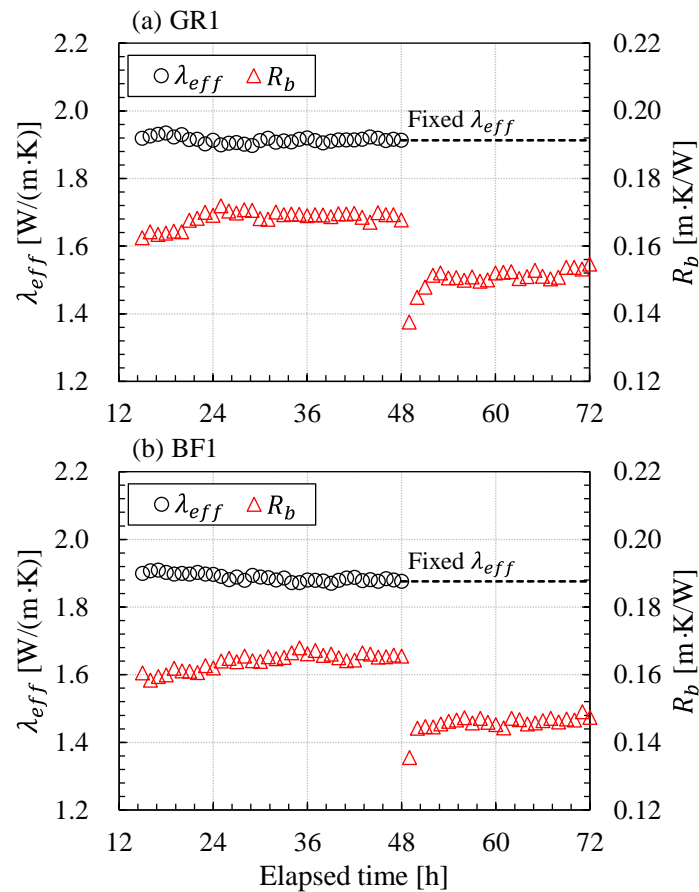


**Fig. 8.11** Estimated effective thermal conductivity and borehole thermal resistance using developed method; (a) GR1 and (b) BF1.

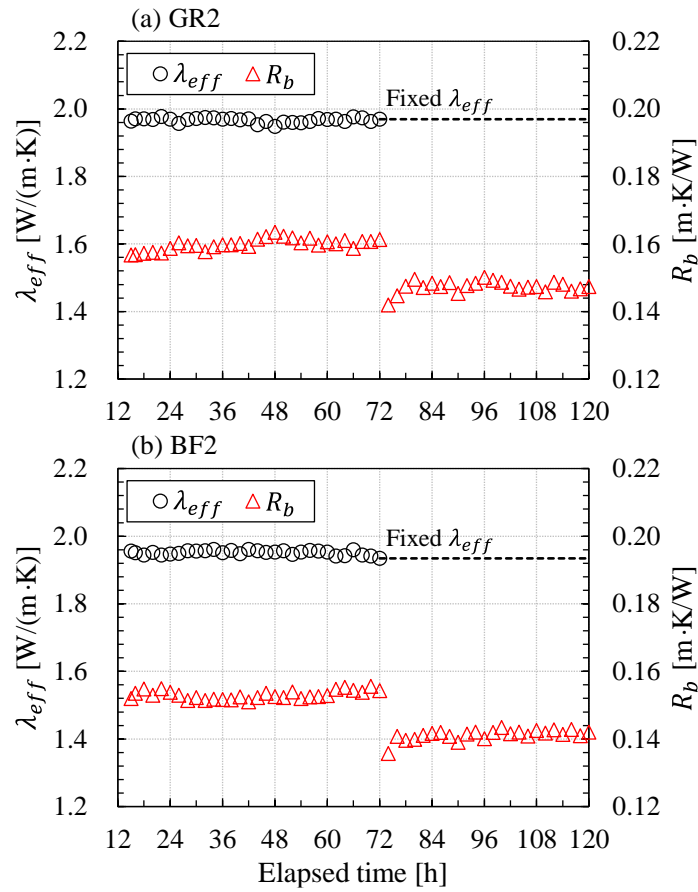


**Fig. 8.12** Estimated effective thermal conductivity and borehole thermal resistance using developed method; (a) GR2 and (b) BF2.

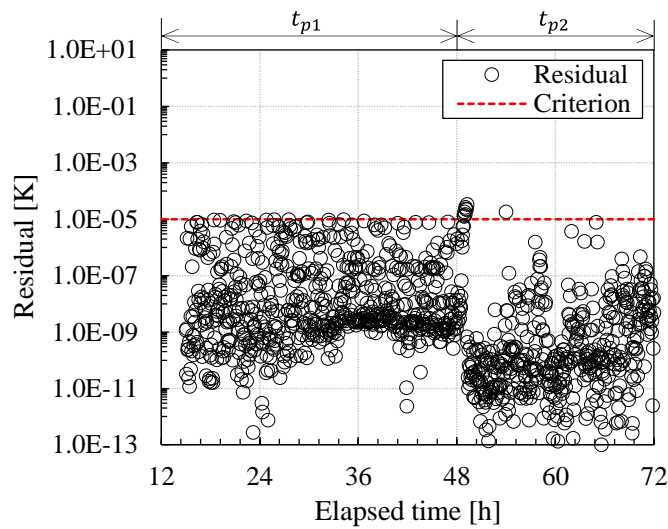


**Fig. 8.13** Residuals of BF1 estimation (3 min intervals from 15 h to 72 h; 1140 time steps in total).

Interesting results were observed in the TRTs with the two BHEs used in this study. The results in Fig. 8.14 were obtained from TRTs conducted from February 2014 to March 2015. All of the results were obtained using the proposed parameter estimation method with a fixed  $\lambda_{eff}$  value of 1.85 W/(m·K) so that only  $R_b$  could be compared. The BHE's performance clearly improved (i.e.,  $R_b$  decreased) over time. The  $R_b$  values obtained from TRTs conducted before August 2014 were 0.18–0.19 m·K/W in GR-BHE and 0.17–0.18 m·K/W in BF-BHE. However, the  $R_b$  values obtained from TRTs conducted after October 2014 were around 0.17 m·K/W in GR-BHE and 0.16 m·K/W in BF-BHE. It is difficult to conclude whether these different results were simply caused by a temporal change in ground conditions or that time was needed for the performance to stabilize after the BHEs were constructed. However, the dependence of the results on the temporal change in conditions, which was the motivation of this work, was clearly observed in the results of the series of TRTs conducted for more than 1 year. A long time interval between TRTs can lead to significant error if the purpose of a series of TRTs is comparing different TRT settings (e.g., heat injection rate) and the resulting thermal behavior of the BHE. The results demonstrate why the temporal change in ground conditions should be minimized and controlled. The proposed method is less-affected by changes in the ground condition and thus can more accurately examine the heat rate dependence of a BHE installed in a saturated porous formation because it requires only a single TRT to be performed around 100 h.

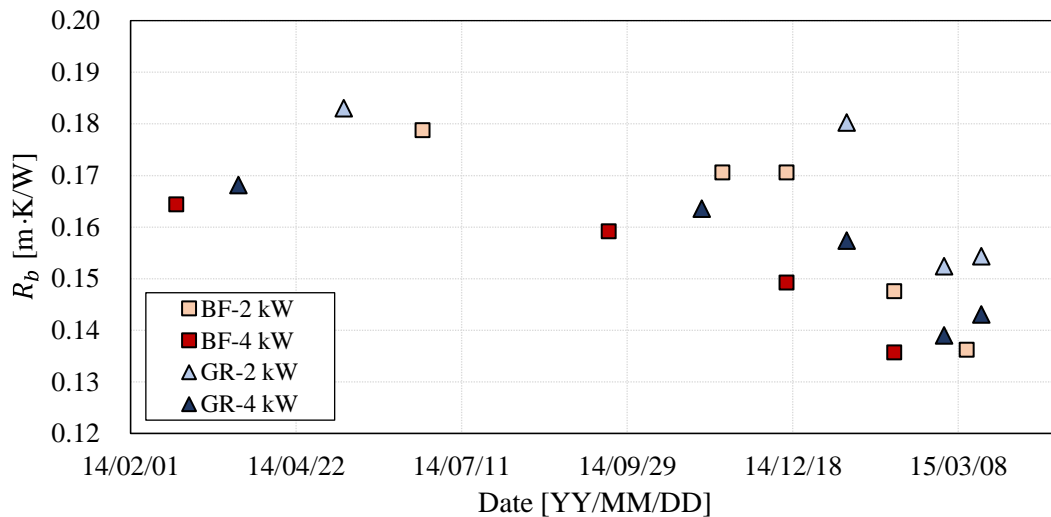


**Fig. 8.14** TRT results obtained at same site from February 2014 to March 2015.

## 8.4 Real-time interpretation method for onsite TRT

The proposed method can be used to perform very fast estimations. Fig. 8.15 shows the estimation times of every time step in GR2 (e.g., from 15 h to 120 h, 2100 time steps in total). The computer used for this had the following specifications: CPU of Intel i7 3.6 GHz and RAM of 16 GB. No parallel computation was applied; only a single core was used for the estimation. As the estimation proceeded, the calculation time linearly increased because the number of heat pulses used for the temporal superposition increased. For example, if parameters are estimated for 20 h, the required number of heat pulses is 400. If the parameters are estimated for 100 h, the required number of heat pulses is 2000. Although the amount of computation increased with the elapsed time of a TRT, the computation time of one time step close to 120 h was less than 0.05 s. The total computation times for GR1, BF1, GR2 and BF2 were 32.9, 33.0, 49.0, and 48.6 s, respectively. Therefore, the proposed method is sufficiently fast for application to real-time estimation in onsite TRTs.

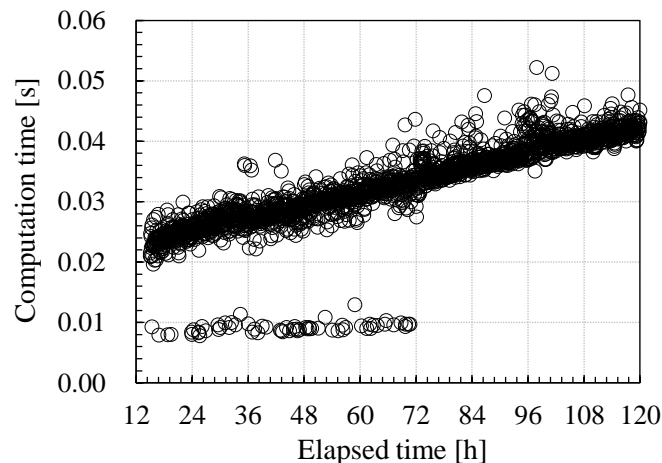


**Fig. 8.15** Computation time for estimation of GR2 (3 min intervals from 15 h to 120 h, 2100 time steps in total, total computation time of 49.0 s)

Fig. 8.16 suggests a flowchart for real-time application. First, sequential estimation is conducted from the 48th hour of heat injection ( $t_{cur} = 48$  h) using the ILS model with the averaged heat rate. If there is no convergence, this is repeated at 3-h intervals until convergence is achieved. Of course, the start time of the sequential estimation and time interval for the next estimation can be changed by the experimenter. The minimum required time of a TRT can be changed according to the BHE configuration and quality of the obtained data. In relation to this, many different arguments can be found in the literature [18,90,96,98–100,146]. The convergence can be determined by the experimenter according to the behavior of the

sequential plot, or the following criterion of  $|\lambda_{eff}(t_{cur}) - \lambda_{eff}(t_{cur} - 3)| \leq 0.01 \text{ W}/(\text{m}\cdot\text{K})$  can be used. Because the sequential estimation cannot consider the disturbance, the convergence of the first period is examined again using the developed parameter estimation method to determine whether the heat transfer is dominated by conduction. The same criterion used to determine the convergence of the sequential estimation or a stricter criterion can be applied. If  $\lambda_{eff}$  shows increasing behavior, the proposed method based on the ILS model is not appropriate for interpreting the TRT. The advection effect of the groundwater flow should be considered with other models, such as the moving line source model [9,32,172], or a numerical method. If the criterion is satisfied, the second injection period can be started. Through the application of this real-time estimation, the overall test time can be reduced.

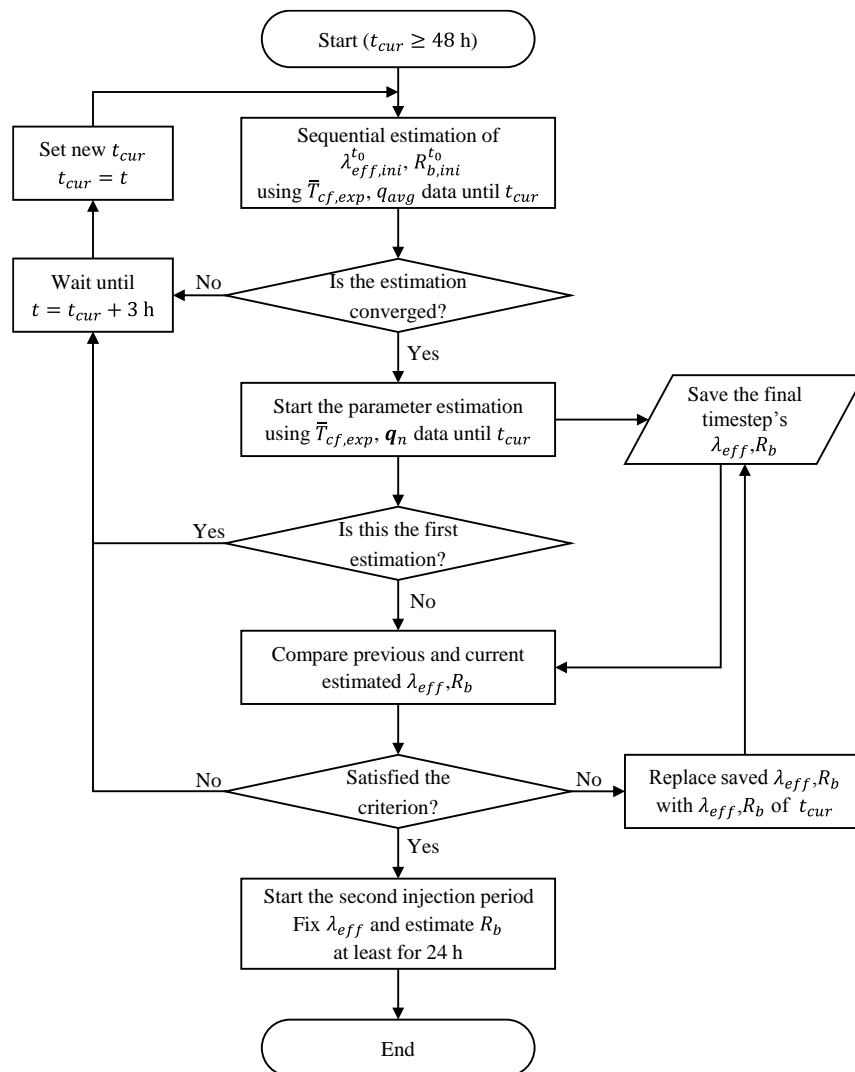


**Fig. 8.16** Flowchart for real-time application of developed method.

## 8.5 Conclusion

In order to consider the temporal change in ground conditions during multiple TRTs, this study proposed a method of combining a multi-heat injection rate TRT with a parameter estimation method to accurately and practically examine the heat rate dependence of the BHE performance in a saturated porous formation with a single TRT. The main results can be summarized as follows:

- The effectiveness and reliability of the proposed method were verified through an estimation using numerically generated TRT data.
- The change in performance by natural convection can be examined with a single TRT taking place over approximately 100 h.
- The BF-BHE showed a greater performance enhancement by the increased heat injection rate than the GR-BHE.
- The total estimation time for 2100 time steps was less than 50 s. Therefore, the required time of the proposed method can be shortened through real-time estimation of onsite TRT. An estimation scheme for real-time application is also provided.

CHAPTER 9  
CONCLUSIONS AND FUTURE STUDIES

## 9.1 Conclusions

This thesis focused on determining the accuracy of a BHE design by estimating the accuracy of design parameters for a TRT. Two main subjects were studied: disturbances to conducting a TRT and the heat rate dependence of TRT results caused by natural convection in a saturated porous formation. This thesis put more emphasis on providing practical advice and alternative methods to the experimenters rather than simply a scientific analysis of phenomena. Theoretical, numerical, and experimental examinations and verifications were performed to provide insight into these problems. An alternative interpretation method for disturbed response data and a method to examine the heat rate dependence of the BHE performance were developed. A detailed discussion and conclusions are given in Chapters 4–8; the main results of this thesis are summarized and emphasized here.

Chapter 4 presents the derivation of an analytical model that describes the heat exchange between the circulating fluid and outdoor environment in an aboveground TRT setup. The accuracy of the derived model was verified against in situ TRT data in Chapter 5. Based on the model, a parametric study and sensitivity analysis were conducted in a systematic manner using disturbance-related parameters such as the test settings (heat injection rate and flow rate), aboveground connecting circuit parameters (insulation thickness, length, and radiation absorptivity), temperature of fluid, and weather conditions (solar irradiation, environmental temperature, and wind velocity). With regard to the perturbation of the temperature response, many researchers simply referred to the coupling effect from the ambient temperature. However, this is not an accurate expression. The results showed that the solar irradiation had the biggest impact on the disturbance. Therefore, care should be taken with regard to radiation-related parameters, such as the radiation absorptivity of the hydraulic circuit's surface and the length of the circuit. If possible, a canopy-like installation that can cover the TRT setup to block solar irradiation is desirable. With regard to the TRT settings, a high heat injection rate should be used because the heat exchange rate with the outdoor environment decreases as the heat injection rate increases. However, as discussed in Chapters 7 and 8, if the formation is saturated, the effect of natural convection should be considered when a high heat rate is used. For the flow rate, it is difficult to draw a general conclusion. Selecting a flow rate that can minimize the relative intrinsic error of the temperature and flow sensors (e.g., intrinsic error of the sensor/measured value) would be the best choice because the flow rate has little impact on the disturbed heat rate.

Chapter 5 examines the applicability and limitations of the conventional interpretation with the ILS model based on numerically generated disturbed TRT data. A fully discretized 3-D numerical model was developed using the finite element method, and the analytical model developed in Chapter 4 was combined with the numerical model as a boundary condition. Typical synthetic weather data of different seasons and 36 cases of measured weather data were used to numerically conduct and interpret TRTs. The results showed that a TRT duration of at least 60 h is required for the error of the estimated data to be within  $\pm 5\%$ . Especially when the TRT is affected by high solar irradiation on the first day of the TRT, the duration should be longer than 60 h. Note that the error in actual situations can be greater than these results because the numerical model did not consider the random error of the sensors and fluctuations in the supply voltage. If the allowed duration is less than 60 h or a temperature perturbation is clearly shown, an interpretation method that can consider a variable heat rate should be applied.

As a solution to interpreting disturbed TRT data, Chapter 6 presents an alternative interpretation method that can consider a variable heat rate and provide additional information about the ground as the sequential estimation method. The proposed method is a discrete parameter estimation method that uses a temporal superposition-applied ILS model combined with the quasi-Newton optimization method. To verify the effectiveness, the proposed method was applied to in situ TRTs, and the results were compared with those of the conventional method in terms of the estimation stability and convergence speed. By applying the limit of the search ranges and an update scheme to the initial guess values, the proposed method achieves robustness, a low computation cost, and fast convergence. When compared to the conventional estimation method in a sequential manner, the proposed method showed a convergence speed that was approximately four times faster. Therefore, if the experimenter already knows information about the formation and the heat transfer is conduction-dominant, then the TRT duration can be shortened with the proposed method.

Chapter 7 examines the effect of natural convection in a saturated porous formation and the performance dependence of BHE on the heat injection rate. TRTs were conducted with two BHEs having the same geometry but different backfill materials: one was cement-grouted, and the other was gravel-backfilled. TRTs were conducted for each BHE at two different heat injection rates (approximately 40 and 80 W/m). The developed parameter estimation method was used for the estimations (Chapter 6). The effective thermal conductivity of the higher heat rate TRT was adjusted to close to that of the lower heat rate TRT by using the ill-posed characteristic of the inverse parameter estimation because natural convection can affect both the effective thermal conductivity and borehole thermal resistance. By doing so, a fair comparison with the estimated borehole thermal resistance becomes possible. In the gravel-backfilled BHE, when the heat rate was increased from 44.8 W/m to 88.4 W/m, the borehole thermal resistance

decreased 11.1%. In the cement-grouted BHE, when the heat rate was increased from 45.0 to 83.8 W/m, the borehole thermal resistance decreased 7.7%. In terms of performance and constructability, completing a BHE with porous backfill material provides more advantages.

Chapter 8 discusses the uncertainty and drawbacks of multiple TRTs using different single-heat injection rates to examine the heat rate dependence in saturated porous formations, that is, the long recovery time between TRTs and the change in ground conditions during the recovery period. A new practical method is proposed to overcome these problems. The new method uses a multi-heat injection rate TRT and the developed parameter estimation method with the ILS model. The quasi-Newton method was successfully corrected to handle a multi-heat injection rate TRT. The effectiveness of the proposed method was verified by using numerically generated multi-heat injection rate TRT data. Four TRTs were conducted with the two different BHEs presented in Chapter 7. Because the estimation method was sufficiently fast and robust (total time for 2300 discrete estimations was less than 50 s), a real-time estimation method for an onsite TRT is also proposed to reduce the test time.

## 9.2 Recommendations for future studies

Most disturbance factors were analyzed with respect to the effect of outdoor environment. However, the voltage fluctuation was not considered in this thesis. Although the developed parameter estimation method can consider the consequent power fluctuation of heaters, future studies should consider the amount of error produced, and the change in the results with the disturbance effect from the outdoor environment when the conventional regression estimation is applied.

Many topics related to the effect of natural convection in a saturated porous formation can be studied. In particular, searching for the critical Rayleigh number that describes the critical driving conditions of natural convection is important. The Rayleigh number is determined by the geometry of the BHE, permeability of the soil, and heat injection rate (temperature difference). This can be examined using reduced-scale experiments and numerical methods. The impact of the thermohydraulic properties of different porous backfill materials on the BHE performance is another important topic for studies. The design method for a BHE should be elaborated upon to consider the effect of natural convection on the BHE performance.

## REFERENCES

- [1] Brundtland Commission. *Our Common Future: World Commission on Environment and Development (The Brundtland Commission)*. New York: 1987.
- [2] International Energy Agency (IEA). *Transition to Sustainable Buildings: Strategies and Opportunities to 2050*. International Energy Agency; 2013. doi:10.1787/9789264202955-en.
- [3] Bernier M. Closed-Loop Ground-Coupled Heat Pump Systems. *ASHRAE Journal* 2006;12–9.
- [4] Mogensen P. Fluid to duct wall heat transfer in duct system heat storages. *Proceedings of International Conference on Subsurface Heat Storage in Theory and Practice*, Stockholm, Sweden: Swedish Council for Building Research; 1983, p. 652–7.
- [5] Eklöf C, Gehlin S. TED—a mobile equipment for thermal response tests. Lulea University of Technology, 1996.
- [6] Gehlin S. Thermal response test: in-situ measurements of thermal properties in hard rocks. Lulea University of Technology, 1998.
- [7] Fujii H, Okubo H, Nishi K, Itoi R, Ohshima K, Shibata K. An improved thermal response test for U-tube ground heat exchanger based on optical fiber thermometers. *Geothermics* 2009;38:399–406. doi:10.1016/j.geothermics.2009.06.002.
- [8] Acuña J, Palm B. Distributed thermal response tests on pipe-in-pipe borehole heat exchangers. *Applied Energy* 2013;109:312–20. doi:10.1016/j.apenergy.2013.01.024.
- [9] Carslaw HS, Jaeger JC. *Conduction of Heat in Solids*. 2nd ed. UK: Oxford University Press; 1959.
- [10] Ingersoll LR, Zobel OJ, Ingersoll AC. *Heat conduction with engineering, geological, and other applications*. Madison: University of Wisconsin Press; 1954.
- [11] Eskilson P. *Thermal analysis of heat extraction boreholes*. Department of Mathematical Physics, University of Lund, 1987.
- [12] Zeng HY, Diao NR, Fang ZH. A finite line source model for boreholes in geothermal heat exchangers. *Heat Transfer—Asian Research* 2002;31:558–67.
- [13] Lamarche L, Beauchamp B. A new contribution to the finite line-source model for geothermal boreholes. *Energy and Buildings* 2007;39:188–98. doi:10.1016/j.enbuild.2006.06.003.
- [14] Austin WAI. *Development of an in situ system for measuring ground thermal properties*. Oklahoma State University, 1998.
- [15] Roth P, Georgiev A, Busso A, Barraza E. First in situ determination of ground and borehole thermal properties in Latin America. *Renewable Energy* 2004;29:1947–63. doi:10.1016/j.renene.2004.02.014.

- [16] Bandos T V, Montero Á, Fernández de Córdoba P, Urchueguía JF. Improving parameter estimates obtained from thermal response tests: Effect of ambient air temperature variations. *Geothermics* 2011;40:136–43. doi:10.1016/j.geothermics.2011.02.003.
- [17] Florides G, Kalogirou S. First in situ determination of the thermal performance of a U-pipe borehole heat exchanger, in Cyprus. *Applied Thermal Engineering* 2008;28:157–63. doi:10.1016/j.applthermaleng.2007.03.026.
- [18] Signorelli S, Bassetti S, Pahud D, Kohl T. Numerical evaluation of thermal response tests. *Geothermics* 2007;36:141–66. doi:10.1016/j.geothermics.2006.10.006.
- [19] Sharqawy MH, Mokheimer EM, Habib MA, Badr HM, Said SA, Al-Shayea NA. Energy, exergy and uncertainty analyses of the thermal response test for a ground heat exchanger. *International Journal of Energy Research* 2009;33:582–92. doi:10.1002/er.1496.
- [20] Shonder JA, Beck J. Field test of a new method for determining soil formation thermal conductivity and borehole resistance. *ASHRAE Transactions* 2000;106:843–50.
- [21] Beier RA, Smith MD. Removing variable heat rate effects from borehole tests. *ASHRAE Transactions* 2003;109:463–74.
- [22] Witte HJL, Van Gelder GJ, Spitler JD. In situ measurement of ground thermal conductivity: A Dutch perspective. *ASHRAE Transactions* 2002;108:263–72.
- [23] Zhang L, Zhang Q, Huang G, Du Y. A p(t)-linear average method to estimate the thermal parameters of the borehole heat exchangers for in situ thermal response test. *Applied Energy* 2014;131:211–21. doi:10.1016/j.apenergy.2014.06.031.
- [24] Borinaga-Treviño R, Pascual-Muñoz P, Castro-Fresno D, Blanco-Fernandez E. Borehole thermal response and thermal resistance of four different grouting materials measured with a TRT. *Applied Thermal Engineering* 2013;53:13–20. doi:10.1016/j.applthermaleng.2012.12.036.
- [25] You S, Cheng X, Guo H, Yao Z. In-situ experimental study of heat exchange capacity of CFG pile geothermal exchangers. *Energy and Buildings* 2014;79:23–31. doi:10.1016/j.enbuild.2014.04.021.
- [26] Esen H, Inalli M. In-situ thermal response test for ground source heat pump system in Elazığ, Turkey. *Energy and Buildings* 2009;41:395–401. doi:10.1016/j.enbuild.2008.11.004.
- [27] Florides GA, Christodoulides P, Pouloupatis P. An analysis of heat flow through a borehole heat exchanger validated model. *Applied Energy* 2012;92:523–33. doi:10.1016/j.apenergy.2011.11.064.
- [28] Chiasson AD, Rees SJ, Spitler JD. A preliminary assessment of the effects of groundwater flow on closed-loop ground source heat pump systems. *ASHRAE Transactions* 2000;106:380–93.
- [29] Diao N, Li Q, Fang Z. Heat transfer in ground heat exchangers with groundwater advection. *International Journal of Thermal Sciences* 2004;43:1203–11. doi:10.1016/j.ijthermalsci.2004.04.009.
- [30] Angelotti A, Alberti L, La Licata I, Antelmi M. Energy performance and thermal impact of a borehole heat exchanger in a sandy aquifer: Influence of the groundwater velocity. *Energy Conversion and Management* 2014;77:700–8. doi:10.1016/j.enconman.2013.10.018.

- [31] Gehlin S, Hellström G, Nordell B. The influence of the thermosiphon effect on the thermal response test. *Renewable Energy* 2003;28:2239–54. doi:10.1016/S0960-1481(03)00129-0.
- [32] Molina-Giraldo N, Blum P, Zhu K, Bayer P, Fang Z. A moving finite line source model to simulate borehole heat exchangers with groundwater advection. *International Journal of Thermal Sciences* 2011;50:2506–13. doi:10.1016/j.ijthermalsci.2011.06.012.
- [33] Wagner V, Blum P, Kübert M, Bayer P. Analytical approach to groundwater-influenced thermal response tests of grouted borehole heat exchangers. *Geothermics* 2013;46:22–31. doi:10.1016/j.geothermics.2012.10.005.
- [34] Raymond J, Therrien R, Gosselin L, Lefebvre R. Numerical analysis of thermal response tests with a groundwater flow and heat transfer model. *Renewable Energy* 2011;36:315–24. doi:10.1016/j.renene.2010.06.044.
- [35] Wang H, Qi C, Du H, Gu J. Thermal performance of borehole heat exchanger under groundwater flow: A case study from Baoding. *Energy and Buildings* 2009;41:1368–73. doi:10.1016/j.enbuild.2009.08.001.
- [36] Choi JC, Park J, Lee SR. Numerical evaluation of the effects of groundwater flow on borehole heat exchanger arrays. *Renewable Energy* 2013;52:230–40. doi:10.1016/j.renene.2012.10.028.
- [37] Lee CK, Lam HN. Determination of groundwater flow direction in thermal response test analysis for geothermal heat pump systems. *HVAC&R Research* 2011;17:991–9. doi:10.1080/10789669.2011.599763.
- [38] Lee CK, Lam HN. A modified multi-ground-layer model for borehole ground heat exchangers with an inhomogeneous groundwater flow. *Energy* 2012;47:378–87. doi:10.1016/j.energy.2012.09.056.
- [39] ASHRAE. *ASHRAE Handbook - HVAC Applications*, Chapter 32. Atlanta, GA: American Society of Heating, Refrigerating and Air-Conditioning Engineers Inc.; 2007.
- [40] International Energy Agency (IEA). *IEA ECES ANNEX 21: Thermal Response Test (TRT) - Final Report*. 2013.
- [41] Nield DA, Bejan A. *Convection in Porous Media*. 4th Ed. New York: Springer; 2013. doi:10.1007/978-1-4614-5541-7.
- [42] Bear J, Cheng A. *Modeling Groundwater flow and contaminant transport*. Springer Netherlands; 2010. doi:10.1007/978-1-4020-6682-5.
- [43] Gray DD, Giorgini A. The validity of the boussinesq approximation for liquids and gases. *International Journal of Heat and Mass Transfer* 1976;19:545–51. doi:10.1016/0017-9310(76)90168-X.
- [44] Perrochet P, Tacher L. *Mathematical modeling of hydro-thermal processes in Mururoa Atoll*. Lausanne, Switzerland: Ecole Polytechnique Federale de Lausanne; 1997.
- [45] Paul ND. *The effect of grout thermal conductivity on vertical geothermal heat exchanger design and performance*. South Dakota State University, USA, 1996.

- [46] Remund CP. Borehole thermal resistance: Laboratory and field studies. *ASHRAE Transactions* 1999;105:439–45.
- [47] Beier RA, Smith MD. Borehole thermal resistance from line-source model of in-situ tests. *ASHRAE Transactions* 2002;108:212–9.
- [48] Bennet J, Claesson J, Hellström G. Multipole method to compute the conductive heat flows to and between pipes in a composite cylinder. *Notes on Heat Transfer 3-1987*. Department of Building Technology and Mathematical Physics, Lund Institute of Technology, 1987.
- [49] Hellström G. Ground heat storage: Thermal analyses of duct storage systems. Department of Mathematical Physics, University of Lund, 1991.
- [50] Zeng H, Diao N, Fang Z. Heat transfer analysis of boreholes in vertical ground heat exchangers. *International Journal of Heat and Mass Transfer* 2003;46:4467–81. doi:10.1016/s0017-9310(03)00270-9.
- [51] Sharqawy MH, Mokheimer EM, Badr HM. Effective pipe-to-borehole thermal resistance for vertical ground heat exchangers. *Geothermics* 2009;38:271–7. doi:10.1016/j.geothermics.2009.02.001.
- [52] Gu Y, O’Neal DL. Development of an equivalent diameter expression for vertical U-tubes used in ground-coupled heat pumps. *ASHRAE Transactions* 1998;104:347–55.
- [53] Shonder JA, Beck J. Determining effective soil formation thermal properties from field data using a parameter estimation technique. *ASHRAE Transactions* 1999;105:458–66.
- [54] Claesson J, Eskilson P. Conductive heat extraction to a deep borehole: Thermal analyses and dimensioning rules. *Energy* 1988;13:509–27. doi:10.1016/0360-5442(88)90005-9.
- [55] Bauer D, Heidemann W, Müller-Steinhagen H, Diersch H-JG. Thermal resistance and capacity models for borehole heat exchangers. *International Journal of Energy Research* 2011;35:312–20. doi:10.1002/er.1689.
- [56] Sagia Z. Borehole resistance and heat conduction around vertical ground heat exchangers. *The Open Chemical Engineering Journal* 2012;6:32–40. doi:10.2174/1874123101206010032.
- [57] Raymond J, Therrien R, Gosselin L. Borehole temperature evolution during thermal response tests. *Geothermics* 2011;40:69–78. doi:10.1016/j.geothermics.2010.12.002.
- [58] Claesson J, Javed S. An analytical method to calculate borehole fluid temperatures for time-scales from minutes to decades. *ASHRAE Transactions* 2011;117:279–88.
- [59] Cimmino M, Bernier M. Preprocessor for the generation of g-functions used in the simulation of geothermal systems. 13th Conference of International Building Performance Simulation Association, Chambéry, France: 2013, p. 2675–82.
- [60] Cimmino M, Bernier M. A semi-analytical method to generate g-functions for geothermal bore fields. *International Journal of Heat and Mass Transfer* 2014;70:641–50. doi:10.1016/j.ijheatmasstransfer.2013.11.037.

- [61] Malayappan V, Spitler JD. Limitations of using uniform heat flux assumptions in sizing vertical borehole heat exchanger fields. Proceedings of Clima 2013, Prague, Czech Republic: 2013.
- [62] ASHRAE. ASHRAE Handbook - HVAC Applications. Atlanta, GA: American Society of Heating, Refrigerating and Air-Conditioning Engineers Inc.; 2003.
- [63] Kavanaugh SP, Rafferty KD. Ground-source heat pumps: Design of geothermal systems for commercial and institutional buildings. Atlanta: ASHRAE; 1997.
- [64] Bernier M. Review of the cylindrical heat source method for the design and analysis of vertical ground- coupled heat pump systems. Fourth International Conference on Heat Pumps in Cold Climates, Aylmer. Quebec: 2000.
- [65] Bernier M. Ground-coupled heat pump system simulation. ASHRAE Transactions 2001;107:605–16.
- [66] Bernier M. Uncertainty in the design length calculation for vertical ground heat exchangers. ASHRAE Transactions 2002;108:939–44.
- [67] Ahmadfard M, Bernier M. An alternative to ASHRAE’s Design Length Equation for Sizing Borehole Heat Exchangers. ASHRAE Transactions 2014;120:1–9.
- [68] Gehlin S, Spitler JD. Thermal response test – State of the Art 2001. International Energy Agency (IEA); 2002.
- [69] Reuß M, Proell M, Nordell B. IEA ECES-Annex 21:Thermal Response Test. Proceedings of Effstock 2009 : 11th International conference on thermal Energy Storage for Energy Efficiency and Sustainability, Stockholm, Sweden: 2009.
- [70] Kavanaugh SP, Xie L, Martin C. Investigation of methods for determining soil and rock formation thermal properties from short-term field tests. Atlanta, Georgia: 2001.
- [71] Gautschi W, Cahill W. Exponential integral and related functions. In: Abramowitz M, Stegun I, editors. Handbook of mathematical functions with formulas, graphs, and mathematical tables. Washington DC: National Bureau of Standards; 1964.
- [72] Gehlin S. Thermal response test: method development and evaluation. Lulea University of Technology, 2002.
- [73] Marcotte D, Pasquier P, Sheriff F, Bernier M. The importance of axial effects for borehole design of geothermal heat-pump systems. Renewable Energy 2010;35:763–70. doi:10.1016/j.renene.2009.09.015.
- [74] Philippe M, Bernier M, Marchio D. Validity ranges of three analytical solutions to heat transfer in the vicinity of single boreholes. Geothermics 2009;38:407–13. doi:10.1016/j.geothermics.2009.07.002.
- [75] Bernier M, Kummert M, Bertagnolio S. Development and application of test cases for comparing vertical ground heat exchanger models. Proceedings of Building Simulation, 2007, p. 1462–9.
- [76] Cimmino M, Bernier M, Adams F. A contribution towards the determination of g-functions using the finite line source. Applied Thermal Engineering 2013;51:401–12. doi:10.1016/j.applthermaleng.2012.07.044.

- [77] Lamarche L. Short-term behavior of classical analytic solutions for the design of ground-source heat pumps. *Renewable Energy* 2013;57:171–80. doi:10.1016/j.renene.2013.01.045.
- [78] Tikhonov A, Arsenin V. *Solution of ill-posed problems*. Washington DC: Winston & Sons; 1977.
- [79] Tikhonov A. *Solution of Incorrectly Formulated Problems and the Regularization Method*. *Soviet Mathematics Doklady* 1963;4:1035–8.
- [80] Tikhonov A. Regularization of incorrectly posed problems. *Soviet Mathematics Doklady* 1963;4:1624–7.
- [81] Tikhonov A. Inverse problems in heat conduction. *Journal of Engineering Physics* 1975;29:816–20. doi:10.1007/BF00860616.
- [82] Alifanov OM. *Inverse Heat Transfer Problems*. Springer; 1994. doi:10.1007/978-3-642-76436-3.
- [83] Alifanov OM. Solution of an inverse problem of heat conduction by iteration methods. *Journal of Engineering Physics* 1974;26:471–6. doi:10.1007/BF00827525.
- [84] Alifanov OM, Artyukhin EA. Regularized numerical solution of nonlinear inverse heat-conduction problem. *Journal of Engineering Physics* 1975;29:934–8. doi:10.1007/BF00860643.
- [85] Beck J, Arnold KJ. *Parameter estimation in engineering and science*. New York: Wiley Interscience; 1977.
- [86] Beck J. *Inverse heat conduction: Ill-posed problems*. New York: Wiley Interscience; 1985.
- [87] Ozisik MN, Orlande H. *Inverse heat transfer: fundamentals and applications*. New York: Taylor & Francis; 2000.
- [88] Nam Y, Ooka R, Hwang S. Development of a numerical model to predict heat exchange rates for a ground-source heat pump system. *Energy and Buildings* 2008;40:2133–40. doi:10.1016/j.enbuild.2008.06.004.
- [89] ISO. *Guide to the Expression of Uncertainty in Measurement*. Geneva, Switzerland: International Organization for Standardization; 1995.
- [90] Gehlin S, Hellström G. Comparison of four models for thermal response test evaluation. *ASHRAE Transactions* 2003;109:131–42.
- [91] Yavuzturk C, Spitler JD, Rees SJ. A transient two-dimensional finite volume model for the simulation of vertical u-tube ground heat exchangers. *ASHRAE Transactions* 1999;105:465–74.
- [92] Wagner R, Clauser C. Evaluating thermal response tests using parameter estimation for thermal conductivity and thermal capacity. *Journal of Geophysics and Engineering* 2005;2:349–56. doi:10.1088/1742-2132/2/4/S08.
- [93] Bozzoli F, Pagliarini G, Rainieri S, Schiavi L. Estimation of soil and grout thermal properties through a TSPEP (two-step parameter estimation procedure) applied to TRT (thermal response test) data. *Energy* 2011;36:839–46. doi:10.1016/j.energy.2010.12.031.

- [94] Spitler JD, Rees SJ, Yavuzturk C. More comments on in-situ borehole thermal conductivity testing. *The Source* 1999;12:4–6.
- [95] Beck J, Woodbury KA. Inverse problems and parameter estimation: integration of measurements and analysis. *Measurement Science and Technology* 1998;9:839–47. doi:10.1088/0957-0233/9/6/001.
- [96] Austin WAI, Yavuzturk C, Spitler JD. Development of an in-situ system and analysis procedure for measuring ground thermal properties. *ASHRAE Transactions* 2000;106:365–79.
- [97] Gehlin S. Thermal response test - In situ measurements of thermal properties in hard rock. Lulea University of Technology, 1998.
- [98] Javed S. Thermal response testing: Results and experiences from a ground source heat pump test facility with multiple boreholes. *Proceedings of Clima 2013, Prague, Czech Republic*: 2013.
- [99] Liu YD, Beier RA. Required duration for borehole test validated by field data. *ASHRAE Transactions* 2009;115:782–92.
- [100] Smith MD, Perry RL. In-situ testing and thermal conductivity testing. *Proceedings of the Georexchange Technical Conference and Exposition, Oklahoma State University, Stillwater, Oklahoma*: 1999.
- [101] Raymond J, Therrien R, Gosselin L, Lefebvre R. A Review of Thermal Response Test Analysis Using Pumping Test Concepts. *Ground Water* 2011;49:932–45. doi:10.1111/j.1745-6584.2010.00791.x.
- [102] Acuña J, Mogensen P, Palm B. Distributed thermal response tests on a multi-pipe coaxial borehole heat exchanger. *HVAC&R Research* 2011;17:1012–29.
- [103] Hu P, Meng Q, Sun Q, Zhu N, Guan C. A method and case study of thermal response test with unstable heat rate. *Energy and Buildings* 2012;48:199–205. doi:10.1016/j.enbuild.2012.01.036.
- [104] Beier RA, Smith MD, Spitler JD. Reference data sets for vertical borehole ground heat exchanger models and thermal response test analysis. *Geothermics* 2011;40:79–85. doi:10.1016/j.geothermics.2010.12.007.
- [105] ASHRAE. *ASHRAE Handbook - Fundamentals*. Atlanta, GA: American Society of Heating, Refrigerating and Air-Conditioning Engineers Inc.; 2009.
- [106] Bliss RW. Atmospheric radiation near the surface of the ground: A summary for engineers. *Solar Energy* 1961;5:103–20. doi:10.1016/0038-092X(61)90053-6.
- [107] Höglund BI, Mitalas GP, Stephenson DG. Surface temperatures and heat fluxes for flat roofs. *Building Science* 1967;2:29–36. doi:10.1016/0007-3628(67)90005-9.
- [108] Mackey CO, Wright LT. Summer comfort factors as influenced by the thermal properties of building materials. *ASHVE Transactions* 1943;49:148–74.
- [109] McAdams WH. *Heat transmission*. 3rd Ed. New York: McGraw-Hill; 1958.
- [110] Jürges W. Der wärmeübergang an einer ebenen wand (heat transfer at a plane wall). *Gesundheits-Ingenieur* 1924;Beihefte 1.

- [111] Ouzzane M, Eslami-Nejad P, Aidoun Z, Lamarche L. Analysis of the convective heat exchange effect on the undisturbed ground temperature. *Solar Energy* 2014;108:340–7. doi:10.1016/j.solener.2014.07.015.
- [112] Rao KG. Estimation of the Exchange Coefficient of Heat During Low Wind Convective Conditions. *Boundary-Layer Meteorology* 2004;111:247–73. doi:10.1023/B:BOUN.0000016495.85528.d7.
- [113] Mostrel M, Givoni B. Windscreens in radiant cooling. *Passive Solar Journal* 1982;1:229–38.
- [114] Gnielinski V. New equations for heat and mass transfer in turbulent pipe and channel flow. *International Chemical Engineering* 1976;16:359–68.
- [115] Petukhov BS. Heat transfer and friction in turbulent pipe flow with variable physical properties. *Advances in Heat Transfer* 1970;6:503–64. doi:10.1016/S0065-2717(08)70153-9.
- [116] Choi W, Ooka R. Interpretation of disturbed data in thermal response tests using the infinite line source model and numerical parameter estimation method. *Applied Energy* 2015;148:476–88. doi:10.1016/j.apenergy.2015.03.097.
- [117] Choi W, Ooka R. The effect of natural convection on thermal response test. *ASHRAE Transactions* 2014;120:SE – 14–C047.
- [118] Gustafsson A-M, Westerlund L. Heat extraction thermal response test in groundwater-filled borehole heat exchanger – Investigation of the borehole thermal resistance. *Renewable Energy* 2011;36:2388–94. doi:10.1016/j.renene.2010.12.023.
- [119] Gustafsson A-M, Westerlund L. Multi-injection rate thermal response test in groundwater filled borehole heat exchanger. *Renewable Energy* 2010;35:1061–70. doi:10.1016/j.renene.2009.09.012.
- [120] Javed S, Nakos H, Claesson J. A method to evaluate thermal response tests on groundwater-filled boreholes. *ASHRAE Transactions* 2012;118:540–9.
- [121] Komaniwa Y, Fujii H, Chou N, Fujita Y. Evaluating heat exchange performance of vertical ground heat exchanger filled with gravel in laboratory experiments (in Japanese). *Journal of the Geothermal Research Society of Japan* 2011;33:169–78.
- [122] Fujii H, Komaniwa Y, Yamaguchi M, Chou N. Interpretation of thermal response test in ungrouted U-tube ground heat exchangers (in Japanese). *Journal of the Geothermal Research Society of Japan* 2010;32:31–40.
- [123] Beier RA. Vertical temperature profile in ground heat exchanger during in-situ test. *Renewable Energy* 2011;36:1578–87. doi:http://dx.doi.org/10.1016/j.renene.2010.10.025.
- [124] Zheng X, Zhang L, Ren Q, Qian H. A thermal response method of calculating a soil's thermal properties when backfill material information is unavailable. *Energy and Buildings* 2013;56:146–9. doi:10.1016/j.enbuild.2012.09.020.
- [125] Mattsson N, Steinmann G, Laloui L. Advanced compact device for the in situ determination of geothermal characteristics of soils. *Energy and Buildings* 2008;40:1344–52. doi:10.1016/j.enbuild.2007.12.003.

- [126] Li X, Chen Y, Chen Z, Zhao J. Thermal performances of different types of underground heat exchangers. *Energy and Buildings* 2006;38:543–7. doi:10.1016/j.enbuild.2005.09.002.
- [127] Zhang C, Chen P, Liu Y, Sun S, Peng D. An improved evaluation method for thermal performance of borehole heat exchanger. *Renewable Energy* 2015;77:142–51. doi:10.1016/j.renene.2014.12.015.
- [128] Gao J, Zhang X, Liu J, Li K, Yang J. Numerical and experimental assessment of thermal performance of vertical energy piles: An application. *Applied Energy* 2008;85:901–10. doi:10.1016/j.apenergy.2008.02.010.
- [129] Gustafsson A-M, Westerlund L, Hellström G. CFD-modelling of natural convection in a groundwater-filled borehole heat exchanger. *Applied Thermal Engineering* 2010;30:683–91. doi:10.1016/j.applthermaleng.2009.11.016.
- [130] Beier RA, Acuña J, Mogensen P, Palm B. Borehole resistance and vertical temperature profiles in coaxial borehole heat exchangers. *Applied Energy* 2013;102:665–75. doi:10.1016/j.apenergy.2012.08.007.
- [131] Witte HJL. Error analysis of thermal response tests. *Applied Energy* 2013;109:302–11. doi:10.1016/j.apenergy.2012.11.060.
- [132] Rainieri S, Bozzoli F, Pagliarini G. Modeling approaches applied to the thermal response test: A critical review of the literature. *HVAC&R Research* 2011;17:977–90. doi:10.1080/10789669.2011.610282.
- [133] Bujok P, Grycz D, Klempa M, Kunz A, Porzer M, Pytlik A, et al. Assessment of the influence of shortening the duration of TRT (thermal response test) on the precision of measured values. *Energy* 2014;64:120–9. doi:10.1016/j.energy.2013.11.079.
- [134] Gehlin S, Nordell B. Determining undisturbed ground temperature for thermal response test. *ASHRAE Transactions* 2003;109:151–6.
- [135] Georgiev a., Busso A, Roth P. Shallow borehole heat exchanger: Response test and charging–discharging test with solar collectors. *Renewable Energy* 2006;31:971–85. doi:10.1016/j.renene.2005.06.002.
- [136] Diersch H-JG. *FEFLOW: Finite element modeling of flow, mass and heat transport in porous and fractured media*. Berlin, Heidelberg: Springer; 2014. doi:10.1007/978-3-642-38739-5.
- [137] Hagen G. Ueber die Bewegung des Wassers in engen cylindrischen Röhren. *Annalen Der Physik Und Chemie* 1839;122:423–42. doi:10.1002/andp.18391220304.
- [138] Poiseuille JLM. Recherches expérimentales sur le mouvement des liquides dans les tubes de très-petits diamètres. *Comptes Rendus, Académie Des Sciences, Paris* 1840;11:961–7.
- [139] Poiseuille JLM. Recherches expérimentales sur le mouvement des liquides dans les tubes de très-petits diamètres. *Comptes Rendus, Académie Des Sciences, Paris* 1841;12:112–5.
- [140] Marcotte D, Pasquier P. On the estimation of thermal resistance in borehole thermal conductivity test. *Renewable Energy* 2008;33:2407–15. doi:10.1016/j.renene.2008.01.021.

- [141] Wagner V, Bayer P, Kübert M, Blum P. Numerical sensitivity study of thermal response tests. *Renewable Energy* 2012;41:245–53. doi:10.1016/j.renene.2011.11.001.
- [142] Ozudogru TY, Olgun CG, Senol a. 3D numerical modeling of vertical geothermal heat exchangers. *Geothermics* 2014;51:312–24. doi:10.1016/j.geothermics.2014.02.005.
- [143] Shewchuk JR. Triangle: Engineering a 2D Quality Mesh Generator and Delaunay Triangulator. *Applied Computational Geometry: Towards Geometric Engineering* 1996;1148:203–22. doi:10.1007/BFb0014497.
- [144] Beier RA, Smith MD. Minimum duration of in-situ tests on vertical boreholes. *ASHRAE Transactions* 2003;109:475–86.
- [145] Soga K, Akasaka H. Study on the method for constructing a reference weather year: A comparison of the EA method and the SHASE method. *Journal of Environmental Engineering in Architectural Institute of Japan* 2004;581:21–8.
- [146] Kavanaugh SP. Field tests for ground thermal properties--methods and impact on ground-source heat pump design. *ASHRAE Transactions* 2000;106:851–5.
- [147] Raymond J, Robert G, Therrien R, Gosselin L. A Novel Thermal Response Test Using Heating Cables. *Proceedings World Geothermal Congress, Bali, Indonesia: 2010*, p. 1–8.
- [148] Raymond J, Lamarche L, Blais M-A. Quality control assessment of vertical ground heat exchangers. *ASHRAE Transactions* 2014;120:in press.
- [149] Sanner B, Hellström G, Spitler JD, Gehlin S. Thermal response test—current status and world-wide application. *Proceedings World Geothermal Congress, 2005*, p. 24–9.
- [150] Ehlig-Economides CA. Well test analysis for wells produced at a constant pressure. Stanford University, 1979.
- [151] Bourdet D, Ayoub JA, Pirard YM. Use of Pressure Derivative in Well Test Interpretation. *SPE Formation Evaluation* 1989;4:293–302. doi:10.2118/12777-PA.
- [152] Hahn DW, Özişik MN. *Heat Conduction*. 3rd ed. Hoboken, NJ: John Wiley & Sons, Inc.; 2012. doi:10.1002/9781118411285.
- [153] Yavuzturk C, Spitler JD. A short time step response factor model for vertical ground loop heat exchangers. *ASHRAE Transactions* 1999;105:475–85.
- [154] Chiasson AD, O’Connell A. New analytical solution for sizing vertical borehole ground heat exchangers in environments with significant groundwater flow: Parameter estimation from thermal response test data. *HVAC&R Research* 2011;17:1000–11. doi:10.1080/10789669.2011.609926.
- [155] Nelder JA, Mead R. A simplex method for function minimization. *The Computer Journal* 1965;7:308–13. doi:10.1093/comjnl/7.4.308.
- [156] Nocedal J, Wright SJ. *Numerical optimization*. 2nd ed. New York: Springer; 2006. doi:10.1007/978-0-387-40065-5.

- [157] Broyden CG. . The convergence of a class of double-rank minimization algorithms 1: General considerations. *IMA Journal of Applied Mathematics* 1970;6:76–90. doi:10.1093/imamat/6.1.76.
- [158] Fletcher R. A new approach to variable metric algorithms. *The Computer Journal* 1970;13:317–22. doi:10.1093/comjnl/13.3.317.
- [159] Goldfarb D. A family of variable-metric methods derived by variational means. *Mathematics of Computation* 1970;24:23–6. doi:10.1090/S0025-5718-1970-0258249-6.
- [160] Shanno DF. Conditioning of quasi-Newton methods for function minimization. *Mathematics of Computation* 1970;24:647–56. doi:10.1090/S0025-5718-1970-0274029-X.
- [161] Wolfe P. Convergence conditions for ascent methods. *SIAM Review* 1969;13:226–35.
- [162] Wolfe P. Convergence conditions for ascent methods. II: Some corrections. *SIAM Review* 1971;13:185–8. doi:10.1137/1013035.
- [163] Kavanaugh SP, Allan M. Testing of thermally enhanced cement ground heat exchanger grouts. *ASHRAE Transactions* 1999;105:446–50.
- [164] Erol S, François B. Efficiency of various grouting materials for borehole heat exchangers. *Applied Thermal Engineering* 2014. doi:10.1016/j.applthermaleng.2014.05.034.
- [165] Lee C, Park M, Min S, Kang S-H, Sohn B, Choi H. Comparison of effective thermal conductivity in closed-loop vertical ground heat exchangers. *Applied Thermal Engineering* 2011;31:3669–76. doi:10.1016/j.applthermaleng.2011.01.016.
- [166] Lee C, Park M, Nguyen T-B, Sohn B, Choi JM, Choi H. Performance evaluation of closed-loop vertical ground heat exchangers by conducting in-situ thermal response tests. *Renewable Energy* 2012;42:77–83. doi:10.1016/j.renene.2011.09.013.
- [167] Alrtimi a. a., Rouainia M, Manning D a C. Thermal enhancement of PFA-based grout for geothermal heat exchangers. *Applied Thermal Engineering* 2013;54:559–64. doi:10.1016/j.applthermaleng.2013.02.011.
- [168] Gustafsson A, Gehlin S. Influence of natural convection in water-filled boreholes for GCHP. *ASHRAE Transactions* 2008;114:416–23.
- [169] Fujii H, Akibayashi S, Ohshima K. Interpretation of thermal response tests in shallow deposits. *Geothermal Resources Council Transactions* 2002;26:143–8.
- [170] Ingersoll LR, Zobel OJ, Ingersoll AC. Heat conduction, with engineering and geological applications. McGraw Hill Book Company Inc.; 1948.
- [171] MacGregor RK, Emery AF. Free convection through vertical plane layers—Moderate and high prandtl number fluids. *Journal of Heat Transfer* 1969;91:391. doi:10.1115/1.3580194.
- [172] Zeng Z, Brown JMB, Vardy a. E. On moving heat sources. *Heat and Mass Transfer* 1997;33:41–9. doi:10.1007/s002310050159.
- [173] Fujii H, Komaniwa Y, Nomoto T, Chou N. Reduction of thermal resistance of ground heat exchangers using large grain size materials. *GRC Transactions* 2011;35:1095–100.

- [174] ANSI Standard Publication. Electric power systems and equipment—Voltage ratings (60 Hertz). National Electrical Manufacturers Association; 2011.
- [175] European Standard. EN 50160: Voltage characteristics of electricity supplied by public distribution systems. CENELEC 2006.
- [176] Aichlmayr HT, Kulacki FA. On the effective thermal conductivity of saturated porous media. 2005 ASME Summer Heat Transfer Conference, San Francisco, California, USA: ASME; 2005, p. 265–73. doi:10.1115/HT2005-72144.
- [177] Aichlmayr HT, Kulacki F a. A transient technique for measuring the effective thermal conductivity of saturated porous media with a constant boundary heat flux. *Journal of Heat Transfer* 2006;128:1217. doi:10.1115/1.2352791.
- [178] Pahud D, Matthey B. Comparison of the thermal performance of double U-pipe borehole heat exchangers measured in situ. *Energy and Buildings* 2001;33:503–7. doi:10.1016/S0378-7788(00)00106-7.
- [179] Kyriakis N, Michopoulos A, Pattas K. On the maximum thermal load of ground heat exchangers. *Energy and Buildings* 2006;38:25–9. doi:10.1016/j.enbuild.2005.02.003.
- [180] Janssen H, Carmeliet J, Hens H. The influence of soil moisture transfer on building heat loss via the ground. *Building and Environment* 2004;39:825–36. doi:10.1016/j.buildenv.2004.01.004.
- [181] Wang K, Wang P, Liu J, Sparrow M, Haginoya S, Zhou X. Variation of surface albedo and soil thermal parameters with soil moisture content at a semi-desert site on the western Tibetan Plateau. *Boundary-Layer Meteorology* 2005;116:117–29. doi:10.1007/s10546-004-7403-z.
- [182] Tarnawski VR, Leong WH. Thermal conductivity of soils at very low moisture content and moderate temperatures. *Transport in Porous Media* 2000;41:137–47. doi:10.1023/A:1006738727206.
- [183] Nakshabandi G Al, Kohnke H. Thermal conductivity and diffusivity of soils as related to moisture tension and other physical properties. *Agricultural Meteorology* 1965;2:271–9.
- [184] Naylor S, Ellett KM, Gustin AR. Spatiotemporal variability of ground thermal properties in glacial sediments and implications for horizontal ground heat exchanger design. *Renewable Energy* 2015;81:21–30. doi:10.1016/j.renene.2015.03.006.
- [185] Liebel HT, Javed S, Vistnes G. Multi-injection rate thermal response test with forced convection in a groundwater-filled borehole in hard rock. *Renewable Energy* 2012;48:263–8. doi:10.1016/j.renene.2012.05.005.

## APPENDIX A. DEVELOPED SUBROUTINE USED IN CHAPTER 5

### A.1 Main code

```
/* Header files */
#include "stdifm.h"
#include "DisturbedTRT.h"
#include <ifm/module.h>
#include <ifm/graphic.h>
#include <ifm/document.h>
#include <ifm/archive.h>
#include <stdio.h>
#include <stdlib.h>
#define _USE_MATH_DEFINES
#include <math.h>
#include "assert.h"
#include <iostream>
#include <vector>

using namespace std;

// Headers for importing heat rate and flow rate
#include "TRTheatload.h"
#include "TRTflowrate.h"

// BHE inlet and outlet nodes ID
static int InletNodeN=120;
static int OutletNodeN=121;

// Time units
const double RefTimeStep = 6.0;
const int YearToHour = 8760; // Year -> Hour
const double DayToHour = 24.0; // Day -> Second
const double DayToMin = 1440.0; // Day -> Min
const double DayToSec = 86400.0; // Day -> Second
const double MinToSec = 60.0; // Min -> Second
const double SecToMin = 1/MinToSec; // Second -> Min
const double MinToDay = 1/DayToMin; // Min -> Day
```

```

// Geometry: BHE, Pipe, Insulation
#define BHELLength 50.0 // Length of BHE [m]
#define rpi 0.0135 // Inner radius of U-tube [m]
#define rpo 0.017 // Outer radius of U-tube [m]
#define rb 0.0825 // Borehole radius [m]
#define ShankSpc 0.05 // Shank Spacing [m]

// TRT experimental setup
double Thkins = 0.01; // Thickness of the insulation [m]
double rinso = rpo + Thkins; // Outer radius of the insulation [m]
double Fcorr = 0.65; // Sol-air temp correction coefficient
double Qpump = 0; // Heat rate from pump
double HydLength = 2.0; // Hydraulic length above the ground [m]

// Thermal properties
double Lins = 0.04; // Thermal conductivity of insul [W/mK]
double Lp = 0.38 ; // Thermal conductivity of pipe [W/mK]
double Lcf = 0.6 ; // Thermal conductivity of water [W/mK]
double Rhocf = 1000.0 ; // Density of water [kg/m3]
double Ccf = 4200.0 ; // Specific heat of water [J/(kgK)]
double VolCcf = Rhocf * Ccf; // Volumetric heat capa of water [J/(m3K)]
double AbsIns = 0.6; // Absorptivity of the insulation surface

//TRT setup data
double Qrig; // Injection heat rate [W]
double FbheExp; // Flow rate [L/min]

//Initial and Boundary Conditions
const double IniTemp = 17.0; // Initial temperature of soil [C]
const double QbhePerLength = 50.0; // Heat rate per unit length [W/m]

//Iteration variables
static int i, j, k;

IfmModule g_pMod; /* Global handle related to this plugin */

#pragma region IFM_Definitions
/* --- IFMREG_BEGIN --- */
/* -- Do not edit! -- */

static IfmResult OnBeginDocument (IfmDocument);
static void OnEndDocument (IfmDocument);
static void PreHeatSimulation (IfmDocument);
static void PostHeatSimulation (IfmDocument);

```

```

static const char szDesc[] =
    "Variable BHE inlet BC, disturbance considering BC";

#ifdef __cplusplus
extern "C"
#endif /* __cplusplus */

IfmResult RegisterModule(IfmModule pMod)
{
    if (IfmGetFeflowVersion (pMod) < IFM_REQUIRED_VERSION)
        return False;
    g_pMod = pMod;
    IfmRegisterModule (pMod, "SIMULATION", "DISTURBEDTRT", "DisturbedTRT", 0x1000);
    IfmSetDescriptionString (pMod, szDesc);
    IfmSetCopyrightPath (pMod, "DisturbedTRT.txt");
    IfmSetHtmlPage (pMod, "DisturbedTRT.htm");
    IfmSetPrimarySource (pMod, "DisturbedTRT.cpp");
    IfmRegisterProc (pMod, "OnBeginDocument", 1, (IfmProc)OnBeginDocument);
    IfmRegisterProc (pMod, "OnEndDocument", 1, (IfmProc)OnEndDocument);
    IfmRegisterProc (pMod, "PreHeatSimulation", 1, (IfmProc)PreHeatSimulation);
    IfmRegisterProc (pMod, "PostHeatSimulation", 1, (IfmProc)PostHeatSimulation);
    return True;
}

static void PreHeatSimulation (IfmDocument pDoc)
{
    CDisturbedtrt::FromHandle(pDoc)->PreHeatSimulation (pDoc);
}

static void PostHeatSimulation (IfmDocument pDoc)
{
    CDisturbedtrt::FromHandle(pDoc)->PostHeatSimulation (pDoc);
}

/* --- IFMREG_END --- */
#pragma endregion

static IfmResult OnBeginDocument (IfmDocument pDoc)
{
    if (IfmDocumentVersion (pDoc) < IFM_CURRENT_DOCUMENT_VERSION)
        return false;

    try {

```

```
    IfmDocumentSetUserData(pDoc, new CDisturbedtrt(pDoc));
}
catch (...) {
    return false;
}

return true;
}

static void OnEndDocument (IfmDocument pDoc)
{
    delete CDisturbedtrt::FromHandle(pDoc);
}
// Constructor
CDisturbedtrt::CDisturbedtrt (IfmDocument pDoc)
    : m_pDoc(pDoc)
{
}

// Destructor
CDisturbedtrt::~CDisturbedtrt ()
{
}

// Obtaining class instance from document handle
CDisturbedtrt* CDisturbedtrt::FromHandle (IfmDocument pDoc)
{
    return reinterpret_cast<CDisturbedtrt*>(IfmDocumentGetUserData(pDoc));
}

/***** CALLBACKS *****/
void CDisturbedtrt::PreHeatSimulation (IfmDocument pDoc)
{
    static int TorF_Weather = 1; // True or false, dummy variable

    /***** INITIALIZE WEATHER DATA ARRAY *****/
    static double Hour[YearToHour],
        Tamb[YearToHour], Tdew[YearToHour], RH[YearToHour],
        Pamb[YearToHour], Rdir[YearToHour], Rdif[YearToHour],
        Wdir[YearToHour], Wvel[YearToHour], Csky[YearToHour];

    FILE * file1 = NULL; // Initialize file1
```

```

/***** READ WEATHER DATA AND ASSIGN THEM TO ARRAYS *****/
if (TorF_Weather) {
    IfmInfo(pDoc, "weather data reading start ");
    file1 = fopen("weatherdata.txt", "r");

    for (int i = 0; i < YearToHour; i++) {
        fscanf(file1, "%lf %lf %lf %lf %lf %lf %lf %lf %lf %lf",
&Hour[i],
        &Tamb[i], &Tdew[i], &RH[i], &Pamb[i], &Rdir[i], &Rdif[i],
        &Wdir[i], &Wvel[i], &Csky[i]);
    }

    fclose(file1);
    TorF_Weather = 0;
    IfmInfo(pDoc, "weather data reading end");
}

double ElapTimeDay, DelTimeDay, ElapTimeHour, DailyElapTimeHour;

// Retrieve elapsed time and timestep length
ElapTimeDay = IfmGetAbsoluteSimulationTime(pDoc);
DelTimeDay = IfmGetCurrentTimeIncrement(pDoc);
ElapTimeHour = ElapTimeDay * DayToHour;
DailyElapTimeHour = fmod(ElapTimeDay * 24, 24);

// If hourly weather data are used ->Choose hour based Reftime (1)
// If minutely weather data are used ->Choose minute based Reftime (2)

// (1) Hour based Reference Time (Retrieve weather data)
const double OneYearPeriod = 365.0;
double PeriodicTime;

PeriodicTime = ElapTimeDay -
OneYearPeriod*Floor(ElapTimeDay/OneYearPeriod);
PeriodicTime *= 24.0;
int RefTime = (int)(PeriodicTime);

// (2) Minute based Reference Time (Retrieve weather data)
const double RefFactor = 60/RefTimeStep;
int RefTime = (int)(ElapTimeHour * RefFactor);

// Get nodes, slices and elements number
static int NoNodesPerSlice = IfmGetNumberOfNodesPerSlice(pDoc);

```

```

static int NoLayer = IfmGetNumberOfLayers(pDoc);
static int NoElements = IfmGetNumberOfElementsPerLayer(pDoc);

/***** Load heat rate, and flow rate from header files *****/
Qrig = HeatLoad(ElapTimeDay, DelTimeDay, RefTimeStep);
// Experimental heat rate [W]

FbheExp = FlowRate(ElapTimeDay, DelTimeDay,
RefTimeStep)/MinToDay/1000 ;
//Experimental flow rate [L/min]->[m3/day]

/***** TRT FLOW RATE ASSIGNMENT *****/
IfmSetBcFlowTypeAndValueAtCurrentTime (pDoc, InletNodeN, 4, 1, -
FbheExp); // Inlet: negative value

IfmSetBcFlowTypeAndValueAtCurrentTime (pDoc, OutletNodeN, 4, 1,
FbheExp); // Outlet: positive value

// Flow rate
static double VRcf = IfmGetBcFlowValue (pDoc, OutletNodeN) /
DayToSec ;

// Circulating flow rate of fluid [m3/day]->[m3/s]
double Velcf = VRcf / (M_PI * pow(rpi, 2)); // Flow velocity [m/s]

/***** Assign temperature BC *****/
double TcfOutBHE = IfmGetResultsTransportHeatPreviousTimeValue (pDoc,
OutletNodeN); // Retrieve BHE outlet temperature at previous timestep

/***** Outflow Inner Surface Convective Coefficient *****/
double DyViscOut = 2.414 * pow(10, -5.0)
* pow(10, (247.8 / (273.15 + TcfOutBHE - 140)));
// Dynamic viscosity
double KiViscOut = DyViscOut / Rhocf;
// Kinematic viscosity
double ReOut = Rhocf * Velcf * 2*rpi / DyViscOut; // Reynolds No
double PrOut = DyViscOut * Ccf / Lcf; // Prandtl No
double FricOut = pow((0.79 * log(ReOut) - 1.64), -2);
// Friction factor
double NuOut = ((FricOut / 8) * (ReOut - 1000) * PrOut)
/ (1 + 12.7 * pow((FricOut/8), 0.5) * (pow(PrOut, 2.0/3.0) - 1));

```

```

        //Nusselt No
double hiOut = NuOut * Lcf / (2 * rpi);          //Inner conv coeff
ic

/***** Outer Surface Convective Coefficient *****/
double ho;          // Rad + Conv heat transfer coefficient [W/m2K]

if (Wvel[RefTime] <= 5.0) {
    ho = 5.7 + 3.8 * Wvel[RefTime];
}
else{
    ho = 7.1 * pow(Wvel[RefTime], 0.78);
}

/***** Overall thermal resistance of outflow circuit *****/
double RciOut = 1 / (2 * M_PI * rpi * hiOut);    // Outflow Rci
double Rp = log(rpo/rpi) / (2 * M_PI * Lp);    // Rp
double Rins = log(rinso/rpo) / (2 * M_PI * Lins); // Rins
double Rco = 1 / (2 * M_PI * rinso * ho);    // Rco
double RtotOut = RciOut + Rp + Rins + Rco ;    // outflow Rtot

// Dimensionless Kappa of outflow
double KappaOut = HydLength / (Rhocf * Ccf * VRcf * RtotOut);
// Kappa outflow

// Sol-air Temperature
double RadTot = Rdir[RefTime] + Rdif[RefTime];
double Tsola = Tamb[RefTime] + Fcorr * AbsIns * RadTot / ho;

/***** Calculation of temperature perturbation *****/
// TcfOutRig,
double TcfOutRig = TcfOutBHE * exp(-KappaOut) + Tsola*(1 - exp(-
KappaOut)) ;

// TcfInRig
double TcfInRig = TcfOutRig + (Qrig + Qpump) / (Rhocf * Ccf * VRcf);

// Inflow Inner Convective coefficient
double DyViscIn = 2.414 * pow(10, -5.0)
    * pow(10, (247.8 / (273.15 + TcfInRig - 140)));

// Dynamic viscosity
double KiViscIn = DyViscIn / Rhocf;          // Kinematic viscosity

```

```

double ReIn = Rhocf * Velcf * 2*rpi / DyViscIn; // Reynolds No
double PrIn = DyViscIn * Ccf / Lcf;           // Prandtl No
double FricIn = pow((0.79 * log(ReIn) - 1.64), -2);
// Friction factor
double NuIn = ((FricIn / 8) * (ReIn - 1000) * PrIn)
              / (1 + 12.7 * pow((FricIn/8), 0.5) * (pow(PrIn, 2.0/3.0) - 1));
// Nusselt No
double hiIn = NuIn * Lcf / (2 * rpi);          // Inner conv coeff

// Additional thermal resistances based on the TcfInRig
double RciIn = 1 / (2 * M_PI * rpi * hiIn);
double RtotIn = RciIn + Rp + Rins + Rco ;

// Dimensionless Kappa inflow
double KappaIn = HydLength / (Rhocf * Ccf * VRcf * RtotIn);

// Inflow temperature of TcfInBHE
double TcfInBHE = TcfInRig * exp(-KappaIn) + Tsola*(1 - exp(-
KappaIn)) ;

/***** ASSIGN NEW INLET BHE TEMP BC VALUE *****/
IfmSetBcHeatTypeAndValueAtCurrentTime (pDoc, InletNodeN, 1, 1,
TcfInBHE) ;
// Input order: (pDoc, NodeNumber, BCType, SteadyOrUnsteady, Value)

// Calculation of Disturbed Temp, Disturbed heat rate, Qdist
double DelTcfOut = TcfOutRig - TcfOutBHE ;// Outflow temp diff [K]
double DelTcfIn = TcfInBHE - TcfInRig ; // Inflow temp diff [K]
double DelTcfTot = DelTcfOut + DelTcfIn; // Total temp diff [K]

double QdistOut = Rhocf * Ccf * VRcf * DelTcfOut;// Qdist outflow [W]
double QdistIn = Rhocf * Ccf * VRcf * DelTcfIn; // Qdist inflow [W]
double QdistTot = QdistIn + QdistOut ; // Qdist total [W]
double QdistRatio = QdistTot / Qrig * 100; // Dist ratio [%]

/***** DISPLAY RESULTS ON THE LOG WINDOW *****/

// Display Results
IfmInfo(pDoc, "ElapTime[d]   DailyHour[h]   TcfOutBHE[C]
TcfOutRig[C]   TcfInRig[C]   TcfInBHE[C]   DelTcfOut[C]
DelTcfIn[C]   DelTcfTot[C]   QdistOut[W]   QdistIn[W]
QdistTot[W]   QdistRatio[per]¥n");

```

```

IfmInfo(pDoc, "%.7f %.7f %.5f %.5f %.5f %.5f %.5f %.5f
%.5f %.5f %.5f %.5f %.5f %n",
ElapTimeDay, DailyElapTimeHour, TcfOutBHE, TcfOutRig, TcfInRig,
TcfInBHE, DelTcfOut, DelTcfIn, DelTcfTot, QdistOut, QdistIn, QdistTot,
QdistRatio);

```

```
//Display Variables
```

```

IfmInfo(pDoc, "ElapTime[d]   DailyHour[h]       Tamb[C]       RadTot[W/m2]
Wvel[m/s]       Tsol[C]       VRcf[m3/s]    RciOut[Wm/K]
RciIn[Wm/K]     Rp[Wm/K]     Rins[Wm/K]    Rco[Wm/K]     RtotOut[Wm/K]
RtotIn[Wm/K]    KappaOut[-]  KappaIn[-]%n");

```

```

IfmInfo(pDoc, "%.7f %.7f %.5f %.5f %.5f %.5f %.5f %.5f
%.5f %.5f %.5f %.5f %.5f %.5f %.5f %.5f%n",
ElapTimeDay, DailyElapTimeHour, Tamb[RefTime], RadTot, Wvel[RefTime],
Tsola, VRcf, RciOut, RciIn, Rp, Rins, Rco, RtotOut, RtotIn, KappaOut,
KappaIn);

```

```
/****** WRITE RESULTS *****/
```

```
static int iniQ = 1;
```

```
static FILE * result1;
```

```
static FILE * result2;
```

```
static FILE * result3;
```

```
if (iniQ) {
```

```
    result1 = fopen("Result_Mea_Wea_TempHeatRate.txt", "w+");
```

```
    result2 = fopen("Result_Mea_Wea_Variables.txt", "w+");
```

```
    result3 = fopen("Result_Mea_Wea_LeffRbEstimation.txt", "w+");
```

```
    iniQ = 0;
```

```
}
```

```

fprintf(result1, "%.7f %.7f %.7f %.7f %.7f %.7f %.7f
%.7f %.7f %.7f %.7f %.7f %.7f %.7f %n",
ElapTimeDay, ElapTimeDay*24, DailyElapTimeHour, TcfOutBHE, TcfOutRig,
TcfInRig, TcfInBHE, DelTcfOut, DelTcfIn, DelTcfTot, QdistOut, QdistIn,
QdistTot, QdistRatio);

```

```

fprintf(result2, "%.7f %.7f %.7f %.6f %.6f %.6f %.6f
%.7f %.7f %.7f %.7f %.7f %.7f %.7f %.7f %.9f %.9f%n",
ElapTimeDay, ElapTimeDay*24, DailyElapTimeHour, Tamb[RefTime], RadTot,
Wvel[RefTime], Tsola, VRcf, RciOut, RciIn, Rp, Rins, Rco, RtotOut,
RtotIn, KappaOut, KappaIn);

```

```

        fprintf(result3, "%.7f    %.7f    %.7f    %.7f    %.7f    ¥n",
        ElapTimeDay*24, ElapTimeDay, TcfInBHE, TcfOutBHE, VRcf*1000*60);
    }

```

## A.2 Header code 1 (TRTheatload.h)

```

#include <stdio.h>
#include <math.h>

double HeatLoad(double ElapTimeDay, double DelTimeDay, double RefTimeStep) {

    const double DayToHour = 24.0;
    const double HourToSec = 3600.0;
    const double MinToSec = 60.0;
    const double Period = 8760.0;
    const double RefFactor = 60/RefTimeStep;

    static int TorF = 1;

    static double Q[8760];

    FILE * file1 = NULL;

    double ElapTimeHour, DelTimeHour;
    double dummyTime, dummyQh, dummyQc, dummyF;
    double returnQ;
    int i, RefTime;

    ElapTimeHour = ElapTimeDay * DayToHour;
    DelTimeHour = DelTimeDay * DayToHour;
    ElapTimeHour = ElapTimeHour - Period * floor(ElapTimeHour/Period);

    if (TorF) {

        file1 = fopen("TRTheatFLowRate.txt", "r");

        for (i = 0; i < 8760; i++) {
            fscanf(file1, "%lf %lf %lf %lf", &dummyTime, &dummyQh,
            &dummyQc, &dummyF);
            F[i] = dummyQc - dummyQh;
        }

        TorF = 0;
    }
}

```

```

}

returnQ = 0.0;

/***** Return heat rate *****/
RefTime = (int)(RefFactor*ElapTimeHour);

returnQ = Q[RefTime] ;
return returnQ;
}

```

### A.3 Header code 2 (TRTflowrate.h)

```

#include <stdio.h>
#include <math.h>

double HeatLoad(double ElapTimeDay, double DelTimeDay, double RefTimeStep) {

    const double DayToHour = 24.0;
    const double HourToSec = 3600.0;
    const double MinToSec = 60.0;
    const double Period = 8760.0;
    const double RefFactor = 60/RefTimeStep;

    static int TorF = 1;

    static double Q[8760];

    FILE * file1 = NULL;

    double ElapTimeHour, DelTimeHour;
    double dummyTime, dummyQh, dummyQc, dummyF;
    double returnQ;
    int i, RefTime;

    ElapTimeHour = ElapTimeDay * DayToHour;
    DelTimeHour = DelTimeDay * DayToHour;
    ElapTimeHour = ElapTimeHour - Period * floor(ElapTimeHour/Period);

    if (TorF) {

        file1 = fopen("TRTHeatFlowRate.txt", "r");

```

```
        for (i = 0; i < 8760; i++) {
            fscanf(file1, "%lf %lf %lf %lf", &dummyTime, &dummyQh,
                &dummyQc, &dummyF);
            F[i] = dummyF;
        }
    TorF = 0;

}

returnQ = 0.0;

/***** Return flow rate *****/
RefTime = (int) (RefFactor*ElapTimeHour);

returnF = F[RefTime] ;
return returnF;
}
```





## PUBLICATIONS

### Peer-reviewed journals

- [1] Choi W, Ooka R. Interpretation of disturbed data in thermal response tests using the infinite line source model and numerical parameter estimation method. *Applied Energy* 2015;148:476–488. doi:10.1016/j.apenergy.2015.03.097.
- [2] Choi W, Ooka R. Effect of disturbance on thermal response test, Part 1: Development of disturbance analytical model, parametric study, and sensitivity analysis. *Renewable Energy* 2016;85, 306–318. doi:10.1016/j.renene.2015.06.042.
- [3] Choi W, Ooka R. Effect of disturbance on thermal response test, part 2: Numerical study of applicability and limitation of infinite line source model for interpretation under disturbance from outdoor environment. *Renewable Energy* 2016;85:1090–105. doi:10.1016/j.renene.2015.07.049.
- [4] Choi W, Ooka R. Effect of natural convection on thermal response test conducted in saturated porous formation: Comparison of gravel-backfilled and cement-grouted borehole heat exchangers. *Energy*, under review.

### Conference proceedings (International)

- [1] Choi W, Ooka R. The effect of natural convection on thermal response test. *ASHRAE Transactions* 2014;120:SE – 14–C047.
- [2] Choi W, Ooka R. Experimental comparison of the effect of natural convection between a gravel backfilled and a cement grouted vertical borehole heat exchanger. *Proceedings World Geothermal Congress, Melbourne, Australia: 2015.*
- [3] Choi W, Ooka R. Parameter estimation method of thermal response test to determine performance dependence in saturated porous formation. *IEA ECES Greenstock 2015, Beijing, China: 2015.*
- [4] Ooka R, Choi W, Nam Y. Environmental impact assessment of long-term operation of ground source heat pump using numerical simulation. *IEA ECES Greenstock 2015, Beijing, China: 2015.*
- [5] Choi W, Ooka R. Development and validation of disturbance-considering numerical model for investigation of error in thermal response tests. *6th International Building Physics Conference, Torino, Italy: 2015.*

### Conference proceedings (Japan)

- [1] 崔元準, 大岡龍三. 地下水流動がある条件での線状熱源理論による有効熱伝導率の利用可能性の検討. 日本建築学会大会, 札幌, 北海道: 2013.
- [2] 崔元準, 大岡龍三. 地下水流動がある土壌条件での無限線状熱源モデルによる有効熱伝導率算定に関するパラメトリックスタディ. 日本空調衛生工学会, 長野: 2013.
- [3] 崔元準, 大岡龍三. 充填材の種類による地中熱交換井の熱的性能検証に関する熱応答試験. 日本建築学会大会, 神戸, 近畿: 2014.
- [4] 崔元準, 大岡龍三. 外乱の影響を考慮したパラメータ推定法による熱応答試験の解析. 日本空調衛生工学会大会, 秋田: 2014.
- [5] 崔元準, 大岡龍三. 飽和多孔質地層の自然対流を把握するための多重注入熱量率熱応答試験とパラメータ推定法. 日本建築学会大会, 関東: 2015.
- [6] 日野俊之, 大岡龍三, 林鍾衍, 崔元準. ヘリカル型地中熱交換器用の空穴掘削試験. 日本建築学会大会, 関東: 2015.
- [7] 日野俊之, 大岡龍三, 林鍾衍, 崔元準. 中深度の地中熱を利用するヘリカル熱交換器の開発. 日本空調衛生工学会, 関西: 2015.

## ACKNOWLEDGMENTS

It has been a long and hectic journey the past three years. I would like to express my gratitude to the people who made this thesis happen.

First and foremost, I express my deepest appreciation to my advisor, Prof. Ryozo Ooka. You have been a tremendous mentor to me. Thanks to your continuous support, advice, and trust, I could research what I really wanted to in a very efficient manner. Although the start of my doctoral course was one year later than planned owing to unpredictable misfortune, I believed that you should be my advisor, and it was the right choice. Your resonant shout of “*tsukareta!*” will remain in my memory forever.

I also thank Prof. Shinsuke Kato, who served as co-advisor during my doctoral course. I learned the definitions of a genius and a person born to do research from you. I was enlightened not only by your advice on engineering but also your attitude towards life.

I extend my appreciation to my advising committee members Prof. Reiko Kuwano, Prof. Yasunori Akashi, and Assoc. Prof. Masayuki Mae for lending their time and providing brilliant comments and suggestions.

I extend my appreciation to all of my Kato & Ooka laboratory colleagues and staff, especially the following:

Dr. Toshiyuki Hino, your knowledge on building HVAC and large network of relationships helped me save time. Your fresh ideas always inspire me.

Dr. Hideki Kikumoto, you taught me numerical techniques in a very clear manner. You are a supremely talented teacher, and attending your lecture was very meaningful to me. You are one of the smartest people that I have ever met.

Dr. Keisuke Nakao, thank you for the lecture on turbulence. Also, we share musical tastes, and I had a great time at the many jazz concerts we went to.

Dr. Jongyeon Lim, thank you for your kind lecture about programming and kindness from the very moment that I first arrived in Japan. Congratulations on the birth of your baby!

Dr. Jeongil Kim, thank you for helping me adapt quickly to the new environment. Your kindness and advice were a really great help to me. Congratulations on your marriage!

Keigo Nakajima, thank you for the meaningful discussions on many subjects. We should go to the batting cages and then eat some of the finest sushi.

## Acknowledgments

---

Kazuo Kodama, thank you for helping me construct the thermal response test apparatus. Without your help, I would not have been able to do as well with such limited time.

Shintaro Ikeda, thank you for the discussions and advice on optimization methods. Sometimes, your precise and fast way of working really takes me by surprise. I think that you should change your name to Shintaro Ikemen.

Hobyung Chae and Seonghyun Park, thank you for helping me with the final editing work of this thesis. It was of great help to me. I am looking forward to seeing your research in the future.

Exergy research group members: Prof. Masanori Shukuya, Dr. Rongling Li, and Hang Yin. The time I spent immersing myself in discussions on a new field of thermodynamics was meaningful and precious to me. Prof. Masanori Shukuya, your clear explanations based on a firm theoretical foundation were especially impressive. Thank you for your lectures.

Laboratory colleagues: Mr. Takeo Takahashi, Assoc. Prof. Kyosuke Hiyama, Assoc. Prof. Minki Sung, Assoc. Prof. Yujin Nam, Assoc. Prof. Weirong Zhang, Dr. Jonghun Kim, Dr. Sihwan Lee, Dr. Beungyong Park, Dr. Yoonkyung Kang, Minsik Kim, Hyokeum Hwang, Kan Lin, Ryouichi Kobayashi, Kazuki Horikoshi, Daisuke Kawahara, Togo Yoshidomi, Yusuke Arima, Naoko Sugisaki, Miko Kobayashi, Masamichi Oura, Shinpei Suzuki, and Wonseok Oh.

Laboratory secretaries: Ms. Yumiko Yamada, Ms. Kyoko Mizumoto, Ms. Miyuki Mori, Ms. Mayumi Matsunaga, Ms. Keiko Higuchi, and Ms. Ai Takeuchi.

Very special appreciation goes to Prof. Jung-Ho Huh, who gave me the opportunity to be a researcher and supported me going abroad to study. You allowed me the maximum freedom that a graduate student can have, and the academic freedom that I fully enjoyed opened my eyes to the joys of research life.

Finally, I express my heartfelt appreciation to my parents, who always supported me and allowed me to do what I want to do. Thanks to your tolerance and understanding, I was able to do my best during the doctoral course. I am forever grateful for your love. Also, my younger brother Eunseok, who is the finest chef in my family, really helped me throughout my study.

I cannot end without thanking everyone who directly or indirectly provided precious help to my study and work. This thesis is dedicated to all of you.

May 18, 2015

Wonjun Choi



